

Numerical experiments on reconnection in magnetic field configurations containing null points and separators

Daniel Thomas Chambers

A thesis submitted for the degree of PhD
at the
University of St Andrews



2021

Full metadata for this item is available in
St Andrews Research Repository
at:

<https://research-repository.st-andrews.ac.uk/>

Identifier to use to cite or link to this thesis:

DOI: <https://doi.org/10.17630/sta/185>

This item is protected by original copyright

Candidate's declaration

I, Daniel Thomas Chambers, do hereby certify that this thesis, submitted for the degree of PhD, which is approximately 45,000 words in length, has been written by me, and that it is the record of work carried out by me, or principally by myself in collaboration with others as acknowledged, and that it has not been submitted in any previous application for any degree. I confirm that any appendices included in my thesis contain only material permitted by the 'Assessment of Postgraduate Research Students' policy. I was admitted as a research student at the University of St Andrews in February 2017. I received funding from an organisation or institution and have acknowledged the funder(s) in the full text of my thesis.

Date **27-09-21** Signature of candidate

Supervisor's declaration

I hereby certify that the candidate has fulfilled the conditions of the Resolution and Regulations appropriate for the degree of PhD in the University of St Andrews and that the candidate is qualified to submit this thesis in application for that degree. I confirm that any appendices included in the thesis contain only material permitted by the 'Assessment of Postgraduate Research Students' policy.

Date **27/09/2021** Signature of supervisor

Permission for publication

In submitting this thesis to the University of St Andrews we understand that we are giving permission for it to be made available for use in accordance with the regulations of the University Library for the time being in force, subject to any copyright vested in the work not being affected thereby. We also understand, unless exempt by an award of an embargo as requested below, that the title and the abstract will be published, and that a copy of the work may be made and supplied to any bona fide library or research worker, that this thesis will be electronically accessible for personal or research use and that the library has the right to migrate this thesis into new electronic forms as required to ensure continued access to the thesis.

I, Daniel Thomas Chambers, confirm that my thesis does not contain any third-party

material that requires copyright clearance. The following is an agreed request by candidate and supervisor regarding the publication of this thesis:

Printed copy

No embargo on print copy.

Electronic copy

No embargo on electronic copy.

Date **27-09-21** Signature of candidate

Date *27/09/2021* Signature of supervisor

Underpinning Research Data or Digital Outputs

Candidate's declaration

I, Daniel Thomas Chambers, hereby certify that no requirements to deposit original research data or digital outputs apply to this thesis and that, where appropriate, secondary data used have been referenced in the full text of my thesis.

Date **27-09-21** Signature of candidate

Acknowledgements

I would like to thank my supervisors, Clare Parnell and Thomas Neukirch, for their guidance during the course of my studies. I am also grateful to Ben Williams for allowing me to make frequent use of the MSAT codes.

Funding

This work was supported by STFC (Science and Technology Facilities Council) [Grant number: ST/N504415/1]

Abstract

Magnetic fields containing null points offer favourable conditions for reconnection. In this thesis, numerical experiments attempt to gain insight into the reconnection process at these topological features.

Null point reconnection is studied under the assumption that the initial state is a quasi-equilibrium. A non-equilibrium field with a current density component parallel to the fan plane is relaxed ideally to obtain the initial condition, forming fan current layers centred on the null point. Rapid reconnection occurs at the beginning of the resistive experiment, before there is a transition to impulsive behaviour. The orientation of the initial current density relative to the strongest magnetic field in the fan plane determines the current layer dimensions and also influences the reconnection rate.

A single separator magnetic field is derived from the 2D Corrugated Sheet Pinch by the addition of a perturbation magnetic field. The evolution of the system is investigated numerically, using the 3D field with the pressure profile from the 2D case. The current is transferred from the original current sheet to the separatrix surfaces and null point bifurcations occur.

A potential double separator field is used as the basis for a study of reconnection at multiply-connected null points. The potential field is perturbed by the addition of flux rings and ideal relaxation results in a quasi-equilibrium with separator current layers. In the resistive experiment, reconnection occurs at the centre of the separators and its effects are localised.

In each of the experiments containing a single null point, reconnection occurs at current layers in the vicinity of the null. When there are multiple nulls connected by separators, the reconnection often takes place away from the nulls. However, the dynamics of separator reconnection appear to be influenced by the choice of initial conditions.

Contents

1	Introduction	1
1.1	Magnetohydrodynamics	6
1.1.1	Maxwell's Equations	7
1.1.2	Fluid Equations	8
1.2	Magnetic Topology	9
1.2.1	Magnetic Null Points	10
1.2.2	Separators	12
1.2.3	Observations	12
1.2.4	Extrapolations	13
1.3	Magnetic Reconnection	14
1.3.1	2D Reconnection	14
1.3.2	3D Reconnection	16
1.3.3	Reconnection Models	18
1.3.4	Applications	19
1.4	Lare3D	21
1.4.1	Equations	22
1.4.2	Grid	22
1.4.3	Timestep	23
1.4.4	Lagrangian Step	24
1.4.5	Remap Step	25
1.4.6	Viscosity	26
1.4.7	Resistivity	28
1.5	Magnetic Skeleton Analysis Tools	28
1.5.1	Null Finder	28
1.5.2	Sign Finder	29
1.5.3	Separatrix Surface Finder	30
2	3D Null Point Reconnection	31
2.1	Introduction	31
2.2	Initial Setup	33
2.3	Nulls with Current Parallel to Major Axis	35
2.3.1	Relaxation	36

2.3.2	Energies	41
2.3.3	Reconnection Rate	46
2.3.4	Flows	49
2.4	Nulls with Current Perpendicular to Major Axis	55
2.4.1	Relaxation	55
2.4.2	Energies	56
2.4.3	Reconnection Rate	60
2.4.4	Flows	61
2.5	Nulls Without a Major Axis	63
2.5.1	Relaxation	64
2.5.2	Energies	65
2.5.3	Reconnection Rate	66
2.6	Discussion	68
3	Single Separator Reconnection	70
3.1	Introduction	70
3.2	Analytical Field	71
3.2.1	Harris Sheet	72
3.2.2	Corrugated Sheet Pinch	73
3.2.3	3D Magnetic Field	74
3.3	Numerical Setup	76
3.3.1	Initial Magnetic Topology	76
3.3.2	Current Density	78
3.3.3	Forces	79
3.4	Reconnection from Non-equilibrium	79
3.5	Parameter Study	90
3.5.1	Varying b , c and r	90
3.5.2	Varying d	93
3.5.3	Varying α	96
3.6	Ideal Relaxation	97
3.7	Reconnection from Quasi-equilibrium State	102
3.8	Discussion	106

4	Multi-separator Reconnection	108
4.1	Introduction	108
4.2	Double Separator Potential Field	110
4.2.1	Derivation	110
4.2.2	Parameter Study	114
4.3	Non-potential Component	119
4.3.1	Introduction	119
4.3.2	Mathematical Form of the Flux Ring	120
4.3.3	Flux Ring Parameters	121
4.4	MHD Relaxation	123
4.4.1	Initial Setup	125
4.4.2	Separatrix Surfaces	125
4.4.3	Perpendicular Magnetic Field	126
4.4.4	Energies	127
4.4.5	Current Density	128
4.4.6	Forces	130
4.5	Summary of the Relaxation	132
4.6	Reconnection	133
4.6.1	Energies	134
4.6.2	Parallel Electric Field	136
4.6.3	Connectivity Changes	140
4.6.4	Flows	141
4.7	Six Separator Case	146
4.7.1	Energies	147
4.7.2	Parallel Electric Field	148
4.7.3	Flows	151
4.8	Asymmetric Cases	152
4.9	Discussion	155
5	Conclusions	158
6	Appendix	164

1 Introduction

Magnetic reconnection is a phenomenon that can occur in a wide variety of astrophysical settings. In this thesis, the context will be the solar atmosphere. A detailed introduction to solar physics can be found in Stix (2004), Lang (2006) and Priest (2014). The following section will briefly describe the layers of the Sun, journeying from the core to the solar wind.

The Sun is a Yellow Dwarf star that formed 4.6 billion years ago due to the collapse of a giant molecular cloud. It was composed (as it is today) primarily of hydrogen with a smaller amount of helium and fragments of heavier elements. The star is currently at the midway point in the *main sequence* of its lifecycle. This means it releases energy by fusing hydrogen atoms to produce helium. Once the stores of hydrogen in the core have been exhausted, the Sun will expand dramatically to become a Red Giant. It will then convert helium to carbon in its core and hydrogen will be burned in a shell surrounding the core. This process will continue for a billion years until the supply of helium expires. The outer layers of the Sun will then be ejected as a nebula, leaving behind a White Dwarf.

The gases that make up the Sun are typically ionised because of the high temperatures in the interior and outer atmosphere. These ionised gases are known as *plasma* and due to their abundance of charged particles, are excellent electrical conductors. The plasma can therefore generate a magnetic field, a process that is said to occur in the *solar dynamo* and the plasma and magnetic field strongly influence each other. This interaction is studied mathematically in a model known as *magnetohydrodynamics*, which is the basis for the work in this thesis. The details of the mathematical formulation will be introduced in section 1.1.

The core of the Sun is the hottest ($15 \times 10^6\text{K}$) and densest ($1.6 \times 10^5\text{kgm}^{-3}$) of its layers because of the strong gravitational force exerted by the surrounding mass. These conditions are sufficiently extreme not only to completely ionise the hydrogen atoms but also to power nuclear fusion- the combination of four protons to form helium. Two of these protons are converted to neutrons with the charge carried away by positrons and the additional mass transferred to neutrinos. The radiation that is produced during

this process consists largely of gamma rays but owing to the high density of the solar interior, the photons carrying the radiation experience a large number of collisions with the solar matter. The time taken for these photons to reach the surface of the Sun is of the order 10^6 years. At a distance of approximately 0.2 times the radius of the Sun, the radiative zone is reached by the propagating radiation. In this region, the temperature is not sufficient to burn hydrogen but the radiation can make faster progress since there are fewer collisions. By the time the radiation leaves the interior of the Sun, the frequency has diminished to such an extent that it mostly occupies the visible part of the spectrum.

At the top of the radiative zone, in a thin layer known as the Tachocline, the solar dynamo is believed to generate the Sun's magnetic field. Although the process by which this occurs is not fully understood, it is thought to be linked to the differential rotation that occurs in the photosphere and convective zone. At the photosphere, the equator completes one rotation in 25 days while the poles are slower and have a rotational period of 33 days. This effect can also be found in the upper part of the interior but not in the radiative zone or core, which rotate rigidly. At the interface between these two rotational regimes, there is a shearing effect on the poloidal magnetic field, stretching it towards the equator to introduce a toroidal component.

The shearing at the Tachocline is only one half of the dynamo process, as the poloidal field needs to be generated somewhere before it is disturbed by the differential rotation. There are a number of proposed mechanisms for this (Charbonneau (2020)) but they are generally thought to occur at a greater distance from the centre of the Sun, whether in the convective zone or the Photosphere (the visible surface). The Convective Zone begins at a distance of 0.713 radii, where the density has decreased further to $2 \times 10^{-4} \text{kgm}^{-3}$ and the temperature is 10^6K . In this region, much of the radiation that has travelled from the core is absorbed, causing temperature increases at the base of the layer. The gas here expands and rises, since it is less dense than the surrounding matter. These columns of hot plasma rise to the surface and once the radiation is released as visible light, the plasma cools and falls at the edge of the columns.

The imprint of the convective cells is seen on the photosphere in the granulation pattern in visible light images. The surface is made up of millions of granules, the bright centres

of which contain the hot plasma, contrasting with the cooler plasma sinking at the boundaries. These granules typically have a length of 1Mm and are superimposed on larger (20 – 70Mm) supergranular cells. The supergranulation pattern is not properly understood (Rincon and Rieutord (2018)) but it is also linked to convection in the interior. Other distinctive features of images of the photosphere include sunspots—regions of strong magnetic field that locally reduce the amount of convection. Since hot plasma cannot rise in these areas, they are cooler and appear as dark spots in visible light images. Sunspots are an indicator of solar activity and their numbers follow an 11 year cycle. At solar minimum, the solar surface appears unblemished due to the lack of sunspots, although there is still a large amount of small scale magnetic activity. The sunspots first appear around 30 degrees latitude in both hemispheres and as the cycle progresses, the total number increases and the new spots form closer to the equator. Individual sunspots have variable duration (of the order 0.01-1 months) and the number varies from less than 10 at solar minimum to as many as 200 at solar maximum mid-way through the cycle. Sunspots typically occur in pairs in bipolar active regions and the leading polarity is that which appears closer to the direction of rotation. The leading polarity is different in the two hemispheres and switches every 11 years. The Sun’s dipole field also reverses at the end of each cycle. The sunspots become clustered close to the equator and it is thought (Petrie (2015)) that the leading polarities of the two hemispheres may cancel, leaving the opposite polarities which are transported to the poles by meridional flows.

Beyond the photosphere, the Chromosphere covers a distance of 1700km. In the quiet sun (away from sunspots), the magnetic field and plasma flows are shaped by the supergranulation pattern. Strong magnetic flux occurs at the boundaries of supergranules, sometimes looping to form fibrils connecting flux from adjacent boundaries but also extending radially into the Corona. Jets of plasma known as spicules occur in these regions of radial field (and also in active regions) travelling at speeds of up to 100kms^{-1} and reaching heights of up to 10000km. The Chromosphere is imaged by using H-alpha filters to detect a particular wavelength of red light. Bright spots in these images (referred to as *plage*) are evidence of strong magnetic field, aligned with the sunspots in the photosphere, while dark ribbons known as filaments are cool, dense plasma structures supported by the magnetic field. In the lower part of this layer, the temperature

reaches a minimum of 4000K before beginning to rise gradually with height to around 10^4 K. The temperature increases rapidly to 10^5 K over the 300km Transition Region between the Chromosphere and Corona. This temperature increase continues into the Corona, where the temperature peaks at over 10^6 K. One of the key questions in modern solar physics is how the Coronal temperature is sustained (Klimchuk (2006)). The flow of thermal energy from the cool surface into the hot Corona would appear to violate the laws of thermodynamics.

The Corona can only be observed in visible light during an eclipse but it emits X-ray and EUV radiation, which can be detected using satellites. Common features of the Coronal magnetic field include coronal loops, which connect oppositely signed magnetic flux in the active regions identified in the Photosphere. These can vary in length from 10 to 1000Mm and their shape is approximately semi-circular (Reale (2014)). The duration is usually around a day for single loops. X-ray bright points are caused by miniature (around 1Mm) loops from ephemeral active regions which emerge in the interior of supergranules before splitting and merging with the network flux, leaving a Coronal signature that lasts for 8 hours on average. Coronal holes are regions of open magnetic field that map to locations dominated by a single polarity in the lower atmosphere. They mostly occur near to the polar regions but can also be found within active regions. The Corona is dominated by the magnetic field (a fact demonstrated mathematically in section 1.1), which means that the plasma is almost everywhere constrained to follow the magnetic field. Coronal jets are an example of this (Raouafi et al. (2016)), moving along the magnetic field in coronal holes at typical speeds of 200kms^{-1} and reaching heights of 50Mm.

Coronal loops play an important role in powering the most explosive phenomena in the solar system- flares and coronal mass ejections (CMEs). Solar flares are instances of brightened emission at multiple wavelengths (chiefly X-rays and radio waves) caused by a sudden release of stored magnetic energy. Coronal mass ejections expel plasma into inter-planetary space and make the most significant contribution to the space weather affecting communications and power grids on Earth. These events are frequently discussed together, since they often occur in tandem as different stages in a single process. Some CMEs are the direct consequence of the most powerful flares of the X or M class but it is also true that CMEs can happen in the absence of flares.

Solar flares typically originate at coronal loops in active regions, where an abrupt loss of force balance in the plasma causes magnetic energy to be converted to kinetic energy and causes particle acceleration. These charged particles (both electrons and ions) can stream away from the Sun along the solar wind but electrons also travel along the loop to collide with the chromosphere. When leaving the energy release site, these particles are moving at relativistic speeds, meaning they emit non-thermal radiation as they collide with the dense region below. This radiation is caused by the interaction of a beam of charged particles with a dense target and mostly produces hard X-rays (HXR). HXRs are found at the coronal loop footpoints, where they align with H-alpha brightening known as flare ribbons, and also sometimes at loop-top sources. The impact of the particle beam with the chromosphere causes the plasma to heat and expand into the Corona in a process known as chromospheric evaporation. As the plasma from the chromosphere fills up the coronal loop structure, it emits soft X-rays by thermal radiation. The lifecycle of a flare is usually split into three stages, namely the pre-flare, impulsive and decline phases. In the pre-flare and decline phases, thermal SXR emissions predominate, whereas the impulsive phase is characterised by HXR non-thermal radiation.

Coronal mass ejections occur most frequently during solar maximum, since they are commonly associated with flaring active regions. Yashiro et al. (2006) found that flares in the C5.7-M3.2 range are accompanied by CMEs in 40 – 60% of cases. The average number of CMEs per day has been estimated to lie between 3 and 8 at solar maximum, while the number is 0.2 to 0.5 at solar minimum. According to Gopalswamy et al. (2003), 73% of prominence (the name for filaments when viewed at the solar limb) eruptions are linked to CMEs. The CMEs that are not accompanied by any obvious flare signatures can be caused by the eruption of quiescent prominences or streamer (elongated loop) blowouts. These occur in the quiet Sun and near the polar caps, where owing to the weaker magnetic field, they propagate at slower speeds of less than 600kms^{-1} compared with 3000kms^{-1} in active regions. So-called *Stealth CMEs*, which lack clear observational signatures in the low corona, are of interest to those engaged in space weather forecasting (Robbrecht et al. (2009)).

Many models have been suggested for the formation and development of flares/CMEs. The standard 2D model for erupting filaments is known as the CSHKP model (Carmichael

(1964), Sturrock (1966), Hirayama (1974), Kopp and Pneuman (1976)). The basis for this model is a prominence which lies above a coronal loop, supported by a magnetic flux rope- a section of twisted closed field. In between the coronal loop and the flux rope, the magnetic topology favours current build-up. According to theory, this flux rope moves upwards prior to the flare, causing a long thin current sheet to appear above the loop top. This current sheet is susceptible to resistive instability, which leads to magnetic reconnection (defined in section 1.4) and the acceleration of charged particles required for the flare non-thermal emission. During the impulsive phase of the flare, plasma outflows accelerate the outer loop of the CME. The remnants of the filament form the bright core of the CME, which is separated from the loop by a cavity that has been drained by the mass flows. This model has clear limitations in that it only offers a 2D explanation of the most intense eruptive events involving a prominence, flare and CME. In reality, these events need not all occur together as previously mentioned but the model remains relevant to the most important cases.

The solar wind consists of plasma that has been released from the outer Corona, where the gravitational force is too low to arrest the expansion caused by high temperatures. It extends across the solar system in all directions, becoming cooler and less dense with increasing distance before terminating after around 100AU. The plasma propagates along the radial magnetic field above coronal holes and streamers. The open magnetic field from coronal holes is associated with the fast solar wind, which travels at speeds of 750kms^{-1} . These occur close to the poles at solar minimum but also at lower latitudes later in the cycle. The origins of the slower wind, which propagates at 400kms^{-1} , are an active area of research (Antiochos et al. (2011)). These speeds are maintained across the vacuous interplanetary space.

1.1 Magnetohydrodynamics

Mathematical descriptions of space plasmas broadly fall into three categories- particle, kinetic and fluid models. The particle models consider the motion of individual particles in the presence of electric and magnetic fields. Kinetic theory describes larger scale systems in a microscopic way by using particle distribution functions. The fluid description averages the quantities (magnetic field, velocity, pressure, etc.) over different particles

(and different species of particle) to provide a macroscopic view of the plasma. This thesis will use the single fluid model *magnetohydrodynamics*, which combines Maxwell's equations of electrodynamics with the fluid equations.

1.1.1 Maxwell's Equations

The *Ampere-Maxwell Law* states that magnetic fields can be generated by electric currents or changing electric fields,

$$\nabla \times \mathbf{B} = \mu_0 \mathbf{j} + \frac{1}{c^2} \frac{\partial \mathbf{E}}{\partial t}. \quad (1)$$

In non-relativistic settings where the characteristic speeds of the plasma are much less than the speed of light, the displacement current term is neglected. According to this assumption, magnetic fields are generated exclusively by electric currents.

Gauss' Law for Magnetism or the *solenoidal constraint* states that magnetic fields cannot contain any sources or sinks. In other words, there are no magnetic monopoles,

$$\nabla \cdot \mathbf{B} = 0. \quad (2)$$

The *Faraday-Maxwell Equation* states that temporal changes in the magnetic field result in spatial changes in the electric field,

$$\frac{\partial \mathbf{B}}{\partial t} = -\nabla \times \mathbf{E}. \quad (3)$$

Gauss' Law states that the electric flux through a closed surface is given by the charge density (ρ^*) within the surface divided by the permittivity of free space (ϵ_0),

$$\nabla \cdot \mathbf{E} = \frac{1}{\epsilon_0} \rho^*. \quad (4)$$

This equation is not used in MHD because the plasma is assumed to be electrically neutral, meaning the number of positive ions and electrons are similar. The charge density can therefore be neglected.

Ohm's Law states that the current density is proportional to the sum of the electric

field at rest and the electric field due to plasma motion through the magnetic field,

$$\mathbf{j} = \sigma(\mathbf{E} + \mathbf{v} \times \mathbf{B}). \quad (5)$$

The constant of proportionality is the conductivity σ , which is the inverse of the resistivity η .

By combining Faraday's Law and Ohm's Law, one arrives at the induction equation. According to this, the magnetic field changes due to advection and diffusion,

$$\frac{\partial \mathbf{B}}{\partial t} = \nabla \times (\mathbf{v} \times \mathbf{B}) + \eta \nabla^2 \mathbf{B}. \quad (6)$$

The magnetic Reynolds number, R_m , is defined as the ratio of the order of magnitude estimates for the advective and diffusive terms,

$$R_m = \frac{vB/l}{\eta B/l^2} = \frac{vl}{\eta}. \quad (7)$$

If $R_m \gg 1$, diffusion occurs much slower than the characteristic timescale of the plasma and the magnetic field is said to satisfy the *frozen-in condition*. In these conditions, magnetic flux is constrained to follow the plasma motions. In the other limit, $R_m \ll 1$, diffusive effects are dominant, as the magnetic field evolves to reduce flux concentrations. In the solar Corona, the resistivity according to Spitzer (Cohen et al. (1950)) is approximately $1\text{m}^2\text{s}^{-1}$. Disturbances typically propagate at the Alfvén speed $v_A = 10^6\text{ms}^{-1}$, so a length scale $l \ll 10^{-6}\text{m}$ is required for the diffusive limit to be activated. This is achievable at current sheets/layers whose thickness can be comparable with the ion skin depth.

1.1.2 Fluid Equations

The continuity equation is the statement of conservation of mass in a fluid. The rate of change of the density is equal to the total mass flowing into or out of the system,

$$\frac{\partial \rho}{\partial t} + \nabla \cdot (\rho \mathbf{v}) = 0. \quad (8)$$

The momentum equation is the analogue of Newton's second law in the context of fluid dynamics. The rate of change of momentum of the fluid is equal to the sum of the forces acting on it,

$$\rho \frac{D\mathbf{v}}{Dt} = -\nabla p + \mathbf{j} \times \mathbf{B} + \rho \mathbf{g} + \mathbf{F}_\nu. \quad (9)$$

The body forces (Lorentz force and gravitational force) act within the volume of the fluid whereas contact forces (pressure gradient and viscous force) act on the exterior surface. A plasma is in equilibrium if the sum of the force densities on the right hand side is zero, i.e. the velocity is steady.

The ideal gas law is the equation of state describing a gas without particle interactions,

$$p = nk_B T. \quad (10)$$

The number density n is the total number of particles per unit volume and $k_B = 1.381 \times 10^{-23} JK^{-1}$ is the Boltzmann constant.

The energy equation states that the rate of change of heat is due to the sum of the energy sinks and sources, which constitutes the energy loss function \mathcal{L} ,

$$\frac{\rho^\gamma}{\gamma - 1} \frac{d}{dt} \left(\frac{p}{\rho^\gamma} \right) = -\mathcal{L}. \quad (11)$$

The ratio of specific heats, $\gamma = c_p/c_V$, compares the amount of heat required to produce a unit change in temperature at constant pressure and at constant volume. In this thesis, $\gamma = 5/3$ will be assumed, which applies to gases with three degrees of freedom that are composed of single atoms.

1.2 Magnetic Topology

The study of magnetic topology is concerned with the basic nature of the magnetic field. The building blocks of the field are magnetic null points, which demarcate regions of oppositely signed magnetic flux. In a 3D system containing multiple null points, these can be connected by separators. In ideal MHD, the topology of a system is fixed in the sense that no nulls or separators can be created or destroyed. Fieldlines can bend and

move smoothly towards or away from each other, including those which compose the topological features but it is only in a resistive setting that the topology can change. The mechanism by which this takes place is magnetic reconnection, which will be studied in detail in later chapters.

1.2.1 Magnetic Null Points

Magnetic null points are locations where all three components of the magnetic field are exactly zero. The properties of linear three dimensional null points were first studied by Cowley (1973) and Fukao et al. (1975), before Parnell et al. (1996) established the categorisation that is widely used today. Such null points have the form:

$$\mathbf{B} = \mathbf{M} \cdot \mathbf{r}, \quad (12)$$

where $\mathbf{r} = (x, y, z)^T$ and the matrix \mathbf{M} can be reduced to the form:

$$\mathbf{M} = \begin{pmatrix} 1 & \frac{1}{2}(q - j_{sp}) & 0 \\ \frac{1}{2}(q + j_{sp}) & b & 0 \\ 0 & j_f & -(b + 1) \end{pmatrix}. \quad (13)$$

Here $b \geq -1$ and $q^2 \leq j_{sp}^2 + 4b$. The matrix has eigenvalues of the form:

$$\lambda_{1,2} = \frac{b + 1 \pm \sqrt{j_{thresh}^2 - j_{sp}^2}}{2}, \quad \lambda_3 = -(b + 1), \quad (14)$$

where the threshold current is defined as $j_{thresh} = \sqrt{(b - 1)^2 - q^2}$. One of the eigenvalues has opposite sign to the other two: a consequence of the fact that the trace of the matrix must be zero to satisfy the solenoidal constraint. According to this definition of \mathbf{M} , which is valid for a positive null point, the eigenvalue λ_3 whose eigenvector is the z -axis must be negative. This eigenvector defines the position of the spine of the null, which is a line that is hyperbolically approached by the fieldlines as they enter or leave the null point. A null point with two positive eigenvalues is described as positive, while a negative null has two negative eigenvalues. For a positive null, fieldlines approach the null along the spine and recede from the null across the fan plane. This

plane, sometimes referred to as a separatrix surface, is defined by the two eigenvectors corresponding to the other eigenvalues.

There are further subcategories of magnetic null points introduced in Parnell et al. (1996) that will be studied in the chapter regarding null point reconnection. These different types, spiral and radial nulls, relate to the importance of the parallel and perpendicular current terms in (13).

All null points that have $|j_{sp}| < j_{thresh}$ are of radial type. The name refers to the behaviour of the fieldlines in the fan plane. For a proper radial null, the fieldlines are truly radial as one would expect, meaning they emanate from the null point (for a positive null) with equal spacing and there is no azimuthal variation in the field strength. This is only achievable for a potential (current-free) null with the parameter choice $b = 1$ in (13). If the value of b is varied, the radial null becomes improper, as the fieldlines in the fan plane no longer have azimuthal symmetry, instead being concentrated upon a major axis. For a potential null with the separatrix surface coincident with the x - y plane, setting $b = 2$ locates the major axis along $x = 0$ while a choice of $b = 0.5$ gives a major axis at $y = 0$.

Improper nulls can also be found having a non-zero current density, so long as the magnitude of the parallel component is less than the threshold current. When the parallel component is equal to zero, this is always satisfied except where $b = j_{thresh} - 1$ and the null is reduced to a continuum of 2D X-points. A non-zero perpendicular component of current breaks the orthogonality of the spine and fan so this case is sometimes referred to as a skewed improper null. The final case is where the perpendicular component is zero but the parallel component is insufficiently large. The spine is once more perpendicular to the fan but the fieldlines show a preference for a major axis in the fan plane.

Spiral nulls have a parallel component of current that exceeds the threshold. The name indicates that the fieldlines in the fan plane spiral about the spine line. The amount of twist experienced by these fieldlines is determined by the magnitude of j_{sp} and the parameter b determines the major axis where the fieldline density is the highest. If there is a non-zero j_f then the fan plane will be tilted as in the improper examples.

1.2.2 Separators

Generic linear null points are created in oppositely signed pairs (Murphy et al. (2015)), which are typically connected to each other by separator lines. The separator marks the intersection of the separatrix surfaces of two oppositely signed nulls. It divides four distinct regions of magnetic connectivity, known as flux domains. A single pair of null points can be connected by multiple separators and Close et al. (2004) found an average of 10.1 separators per null in their model field derived from a distribution of photospheric point sources. Just 1.8% of their nulls were unconnected and the maximum number of separators connecting a single null was 100.

1.2.3 Observations

Null points in the solar corona cannot be observed directly, as the magnetic field is currently only measured at the photosphere. In spite of this fact, there have been attempts to infer the presence of null points using observational signatures. For example, Filippov (1999) presented Fe IX/X images showing the coronal loops in Active Region NOAA 8113, focusing on an X-type structure representative of the hyperbolic field around a null point. The appearance of the structure was attributed to the emergence of parasitic flux but did not show the increased temperatures expected from the reconnection accompanying such an event. More recently Sun et al. (2014) identified another X-shaped structure where four groups of coronal loops appear to converge in AIA images of an active region. The authors suggest that flares caused by flux emergence in one of the loop clusters could have caused reconnection and the eventual collapse of the null, which also coincided with a jet eruption. They also used non-linear force free-field extrapolations, an alternative to the PFSS model described in the next section, showing good agreement between modelling and observations regarding the existence of a null point. Another example of a mixed approach combining observations and extrapolations can be found in Freed et al. (2015). They undertook a survey using PFSS extrapolations over a three year period to identify possible null point locations and then manually cross-referenced these predictions with SDO/AIA observations to attempt to find the requisite saddle/X-point structures. Of the 582 null points predicted by the model, 31% showed up in the observations, although a further 19% of the images were

saturated.

1.2.4 Extrapolations

The presence of null points in the corona has been further supported by extrapolations using the photospheric magnetic field data as a boundary condition to solve for the coronal field. The most common method used for such extrapolations is the Potential Field Source Surface (PFSS) model, which assumes that the coronal magnetic field is potential. When this assumption is combined with the solenoidal constraint, it is possible to solve Laplace's equation and then determine the magnetic field. The equation is solved analytically subject to the boundary conditions that B_r is prescribed at the photosphere and the field is radial beyond a certain radius, usually taken to be around 2.5 solar radii.

Régnier et al. (2008) used the line-of-sight magnetograms from Hinode/SOT to perform PFSS extrapolations for a $102 \times 116Mm$ field of view. They found 80 nulls in total, only two of which were located in the corona. Cook et al. (2009) performed a global analysis using synthetic synoptic maps created by simulations of flux transport. Their study was mostly concerned with nulls occurring at high altitudes over active regions. The number of nulls appeared to be correlated with the solar cycle, with 15-17 nulls typically appearing per day during solar maximum. These nulls were mostly found at lower latitudes so most did not connect to the global dipole and there was little difference between the rising and declining phases. Platten et al. (2014) undertook a comprehensive survey of the topological features resulting from global extrapolations using Kitt Peak/SOLIS magnetograms covering a 37 year period. Global features such as the Heliospheric Current Sheet, Heliospheric curtains, separatrix domes/tunnels and separators were all identified. In contrast with Cook et al. (2009), the number of nulls was found to be greatest at solar minimum, although the previous study did not attempt to resolve the small scale flux features, instead prioritising the bipolar active regions. Edwards and Parnell (2015) used global magnetograms from MDI, HMI and SOLIS for their PFSS extrapolations. They found that the number of nulls is generally out of phase with the solar cycle except at high altitudes, thereby reconciling the previous works. Another feature of their work is the larger total number of nulls that results

from using higher resolution magnetograms, coupled with a larger number of spherical harmonics during the PFSS calculations. They were able to find between 1000-2500 nulls per Carrington rotation compared with the 40-120 in Platten et al. (2014).

1.3 Magnetic Reconnection

Magnetic reconnection has long been believed to be an important process in astrophysical plasmas. In general terms, reconnection is the fundamental change in the magnetic field connectivity that occurs in high current regions. The process acts to convert magnetic energy into heat and kinetic energy. It was studied extensively in two dimensions before computational limitations were lifted in the 1990s, allowing the three dimensional process to be explored.

1.3.1 2D Reconnection

There are two classical models of 2D reconnection upon which much of the early literature was based. These are the original Sweet-Parker model (Parker (1957), Sweet (1958)) and the Petschek model (Petschek (1964)). The Sweet-Parker model was hailed as a major breakthrough, since it reduced the timescales upon which diffusion could take place by several orders of magnitude but it could not explain the accelerated energy release that had been observed in solar flares. Petschek was able to improve this rate of reconnection mathematically so that in the limiting case where the length scale approaches a minimum, the fast reconnection required for solar flares could be achieved. The Petschek model has been challenged by authors including Biskamp (1986) and Uzdensky and Kulsrud (2000), who found that the long thin reconnection region proposed by the Sweet-Parker model was more appropriate.

The Sweet-Parker model consists of a null point embedded in a hyperbolic magnetic field that has undergone X-point collapse. As a result of the null point collapse, the fieldlines in the vicinity of the null are now running parallel to the x -axis and since the separatrices of a null point divide regions of oppositely directed magnetic field, the fieldlines are anti-parallel with a current layer enveloping the null point and neighbouring fieldlines. This model makes a number of simplifying assumptions, including that the reconnection is

a steady state with a balance of fluxes into and out of the current layer and also that the effects of resistivity are confined to the current layer. The length $2L$ of the current layer (also known as the diffusion/reconnection region) is assumed to greatly exceed the width $2l$. The inflows move perpendicular to the magnetic field in the y -direction, whereas the outflows are parallel to the length of the current layer (and to the magnetic field close to the null point).

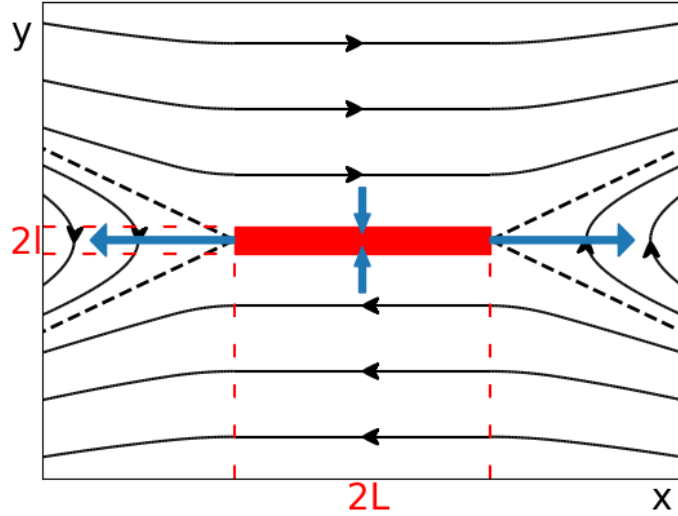


Figure 1: Sweet-Parker reconnection. Magnetic fieldlines are shown in black; blue arrows indicate the plasma flows into and out of the current layer (red).

The fundamental result of the model is obtained by an order of magnitude analysis. The resistive electric field in the vicinity of the null point is matched with the electric field away from the null point due to the magnetic force. Conservation of mass is then used to obtain a relationship between the inflows and outflows. Lastly, it is assumed that the initial magnetic energy is converted entirely to kinetic energy, meaning the outflows travel at approximately the Alfvén speed $v_A = B/\sqrt{\mu\rho}$. The inflow velocity is an estimate for the reconnection rate:

$$\frac{v_{in}}{v_{out}} \approx \frac{l}{L} \approx \sqrt{\frac{\eta}{\mu L v_A}}. \quad (15)$$

Petschek modified the Sweet-Parker model by including slow mode shock waves that

spread diagonally from the corners of the diffusion region. These shock waves have the effect of diverting the inflows so that only the plasma close to the null passes through the diffusion region. This greatly improves the efficiency of the model, as the Sweet-Parker reconnection rate is limited by the large amount of plasma passing through the diffusion region, which needs to flow out of its narrow width. Because of the redirection of the inflows, the length of the Petschek diffusion region is similar to its width and much less than the global length scale. Petschek derived a maximum possible reconnection rate for the model (corresponding to the minimum diffusion region length) of $\pi v_A/8 \ln S$, where S is the Lundquist number, which is equivalent to the magnetic Reynolds number with $v = v_A$.

1.3.2 3D Reconnection

First consider an ideal fluid satisfying Ohm's law,

$$\mathbf{E} + \mathbf{v} \times \mathbf{B} = 0. \quad (16)$$

For a flux tube within this magnetic field, all plasma elements initially composing the tube will remain a part of the structure at later times. The rate of change of the magnetic flux through the surface is given by:

$$\frac{d}{dt} \int \mathbf{B} \cdot \mathbf{ds} = \int \frac{\partial \mathbf{B}}{\partial t} \cdot \mathbf{ds} + \int \mathbf{B} \cdot \mathbf{v} \times \mathbf{ds}. \quad (17)$$

The second integral on the right expresses the change in the boundary C during the time dt resulting in a new area $\mathbf{v} \times \mathbf{ds}dt$. The two integrals can be combined by using the fact that $\mathbf{B} \cdot \mathbf{v} \times \mathbf{ds} = -\mathbf{v} \times \mathbf{B} \cdot \mathbf{ds}$ and making use of Stokes' theorem,

$$\frac{d}{dt} \int \mathbf{B} \cdot \mathbf{ds} = \int \left[\frac{\partial \mathbf{B}}{\partial t} - \nabla \times (\mathbf{v} \times \mathbf{B}) \right] \cdot \mathbf{ds} = 0. \quad (18)$$

The new integrand is zero according to the ideal induction equation. Hence magnetic flux is conserved- a result known as Alfvén's frozen flux condition.

By considering two intersecting flux tubes that have a single fieldline in common, the result can be extended to give fieldline conservation. In each of the flux tubes, the

magnetic flux is frozen in to the plasma so if a fieldline is common to both tubes initially, it will remain a constituent part of both. Since this argument can be applied to any fieldline in an ideal plasma, it is clear that flux conservation implies fieldline conservation. In a non-ideal plasma,

$$\mathbf{E} + \mathbf{v} \times \mathbf{B} = \mathbf{R}. \quad (19)$$

where \mathbf{R} is the sum of the resistive terms in Ohm's law. For flux conservation to be satisfied in a non-ideal plasma, the following condition has to be satisfied by the resistive term:

$$\nabla \times \mathbf{R} = 0. \quad (20)$$

This is equivalent to requiring that the ideal form of the induction equation (6) is satisfied. As before, if the plasma conserves magnetic flux, fieldline conservation follows automatically. The reverse is not true however, as the definition of fieldline conservation is less restrictive:

$$\mathbf{B} \times (\nabla \times \mathbf{R}) = 0. \quad (21)$$

Hence at null points ($\mathbf{B} = 0$), it is possible to have fieldline conservation but not flux conservation. Away from null points, the fieldline conservation condition can be written as $\nabla \times \mathbf{R} = \lambda \mathbf{B}$.

Building on the work of Axford (1984), Schindler et al. (1988) and Hesse and Schindler (1988) defined three dimensional magnetic reconnection as the localised breakdown of magnetic fieldlines, which is equivalent to the violation of fieldline conservation. As well as deriving the condition in (21), the authors stressed the importance of the integral of the parallel electric field,

$$\int \mathbf{E} \cdot \mathbf{B} \, dl. \quad (22)$$

If this integral is non-zero along a measurable set of fieldlines, there is global magnetic reconnection. Hesse and Birn (1993) further showed that the maximum absolute value of this integral gives the reconnection rate. Of the two mathematical statements, this is the more practical definition when dealing with numerical data and it will be frequently employed throughout this thesis.

The above definition was motivated by the discovery that three dimensional reconec-

tion does not occur exclusively at null points. Priest and Démoulin (1995) coined the term *quasi-separatrix layers* (QSLs) to describe regions of magnetic field where there is a large connectivity gradient. If the distance between two fieldlines in a QSL is small at one boundary, their footpoints at the other boundary will be far apart. They are the generalisation of the separatrix surfaces separating flux domains at a 3D null point but the difference is that at QSLs, the connectivity of fieldlines remains continuous.

1.3.3 Reconnection Models

- **Null point reconnection**

2D reconnection- which can only occur at magnetic null points- has been the subject of decades of research and is now quite well understood (Priest and Forbes (2000)). Recent modelling has studied the reconnection that occurs at 3D null points. The first such studies provided kinematic solutions for reconnection at a null with current aligned with the spine (Pontin et al. (2004)) and the fan (Pontin et al. (2005)). Pontin and Galsgaard (2007) performed a numerical experiment in which a perturbation field was added to a potential null point. Several experiments have introduced electric current to a potential null through boundary driving. In Pontin et al. (2007) the driving was applied to both the spine and fan footpoints in separate cases. Galsgaard and Pontin (2011b) used continuous driving to achieve a steady state, varying the magnitude of the driving velocity and the resistivity. Galsgaard and Pontin (2011a) varied the direction of the driver relative to the null eigenvalues, as well as considering both continuous and impulsive driving. Wyper and Pontin (2014b) used a driven configuration to study the tearing instability and resulting null point bifurcations. Recent studies have attempted to model solar phenomena, sometimes using extrapolated magnetic fields as the basis for simulations. Masson et al. (2009) and Baumann et al. (2013) have modelled solar flares using these techniques, while Pariat et al. (2009) offered a model for solar jets. A subset of these models will be discussed in more detail in chapter 2.

- **Separator reconnection**

The first work to raise the possibility of separator reconnection was Lau and

Finn (1990), which presented a kinematic model identifying potential reconnection sites with singularities in the perpendicular velocity. Longcope and Cowley (1996) proposed a method for current sheet formation, which would allow a separator configuration to asymptotically behave like a potential field. Galsgaard and Nordlund (1997) and Galsgaard et al. (2000b) performed a numerical experiment on a triply-periodic magnetic field containing eight nulls connected by separators. The force-free field is subjected to boundary driving and the resulting current redistribution and plasma evolution are discussed. Pontin and Craig (2006) superpose a disturbance to a background magnetic field containing two null points. The model details both the null point and separator reconnection that can occur depending on the magnitude of the disturbance. Galsgaard et al. (2000a) and Haynes et al. (2007) studied the separator reconnection that occurs when two magnetic null points are advected such that their separatrix surfaces pass through each other. Stevenson and Parnell (2015a) and Stevenson and Parnell (2015b) numerically investigated spontaneous reconnection at an equilibrium separator current layer. These works will be revisited in chapters 3 and 4 of the thesis.

1.3.4 Applications

We have seen that observations showing topological features in the solar atmosphere are scarce, owing to the difficulty of measuring the magnetic field and confirming the presence of a null point. In spite of this, the number of observations providing evidence of magnetic reconnection is quite large because of the accompanying flows and radiation.

- **Solar flares**

There are many studies linking magnetic reconnection to solar flares (Janvier (2017)). Early observational papers sought evidence to support the CSHKP model for eruptive flares. Masuda et al. (1994) found a hard X-ray source at the top of a coronal loop that was suggested as the location of the fast shock due to reconnection outflows. Shibata et al. (1995) claimed to observe these reconnection jets directly, arguing that their collision with the loop leads to plasma heating and particle acceleration. Tsuneta (1996) interpreted high temperature ridges

separated by a cool channel as evidence of slow shocks that fan out from the diffusion region (Petschek reconnection). Yokoyama et al. (2001) identified the plasma inflows to the X-point carrying magnetic flux into the reconnection site. Magnetic field extrapolations in flaring regions have discovered that the 3D field can contain both null points and QSLs (Masson et al. (2009) for example). The flare ribbons seen in H-alpha images correspond to the footpoints of QSLs (Yang et al. (2015)) and the apparent motion of the emission along these ribbons is indicative of slip-running reconnection (Chandra et al. (2011)). According to Reid et al. (2012), the QSLs have a greater capacity for energy release because their finite width allows for a longer current build-up than at null points. However null points play an important role in the magnetic breakout model (Antiochos et al. (1999)), which is one of the most popular descriptions of eruptive flares. An overview of the MHD models for solar flares can be found in Priest and Forbes (2002) and Shibata and Magara (2011). The observational literature is reviewed in Fletcher et al. (2011) and Benz (2017).

- **Earth’s magnetosphere**

The interaction of the solar wind with the Earth’s magnetosphere leads to a pattern of reconnection described by the Dungey cycle. The interplanetary magnetic field (IMF) carried by the solar wind meets the Earth’s dipole field at the magnetopause. If the IMF is directed antiparallel to the northward dipole field, reconnection will occur along the neutral line at the dayside magnetopause. During this reconnection, magnetic fieldlines emanating from the Earth are opened and carried along with the solar wind to form the lobes of the magnetotail on the opposite side of the Earth. The cycle is completed by reconnection occurring in a second neutral line in the magnetotail, which reattaches the open fieldlines to the Earth.

The Earth’s magnetosphere is one of the few places where magnetic reconnection can be directly observed. The Cluster (Escoubet et al. (2001)) and Magnetospheric Multiscale (Burch et al. (2016)) missions have been launched to provide high time resolution 3D observations using a tetrahedral configuration of instruments. The presence of null points (Xiao et al. (2006)) and separators (Guo et al. (2013)) has been inferred during reconnection at the magnetotail. Buzu-

lukova et al. (2017) also found a complex magnetic topology at the dayside magnetopause, with a separator being located within $0.5R_E$ of the diffusion region. Separator reconnection on the dayside has been modelled by Dorelli et al. (2007) and Glocer et al. (2016).

- **Laboratory**

Magnetic reconnection has been observed in laboratory experiments where the plasma is confined by toroidal and/or poloidal magnetic field configurations. A famous example is the sawtooth crash occurring in toroidal tokamak experiments, where the cross-section contains nested flux surfaces. The electron temperature becomes peaked in the central surfaces and a kink instability is excited, causing reconnection of adjacent flux surfaces and the flattening of the temperature profile. The Reversed Field Pinch is another example of a laboratory device susceptible to reconnection. The setup has a unique magnetic field configuration in which the toroidal field is strongest at the core but reverses direction at the edges, where the poloidal field dominates. The system evolves through force-free states interspersed with reconnection events due to the tearing instability at the highly sheared fieldlines. These events occur at multiple locations and are thought to be coupled. Further information regarding research into reconnection in laboratory plasmas can be found in Zweibel and Yamada (2009) and Yamada et al. (2010).

1.4 Lare3D

Lare3D is a FORTRAN code that solves the resistive MHD equations in three dimensions and will be used throughout this thesis. Each iteration of the code contains a Lagrangian step and a remap step, which is the origin of the name. In the Lagrangian step, the MHD equations are solved numerically using a second order finite difference scheme over a staggered Lagrangian grid. The remap step restores the quantities to an Eulerian grid using finite volume methods. The physics of the system are determined by the Lagrangian calculations, while the remap phase is solely concerned with the geometry of the numerical grid. Although the equations are not solved in conservative form, Lare3D has been shown to conserve energy during both the Lagrangian step and (after adjustment of the kinetic energy) the remap step. The solenoidal constraint is satisfied

because of the implementation of constrained transport over the staggered grid. Like the traditional Riemann solvers, the code gives an accurate solution at shocks but it is also able to calculate the local temperature correctly in a low beta plasma. The code is described by the developers in Arber et al. (2001).

1.4.1 Equations

The Lare3D code uses the Lagrangian form of the MHD equations listed in section 1.1.

$$\frac{D\hat{\rho}}{D\hat{t}} = -\hat{\rho}\nabla \cdot \hat{\mathbf{v}} \quad (23)$$

$$\frac{D\hat{\mathbf{v}}}{D\hat{t}} = \frac{1}{\hat{\rho}}\hat{\mathbf{j}} \times \hat{\mathbf{B}} - \frac{1}{\hat{\rho}}\nabla\hat{p} + \mathbf{F}_\nu \quad (24)$$

$$\frac{D\hat{\mathbf{B}}}{D\hat{t}} = (\hat{\mathbf{B}} \cdot \nabla)\hat{\mathbf{v}} - \hat{\mathbf{B}}(\nabla \cdot \hat{\mathbf{v}}) - \nabla \times (\hat{\eta}\nabla \times \hat{\mathbf{B}}) \quad (25)$$

$$\frac{D\hat{\epsilon}}{D\hat{t}} = -\frac{\hat{p}}{\hat{\rho}}\nabla \cdot \hat{\mathbf{v}} + \frac{\hat{\eta}}{\hat{\rho}}\hat{j}^2 + \mathbf{H}_\nu \quad (26)$$

The equations are listed in nondimensional form and the normalising constants are defined in terms of a typical length scale $L_0 = \frac{x}{x}$, magnetic field $B_0 = \frac{B}{B}$ and density $\rho_0 = \frac{\rho}{\rho}$. The normalising constants are as follows:

$$v_0 = \frac{B_0}{\sqrt{\mu_0\rho_0}} \quad p_0 = \frac{B_0^2}{\mu_0} \quad t_0 = \frac{L_0}{v_0} \quad j_0 = \frac{B_0}{\mu_0 L_0} \quad \epsilon_0 = v_0^2 \quad (27)$$

1.4.2 Grid

As has already been mentioned, this code stores quantities on a staggered Eulerian grid. Scalar variables are defined at the centre of a grid cell, namely the density and pressure. The plasma velocity is naturally located at the boundary to a grid cell because of the need to calculate fluxes into and out of the volume. In this code, the velocity is stored at the cell vertices because the shock viscosity calculations include contributions from the cell edges, which can be easily interpolated. The magnetic field is defined on the cell faces corresponding to the field component, i.e. B_x is found at the centre of the x faces. The advantage of this is that it facilitates constrained transport (Evans and

Hawley (1988)), since the electromotive force can be calculated along the edge of a face to give the magnetic flux through it by Stokes' theorem. For any grid cell, the EMF along each edge contributes to two separate fluxes with opposite signs. Hence, the net total flux into a cell must be zero and the solenoidal constraint is satisfied (assuming the field is initially divergence-free).

1.4.3 Timestep

The code uses different timesteps for the Lagrangian and remap steps. The Lagrangian timestep is determined from the Courant-Friedrichs-Lewy (CFL) stability criterion. The Courant number in this case is equal to one so that the timestep is a ratio of length to speed,

$$dt = \frac{l}{\sqrt{c_\nu^2} + \sqrt{c_s^2 + c_\nu^2}}. \quad (28)$$

Here, l is the smallest of the three grid scales, c_s is the sound speed and c_ν is the effective speed due to viscous pressure.

There are several possibilities for the remap timestep, based on fluxes, viscosity and resistivity. Three estimates for the timestep are given by the fluxes in each direction in a grid cell. The volume of the cell is divided by either the magnitude of the flux through the positive or negative boundary or the net flux, depending on which gives the smallest estimate. These flux estimates are calculated at every grid cell and the minimum for each direction gives the final candidate value. The viscous timestep is calculated by:

$$dt_\nu = 0.2 \frac{dx_l \rho}{\nu}, \quad (29)$$

where the length scale is $dx_l = 1/(1/dx^2 + 1/dy^2 + 1/dz^2)$ and ν is the coefficient of the background viscosity discussed in section 1.6.6. Collecting the various estimates, the ideal remap timestep is given by the minimum of the Lagrangian timestep, the three flux timesteps and the viscous timestep. A separate resistive timestep is calculated in the same way as the viscous timestep, replacing ρ/ν with $1/\eta$, where η is the local resistivity.

1.4.4 Lagrangian Step

The predictor-corrector step begins by advancing all variables by a half timestep. The density is not calculated using the continuity equation but instead the initial value is divided by the ratio of the control volumes. This ratio is defined as:

$$\Delta = 1 + \frac{dt}{2} \nabla \cdot \mathbf{v}. \quad (30)$$

The predicted value of the magnetic field is not taken directly from the induction equation. Instead (6) is integrated over the volume of a cell and the Divergence Theorem is used on the first advective term to give:

$$\frac{D}{Dt} \int B_i dV = \int v_i \mathbf{B} \cdot d\mathbf{s} + \int [\nabla \times (\eta \nabla \times \mathbf{B})]_i dV. \quad (31)$$

The core solver only handles ideal MHD so the diffusion term in the induction equation is implemented separately. Hence the predictor (averaged) magnetic field is calculated as:

$$B_{x_{1/2}} = \frac{1}{\Delta_{1/2}} [B_x + dt (\frac{v_x B_x}{dx} + \frac{v_x B_y}{dy} + \frac{v_x B_z}{dz})]. \quad (32)$$

The internal energy is calculated using the finite difference equivalent of the energy equation (11),

$$\epsilon_{1/2} = \epsilon_0 - \frac{P_0 \nabla \cdot \mathbf{v}_0}{\rho}. \quad (33)$$

The pressure used is actually the sum of the thermal pressure and an artificial viscous pressure ($P = p + q$).

Using the predictor internal energy and density, the predicted total pressure is calculated. The viscous pressure is not updated during the predictor-corrector step. From the gas law,

$$P_{1/2} = \epsilon_{1/2} \rho_{1/2} (\gamma - 1) + q. \quad (34)$$

The total inviscid force on the right hand side of the momentum equation is the sum of the pressure gradient, Lorentz force and gravitational force:

$$\mathbf{F}_{1/2} = -\nabla p_{1/2} + \mathbf{j}_{1/2} \times \mathbf{B}_{1/2} - \rho_v \mathbf{g}. \quad (35)$$

The half step velocity is given by the initial velocity plus the total force (including the viscous force \mathbf{F}_ν , divided by the pressure (at the cell vertices) multiplied by the intermediate timestep:

$$\mathbf{v}_{1/2} = \mathbf{v}_0 + dt2(\mathbf{F}_\nu + \mathbf{F}_{1/2})/\rho_v. \quad (36)$$

Now that the predictor variables $\mathbf{v}_{1/2}$, $p_{1/2}$ and $V_{1/2}$ have been calculated, the corrector step requires minimal calculations. The velocity, internal energy and control volumes calculated as before, only substituting in the intermediate values for the total force, velocity and pressure.

$$\mathbf{v}_1 = \mathbf{v}_0 + dt(\mathbf{F}_\nu + \mathbf{F}_{1/2})/\rho_v \quad (37)$$

$$V_1 = V_0(1 + \nabla \cdot \mathbf{v}_{1/2}) \quad (38)$$

$$\epsilon_1 = \epsilon_0 - \frac{p_{1/2}\nabla \cdot \mathbf{v}_{1/2}}{\rho} \quad (39)$$

1.4.5 Remap Step

In the remap step, constrained transport is implemented following Evans and Hawley (1988). This remap is entirely geometrical, which enables the use of Strang splitting to simplify the process. This means that the remap is completed in 1D sections so the example below will apply to the x direction but subscripts can be changed where appropriate to remap in y and z . The density is first remapped using conservation of mass. The final mass in an Eulerian cell is equal to the initial value plus the mass overlapping from the Lagrangian cell ($i - 1$) minus the mass from this Lagrangian cell overlapping the Eulerian cell (i),

$$\rho_i^{n+1} = \rho_i + \frac{1}{dx_i}(dM_{i-1} - dM_i). \quad (40)$$

The overlapping mass is found by adding an effective density- the product of the density gradient D_i and the length scale- to the Lagrangian density. The modified density is

multiplied by the distance moved by the boundary:

$$dM_i = (\rho_i^1 + \frac{dx_i}{2} D_i (1 - \psi_i)) vx_i^* dt. \quad (41)$$

The ψ_i term appearing in the formula for dM_i and the gradient D_i is a ratio comparing the speed of the boundary vx_i^* to the speed required to traverse the Lagrangian cell length in a time dt ,

$$\psi_i = \frac{|vx_i^*| dt}{dx_i}. \quad (42)$$

The remap uses the third order Van Leer upwind gradient, which has two possible forms depending on the direction of the boundary velocity. The subscripts required in the case where $vx_i^* \leq 0$ are shown in curly brackets in (43).

$$|\bar{D}_i| = \frac{2 - \psi_i}{3} \frac{|\rho_{i+1} - \rho_i|}{dxc_i} + \frac{1 + \psi_i}{3} \frac{|\rho_{i\{i+2\}} - \rho_{i-1\{i+1\}}|}{dxc_{i-1\{i+1\}}} \quad vx_i^* > 0 \quad \{\leq 0\} \quad (43)$$

The magnitude of the gradient is limited so that shocks do not leave an imprint on the Eulerian grid,

$$D_i = s \max(|\bar{D}_i| dx_i, 2|\rho_{i+1} - \rho_i|, 2|\rho_i - \rho_{i-1}|). \quad (44)$$

Here $s = \text{sign}(\rho_{i+1} - \rho_i)$ if the sign of the upwind difference matches that of the downwind difference. Otherwise the gradient is set equal to zero.

The remaps of internal energy and velocity are performed using the same method. However mass coordinates are used to ensure conservation of internal energy and momentum.

1.4.6 Viscosity

The viscosity has a real component and an artificial component that applies to shocks. The real viscosity is assumed to be isotropic and the viscous force density is calculated as the Laplacian of the velocity field:

$$\mathbf{F}_\nu = \nu \nabla^2 \mathbf{v}, \quad (45)$$

where ν is the user-defined ‘background viscosity. The viscous heating term is calculated from the product of the stress and strain tensors:

$$\begin{aligned}\mathbf{H}_\nu &= \frac{1}{\rho}\epsilon_{ij}\sigma_{ij} \\ \epsilon_{ij} &= \frac{1}{2}\left(\frac{\partial v_i}{\partial x_j} + \frac{\partial v_j}{\partial x_i}\right) \\ \sigma_{ij} &= 2\nu\left(\epsilon_{ij} - \frac{1}{3}\delta_{ij}\nabla \cdot \mathbf{v}\right)\end{aligned}\tag{46}$$

The form of artificial viscosity used in the code is consistent with Caramana et al. (1998). It adds shock limiters and a ‘switch-off’ condition to the Kuropatenko artificial velocity given by:

$$q_{kur} = \rho\left(c_2\frac{(\gamma+1)}{4}|\Delta v| + \sqrt{c_2^2\left(\frac{\gamma+1}{4}\right)^2(\Delta v)^2 + c_1^2c_s^2}\right)|\Delta v|.\tag{47}$$

This is basically an expression for the inelastic collision of two finite masses, adjusted by adding a linear term to prevent unphysical oscillations from occurring behind the shock. The viscosity limiters described in Caramana et al. (1998) take the ratio of the velocity derivative at a point on the grid with its two neighbours. In this case, the artificial velocity is defined on the cell edges, so the left and right neighbours are easily seen to be those on the adjacent edges. The left and right limiters r_l and r_r can be written as:

$$r_l = \frac{\Delta v_+ \cdot \hat{\Delta v}}{\Delta x_+ \cdot \hat{\Delta x}} \frac{|\Delta v|}{|\Delta x|}, \quad r_r = \frac{\Delta v_- \cdot \hat{\Delta v}}{\Delta x_- \cdot \hat{\Delta x}} \frac{|\Delta v|}{|\Delta x|}.\tag{48}$$

The limiter Ψ is now taken as $\text{MIN}(1/2(r_l + r_r), 2r_l, 2r_r, 1.0)$ so that the final form of the shock viscosity can be stated as:

$$\begin{aligned}q_z &= q_{kur}(1 - \Psi)\hat{\Delta v}^2 && \text{if } \Delta v \cdot S_z < 0, \\ & && \text{else } q_z = 0.\end{aligned}\tag{49}$$

1.4.7 Resistivity

The core MHD solver in the Lagrangian step solves the ideal equations, meaning the resistive terms need to be added separately. A background value for the resistivity can be given in terms of the Spitzer value. Anomalous resistivity can also be implemented by declaring a critical value for the current density above which the resistivity applies.

1.5 Magnetic Skeleton Analysis Tools

In this thesis, the magnetic topology will be visualised using the Magnetic Skeleton Analysis Tools (MSAT) software introduced in Williams (2018). In a magnetic skeleton plot, the positive nulls are marked by red spheres and the negative nulls are represented by blue spheres. The separatrix surfaces are plotted as concentric rings around the null point in the matching colour and the spines are also shown. The separators are the green lines connecting null points. A selection of magnetic skeleton plots can be found in section 4.2.2 of the thesis.

1.5.1 Null Finder

The Null Finder algorithm is an implementation of the trilinear method described in Haynes and Parnell (2007). This method assumes that each of the magnetic field components varies linearly within a grid cell. The first stage of the algorithm is the ‘reduction’, which tests each grid cell in the data set to determine whether it can contain a null point. The values of the magnetic field are checked at eight corners of the cell, as all three components must change sign in order for a null point to exist. Each magnetic field component will be equal to zero over a surface and the algorithm finds the two end points (at the cell boundary) of the lines where pairs of surfaces intersect. The sign of the non-zero component at the end points is then checked, as it must change sign within the volume at the null point. Each grid cell that contains a null point according to the algorithm is then split into a $10 \times 10 \times 10$ subgrid and the trilinear method is repeated over the finer grid. This method is implemented iteratively over smaller and smaller grids until the null point has been found to the desired precision. The current

algorithm is only able to find one null point per grid cell, so a finer grid resolution must be used to find clusters of nulls- or an alternative method if the field is not trilinear.

1.5.2 Sign Finder

The Sign Finder begins by defining a small sphere of start points enclosing the null point. Each point in the sphere is then moved a small distance in the direction of the magnetic field before being renormalised so it lies on the sphere again. This process is repeated until successive iterations are sufficiently close together and convergence to either the spine or fan has been achieved. In order to identify both the spine and the fan, the start points are traced forwards (parallel to the magnetic field) and backwards (antiparallel). Of the two sets of points, that which converges the fastest will give the spine vector. If the convergence rate is similar, the dot product of the converged position vectors is taken with the magnetic field. Since the magnitude of the spine eigenvalue is larger than the two fan eigenvalues, the larger dot product will identify the points that have converged to the spine. The size of the sets of converged points is reduced by taking each point individually and removing all points within a small radius. There should be two spine points remaining, which lie on opposite parts of the spine vector. The first fan vector is found by locating where the density of converged points is the greatest prior to the reduction. If the points are distributed around a ring, the position vector that gives the smallest dot product with the first fan vector is the second fan vector. These do not correspond to the fan eigenvectors but are two perpendicular vectors within the fan whose cross product gives the normal vector to the fan plane. If the points converged to two clusters instead of a ring, the convergence algorithm is repeated but the start points are traced in the direction of the magnetic field minus the component parallel to the first fan vector. In the case of a null point with large current parallel to the spine, the spine points converge to rings surrounding the spine vector, which is located at their centre.

1.5.3 Separatrix Surface Finder

A ring of start points around the null point is aligned with the fan plane (defined by the normal vector found previously). Each of these points is then traced along the magnetic field by a fixed distance using the Runga-Kutta-Fehlberg (RKF45) scheme. Hence a new ring is defined and the code also stores the mapping between points on adjacent rings. After a new ring has been traced, points are added to or removed from the ring in order to ensure an even spacing. Any points on the ring that are within a certain distance of an oppositely signed null point are flagged. The maximum spacing between flagged points and their neighbours is halved, as is the integration step size (for the whole ring). A chain is formed containing all the flagged points and fieldlines are traced from these far enough so that their asymptotic behaviour becomes evident. A dot product is taken of the spine vector and the position of the last point on the fieldlines relative to the oppositely signed null. If this dot product changes sign between adjacent points in the chain, a separator has been identified, as the traced fieldlines are in different flux domains. The Separatrix Surface Finder continues to trace rings of points in this way until all the points on a ring are outside the domain or either the number of points per ring or the total number of rings is too high. When the ring tracing has ceased, any separators can be traced backwards from the point where they were identified using the mapping between successive rings. The spines are also traced with the RKF45 scheme, with the first point at either end being provided by the spine vector.

2 3D Null Point Reconnection

2.1 Introduction

Null points are the focus of many reconnection studies, as they are locations where strong current concentrations can build up naturally. In three dimensions, the magnetic field in the vicinity of linear nulls has a particular geometry defined by the *spine* line and *fan* plane. One of these structures is aligned with fieldlines approaching the null and the other aligns with fieldlines directed away from the null, depending on whether it is positive or negative. As a result of the solenoidal constraint, 3D null points must be surrounded locally by a hyperbolic magnetic field, unlike 2D nulls which can also have elliptic fieldlines. There are two different types of 3D linear null points, namely *improper* and *spiral* nulls. The fieldlines extend radially from improper nulls, whereas spiral nulls have spiral fieldlines.

In two dimensions, reconnection occurs exclusively at (hyperbolic) magnetic null points. A current sheet overlays the null to form the *diffusion region*, where resistive effects become important. Plasma flows advect fieldlines into the diffusion region, where they break and reform in pairs, causing reconnection outflows. The two parameters that are typically important in determining the rate of reconnection are the aspect ratio of the current sheet and the plasma resistivity. Debate has centred on how to model fast reconnection that is independent of the resistivity. A detailed description of 2D reconnection is provided by Vasyliunas (1975), Priest and Forbes (2000) and Biskamp (2000). Three dimensional reconnection can occur at null points but also has been modelled along separators and in the absence of nulls at quasi-separatrix layers. Evidence of the null point structure has been found in flare reconnection sites by Masson et al. (2009) amongst others. In three dimensions, the diffusion region is a current layer with finite thickness and fieldlines reconnect continuously as they pass through the volume. Consequently, the reconnection is not pairwise as in the 2D case.

Different types of 3D null point reconnection have been defined by Priest and Pontin (2009), namely torsional spine, torsional fan and spine-fan reconnection. These categories were largely inspired by the kinematic work of Pontin et al. (2004) and Pontin et al. (2005). In these papers, Ohm's Law is solved by integrating the product of

the parallel current with a localised resistivity. The integration gives the electrostatic potential, from which the electric field and then the perpendicular velocity can be established. The spine reconnection example has a uniform current density that is everywhere parallel to the spine, i.e. a spiral null. The steady solution features rotational flows within the diffusion region and fieldlines that are anchored within the ideal region experience slippage due to this localised rotation. In Pontin et al. (2005), the magnetic field has a constant current density parallel to the fan plane, meaning the spine and fan are not orthogonal. The solution to the kinematic problem has a stagnation point flow which crosses both the spine and fan. By altering the current density so that it is non-uniform and vanishes at the null, solutions can be found where the velocity crosses either the spine or the fan.

In numerical experiments, current layers are typically introduced by driving a potential null point, either by imposing a velocity at the simulation boundary or by introducing a perturbation to the magnetic field. In Pontin et al. (2007) and Wyper and Pontin (2014b) the potential null is driven by advecting the spine footpoints in opposite directions, causing the angle between spine and fan to close and a magnetic pressure force to develop near the fan plane. The alternative form of driving was studied by Pontin and Galsgaard (2007), who found that additional magnetic field components caused either a rotational or shearing force. The rotation distributed currents evenly across the topological features while shearing focused the current in the vicinity of the null.

The work in this chapter will compare the reconnection that occurs at spiral and improper nulls. Improper null point reconnection has previously been studied numerically by Al-Hachami and Pontin (2010) and Thurgood et al. (2018). The key point of these works is that the length and magnitude of the current layer formed is dependent on the azimuthal variation in field strength in the fan plane. For more rotationally symmetric configurations, although the peak current is higher, the current layer has a smaller extent. The integrated E_{\parallel} along fieldlines is strongly affected by the dimensions of the current layer, so the reconnection rate is lower in the symmetric case. Spiral null point reconnection has been considered by Williams (2018). This chapter will consider more generic null points that have current layers along both the spine and fan.

All of the null points considered here will be ‘tilted’, meaning there is some compo-

ment of current perpendicular to the spine, since it has been shown that these produce localised current layers away from the simulation boundaries. Fuentes-Fernández and Parnell (2013) studied the current layers that result from relaxing an initial non-potential null point with current directed either parallel or perpendicular to the spine. This work forms the basis of the reconnection experiment performed in this chapter, as the quasi-equilibrium fields are obtained using the same techniques but different parameter choices. The non-potential magnetic field is relaxed ideally using viscous damping in order to achieve a quasi-equilibrium state. Then an anomalous resistivity will be switched on to initiate the reconnection and dissipate the current that has accumulated.

Section 2 will give an overview of the setup used in the numerical experiments. In sections 3, 4 and 5, the results of the reconnection experiments will be presented. The experiments are grouped according to the position of the major axis in the fan plane. The nulls in section 3 have a major axis that is approximately aligned with the current density, whereas in section 4, the two vectors are almost perpendicular. Section 5 deals with the case where there is no major axis because the magnitude of the two fan eigenvalues is the same. Each of the three results sections compares an improper null with a spiral null, which have in common the orientation of their major axis. In section 6 some conclusions will be drawn regarding the significance of the different categories of null points.

2.2 Initial Setup

The initial magnetic field used in the experiment is taken from the classification of linear 3D nulls given in Parnell et al. (1996).

$$\mathbf{B} = \left(x - \frac{1}{2}j_{sp}y, \frac{1}{2}j_{sp}x + by, j_fy - (b+1)z \right) \quad (50)$$

where $\mathbf{j} = (j_f, 0, j_{sp})$. This model contains a single linear null point located at the origin. If the current components are set to zero, the spine sits along the z -axis and the separatrix surface aligns with the $x - y$ plane. Hence, j_{sp} is the current component parallel to the potential spine and j_f is the component parallel to the fan. For simplicity,

Type	j_{sp}	j_f	b
Spiral	1	1	2/3
Improper	0	1	2/3
Spiral	1	1	3/2
Improper	0	1	3/2
Spiral	1	1	1
Critical spiral	0	1	1

Table 1: Parameter choices for the six experiments

j_f is in fact aligned with the x -axis and it is important to remember that j_y is initially zero. The parameter b determines the nature of the fieldlines surrounding the null point. The threshold current is defined as $j_{thresh}^2 = (b - 1)^2$ and if the magnitude of this current exceeds j_{sp} , the null is improper. Otherwise, if the spine current has greater magnitude than the threshold current, the null is of spiral type.

In this chapter, the six experiments listed in Table 1 will be discussed. Half of these only have current parallel to the fan initially ($j_{sp} = 0$). These are all improper nulls, with the exception of the critical spiral case. This is not a generic case, since it has the only possible b for which $j_{thresh} = j_{sp}$, but it has been studied extensively by previous authors. The three spiral null experiments have the same parameters as the aforementioned cases, except that j_{sp} is non-zero. The similarities between the parameter sets should facilitate comparison between the improper and spiral nulls.

Both the relaxation and reconnection phases of the experiment are performed numerically using Lare3D, a code which solves the equations of MHD over a Lagrangian grid before restoring the variables to an Eulerian grid (the *remap* stage) at each timestep. The equations used in this work are listed in section 1.4.1, with the resistivity η set to zero during the relaxation so that the ideal equations are solved during the formation of the current layer. Although reconnection by numerical resistivity cannot be prevented, this occurs on a timescale that is much slower than the relaxation. The experiment is performed over a grid of $512 \times 512 \times 512$ points and the domain is $-1 < x, y, z < 1$ so that the null is positioned in the centre of the box. Line-tied boundary conditions are used so all velocity components and the normal derivatives for B, ρ and ϵ are all set to zero.

For practical reasons, the experiment has a plasma beta ($\beta = 2p/B^2$) greater than one across the majority of the domain. The plasma pressure is not explicitly declared but is calculated by the code under the assumption of constant temperature as $p = \rho\epsilon(\gamma - 1)$. Here, $\rho = 1$, $\epsilon = 3/2$ and $\gamma = 5/3$ so that the uniform plasma pressure is $p = 1$. As discussed in section 1.4.3, the timestep in Lare3D has a dependence on the density, so a lower beta plasma could be achieved at the expense of increased computational demands. The shock viscosity coefficients (from equation (47)) are $c_1 = 0.1$ and $c_2 = 0.5$ throughout the experiment and the background component is $\nu = 0.01$ during the relaxation. The initial plasma velocity is zero across the domain, including at the boundaries.

The second phase of the numerical experiment differs from the first in that the resistive MHD equations are solved with an anomalous resistivity given by:

$$\eta = \begin{cases} 0 & |j| < j_{crit} \\ 0.001 & |j| \geq j_{crit} \text{ and } |x|, |y|, |z| < 0.8 \end{cases}$$

The critical current value is equal to 70% of the maximum magnitude and was chosen to constrain the spatial extent of the reconnection region. The background viscosity was decreased by an order of magnitude to $\nu = 0.001$ to prevent needless damping of flows that could carry flux into and away from the reconnection site.

2.3 Nulls with Current Parallel to Major Axis

The first results section will compare a spiral null point ($j_{sp} = 1$) with an improper null ($j_{sp} = 0$), both of which share the parameter values $j_f = 1$ and $b = 2/3$. The eigenvalues and eigenvectors for these nulls are displayed in table 2. All the nulls considered in this chapter will have positive sign, meaning the real part of the fan eigenvalues (λ_1 and λ_2) is positive and the spine eigenvalue (λ_3) is negative. Another property of the nulls in all six experiments is that the spine is aligned with the z -axis ($\mathbf{x}_3 = (0, 0, 1)$).

In the improper case, λ_1 is the larger of the two fan eigenvalues, meaning its corresponding eigenvector \mathbf{x}_1 is the major axis. This is parallel to the current density, which in the absence of a current parallel to the spine is $\mathbf{j} = (j_f, 0, 0)$. For the spiral case, there is not a unique major axis but the fan fieldlines will oscillate between the vectors

\mathbf{x}_1 and \mathbf{x}_2 . Therefore, the direction in which the angle between the vectors is smaller will have the strongest magnetic field.

	Spiral	Improper
λ_1	$0.83 + 0.47i$	1.0
λ_2	$0.83 - 0.47i$	0.67
λ_3	-1.67	-1.67
\mathbf{x}_1	(0.39, 2.5, 1.0)	(1, 0, 0)
\mathbf{x}_2	(2.51, 0.47, 0.0)	(0, 2.33, 1)
\mathbf{x}_3	(0, 0, 1)	(0, 0, 1)

Table 2: Eigenstructure of the $b = 2/3$ nulls

2.3.1 Relaxation

The field was relaxed in Lare3D with the aim of creating a force balance and attenuating the flows to achieve a quasi-equilibrium. There is a substantial force imbalance at the start of the relaxation as the current is a constant vector in the $x - z$ plane, which has a strong component perpendicular to the field, especially where B_y peaks. The pressure is also initially constant and there is no viscous force, implying that the Lorentz force is the only contribution to the right hand side of the equation of motion. The purpose of the relaxation is to introduce additional forces to balance the $\mathbf{j} \times \mathbf{B}$ force.

Figure 2 shows the energy changes during the relaxation of the spiral null. Approximately 1% of the total magnetic energy is converted to internal energy due to viscous heating and the work done by the Lorentz/pressure forces. The total energy change is five orders of magnitude smaller than the magnetic energy transferred, which is expected because of the closed boundary conditions. The important aspect of these plots is that the energy changes are steady after $t = 10$, which is an indication that the field has reached a quasi-equilibrium. The kinetic energy is small (compared with the initial magnetic energy) when the relaxation is halted, although it is clearly still declining.

Another way to judge the state of the quasi-equilibrium is to look at the magnitude of the total force, defined as the sum of the plasma pressure force and the Lorentz force. Figure 3 shows the integrated total force at the end of the relaxation. The individual bars show different parts of the domain, which has been split into a $3 \times 3 \times 3$

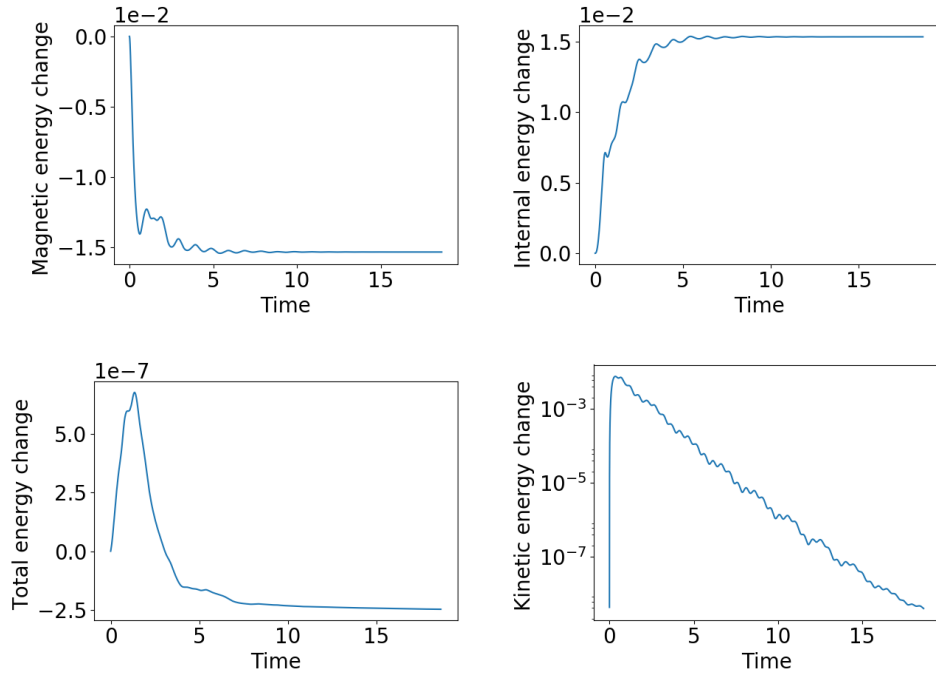


Figure 2: Time and volume integrated energy changes for the spiral null relaxation ($b = 2/3$), normalised by initial total energy

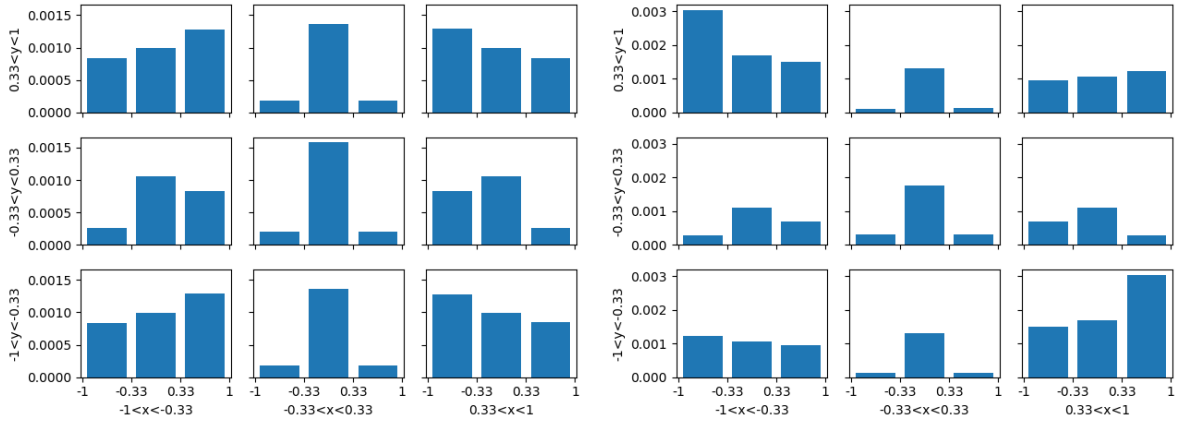


Figure 3: Integrated total force in 27 subvolumes within the domain. The columns correspond to different x ranges and the rows show the y ranges. The three bars within each of the nine histograms are the z ranges. The forces for the improper null are shown on the left and the spiral null on the right.

grid. The magnitude of the force varies spatially, with the largest forces being found at the boundaries in both experiments and also at the central subvolumes where $-0.33 < x, z < 0.33$. The boundary forces are caused by the line-tied boundary conditions, which lead to current build-up in a boundary layer. As the relaxation progresses, the magnetic fieldlines will smoothly bend within the volume to allow for a reduction in the Lorentz force but there will be no corresponding change in the field vector at the boundary. The central force is concentrated at the separatrix surface, where the current density evolves towards a singularity. The current layer continues to intensify as its thickness decreases, so the plasma must respond to the changing $\mathbf{j} \times \mathbf{B}$ force. The integrated forces in the two $b = 2/3$ experiments are similar, although the improper case is more symmetric. There is a stronger force along two edges of the domain for the spiral null due to the geometry of the null point.

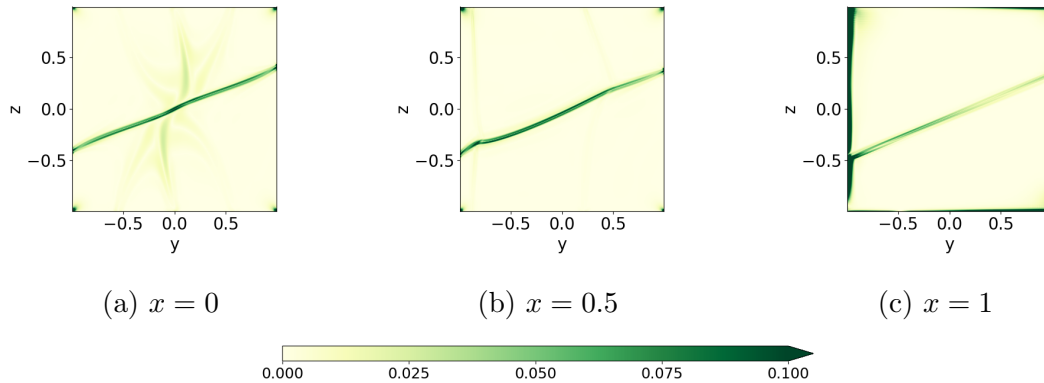


Figure 4: Contour plots showing modulus of the post-relaxation total force for the spiral null

In figure 4, the magnitude of the total force in the spiral case is shown at three different x cuts. In the $x = 0$ cut, the total force is focused on the separatrix surface and peaks close to the null point. There is a much weaker force along the spine, even though figure 5 shows that the spine currents are substantial. This is a consequence of the fact that the spine does not separate oppositely directed flux and the current layer is not evolving towards a singularity. At $x = 0.5$, the forces are balanced across a larger area but the imbalance at the separatrix surface is slightly stronger. At $x = 1$, the strongest net force in the domain is found at the $y = -1$ boundary.

The current layers that result from the relaxation of the improper and spiral nulls

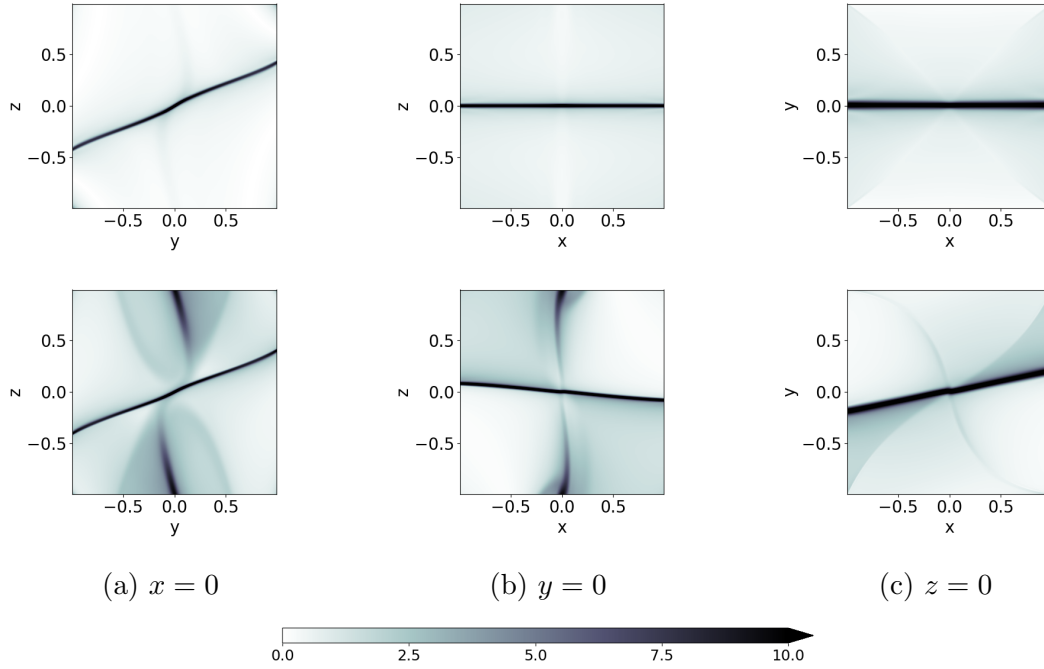


Figure 5: Contour plot showing modulus of the post-relaxation current density. First row: improper, second row: spiral.

are quite different, as shown in figure 5. In both experiments, the strongest current has accumulated along the separatrix surface. The layer appears to have a similar thickness in both cases and the difference in orientation in the $y = 0$ and $z = 0$ reflects the differing null point geometry. The spiral case has additional current enhancements along the spine that are strongest at the z -boundaries. Away from the current layers, the background current density is also higher in the spiral case because the magnitude of the initial current vector is larger.

There cannot be any change in the number of topological features when solving the ideal equations but the existing spine and fan are distorted significantly. The spine has collapsed towards the fan in the vicinity of the null, while the fan plane curves towards $z = 1$ for $y > 0$ and towards $z = -1$ for $y < 0$. Figure 6 shows the topology of the fields before and after relaxation. The current contour shown is taken at 70% of the maximum magnitude and will be used as the critical current during the reconnection experiments. It was also possible to choose this contour to be the same value across all experiments, or to match the length of the current layers. Using the same value would

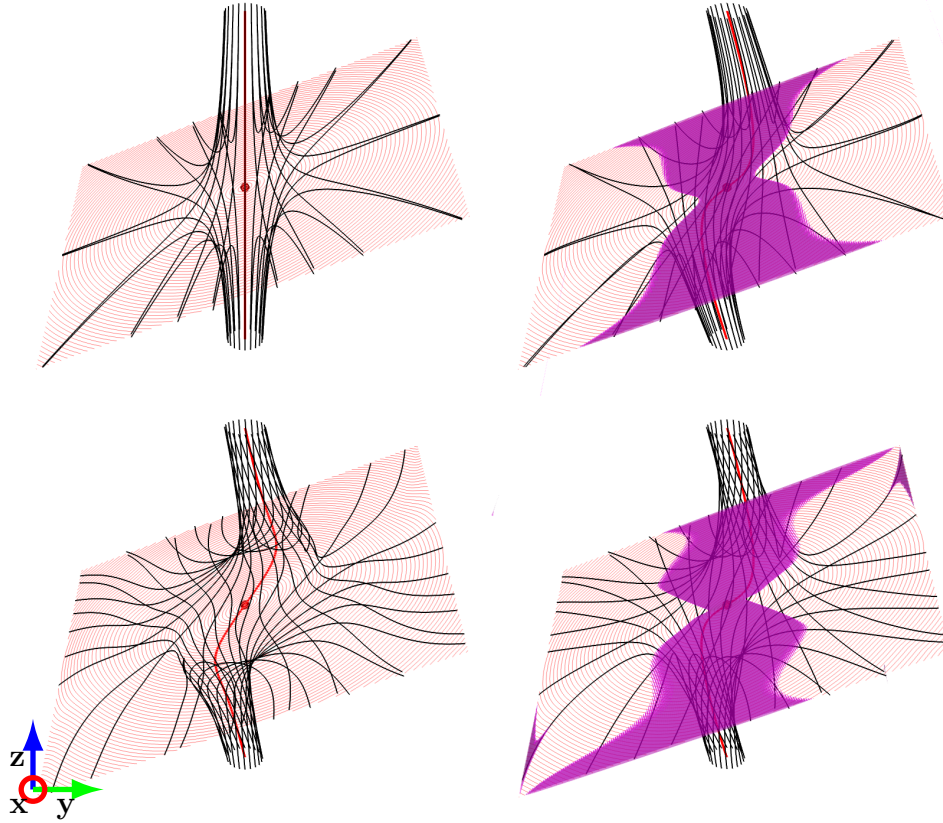


Figure 6: Magnetic skeleton before (left) and after (right) relaxation. Isosurfaces show the critical current used in the reconnection experiment. First row: improper null; isosurface shows $|j| = 10.06$. Second row: spiral null; isosurface shows $|j| = 11.26$. Note that the image is rotated by 30 degrees about the y -axis to improve fieldline visibility.

lead to a significant difference in the thickness of the $b = 2/3$ and $b = 3/2$ current layers, which would affect the reconnection rate. If the dimensions of the current layers were comparable, this would ignore the fact that the different null point configurations lead to different current distributions. Such an approach could be used to eliminate boundary effects from the reconnection by localising the current layer in the centre of the domain. However it was deemed that a current layer that spans the length of the x -axis was more representative of the current distribution for these experiments. The contour used does exclude the spine currents from the spiral null reconnection, which means there is a single diffusion region rather than three. This will simplify the analysis but it is possible that the weaker currents at the spine would play an important role in

the overall dynamics.

Galsgaard and Pontin (2011a) found that, except in cases where the boundary driving is almost perpendicular to the eigenvector associated with the larger eigenvalue, the null point would collapse in this direction. As the null collapses towards the strong eigenvector, the current density grows perpendicular to this along the weak eigenvector in the fan. This experiment does not show the same behaviour, although later cases are in agreement. Here, the spine collapses in the y -direction, which is aligned with the weak eigenvector, while the current density spreads along the x -axis.

2.3.2 Energies

In figure 7, the integrated energy changes are plotted. These are the magnetic energy change (51), the internal energy change (52) and the kinetic energy change (53). The total energy change is the sum of these three integrals. All of the integrals are normalised by the initial total energy.

$$\int \int \frac{B^2}{2} dV dt - \int \frac{B_0^2}{2} dV_0 \quad (51)$$

$$\int \int \rho \epsilon dV dt - \int \rho_0 \epsilon_0 dV_0 \quad (52)$$

$$\int \int \frac{\rho v^2}{2} dV dt - \int \frac{\rho_0 v_0^2}{2} dV_0 \quad (53)$$

The free magnetic energy in these experiments is converted to both internal and kinetic energy, as shown in figure 7. The rate of change of magnetic energy is almost steady, except for gentle declines in the magnitude of the gradient that can be linked to the movement of the plasma through the numerical box. The kinetic energy increases sharply at the start of the experiment when the quasi-equilibrium is broken by the introduction of a resistivity. The flows begin to diminish shortly after $t = 1$ and the kinetic energy drops accordingly. The peak kinetic energy change is a mere 1% of the total magnetic energy converted during the experiments.

There are few significant differences between the energy changes of the spiral and improper experiments. The amount of magnetic energy converted by the improper null

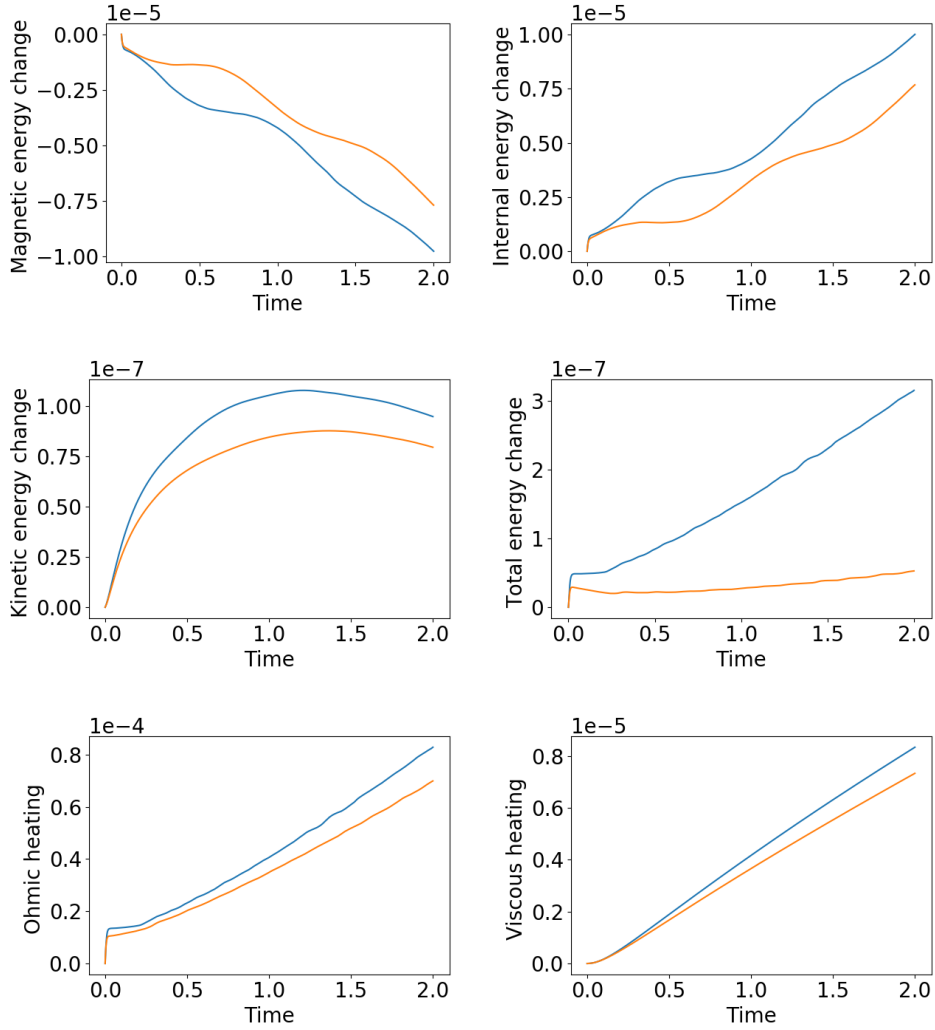


Figure 7: Time and volume integrated energy changes for the $b = 2/3$ null reconnection, normalised by initial total energy. Blue: improper, orange: spiral.

is fractionally higher. The small oscillations in the rates of magnetic/internal energy change also seem to be out of phase with each other. For example at $t = 0.4$, the improper null is converting magnetic energy while the spiral case is not. Later at $t = 0.8$, the opposite situation occurs, as the energy conversion at the improper null pauses.

The Ohmic heating converts magnetic energy to internal energy directly and is therefore a major factor in these experiments. A significant amount of Ohmic heating occurs in a short space of time at the start of the experiment as the super-critical current in the

initial condition is dissipated rapidly. After this time, the rate of Ohmic heating in the improper case is close to zero before reaching a constant value that is maintained thereafter. The Ohmic heating is always non-zero in the spiral case but also transitions from the high rate of $t < 0.2$ to a slower rate, slightly less than that seen in the improper case. The time evolution of the total energy change indicates that it is strongly related to the Ohmic heating. In the improper case, the total energy change exceeds the peak kinetic energy but it is much less important for the spiral null. There should not be any flow of energy into or out of the system so the total energy change is a type of numerical error. However, it is small compared with the magnetic energy converted in both experiments.

Previous studies of 3D null point reconnection have rarely calculated the energy changes in the system. In Williams (2018), the magnetic energy was transferred to internal energy linearly, as Ohmic heating was dominant over the viscous and adiabatic heating. However, the current layers in those experiments were located along the spine close to the boundaries of the domain. Such a current layer will be difficult to dissipate when line-tied boundary conditions are used, which could explain the steady Ohmic heating. Nonetheless, the greater importance of adiabatic heating is an interesting feature of the present example of spiral null point reconnection.

By calculating the individual terms contributing to the rate of change of the energies, one can gain some insight into how the reconnection proceeds. Figure 8 shows these quantities for the spiral experiment, since the plots are qualitatively similar for both $b = 2/3$ nulls. The rate of change of magnetic energy is given by the negative sum of the Poynting flux, Ohmic heating and work done by the Lorentz force:

$$\frac{\partial}{\partial t} \left(\frac{B^2}{2} \right) = -\nabla \cdot (\mathbf{E} \times \mathbf{B}) - \eta j^2 - \mathbf{v} \cdot (\mathbf{j} \times \mathbf{B}) \quad (54)$$

The Ohmic heating and the work done by the Lorentz force combine to give the magnetic energy loss across the entire domain. The Ohmic heating is dominant at the very start of the experiment but the Lorentz force is more important for $0.02 < t < 0.25$ and $t > 0.6$. At other times the two terms are approximately of equal importance.

As the plasma flows through (and drags with it) the magnetic field, the Lorentz force does work. Hence the oscillatory nature of figure 8(b) reflects the changing direction

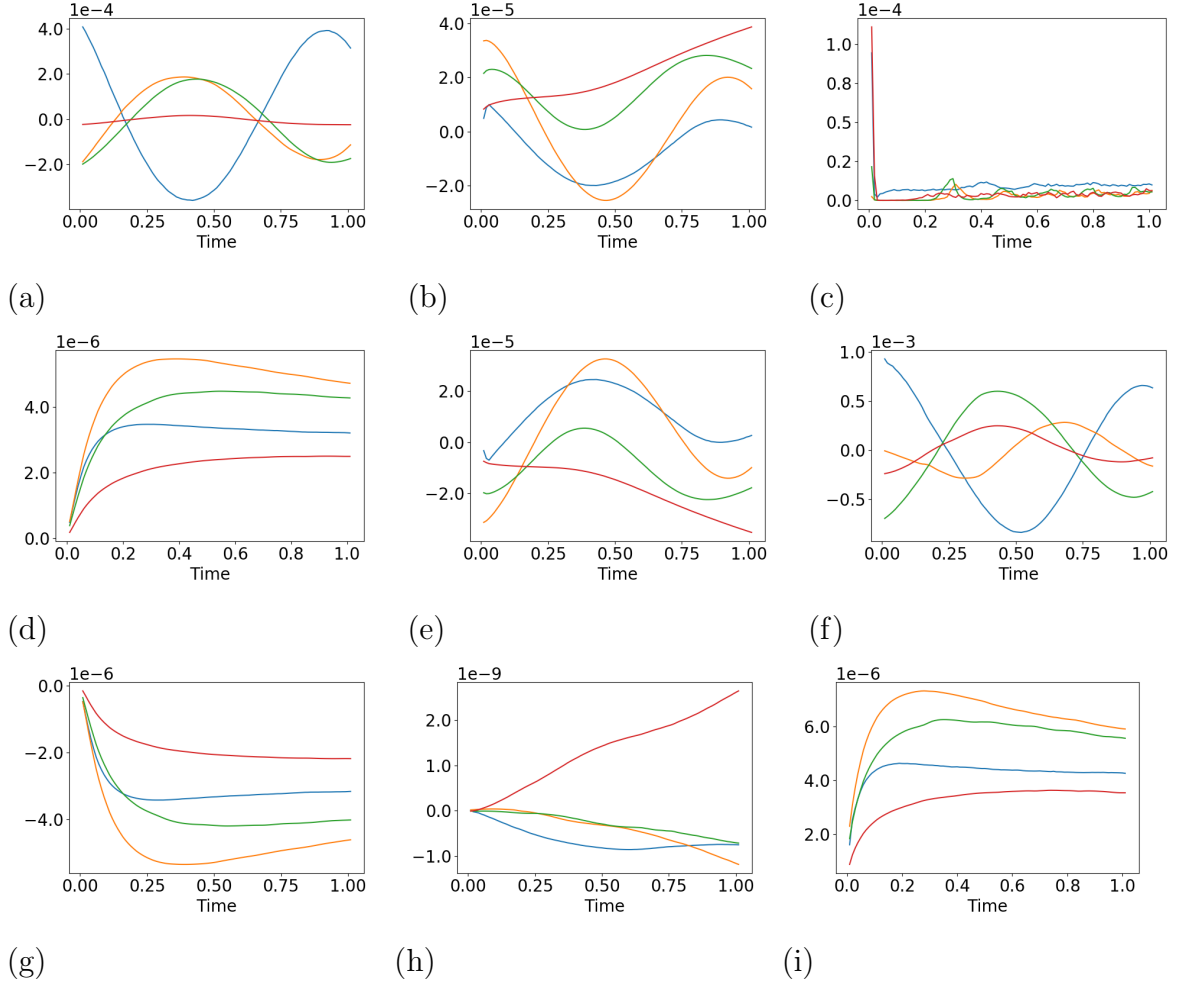


Figure 8: Terms contributing to rate of change of energies for spiral null. These instantaneous values are integrated across four distinct subvolumes (blue: $0.75 < |x, y, z| < 1$, yellow: $0.5 < |x, y, z| < 0.75$, green: $0.25 < |x, y, z| < 0.5$, red: $|x, y, z| < 0.25$). a) Poynting flux; b) Work done by the Lorentz force; c) Ohmic heating; d) Viscous heating; e) Work done by the pressure force; f) Enthalpy flux; g) Work done by the viscous force; h) Kinetic energy flux; i) Difference between work done terms.

of the bulk plasma flow relative to the $\mathbf{j} \times \mathbf{B}$ force. The Lorentz force does not play a significant role in the outer subvolume but the inner shell grows in importance without being affected by the flow reversals.

The Ohmic heating has the same time dependence across each of the subvolumes. This can be explained by observing that the current layer in figure 6 stretches along the entire x -axis so that the Ohmic dissipation occurs in every subvolume. When the resistivity is switched on initially, a large amount of Ohmic heating occurs as the super-critical current is dissipated. Then between $0.02 < t < 0.25$, the rate of Ohmic heating is lowest as the current layer needs to rebuild before additional reconnection can occur. Subsequently, the Ohmic heating rate is impulsive, as the system responds quickly to instances of $j > j_{crit}$.

There is no Poynting flux through the simulation boundary because of the choice of boundary conditions. This flux is also negligible in the innermost subvolume, as the magnetic energy transport is limited to the middle shells. Again, there is a periodicity owing to variations in the flow direction caused by plasma collisions. Initially the flow transports magnetic energy into the middle subvolumes from the outermost shell, before the process is reversed at $t = 0.2$.

The rate of internal energy change is equal to the sum of the Ohmic heating, viscous heating and the work done by the pressure gradient minus the enthalpy flux:

$$\frac{\partial}{\partial t} \left(\frac{p}{\gamma - 1} \right) = \eta j^2 + \epsilon_{ij} \sigma_{ij} + \mathbf{v} \cdot \nabla p - \nabla \cdot \left(\frac{\gamma p}{\gamma - 1} \mathbf{v} \right) \quad (55)$$

Similarly to the magnetic energy change, the internal energy is dominated by the Ohmic heating initially, before the work done by the pressure force gains in importance and becomes the main factor around $t = 0.5$. The viscous heating is a steady contribution to the internal energy that is roughly a factor of 2 less than the impulsive Ohmic heating rate.

The work done by the pressure force is to a large extent equal to that done by the Lorentz force, since the initial condition is a quasi-equilibrium. The spatial variation of this quantity is very similar to that in figure 8(b), with the middle subvolumes accounting for most of the early energy release and the inner shell dominating for

$t > 0.5$. The difference between the two work done terms can be seen in figure 8(i).

The enthalpy flux shows slightly more complicated behaviour than the Poynting flux, as the two middle subvolumes behave differently. Initially there is a flow of internal energy from the outer subvolume inwards and the flow reverses at $t = 0.25$, so that the flow is directed out of the inner shells. The outer middle shell has intermediate behaviour, as the flux direction sometimes matches the central subvolumes and sometimes matches the outer shell.

The rate of change of kinetic energy is defined as the sum of the work done by the Lorentz force and the work done by the viscous force minus the work done by the pressure gradient and the kinetic energy flux:

$$\frac{\partial}{\partial t} \left(\frac{1}{2} \rho v^2 \right) = \mathbf{v} \cdot (\mathbf{j} \times \mathbf{B}) + \mathbf{v} \cdot \mathbf{F}_\nu - \mathbf{v} \cdot \nabla p - \nabla \cdot \left(\frac{1}{2} \rho v^2 \mathbf{v} \right) \quad (56)$$

Any net kinetic energy change during the experiment is due to a force imbalance in the system. Owing to the quasi-equilibrium initial condition, the viscous, Lorentz and pressure forces approximately balance each other at all times, meaning figure 8 (g) and (i) are equal and opposite. The work done by the viscous force in (g) does not include the small contribution from the shock viscosity but it is nonetheless clear that there is an approximate force balance throughout the experiments. The kinetic energy flux indicates that the kinetic energy in the central shell is steadily rising at the expense of the other subvolumes.

2.3.3 Reconnection Rate

The definition of magnetic reconnection in 3D states that over a domain of measure greater than zero, i.e. a volume of flux rather than a single fieldline,

$$\int \mathbf{E} \cdot \mathbf{B} dl \neq 0 \quad (57)$$

and with the form of Ohm's law used by MHD, the parallel electric field is proportional to the parallel current.

Hence, figure 9 shows the integrated parallel current along fieldlines passing through

$z = 0$ for the $b = 2/3$ experiments. The three frames shown correspond to the maxima/minima of the lines in figure 10. Once the anomalous resistivity is activated, there is a significant reconnection event that dissipates some of the current in the current layer, causing the bands of positive and negative E_{\parallel} to shrink inwards towards the null. In the second row of figure 9, the initial reconnection has expired as the current layer is rebuilding. There is still weak reconnection occurring close to the null but the E_{\parallel} is fragmentary and does not cover a significant part of the current layer. In the third row, the E_{\parallel} is quite strong again, indicating that the critical current has been exceeded across much of the current layer. Although the E_{\parallel} covers the length of the x -axis and bears a strong resemblance to the initial current layer, it remains fragmentary as the reconnection is of an impulsive nature. The current layer itself is smooth with magnitude close to the critical value.

Comparing the two experiments, the E_{\parallel} for the improper null is more localised about the x -axis, while the spiral fieldlines cause plumes of E_{\parallel} near to the null extending to $y = \pm 0.2$. The plumes are weaker than the main E_{\parallel} concentration, so the improper E_{\parallel} intensity is more uniform and the strong E_{\parallel} also covers a larger region. However, the reconnection in the improper case seems to cease almost completely at $t = 0.04$, whereas the spiral E_{\parallel} remains non-zero.

It is possible to visualise the reconnection rate by taking the maximum value of the integrated parallel electric field along fieldlines threading $z = 0$. This is a proxy for the rate of flux transfer across the fan, as it would be a major numerical challenge to locate start points within the plane itself. If the magnitude of the current density in the spine current layers was sufficiently high, the E_{\parallel} values would represent a combination of fan and spine slippage. In this case however, the reconnection is almost entirely limited to the fan. Figure 10 shows the maximum and minimum E_{\parallel} against time for the $b = 2/3$ experiments. The three phases suggested by figure 9 are clearly visible in the reconnection rate, namely the initial rapid reconnection; the slow reconnection as the current layer rebuilds and the impulsive reconnection after $t = 0.2$. It is also clear that the initial reconnection is stronger in the improper case, while the miniature events occurring during the impulsive reconnection are also typically larger in the improper experiment. It should be noted from figure 9 that the locations of the maximum and minimum E_{\parallel} change during the course of the experiment. Initially, the strongest values

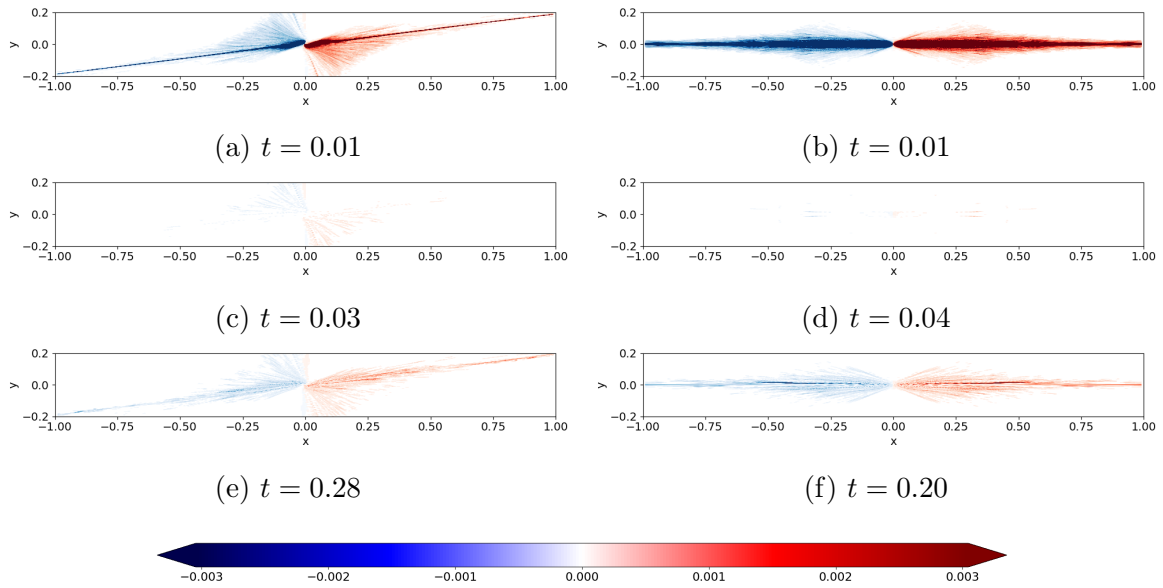


Figure 9: Parallel electric field integrated along fieldlines passing through $z = 0$, left: spiral, right: improper

are found close to the null point and measure the maximum slippage of flux about the spine. At later times, the bursts occur away from the null and the E_{\parallel} values measure the rate of spine-fan reconnection.

In the spiral null experiments of Williams (2018), the reconnection rate declines slowly from the initial peak. In their main experiment, the integrated E_{\parallel} falls by an approximate factor of 2 after several Alfvén crossing times. There is little evidence of impulsive reconnection, as this occurs in regions where the majority of the current is sub-critical and the reconnection rate is close to zero. Other works studying the time dependence of the reconnection rate form the current layer during the resistive experiment. Consequently the reconnection rate rises from zero and peaks at the same time as the current (Pontin and Galsgaard (2007)). In driven experiments, the reconnection rate either tends to a quasi-steady state if the driving is continuous (Galsgaard and Pontin (2011b)) or begins to decrease if the driving is impulsive and the field is allowed to relax (Galsgaard and Pontin (2011a)).

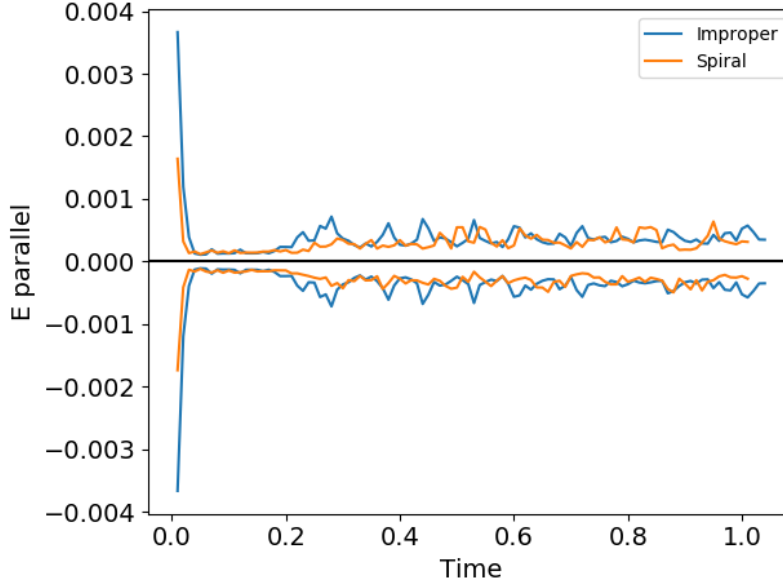


Figure 10: Time evolution of the maximum and minimum values of the integrated E_{\parallel} along fieldlines passing through $z = 0$

2.3.4 Flows

The plasma flows play an important role in regulating the reconnection process. This is because the background resistivity is zero across the majority of the domain at any given time so the magnetic field evolution is ideal away from the diffusion region. This means the magnetic field is 'frozen in' to the plasma and the plasma velocity carries the magnetic flux.

Figure 11 shows the local flow pattern in the vicinity of the null at two different times. The quasi-equilibrium velocity is shown on the left to illustrate that the flow pattern is intrinsic to the null point and not necessarily indicative of reconnection. Of course, the initial velocity is close to zero by design but due to either the force imbalance or possibly numerical reconnection, there are flows in the neighbourhood of the separatrix surface. These are intensified during the reconnection so that strong outflows can be seen in the $x = 0$ and $y = 0$ planes. The outflows are directed normal to the separatrix surface and parallel to the spine (at $x = 0$), which is consistent with the ideal flow pattern. There is limited evidence of inflows but these are diverted by the faster outflows as they

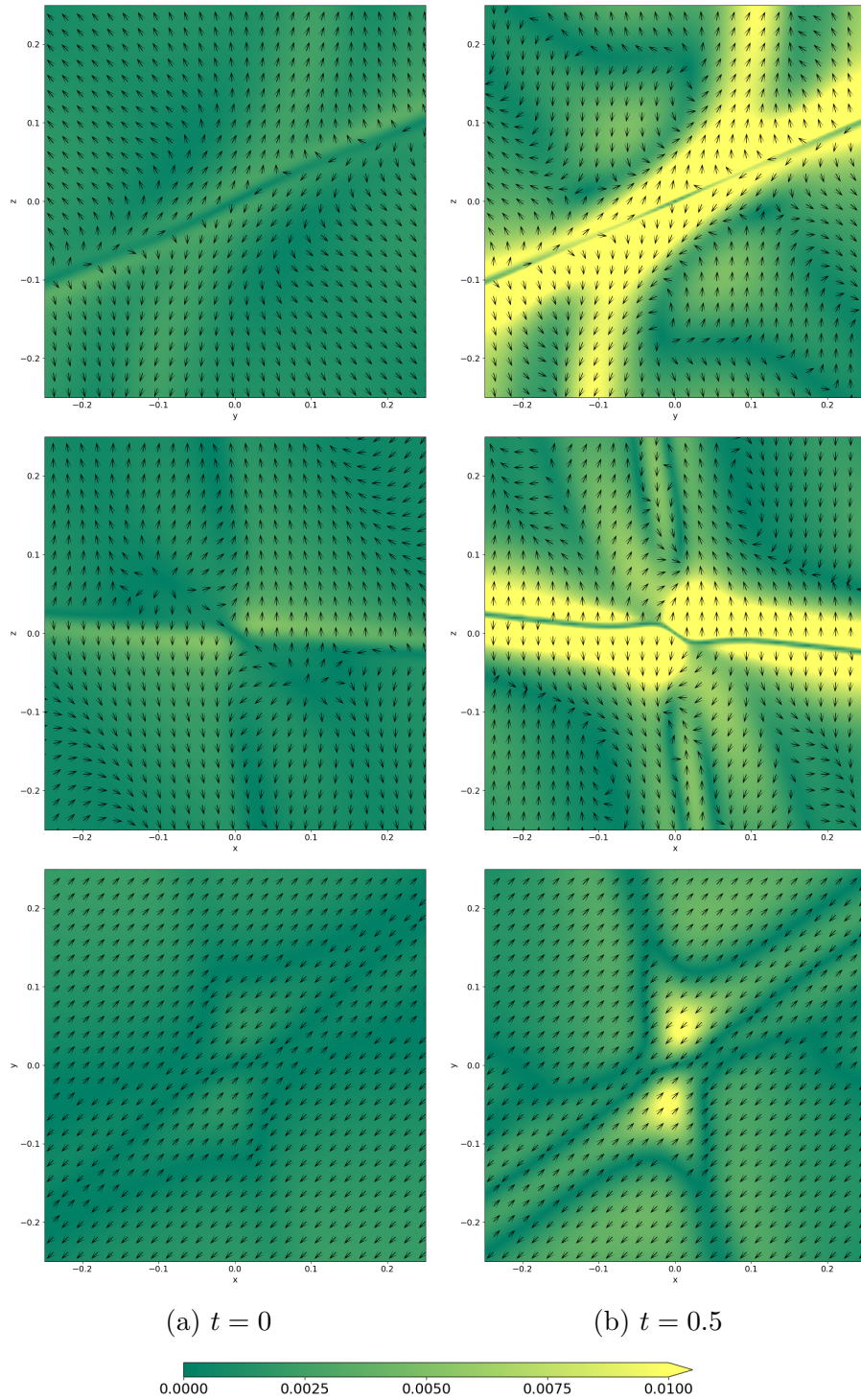


Figure 11: Magnitude and direction of the in-plane plasma velocity for the spiral null. Top: $x = 0$, middle: $y = 0$, bottom: $z = 0$.

approach the current layer. The inflows are only seen in the $t = 0.5$ velocity, where the evacuation of the plasma after the onset of reconnection leads to backflows which replenish the current layer. In the $y = 0$ plane, new outflows can also be identified in the positive z direction for $x < 0$ and towards negative z for $x > 0$. The weakest flows occur in the $z = 0$ plane at both times because this is the plane that agrees most closely with the location of the separatrix surface. It is clear from the other cuts that there are strong flows here but they are directed normal to the plane. The in-plane flows are homogeneous on either side of the fan plane, which suggests that this plane is exempt from the nonlinear dynamics of the colliding perpendicular flows.

There is no evidence of the rotational flows about the spine seen in Pontin et al. (2004), as these are associated with spine reconnection. Although the spiral null has a current layer along the spine, the critical current is too high to allow it to reconnect in the main experiment. The stagnation point flow has been identified in the literature (Pontin et al. (2005), Pontin et al. (2007)) as a major feature of spine-fan reconnection. Here the flow clearly vanishes along the separatrix surface, although the magnitude of the inflows is clearly less than that of the outflows. The inflows are more important in previous works because the initial configuration does not have a localised current, which arises due to the resistive null point collapse. In this case, the initial conditions of the resistive experiment has the most stressed magnetic field and the outflows act to restore the angle between the spine and fan.

In addition to the local flows associated with the topological features, there is also a global reconnection outflow that can be visualised by following perturbations in the current and pressure. Longcope and Priest (2007) first proposed this analytically by coupling a wave equation to a diffusion equation and it has since been studied numerically by Fuentes-Fernández et al. (2012a) and Stevenson and Parnell (2015a).

The wave propagates in all directions, highlighting the dimensions of the current layer in the left panel in figures 12 and 13. When the resistivity is switched on, the supercritical current is dissipated rapidly and a current deficit appears in the centre of the layer. The middle panel shows the perturbation, consisting of multiple enhancements and deficits, moving perpendicular to the separatrix surface. At $t = 0.3$, the wave is no longer visible in all three cuts but there is a lot of small scale activity occurring along

the current layer, as miniature perturbations accompany the impulsive reconnection.

In the $x = 0$ plane, the width of the current layer is visible and the wave propagates radially outwards. There appear to be two distinct sections to the wave on either side of $z = 0$, which eventually overlap at $t = 0.3$. At $y = 0$, the wave is emitted from the length of the current layer and is of a planar nature. After the wave has moved away from the current layer, there are a large number of smaller waves (figure 13) emerging from different locations along the separatrix surface. The wave is again planar for $z = 0$ but the magnitude of the perturbation is greater than in the other cuts. The peculiar shape of the wave is especially visible, as the magnitude diminishes at $x = 0$ as both sections bend towards the fan. Again there are a number of pressure enhancements close to the separatrix surface which are associated with secondary waves.

The perturbation is much clearer in the pressure than in the current density (which will be omitted in the future). The changes in the current reflect not only the reconnection outflows but also the relaxation process occurring at the spine. This relaxation can even be seen in the left panel of figure 12, so it is not triggered by the reconnection, whose effects are localised to the fan at $t = 0.01$.

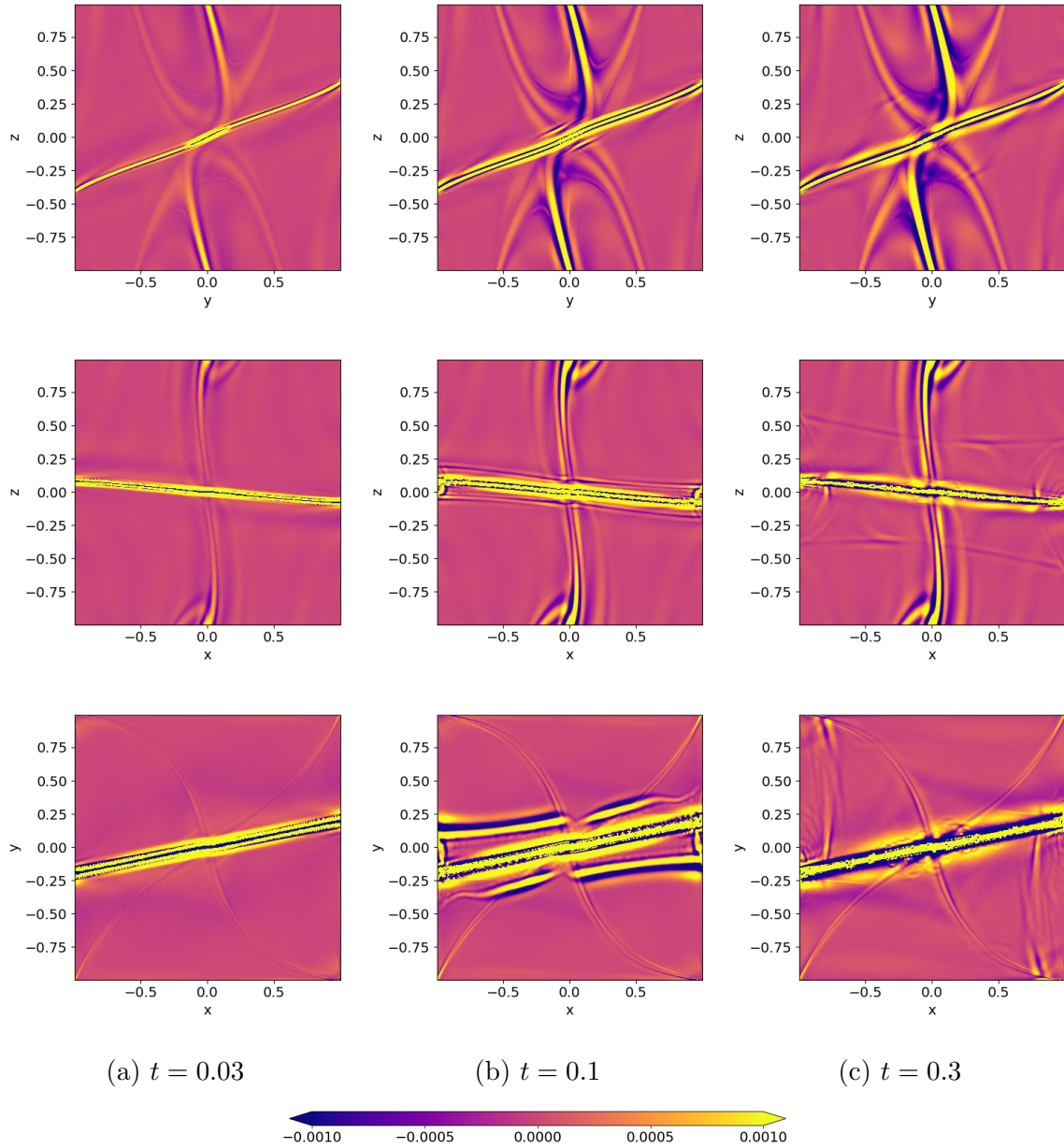


Figure 12: Running difference contour showing perturbations in the modulus of the current density ($|j| - |j_0|$). Top: $x = 0$, middle: $y = 0$, bottom: $z = 0$. The time interval between successive frames is 0.01.

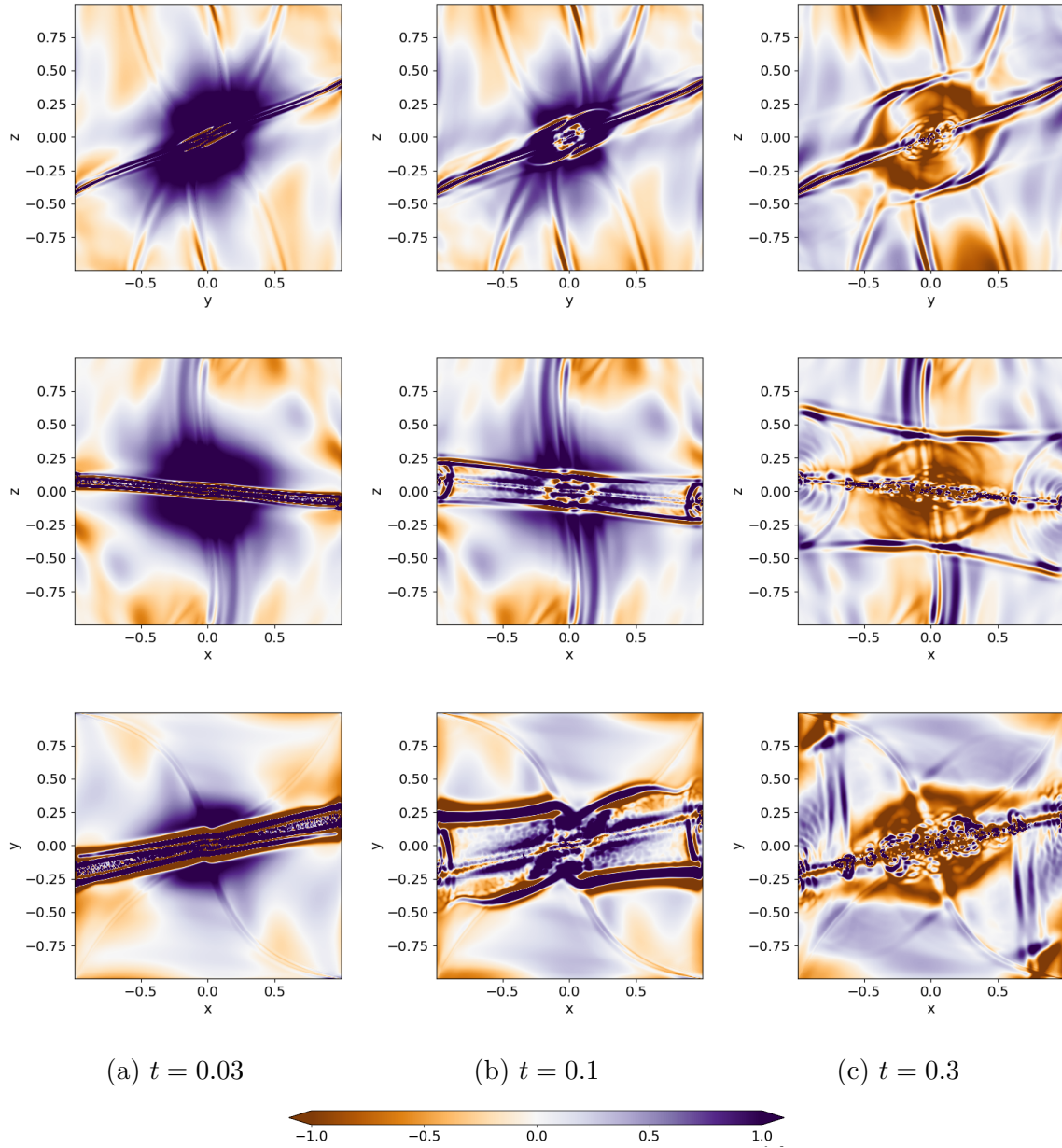


Figure 13: Running difference contour showing perturbations in the plasma pressure ($\times 10^{-5}$). Top: $x = 0$, middle: $y = 0$, bottom: $z = 0$.

2.4 Nulls with Current Perpendicular to Major Axis

In this section, a spiral null point ($j_{sp} = 1$) will again be compared with an improper null ($j_{sp} = 0$), both of which share the parameter values $j_f = 1$ and $b = 3/2$. For the improper null in this chapter, the major axis is $\mathbf{x}_1 = (0, 4, 1)$, which is perpendicular to the current $\mathbf{j} = (j_f, 0, 0)$.

	Spiral	Improper
λ_1	$1.25 + 0.43i$	1.5
λ_2	$1.25 - 0.43i$	1
λ_3	-2.5	-2.5
\mathbf{x}_1	(-2.25, 3.75, 1.0)	(0, 4, 1)
\mathbf{x}_2	(3.03, 0.43, 0.0)	(1, 0, 0)
\mathbf{x}_3	(0, 0, 1)	(0, 0, 1)

Table 3: Eigenstructure of the $b = 3/2$ nulls

2.4.1 Relaxation

The ideal relaxation of the null point systems was carried out in Lare3D as described in the previous section. The artificially high background viscosity ($\nu = 0.01$) was again employed to accelerate the viscous damping of the flows to achieve a quasi-equilibrium state. The same criteria as before were used to terminate the relaxation. The magnitude of the total force away from the boundaries must be small. Additionally, the integrated kinetic energy should be relatively small and the internal and magnetic energies should be constant.

It is clear from figure 14 that the extent of the relaxation is not the same in the two experiments. The magnitude of the total force in the improper case is at least twice that of the spiral experiment across the entire domain and is almost ten times higher at the z boundaries where $-0.33 < x, y < 0.33$. The relaxation of the improper null was cut short because it was particularly susceptible to numerical diffusion, which would lead to a null point bifurcation if allowed to continue. This chapter is solely concerned with reconnection at isolated null points but chapters 3 and 4 will deal with systems containing multiple connected nulls.

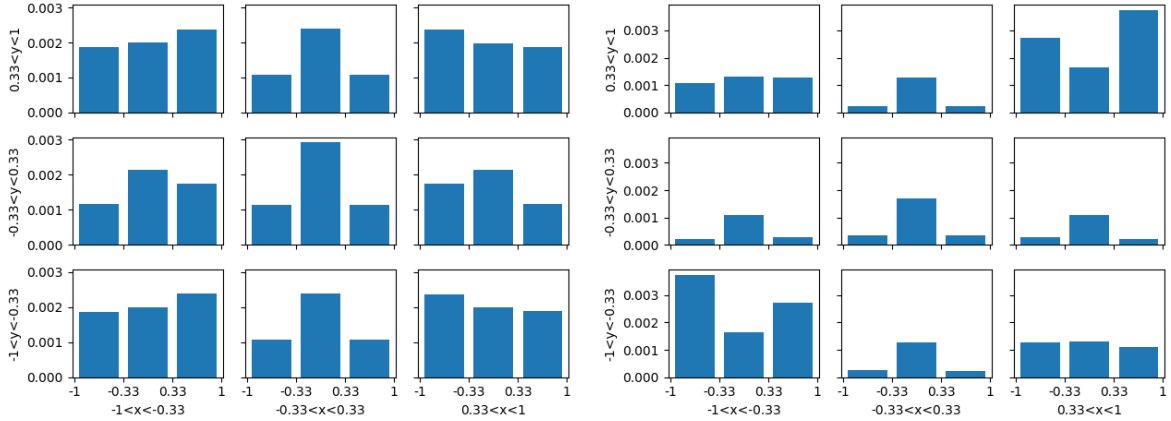


Figure 14: Integrated total force in 27 subvolumes within the domain. The columns correspond to different x ranges and the rows show the y ranges. The three bars within each of the nine histograms are the z ranges. The forces for the improper null are shown on the left and the spiral null on the right.

The current layers are much smaller for $b = 3/2$ than they were in the $b = 2/3$ case. The alignment of the current is still parallel to the x -axis, which is the direction of the initial fan current. However, the current is localised about the null point (along the separatrix surface) and does not extend to the boundaries of the numerical box. The other key difference between figure 15 and figure 6 is the direction of the fieldlines along the fan plane. For $b = 2/3$, the fieldlines were aligned with the x -axis but here the major axis is in the y direction. The direction of the fieldlines and the nature of the current layers are connected, as an initial current directed along the fieldlines allows for more efficient transport of current away from the null point.

2.4.2 Energies

The energy changes for the $b = 3/2$ experiments are shown in figure 16. As for the $b = 2/3$ experiments, there is a conversion of magnetic energy to internal energy and (to a lesser extent) kinetic energy. However, there is a clear distinction between these two experiments due to the non-equilibrium initial condition of the improper null. The energy changes for the improper null are marked by large oscillations caused by the plasma motions. The same oscillations can be vaguely seen in the spiral case occurring

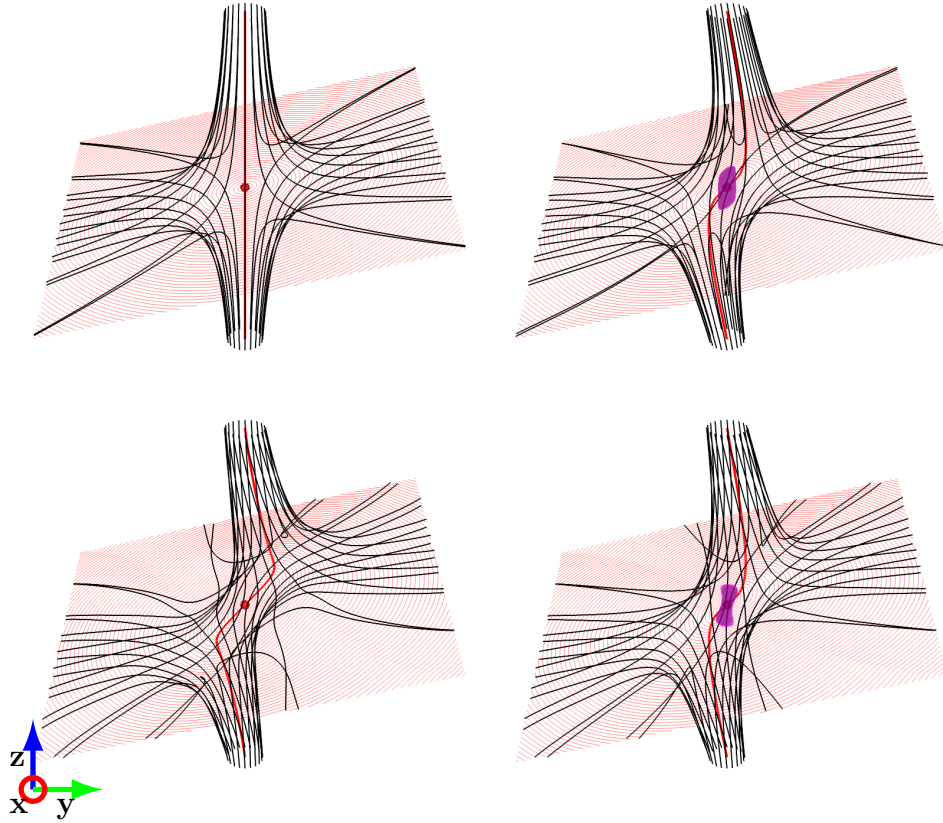


Figure 15: Magnetic skeleton before (left) and after (right) relaxation. Isosurfaces show the critical current used in the reconnection experiment. First row: improper null; isosurface shows $|j| = 20.19$. Second row: spiral null; isosurface shows $|j| = 22.73$. Note that the image is rotated by 30 degrees about the y -axis to improve fieldline visibility.

at approximately the same times. The period of these oscillations is approximately 1, as the times are normalised by the transit time for an Alfvén wave through the box. The improper null experiences a net loss of kinetic energy since the velocity damping due to the relaxation process outweighs the velocity gain due to reconnection. The spiral null experiences a relative kinetic energy gain of the order 10^{-8} which is 1% of the internal energy gain in keeping with the $b = 2/3$ experiments. The improper null converts more magnetic energy because the greater initial plasma velocity drives more reconnection but the quantity is still only half that converted by the $b = 2/3$ nulls.

In figure 17 the terms contributing to the energy changes in the spiral experiment are

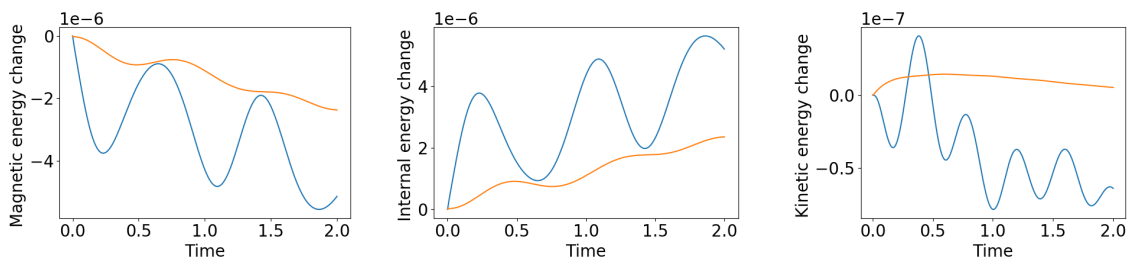


Figure 16: Time and volume integrated energy changes for the $b = 3/2$ null reconnection, normalised by initial total energy. Blue: improper, orange: spiral.

shown. There is a considerable difference in the time evolution of these terms for the two $b = 3/2$ experiments but the spiral case is shown because these plots are more representative of the reconnection process. If the same quantities were plotted for the improper nulls, there would be signs of both relaxation and reconnection, which would be difficult to distinguish.

The Poynting flux once more indicates a flow of magnetic energy between the outer subvolume and the two middle shells. The flux is initially close to zero in all subvolumes unlike the $b = 2/3$ case, where the flux is initially at a maximum or minimum (depending on the shell). The work done by the Lorentz force is similar to that seen for $b = 2/3$. The outer subvolume does the least work and the middle shells dominate at the start, before the inner shell becomes the most important. As with the Poynting flux, the work done by the Lorentz force is close to zero at the start of the experiment before ascending to the first peak. The principal difference affecting the magnetic energy change is in the Ohmic heating. Here it is contained almost entirely within the central subvolume, whereas for $b = 2/3$ it is distributed across all of the shells. This has a straightforward explanation, as the current layer in figure 15 is localised about the null point while that in figure 6 covers the whole of the x -axis. The nature of the Ohmic heating in inner subvolume is the same as before, with an initially high rate of heating being followed by a brief delay and then impulsive heating after $t = 0.1$.

The viscous heating for the $b = 3/2$ experiment is approximately half that of the $b = 2/3$ case. The larger current layer for $b = 2/3$ should lead to a more widespread non-equilibrium and hence a higher integrated viscous heating. In the outer subvolume, it is only one third of the $b = 2/3$ value, as the difference increases with distance from

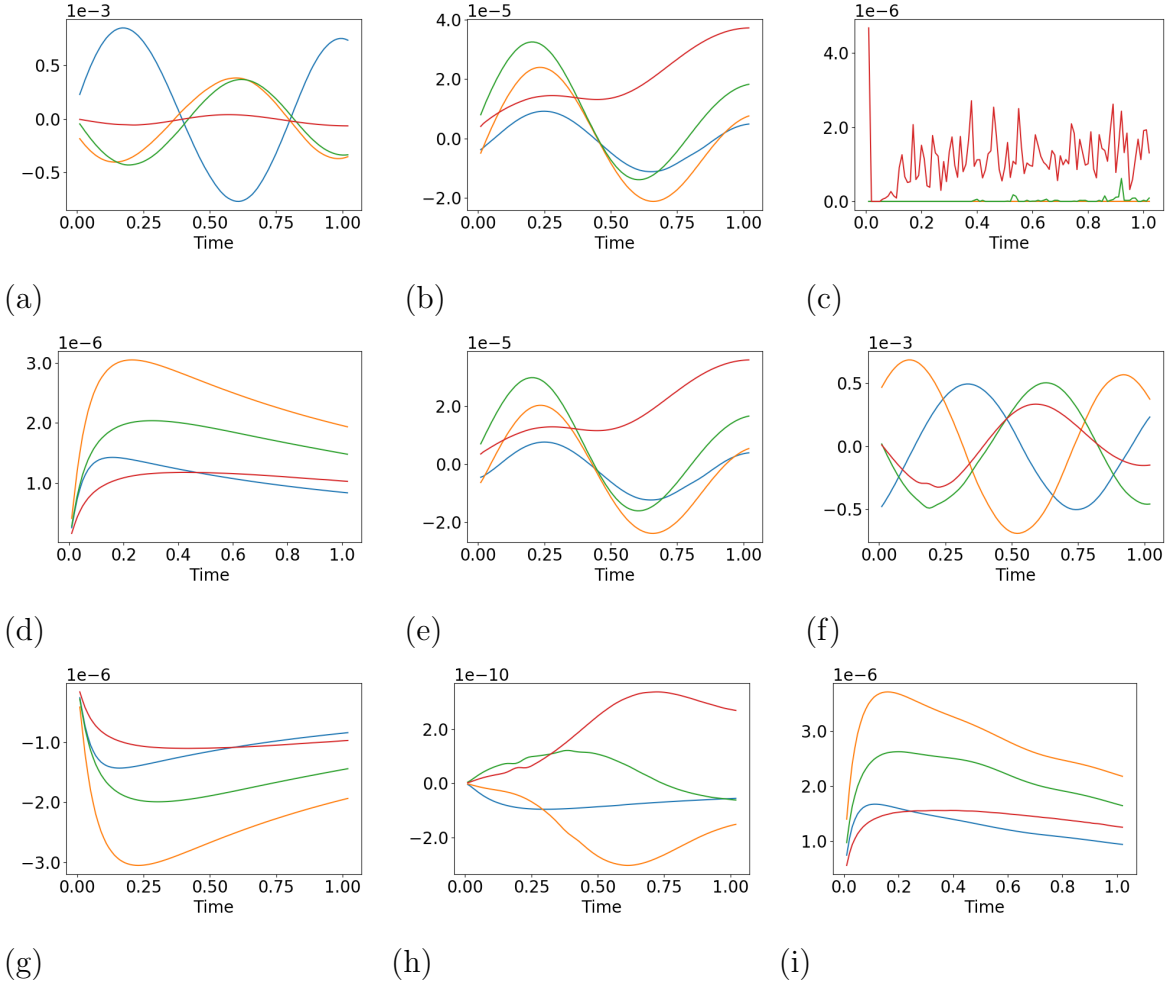


Figure 17: Terms contributing to rate of change of energies for spiral null. These instantaneous values are integrated across four distinct subvolumes (blue: $0.75 < |x, y, z| < 1$, yellow: $0.5 < |x, y, z| < 0.75$, green: $0.25 < |x, y, z| < 0.5$, red: $|x, y, z| < 0.25$). a) Poynting flux; b) Work done by the Lorentz force; c) Ohmic heating; d) Viscous heating; e) Work done by the pressure force; f) Enthalpy flux; g) Work done by the viscous force; h) Kinetic energy flux; i) Difference between work done terms.

the centre. Although this experiment is generally closer to an equilibrium than that in the previous section, it is important to remember that the forces were approximately balanced in the $b = 2/3$ case. Hence, the work done by the pressure force (figure 16(e)) is almost indistinguishable from that done by the Lorentz force (figure 16(b)). The enthalpy flux is not only a factor of 2 less but also distributed among the subvolumes differently. The outer middle shell is of greater importance here, although the mag-

nitudes of the fluxes are similar for each of the four shells. This is surprising, since it suggests that the energy transfer is less localised than in the case with the larger current layer.

As in the $b = 2/3$ experiments, the kinetic energy change is modest as the work done by the viscous force balances the net work done by the Lorentz and pressure forces. The kinetic energy flux is an order of magnitude less than for $b = 2/3$. The flux is also directed into the inner two subvolumes while it was previously only feeding the inner shell. This evidence also conflicts with the idea that the reconnection is more localised for $b = 3/2$.

2.4.3 Reconnection Rate

The nature of the reconnection can again be studied by looking at the parallel electric field along fieldlines passing through $z = 0$. Three frames from both the spiral and improper nulls are shown in figure 19 to give an impression of the spatial distribution of E_{\parallel} . In the first row, the reconnection is commencing at the start of the experiment and the E_{\parallel} covers a continuous region, being strongest in the vicinity of the null. The reconnection has ceased altogether in the second row as the super-critical current has been exhausted. In the bottom row, the reconnection continues in small disconnected parts of the original current layer. This sequence of reconnection events is consistent with the behaviour seen for $b = 2/3$. The E_{\parallel} here covers a smaller length of the x -axis because the current layer in figure 15 is localised about the null. The spiral null also does not feature the plumes of weaker E_{\parallel} spreading in the y -direction, as the E_{\parallel} is generally more homogeneous. Additionally, the E_{\parallel} is more fragmented during the impulsive reconnection for $b = 2/3$, as the critical current is only exceeded in sporadic locations. As before, the current layer does not undergo significant changes during the impulsive reconnection, as the bursts of E_{\parallel} act to smooth those localised regions where $|j| > j_{crit}$.

The reconnection rates in figure 20 again show the three phases discussed previously in the $b = 2/3$ experiments. There is an apparent difference in the timescales over which the reconnection takes place, as the rapid reconnection expires more quickly and the impulsive reconnection starts around $t = 0.1$ compared with the $t = 0.2$ previously

Figure 18: Parallel electric field integrated along fieldlines passing through $z=0$, left: $j_{sp} = 0$, right: $j_{sp} = 1$

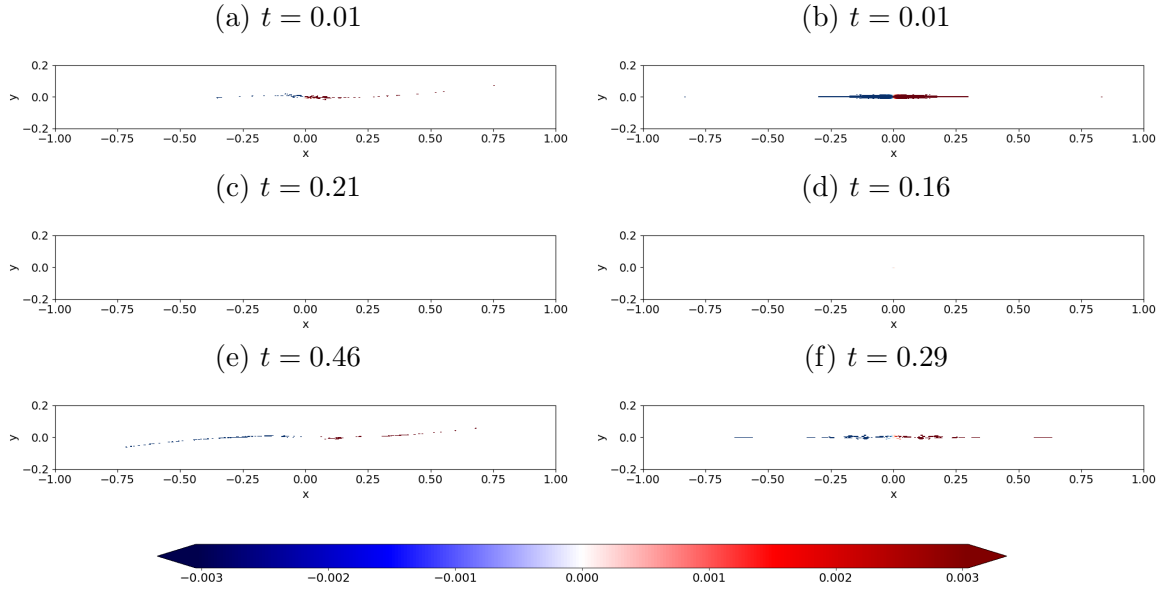


Figure 19: Parallel electric field integrated along fieldlines passing through $z = 0$, left: spiral, right: improper

seen. The magnitude of the E_{\parallel} is also lower during the rapid reconnection. This is due to the more localised current layer, as fieldlines passing through the diffusion region will experience a non-zero resistivity across a shorter length.

2.4.4 Flows

Although one might expect that the localised current layer would lead to a localised flow pattern, figure 21 shows the wave communicating the loss of equilibrium to the edges of the domain. The pressure perturbation is shown for clarity but the wave can also be identified in current contours as in figure 12. The first column shows the instant that the wave is released from the reconnection site and the current layer is outlined. The wave is clearly visible in the second column, along with a widespread pressure increase encircling the null with embedded localised reductions. In the third column, the leading wavefront is succeeded by a train of smaller disturbances, which are emitted

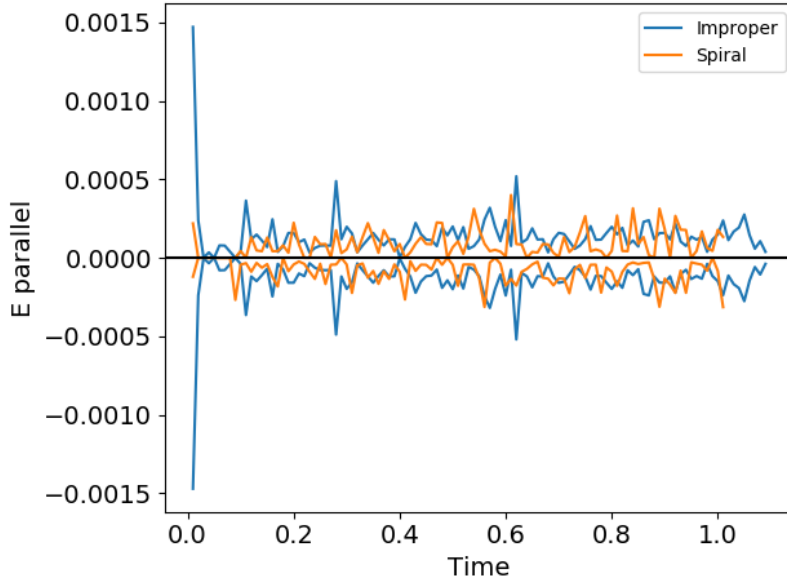


Figure 20: Time evolution of the maximum and minimum values of the integrated E_{\parallel} along fieldlines passing through $z = 0$

continuously from the null point during the impulsive reconnection.

The structure of the wave seems to be simpler than its $b = 2/3$ counterpart. In the $x = 0$ plane, there are two wavefronts propagating parallel to the width of the current layer. By contrast, for $b = 2/3$ four separate features can be identified and their motion is perpendicular to the current layer width. For $y = 0$, the length of the planar waves is obviously less than that previously seen, since the current layer does not extend to the boundaries. The direction of travel is consistent however, which is also the case for $z = 0$. Again, the wave here consists of two fronts travelling parallel to the line $x = 0$. The differences in wave morphology can be explained by the interaction with the flattened S-shape fieldlines associated with the spiral nulls. In the $b = 3/2$ case, the current has accumulated in the centre of the S-shape, where the fieldline is almost straight. For $b = 2/3$, the current is more aligned with the curved parts of the fieldlines so the corresponding pressure perturbations move slightly apart from each other.

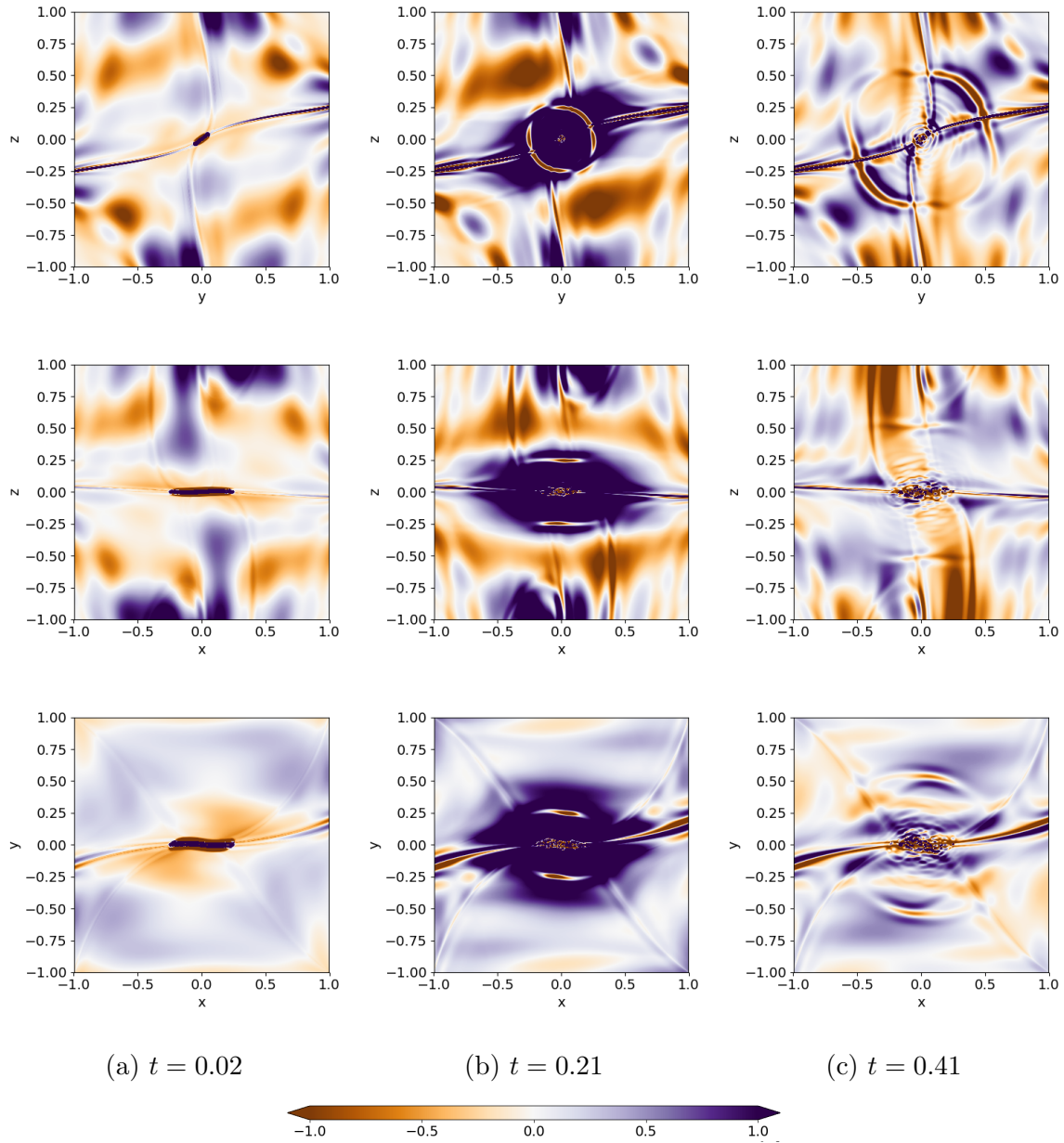


Figure 21: Running difference contour showing perturbations in the plasma pressure ($\times 10^{-5}$). Top: $x = 0$, middle: $y = 0$, bottom: $z = 0$. The time interval between successive frames is 0.01.

2.5 Nulls Without a Major Axis

In the final results section, another pair of null points will be compared. As before, these satisfy $j_{sp} = 0$ (improper) and $j_{sp} = 1$ (spiral) and both have $j_f = 1$. The

difference from the previous sections is that $b = 1$, which means that the improper null has a repeated fan eigenvalue. The consequence of this fact is that the null does not have a major axis.

	Spiral	Improper
λ_1	$1.0 + 0.5i$	1.0
λ_2	$1.0 - 0.5i$	1.0
λ_3	-2.0	-2.0
\mathbf{x}_1	(-0.5, 3.0, 1.0)	(0, 3, 1)
\mathbf{x}_2	(3.0, 0.5, 0.0)	(0, 3, 1)
\mathbf{x}_3	(0, 0, 1)	(0, 0, 1)

Table 4: Eigenstructure of the $b = 1$ nulls

2.5.1 Relaxation

The relaxation was performed as in the previous two subsections. The integrated total force for the final state has once more been plotted in figure 22. The force distribution in the critical spiral null is very similar to the improper null seen in figure 3 for $b = 2/3$. Since the previous field was deemed to be an acceptable quasi-equilibrium according to both the energy changes and forces, it is fair to conclude that this case is also sufficiently relaxed. The spiral null force distribution is different from those seen before, as there is symmetry in both the x and y directions. In spite of this, the forces are still confined to the boundary and the topological features, meaning the forces for $|z| > 0.33$ are negligible for $|x| < 0.33$ and $|y| < 0.33$. The peak magnitude of the total force is slightly lower than previous spiral nulls so this case also appears to be a quasi-equilibrium.

The magnetic skeleton for the $b = 1$ nulls can be seen in figure 23. The fieldlines are traced from a ring of evenly spaced points surrounding the spine footpoints and remain evenly spaced when they spread across the fan plane. This is the effect of setting $b = 1$, as there is no major axis upon which the fieldlines are concentrated (unlike in figures 6 and 15). The dimensions of the current layer are closer to the $b = 3/2$ case than $b = 2/3$, although the extent is slightly larger in both the x and y directions. The magnitude of the current in the isosurface is between the values for $b = 2/3$ and $b = 3/2$. This is consistent with the results in Al-Hachami and Pontin (2010), which found that the

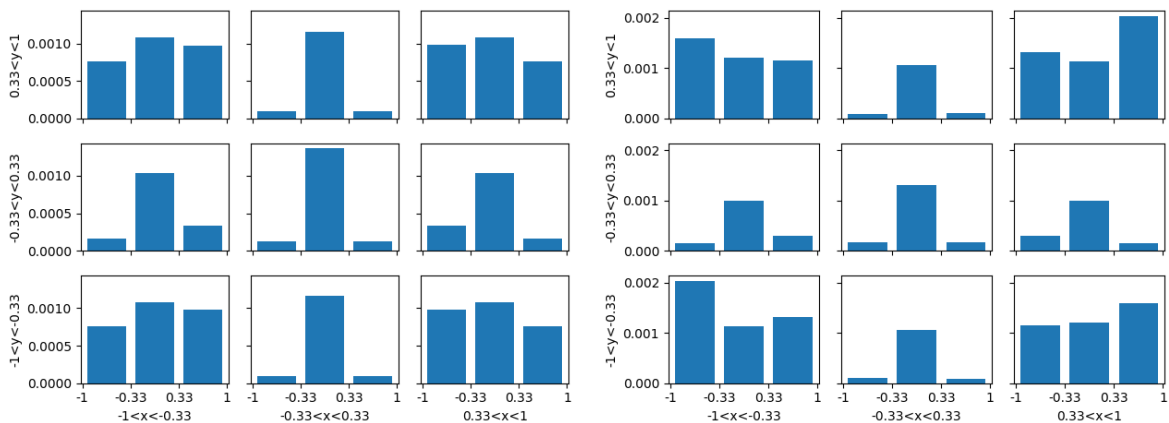


Figure 22: Integrated total force in 27 subvolumes within the domain. The columns correspond to different x ranges and the rows show the y ranges. The three bars within each of the nine histograms are the z ranges. The forces for the improper null are shown on the left and the spiral null on the right.

magnitude of the current increases with the parameter b , whereas the length of the current layer decreases.

2.5.2 Energies

The total amount of magnetic energy converted (in figure 24) is similar to that in the $b = 3/2$ experiments. This energy transfer occurs in phases, which has been shown to reflect the flow reversals occurring in the numerical box. It is interesting that the amount of energy transferred by the improper null lags behind the spiral null before $t = 0.7$. This initially slow rate of energy transfer for the improper null is evident in the internal energy but not the kinetic energy, which always exceeds the spiral case.

It is unusual that the Ohmic heating and the viscous heating are not in agreement. Generally, one would expect that the system with the higher reconnection rate would dissipate more current and would also produce stronger reconnection outflows, leading to a higher viscous heating. Clearly this association can not be made in these experiments. The Ohmic heating at the spiral null is higher during both the fast and impulsive phases of the reconnection but the viscous heating at the improper null is greater (reflecting the greater kinetic energy in the system).

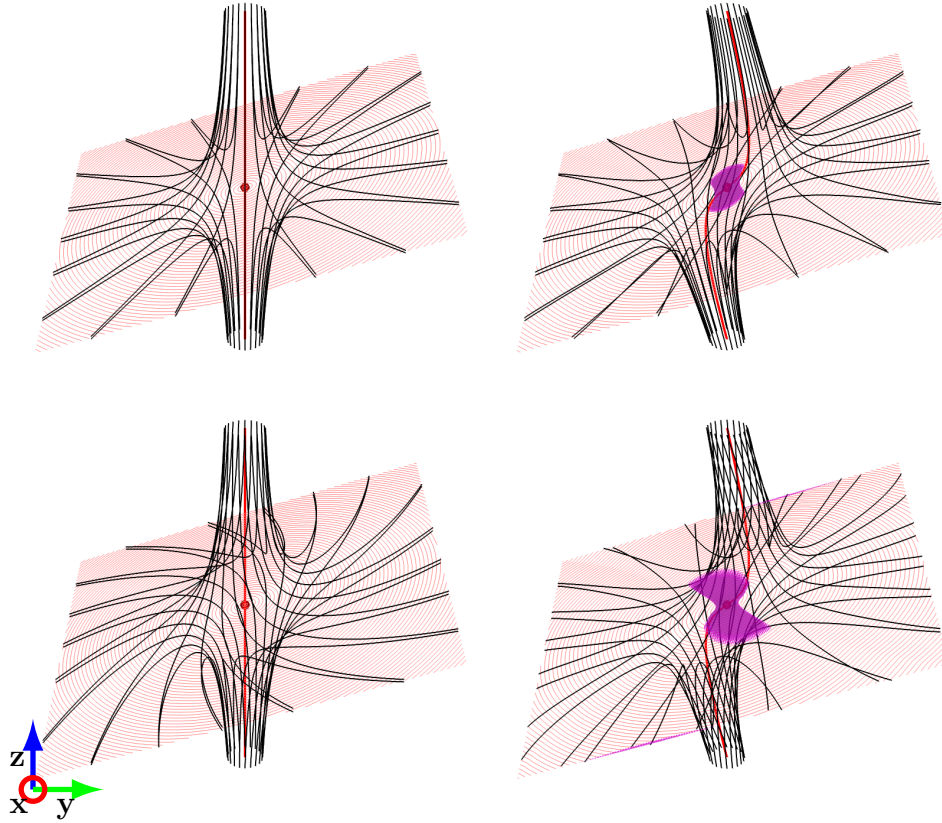


Figure 23: Magnetic skeleton before (left) and after (right) relaxation. Isosurfaces show the critical current used in the reconnection experiment. First row: improper null; isosurface shows $|j| = 14.58$. Second row: spiral null; isosurface shows $|j| = 14.67$. Note that the image is rotated by 30 degrees about the y -axis to improve fieldline visibility.

2.5.3 Reconnection Rate

The spatial distribution of the parallel electric field is very similar to that seen in the $b = 3/2$ experiments (figure 19). The contours for $t = 0.01$ still show strong continuous regions of E_{\parallel} , indicating that the rapid reconnection occurs over a timescale that is closer to the $b = 2/3$ experiments. The impulsive E_{\parallel} is also slightly stronger than that seen for $b = 3/2$ and involves more of the current layer.

Figure 26 shows that the reconnection rate is higher at the spiral nulls, notwithstanding the large burst of reconnection at the improper null shortly before $t = 0.2$. This

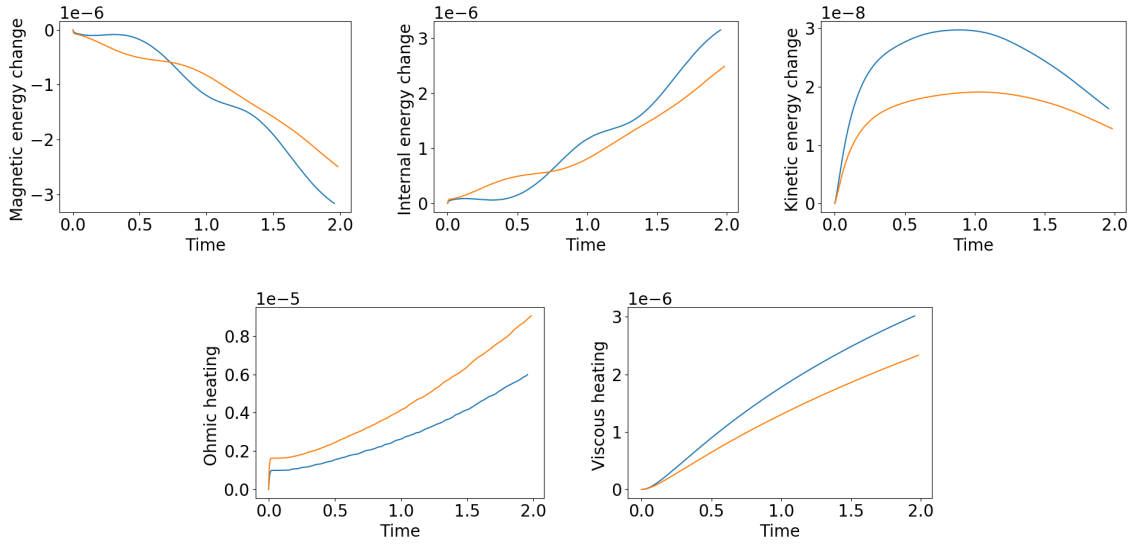


Figure 24: Time and volume integrated energy changes for the $b = 1$ null reconnection, normalised by initial total energy. Blue: improper, orange: spiral.

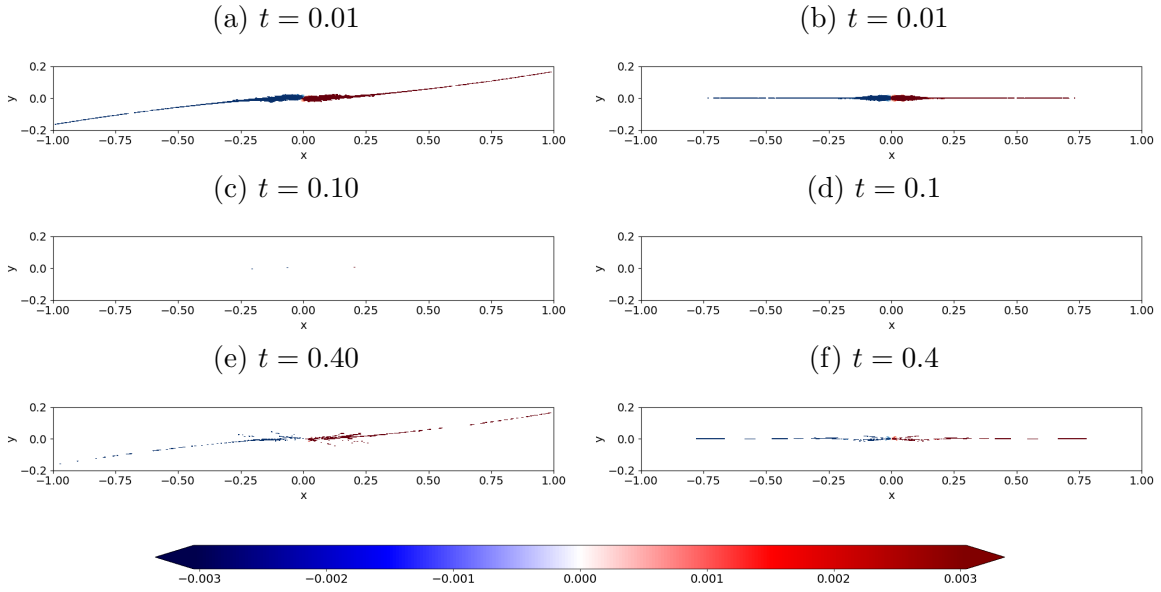


Figure 25: Parallel electric field integrated along fieldlines passing through $z=0$, left: $j_{sp} = 0$, right: $j_{sp} = 1$

corroborates the Ohmic heating plot in figure 24 but it does not agree with the evidence of previous sections (figures 10 and 20), which suggested that reconnection is stronger

at improper nulls. One conclusion that can be drawn is that the nature of the diffusion region is critically important in determining the reconnection rate. The $b = 3/2$ and $b = 1$ experiments all have localised current layers surrounding the null point, while for $b = 2/3$, the current layer reaches the x boundaries. The reconnection rate is higher for the $b = 2/3$ experiments because the critical current is exceeded across a greater length of the reconnecting fieldlines, even though the magnitude of the current is smaller. This property agrees with Al-Hachami and Pontin (2010), where the experiments with larger current layers (and smaller maximum current) had the greatest reconnection rates.

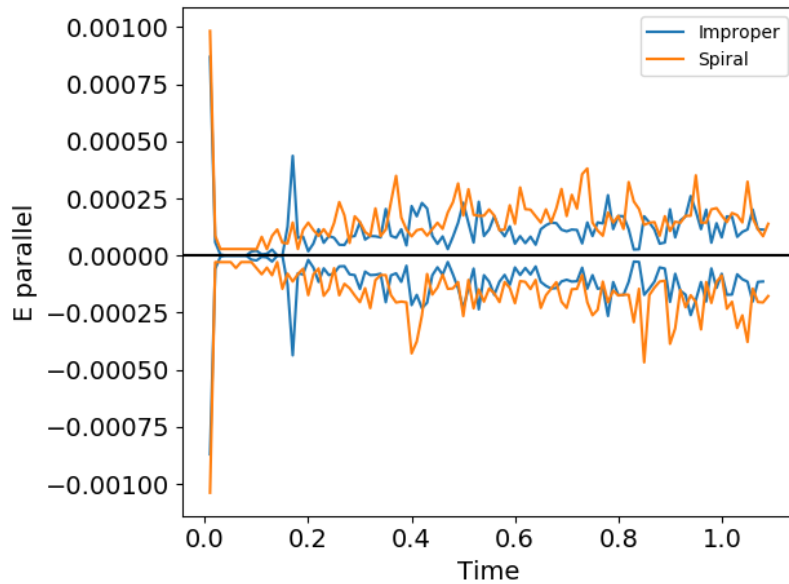


Figure 26: Time evolution of the maximum and minimum values of the integrated E_{\parallel} along fieldlines passing through $z = 0$

2.6 Discussion

This work has studied null point reconnection at an equilibrium current layer, comparing the two categories of generic linear nulls- *improper* and *spiral*. In each of the six experiments, an initial non-equilibrium magnetic field was relaxed to form a current layer that coincided with the fan plane. Using this equilibrium field, a reconnection experiment was performed by imposing an anomalous resistivity where the current

exceeded a critical value (chosen to localise the diffusion region about the null).

The nature of the reconnection at the two different types of null was found to be quite similar, although there were some differences. In both cases, the majority of the free magnetic energy was converted to internal energy by Ohmic and adiabatic heating. All of the experiments featured rapid reconnection after the resistivity was switched on, before the current layer would rebuild to allow further reconnection to occur in an impulsive manner. The reconnection rates at the improper null points were slightly higher than the spiral cases, as was the amount of magnetic energy converted. This could be linked to the fact that the critical current was slightly higher in the spiral experiments, meaning the reconnection was fractionally more widespread in the improper cases.

The nature of the fan fieldlines (spiral or improper) is shown to be of secondary importance to the extent of their azimuthal symmetry, governed by the parameter b . In keeping with Al-Hachami and Pontin (2010), a higher value of b leads to a more localised current layer containing stronger current. The reconnection rate declines as b is increased because the parallel electric field is non-zero along a smaller portion of the length of the fieldlines.

There are a number of possible extensions to this work studying null point reconnection. This chapter presents only a small portion of the parameter space and there are a number of changes that can be made affecting both the initial null point configuration (varying b , j_{sp} and j_f) and the reconnection experiment (altering the magnitude or spatial profile of η and ν ; varying the size of the current layer through j_{crit}). Although there are clear benefits to starting the reconnection from a quasi-equilibrium state, it could be informative to run the experiment without a relaxation phase, for example to test whether the results are qualitatively the same if the magnitude of the flows is greater. Another possible way to achieve greater flow speeds would be to perform a low beta experiment by reducing the initial plasma pressure.

3 Single Separator Reconnection

3.1 Introduction

The null points that occur high in the solar corona are not thought to exist in isolation but rather in oppositely signed pairs. These pairs of nulls can be connected by a separator line if their separatrix surfaces intersect. Although null points are modelled mathematically by a linear magnetic field, global configurations containing multiple null points are nonlinear. This means that although the linear approximation is valid locally around the nulls, their spines and separatrix surfaces can bend. Consequently, two nulls can be connected by multiple separators, as will be studied in depth in Chapter 4.

Separator reconnection has been proposed as a possible mechanism for energy release in the solar atmosphere. It is thought to be more viable than pure null point reconnection because photospheric extrapolations suggest that the number of nulls that are connected greatly exceeds the number that are isolated. Additionally, separators can be longer than 1000Mm (Platten et al. (2014)), which hypothetically allows the diffusion region to be much larger than those seen in null point reconnection. It has been shown analytically (Longcope (2001)), as well as numerically (Stevenson et al. (2015)), that the current in a magnetic field with connected nulls preferentially builds along the separator.

The concept of separator reconnection was introduced in Lau and Finn (1990), which analytically reviewed a number of different types of reconnection, both null and non-null, in two and three dimensions. The work studied magnetostatic reconnection (with a magnetic field that does not evolve in time) and kinematic reconnection, which prescribes a time-dependent magnetic field but does not account for the changes caused by plasma flows and current. In both of these cases, the goal is to solve for the electrostatic potential and identify the locations where it becomes singular, meaning ideal MHD breaks down. In another early work in this area, Longcope and Cowley (1996) offered an alternative to kinematic reconnection by adding a singular current layer to potential 2D and 3D null point fields.

In more recent work, Haynes et al. (2007) identified separator reconnection in a 3D

numerical MHD experiment where two oppositely signed magnetic flux fragments were brought together. This simulation not only demonstrated that separator reconnection could be at the centre of dynamic phenomena occurring in the solar atmosphere, but also showed that a single pair of null points could be connected by multiple separators. In Stevenson and Parnell (2015a), reconnection at a single separator was studied in detail numerically for the first time. The authors took an initially non-potential quadratic magnetic field and relaxed the system to form a current layer aligned with the separator. An anomalous resistivity was used to initiate reconnection within this current layer, which was found to consist of two phases- *fast* and *impulsive* reconnection. These terms will be used to describe the results in the experiment presented in this chapter, drawing parallels between the two works.

This numerical experiment will analyse reconnection of a magnetic field containing two null points connected by a separator, as well as a current sheet initially located away from the separator. There are relatively few separator reconnection experiments in the literature. The most comprehensive study was performed by Stevenson and Parnell (2015a), where the non-potential initial field was relaxed to form a quasi-equilibrium before initiating the reconnection. Instead of the quadratic magnetic field used in previous work, the field here will be constructed from hyperbolic functions, giving the separatrix surfaces a more complicated geometry. In addition, the initial field has an embedded current sheet rather than a constant component of current across the domain. This work will investigate whether the specific initial current distribution significantly effects the reconnection. Another important aspect of (the second part of) this work is that the initial condition is chosen to be close to an equilibrium. Since the initial flows are small, it is not necessary to include a relaxation phase in the experiment.

3.2 Analytical Field

This section will explain the origins of the magnetic field (and balancing pressure) used throughout the Chapter. When studying 3D reconnection, it can be advantageous to start with an equilibrium current layer. However, a 3D non-potential equilibrium containing null points is yet to be discovered. This means that such reconnection studies must be carried out numerically, using a non-equilibrium initial condition. In

Stevenson and Parnell (2015a) and chapter 2 of this thesis, the initial non-potential field has to be relaxed ideally before a reconnection study can be commenced. Although this process results in a convincing force balance, the ideal treatment of the field is numerically expensive, requiring on average eight nodes on an HPC cluster to run for a week. Furthermore, the subsequent reconnection converts only a small fraction of the free magnetic energy, as the flow speeds remain low throughout the experiment when beginning with an equilibrium. Here, a different approach is essayed, building an analytical initial condition that does not require relaxation. Rather than starting with a fully 3D separator field, this work begins with an exact 2D equilibrium containing a single X-point and adds a perturbation field that converts the 2D X-point to two 3D null points. The 2D Corrugated Sheet Pinch field is a well known solution to the Grad-Shafranov equation, which is often viewed as a generalisation of the 1D Harris Sheet. Not only does the 2D field feature X-points embedded in a current sheet structure but the field components are also finite unlike previous separator models, which use a truncated expansion field that diverges at infinity.

3.2.1 Harris Sheet

The *Harris Sheet* is a simple example of a current sheet, which is of fundamental importance in the study of reconnection and other phenomena. This field has been used in a variety of astrophysical experiments, both numerical and analytical, MHD and collisionless. As has already been discussed, current sheets are necessary to achieve the low Magnetic Reynolds number required for diffusive processes. The small length scales present in the current sheet compensate for the low plasma resistivity operative in the solar corona and Earth's magnetosphere. More precisely, the Harris Sheet is a *neutral sheet*, in that the magnetic field direction reverses about the current sheet, meaning the field strength is zero at the location of the peak current.

In the following work, it will be assumed that the Harris Sheet magnetic field is directed along the x -axis with a constant guide field in the y -direction. The magnetic field has a tanh profile that varies with z so the current density is directed parallel to the y -axis and has a sech^2 profile. One of the reasons why the Harris Sheet is so frequently studied is that it is an exact equilibrium- the Lorentz force associated with the magnetic field

is balanced by a pressure gradient. As shown in equation (58), the pressure thus has the same spatial variation as j_y , although there can be a background component p_0 .

$$\begin{aligned}\nabla p &= \mathbf{j} \times \mathbf{B} \\ \frac{dp}{dz} &= (0, \operatorname{sech}^2(z/L_z), 0) \times (\tanh(z/L_z), B_{y0}, 0) \\ p &= p_0 + \operatorname{sech}^2(z/L_z)\end{aligned}\tag{58}$$

3.2.2 Corrugated Sheet Pinch

The Harris Sheet can be regarded as a 1D solution to the *Grad-Shafranov* equation. This equation provides equilibrium solutions for MHS systems with an invariant direction (in this case the y -direction). The magnetic field in such a scenario can be decomposed into poloidal and toroidal components as $B = \nabla \times (A(x, z)\mathbf{e}_y) + B_y(x, z)\mathbf{e}_y$, with the flux function A constant along fieldlines. It can be shown by manipulating the equation of motion (see Schindler (2006)) that $p = p(A)$ and $B_y = B_y(A)$. The equation to be solved once these functions have been specified is then:

$$-\Delta A = \mu_0 \frac{dp}{dA} + B_y \frac{dB_y}{dA}\tag{59}$$

Setting $p = p_0 e^{2A}$ and $B_y = b$ gives Liouville's equation, $-\Delta A = \lambda e^{2A}$. This chapter will use the *Corrugated Sheet Pinch* or *Cat's Eye solution*. The magnetic field is:

$$\begin{aligned}B_x &= \frac{\sinh(z/L_z)}{\cosh(z/L_z) + (1 - \alpha^2) \cos(x/L_x)} \\ B_y &= B_{y0}\end{aligned}\tag{60}$$

$$B_z = -\frac{(1 - \alpha^2) \sin(x/L_x)}{\cosh(z/L_z) + (1 - \alpha^2) \cos(x/L_x)}\tag{61}$$

This field reduces to the Harris Sheet if $\alpha = 1$. Otherwise, the poloidal field contains a sequence of X-points and O-points along the x -axis. It is important to note that although the 2D field resembles a null point structure, the constant guide field ensures that there are no 3D nulls. However, the value of the 2D magnetic field in this chapter is the possibility to transform the poloidal X-points into 3D null points by the addition

of a B_y term that cancels with the guide field component at the X-points. Because B_y is constant the only non-zero component of the current density is j_y . As in the Harris Sheet, the spatial variation of the current density is equivalent to that of the pressure. For general choices of p and B_y the pressure varies like j_y but this is a special case because of the unidirectional current density.

$$\mathbf{j} = \left(0, -\frac{\alpha^2(\alpha^2 - 2)}{(\cosh(z/L_z) + (1 - \alpha^2)\cos(x/L_x))^2}, 0 \right) \quad (62)$$

$$p = -\frac{p_0\alpha^2(\alpha^2 - 2)}{(\cosh(z/L_z) + (1 - \alpha^2)\cos(x/L_x))^2} \quad (63)$$

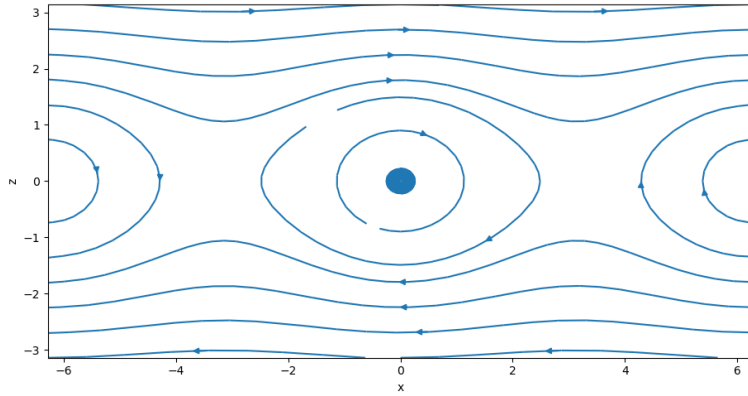


Figure 27: Corrugated Sheet Pinch magnetic field with $\alpha = 0.5$ and $L_x = L_z = 1$. There are 2D X-points located at $(\pm\pi, 0)$ and an O-point at $(0, 0)$.

3.2.3 3D Magnetic Field

The flux function given in equation (39) is in fact the y -component of the vector potential \mathbf{A} for the 3D magnetic field:

$$\mathbf{B} = \left(\frac{\partial A_z}{\partial y} - \frac{\partial A_y}{\partial z} \right) \mathbf{e}_x + \left(\frac{\partial A_x}{\partial z} - \frac{\partial A_z}{\partial x} \right) \mathbf{e}_y + \left(\frac{\partial A_y}{\partial x} - \frac{\partial A_x}{\partial y} \right) \mathbf{e}_z \quad (64)$$

The constant guide field is achieved by setting $A_z = -B_{y0}x$. In the 2D field, B_x and B_z vanish at $(0, 0)$ but the constant guide field in the y -direction means there are no 3D

nulls. It is necessary to alter the vector potential so that B_y vanishes in two locations. This is a matter of assuming $A_x = A_x(y, z)$ or $A_z = A_z(x, y)$. The former assumption would also introduce a B_z term that is independent of x , while the latter adds a B_x term that does not vary with z . Of these two possibilities, the extra B_z term is the least injurious because it does not disturb the Harris Sheet, which will remain a limiting case of the 3D field. Hence, we can choose:

$$A_x = B_{y_1} L_1 g(y) h(z) \quad (65)$$

The magnetic field components affected by the addition of this term to the vector potential now have the following forms:

$$\begin{aligned} B_y &= B_{y_0} + B_{y_1} L_1 g(y) h'(z) \\ B_z &= -\frac{B_{x_0} (L_{z_0}/L_{x_0}) (1 - \alpha^2) \sin(x/L_{x_0})}{\cosh(z/L_{z_0}) + (1 - \alpha^2) \cos(x/L_{x_0})} - B_{y_1} L_1 g'(y) h(z) \end{aligned} \quad (66)$$

Now, the functions $g(y)$ and $h(z)$ must be carefully chosen to meet certain criteria. The foremost requirement is that B_y must have two zeros, which means that $g(y)$ should not be monotonic. If $g(y_1) = g(y_2)$ then it will be possible to cancel the constant guide field, assuming the additional B_y term is negative. The additional B_z term must also vanish at the desired location of the null points, $z = 0$. Finally $g(y)$ and $h(z)$ should be finite functions, along with their derivatives. The Corrugated Sheet Pinch was chosen as a starting point in part because its field components are all finite, so this should be maintained with the added terms. Choosing $g(y) = \text{sech}^2(y/L_{z_1})$ and $h(z) = \tanh(z/L_{z_1})$, the 3D flux function becomes:

$$\begin{aligned} A_x &= B_{y_1} L_{z_0} \text{sech}^2(y/L_{y_1}) \tanh(z/L_{z_1}) \\ A_y &= -B_{x_0} L_{z_0} \ln [\cosh(z/L_{z_0}) + (1 - \alpha^2) \cos(x/L_{x_0})] \\ A_z &= -B_{y_0} x \end{aligned} \quad (67)$$

The corresponding 3D magnetic field is equal to the Corrugated Sheet Pinch plus additional terms in B_y and B_z :

$$\begin{aligned}
B_x &= \frac{\sinh(z)}{\cosh(z) + (1 - \alpha^2) \cos(ax)} \\
B_y &= b + cr \operatorname{sech}^2(dy) \operatorname{sech}^2(rz) \\
B_z &= -\frac{a(1 - \alpha^2) \sin(ax)}{\cosh(z) + (1 - \alpha^2) \cos(ax)} + 2cd \frac{\sinh(dy)}{\cosh^3(dy)} \tanh(rz)
\end{aligned} \tag{68}$$

The magnetic field has been normalised as follows:

$$a = \frac{L_{z_0}}{L_{x_0}} \quad b = \frac{B_{y_0}}{B_{x_0}} \quad c = \frac{B_{y_1}}{B_{x_0}} \quad d = \frac{L_{z_0}}{L_{y_1}} \quad r = \frac{L_{z_0}}{L_{z_1}} \tag{69}$$

The nulls are located at $(0, \frac{1}{d} \cosh^{-1}(\sqrt{\frac{-cr}{b}}), 0)$.

3.3 Numerical Setup

This experiment uses the 3D magnetic field given in (68) and an initial plasma pressure of the form (63), which balances the 2D Corrugated Sheet Pinch field. The simulation is performed using Lare3D to solve the resistive MHD equations (as described in Chapter 1). The magnetic field parameters used in the main experiment are $\alpha = 0.9$, $a = 1.0$, $b = 0.1$, $c = -0.2$, $d = 1.0$, $r = 1.0$ and the background pressure is $p_0 = 0$. The main experiment uses a non-uniform resistivity, which is only non-zero ($\eta = 0.001$) where the current density exceeds the critical value $j_c = 1$. The viscosity has a background value of $\nu = 0.001$ and the shock viscosity is as described in Chapter 1. The simulation box has $|x, y, z| < 1.5$ and the grid size is 512^3 points. As in the previous chapter, line-tied boundary conditions are used.

3.3.1 Initial Magnetic Topology

The initial magnetic topology is shown in figure 28, featuring two null points (positive and negative respectively) at $(0, \pm 0.88, 0)$. The positive spine is inclined at 2.69 radians to the x -axis and the negative spine at 0.45 radians. The separatrix surfaces are almost

planar due to the choice of parameters but there is a visible displacement in the z -direction at the $x = -1.5$ boundary, which is mirrored at $x = 1.5$.

The separator connecting the two nulls sits along the y -axis and splits the magnetic field into four flux domains, illustrated in figure 28. Domain I consists of flux that travels in to the box from the positive x boundary along the negative fan and exits the same boundary along the negative spine. The flux in domain II enters via the negative x boundary along the positive spine and leaves through the positive x boundary along the negative spine. In domain III, flux enters and leaves the box at $x = -1.5$ and in domain IV, the flux enters at the upper boundary and leaves through the lower boundary.

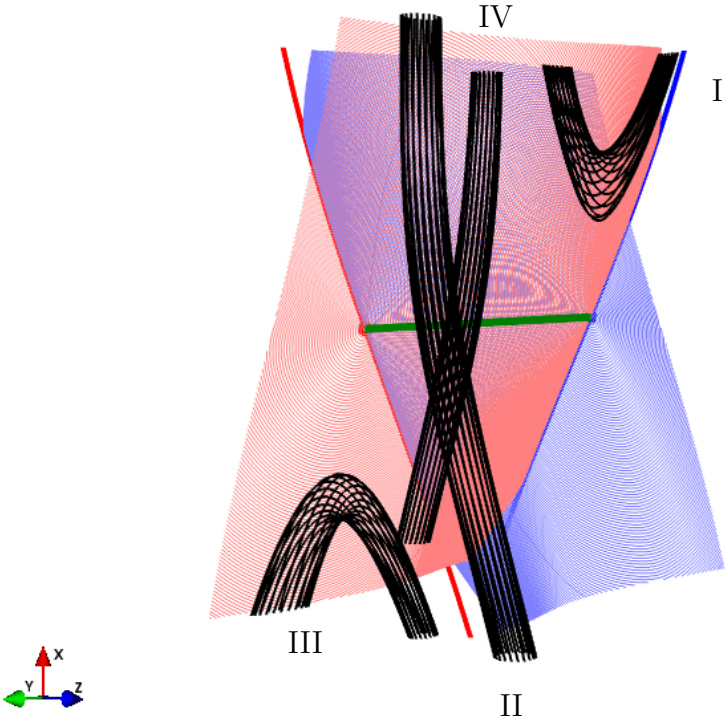


Figure 28: Magnetic skeleton for the 3D separator field. Four ‘flux tubes’ are plotted to show fieldlines in each of the four flux domains.

3.3.2 Current Density

The current density for the 3D field is equal to the 2D current in equation (62) plus a j_x term that is dependent on y and z .

$$j_x = \frac{2cd^2 \tanh rz}{\cosh^2 dy} - \frac{6cd^2 \sinh^2 dy \tanh rz}{\cosh^4 dy} + \frac{2cr^2 \sinh rz}{\cosh^2 dy \cosh^3 rz} \quad (70)$$

Figure 29 shows the magnitude of the current density in the three mid-planes. The current density reduces to the 2D form in the plane $z = 0$. Here, there is no y dependence and $j_y \sim -\frac{1}{(\cos x - 1)^2}$. The same x variation applies to any y or z cut but the z dependence in $y = 0$ is more complicated. Clearly the magnitude of the current is highest closer to $z = 0$ but the additional current due to the 3D field varies like $\tanh z(1 + \text{sech}^2 z)$. The most complicated picture arises in the $x = 0$ plane, where two current sheets appear to intersect. The 2D current in this plane is simply $j_y \sim \text{sech}^2 z$ but the j_x term is a function of both y and z . As already discussed, this j_x vanishes at $z = 0$ but otherwise, it is strongest in the neighbourhood of $y = 0$ and seems to be weakest around $y = \pm 0.7$.

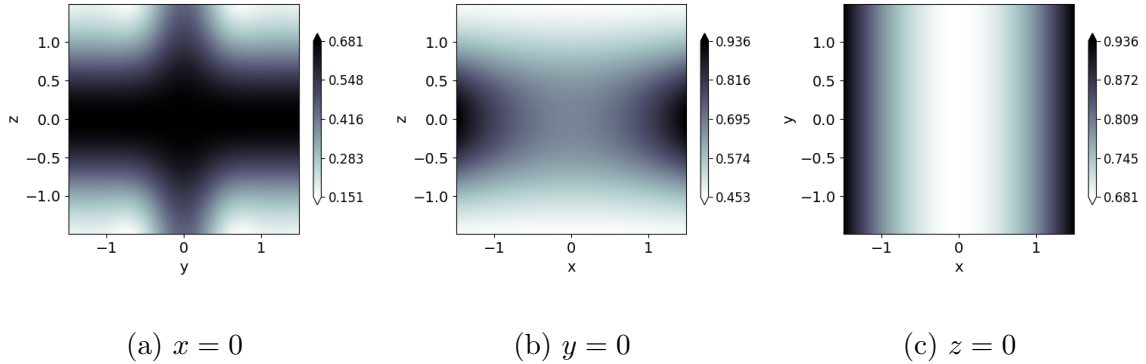


Figure 29: Magnitude of the current density in the three mid-planes. Note that the contour levels are different in each cut.

3.3.3 Forces

Since this experiment uses the balancing pressure for the 2D field, the initial condition is not an equilibrium. As discussed in the previous section, the current density consists of the Corrugated Sheet Pinch $j_y(x, z)$ term and the new $j_x(y, z)$. In the $z = 0$ plane, the j_x term is equal to zero, meaning the Lorentz force is the same as in the 2D case and there is a local force balance. For $y = 0$, there is current at the z boundaries resulting in an unbalanced Lorentz force. From looking at the total force, it is also clear that there is a force imbalance for $|z| < 0.7$ although its magnitude is small compared to the Lorentz and pressure forces. Of the three mid-planes, $x = 0$ is the farthest from an equilibrium because of the strong j_x term close to $y = 0$. The resulting force consists of two ring shapes centred on $y = \pm 0.7$ and the vectors point inwards towards these centres.

3.4 Reconnection from Non-equilibrium

The energy transfer in this experiment is not a straightforward transaction between the magnetic energy and internal energy as in the null point reconnection in chapter 2. This can be explained by the force imbalance in the initial condition, which results in a significant amount of kinetic energy in the early part of the experiment ($t < 5$). In figure 31, the energy changes for an ideal experiment are displayed alongside the resistive case to emphasise the importance of the ideal flows. The ideal experiment will be discussed separately in section 3.6. Both the internal and magnetic energies experience an initial decrease due to the plasma motions. At around $t = 1$, this decrease is cancelled because the flow direction reverses, meaning the resultant force now opposes the velocity and the plasma decelerates. Around $t = 3$, the second reversal occurs, allowing the plasma to accelerate once more. Hence there is a second peak in the kinetic energy, accompanied by another loss of magnetic and internal energies.

The impact of the flows becomes less important around $t = 4$ as the rate of Ohmic heating reaches its peak. This marks the first (and largest) reconnection event, caused by the build-up of current along the separatrix surfaces. This ohmic heating accounts for a transfer from magnetic to internal energy of roughly 8×10^{-4} . After the super-

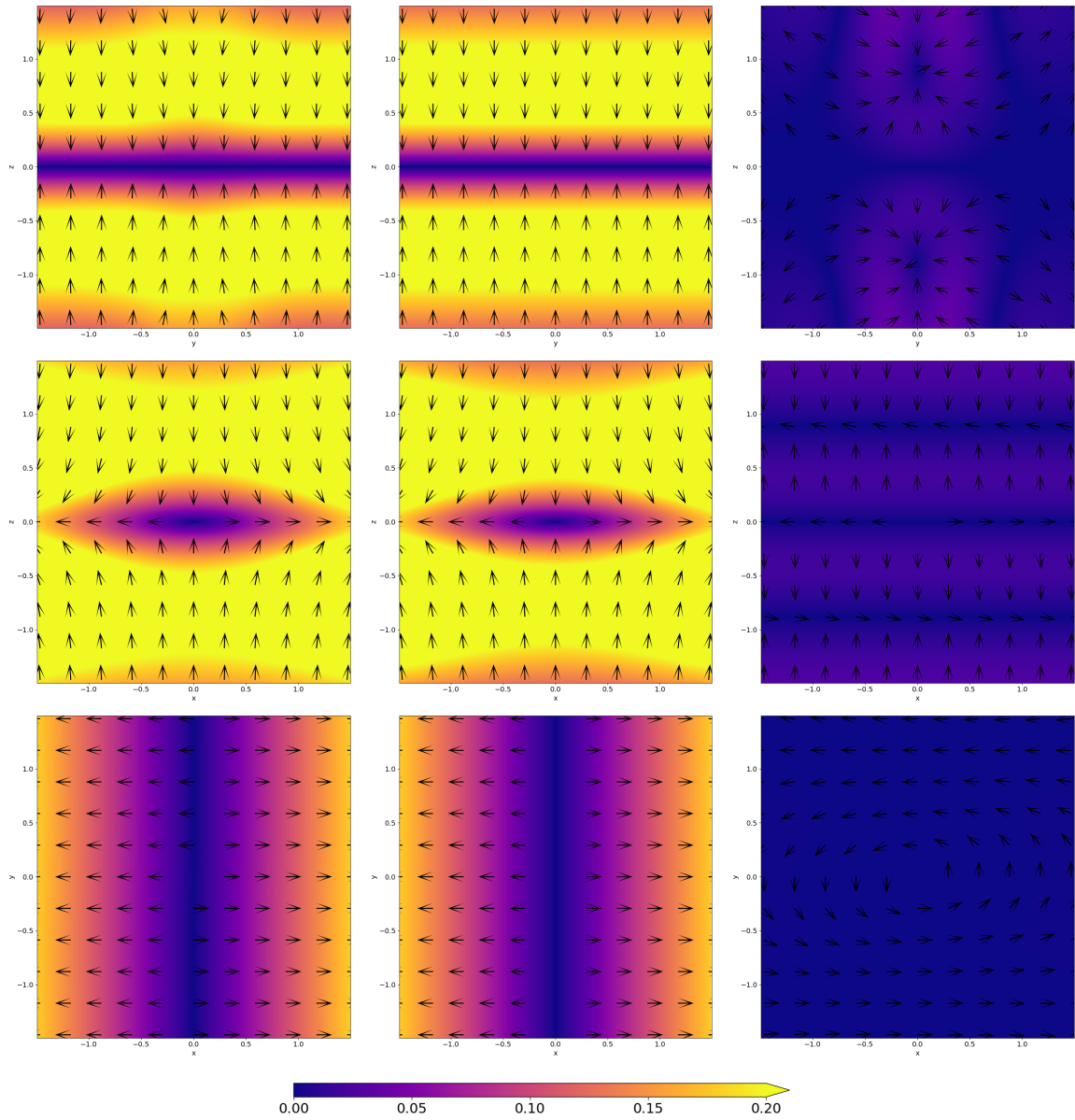


Figure 30: Forces in the three mid-planes of the analytical separator field. The three columns show the Lorentz force, pressure force and total force respectively. The rows show the different cuts: $x = 0$, $y = 0$ and $z = 0$.

critical current has been mostly dissipated, the internal energy is steady between $t = 6$ and $t = 8$. During this time, the current layer is rebuilding and the second reconnection event occurs from $t = 8$ to $t = 12$. A further 9×10^{-4} energy conversion takes place here. At $t = 14$, the Ohmic heating reaches a second trough and there is a brief respite

in the magnetic and internal energy changes before the third reconnection event begins at $t = 15$, continuing until the experiment is terminated. In spite of using a 'switch-off' resistivity, there is a non-zero Ohmic heating rate throughout the period studied, to which the oscillations are superposed.

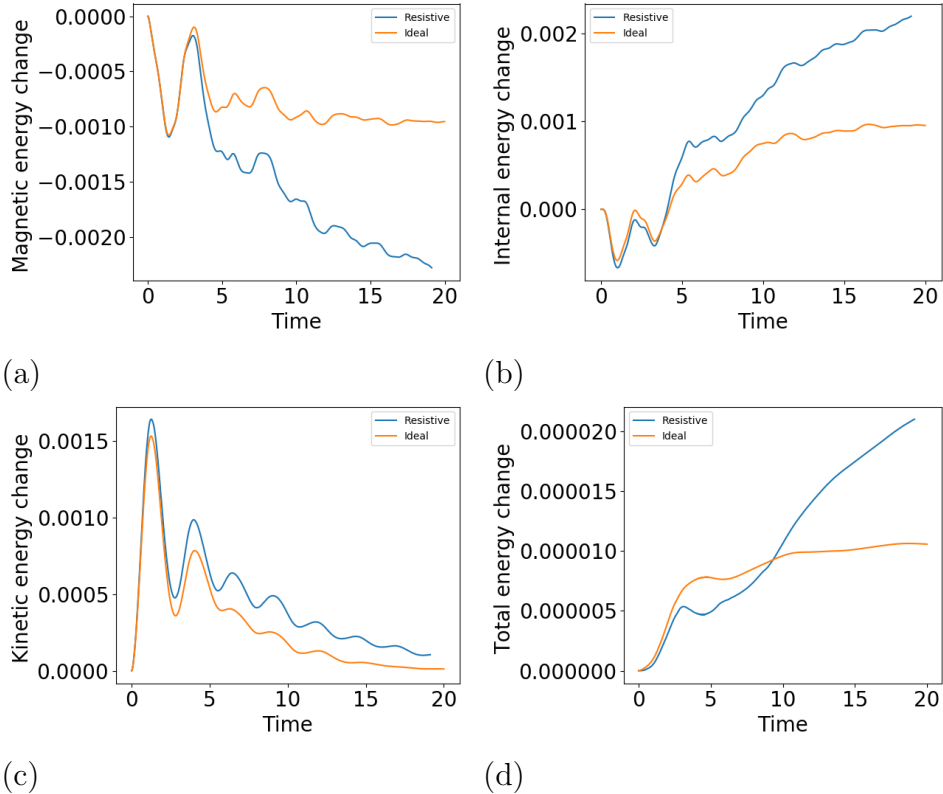


Figure 31: Time and volume integrated energy changes (normalised by the initial total energy): a) magnetic energy; b) internal energy; c) kinetic energy; d) total energy

Figure 33 shows the terms contributing to the energy changes in figure 31, integrated over subvolumes within the domain.

The Poynting flux carries electromagnetic energy between the different subvolumes. It is initially negative across all the subvolumes as the energy is transported from the boundaries towards the centre of the domain. The flow reverses around $t = 2$ such that the Poynting flux carries energy into the outer subvolumes. The direction of the flow changes once again at $t = 3.5$, establishing the oscillatory pattern caused by collisions with the line-tied boundaries. The Poynting flux is initially greatest in the middle

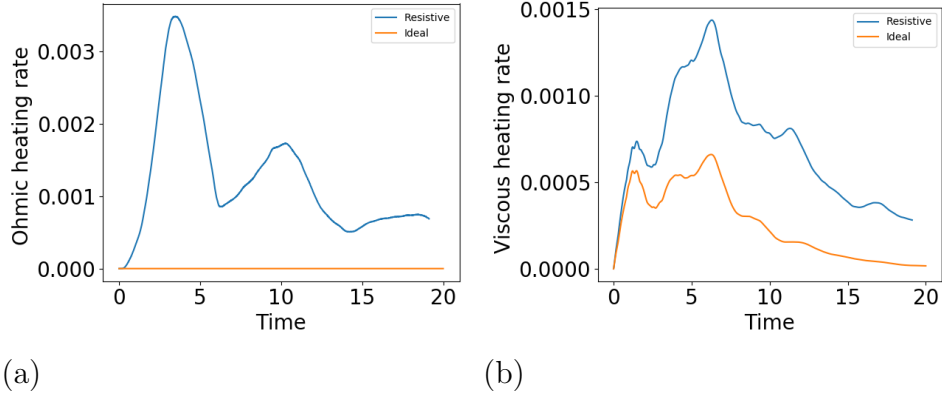


Figure 32: Rates of change for the heating terms contributing to the energy changes: a) Ohmic heating; b) viscous heating

subvolumes, although after the flows have traversed the box at $t = 3.5$, the inner shell becomes more important. This suggests that the restructuring of the magnetic field shifts the energetically important sites towards the centre of the domain.

The work done by the Lorentz force displays a similar periodicity to the Poynting flux, as the initial sign changes are consistent with those seen in (a). As the direction of the flow changes, it acts to either support or oppose the Lorentz force. At the start of the experiment, the work done is positive since the Lorentz force is generally directed towards the centre of the box (figure 30). The majority of the work done occurs in the middle subvolume at the beginning of the experiment but after the flow reverses, this subvolume loses its importance compared with the outer subvolumes. This implies that either the magnetic field in the middle subvolume is undergoing significant changes or there are smaller scale flows developing. The work done in the inner subvolume is also indicative of complexity in the system, since it does not become negative until $t = 5$. There is no integrated work done in the inner shell between $t = 2$ and $t = 3$, suggesting that the direction of the flows both agrees and disagrees with the Lorentz force within this region.

According to the plot in (c), the Ohmic heating is experienced across each of the subvolumes in distinct events which peak at $t = 3.5$ and $t = 10.5$. The pulses are separated by a short period of constant heating, during which only the outermost subvolumes play a role. The Ohmic heating is a good indicator of magnetic reconnection

since it measures the current that is dissipated due to the resistivity. The Ohmic heating is rising at $0 < t < 3.5$ and $8 < t < 10.5$ as the current builds along the topological features and declines once the excess current has been dissipated. There is not an obvious correlation between the Ohmic heating and the Poynting flux or the work done by the Lorentz force. An inflow is clearly visible in the other quantities for $t < 2$ but the flow reverses before the peak Ohmic heating occurs, indicating that the outflow is not attributable to reconnection.

The work done by the pressure force is initially most significant in the outer subvolumes. In the outer shells, the amplitude of the work done decays fairly smoothly but this is not the case in the green and red shells. The amplitude of the work done in these subvolumes peaks at $2 < t < 3$ and $8 < t < 9$, when the velocity is oppositely directed to the pressure gradient. It is not clear why there are no corresponding positive peaks but it is likely that the pressure gradient exhibits greater complexity in these regions.

The enthalpy flux gives an impression of the heat energy transfer occurring within the volume. It has the same period as the other quantities (excluding the Ohmic heating) but the flux has opposite direction to the Poynting flux. The enthalpy flux is experienced in all subvolumes, including the innermost shell, but is strongest in the middle shells. It has been seen in (a), (c) and (d) that the middle subvolume is of central importance in the evolution of the system. The work done by the Lorentz and pressure forces converts magnetic energy to internal energy so the regions where these terms are important will be associated with an enthalpy flux.

The kinetic energy flux is two orders of magnitude smaller than the other flux terms but still reaffirms the importance of the middle subvolume. The inner shell experiences the greatest flux (magnitude) of any shell at $t = 5$ and $t = 8$ in spite of its diminutive size. The flux into the outer subvolume is relatively modest considering its greater size, while the central shell once again does not appear to be important.

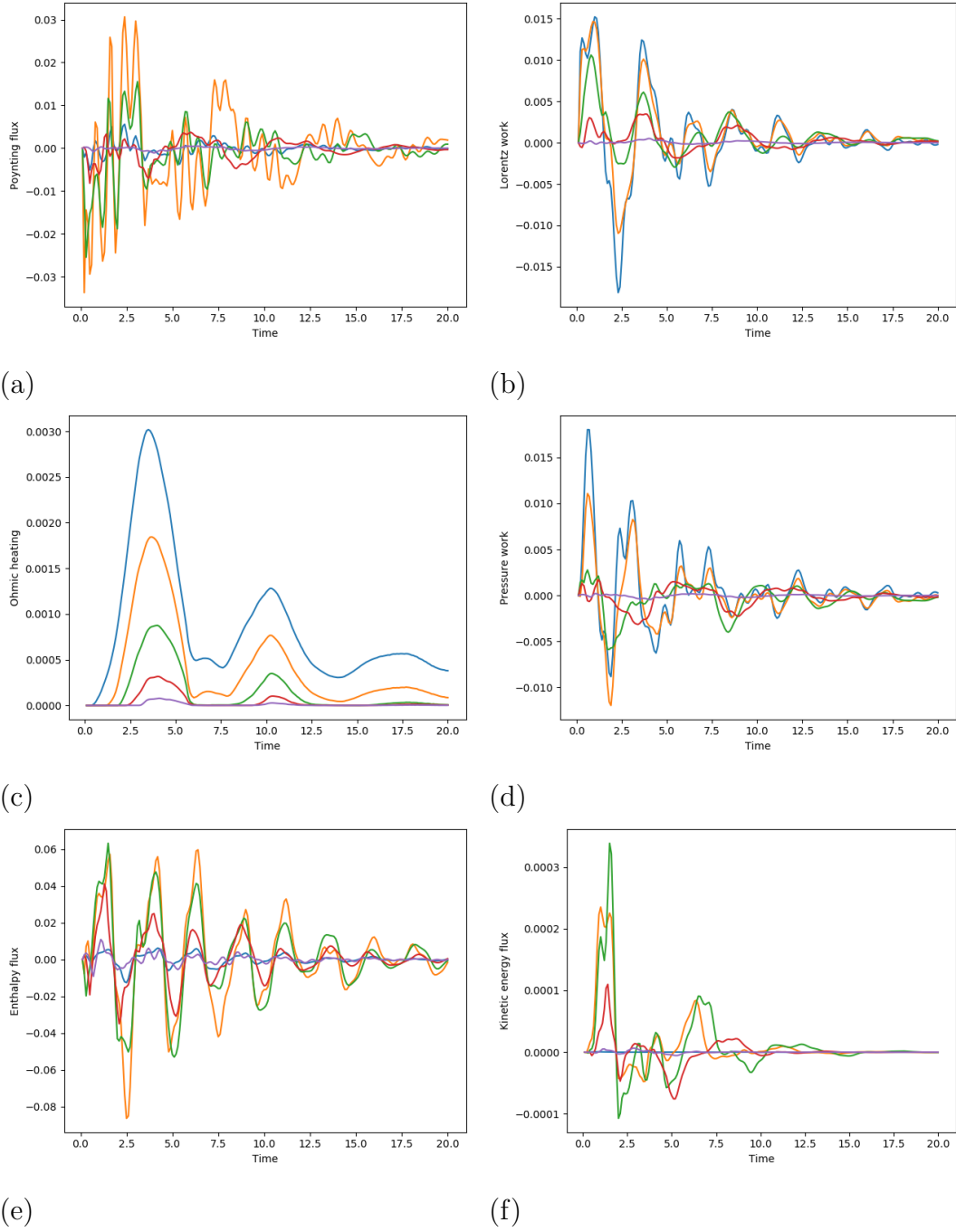


Figure 33: Terms contributing to the energy changes integrated over subvolumes within the domain: a) Poynting flux; b) Work done by the Lorentz force; c) Ohmic heating; d) Work done by the pressure force; e) Enthalpy flux; f) Work done by the viscous force; g) Kinetic energy flux. Blue: $|x, y, z| < 1.5$, yellow: $|x, y, z| < 1.2$, green: $|x, y, z| < 0.9$, red: $|x, y, z| < 0.6$, brown: $|x, y, z| < 0.3$

Figure 34 shows isosurfaces of the current density for four different frames during the experiment. The figure shows that there are always strong currents at the boundary that exceed the threshold. However the reconnection events referred to earlier see the current layers spread to cover the entire separatrix surfaces.

There is reconnection occurring in all four of the frames in figure 34 but a distinction can be drawn between the more diffusive process happening in the left column and the dynamic reconnection in the right column. At times $t = 2$ and $t = 8$, the system is relaxing to form larger current layers. In the first frame, the flows are the dominant feature governing the energy changes and the associated relaxation timescale is shorter than the diffusion timescale operative at the boundaries. The situation is slightly different at $t = 8$ because the flows have calmed somewhat but the currents at the boundaries have also diminished a little. The relaxation timescale is still dominant over the diffusion, leading to the second reconnection event.

It is clear that the current density spreads across most of the separatrix surfaces during the reconnection events. The current layer also encompasses the separator and to a lesser extent the nulls. The key characteristics of these reconnection events are topological changes, which are brought about as the fan planes collapse into each other. In the right column, the deformation of the fans is apparent from the kink in the positive spine line. While in the left column this spine is a straight line forming half of a 2D X-point in projection, on the right it sinks into the positive fan plane. This geometrical change is localised about the separator as the line-tied boundaries ensure that the spine remains at roughly 30 degrees to the vertical along most of its course. Once the angle between the two surfaces becomes negligible locally, the null points undergo bifurcation to form new pairs of nulls (figure 36) and additional separators (figure 37b).

Figure 35 shows the parallel electric field along the length of the separator. As discussed in the previous chapter, E_{\parallel} is a crucial feature of 3D reconnection and when integrated along fieldlines, can also serve as a measure of the reconnection rate over a compact high current region. In this experiment, the current fills the entire box in spite of showing a clear preference for the separatrix surfaces. Therefore in this case, E_{\parallel} is not a good indicator of the reconnection rate, since there is no well-defined diffusion region. However, the use of a non-uniform resistivity means that the E_{\parallel} is somewhat localised

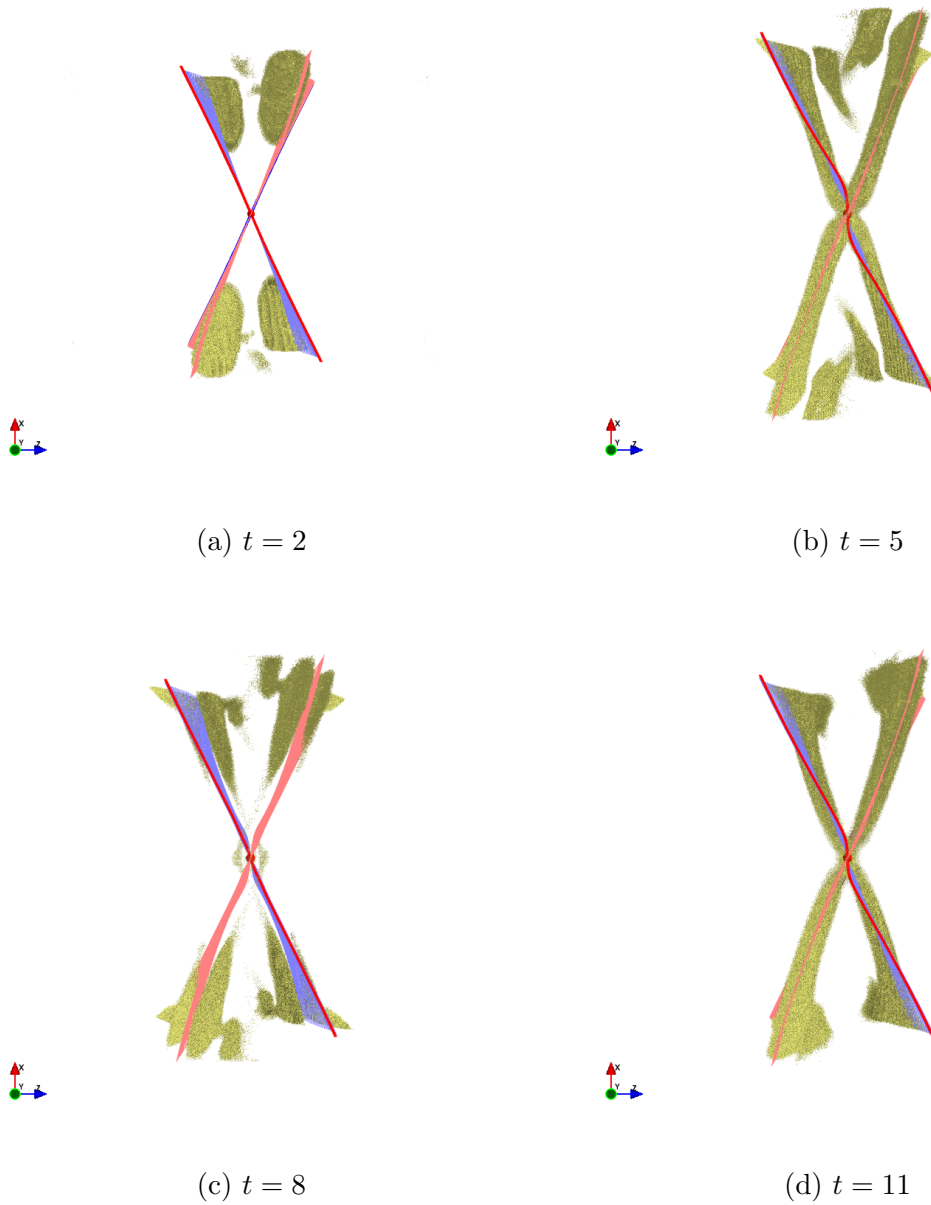


Figure 34: Current isosurfaces showing $|j| = 1$ at different times during the reconnection, viewed from the negative y boundary

unlike the current density. So it is possible to determine when separator reconnection is occurring from figure 35 and also which parts of the fieldline exceed the critical current. Of course, this figure does not give an indication of where else in the domain

reconnection is taking place and how this compares with (and interacts with) the local process along the separator.

This plot is only concerned with the local E_{\parallel} at points within the separator line. Because the separator initially sits along the y -axis and does not deviate significantly from this position, the y -coordinate of the separator points is used in this space-time plot. The two reconnection events are clearly distinguished, since there is no reconnection along the separator at other times. The separator reconnection begins shortly after $t = 3$ at the centre of the separator, before spreading to $y = \pm 0.5$. The strength of the E_{\parallel} along the separator at this time shows little variation but the peak is at the centre. Once the current at the centre of the separator has been dissipated and the E_{\parallel} tends to zero, weaker reconnection occurs close to the nulls. This is perhaps driven by the reconnection outflows pushing plasma parallel to the separator.

The reconnection along the separator is evidently different from that seen in Stevenson and Parnell (2015a). The previous work began with a separator current layer, so the separator reconnection commenced immediately and also was strongest at the start of the experiment. Here, the global current sheet must first diffuse before the current redistributes itself along the skeleton features. Once the current has exceeded the critical value, the separator reconnection initially occurs at the centre away from the nulls, similarly to Stevenson and Parnell (2015a). However, the E_{\parallel} seems to intensify after the reconnection event begins, as well as spreading along the separator towards the nulls. The majority of the ‘super-critical’ current along the separator is dissipated and there is a pause in the E_{\parallel} before the reconnection commences as seen before. A major distinction is the fragmentary E_{\parallel} occurring close to the nulls between the two reconnection events. It should be noted that the separator used in figure 35 is not the only connection between the two nulls at $6.6 < t < 6.8$ (according to figure 37b). Hence the parallel electric field along the separator is a lower bound for the reconnection rate.

As the separatrix surfaces are warped during the reconnection events, the null points move apart and the separator lengthens (shown in figure 37(a)). When the separator reaches the maximum length around $t = 6.5$, the angle between the separatrix surfaces tends to zero and topological change occurs.

From figure 37(b), it can be seen that the maximum number of nulls at any time during

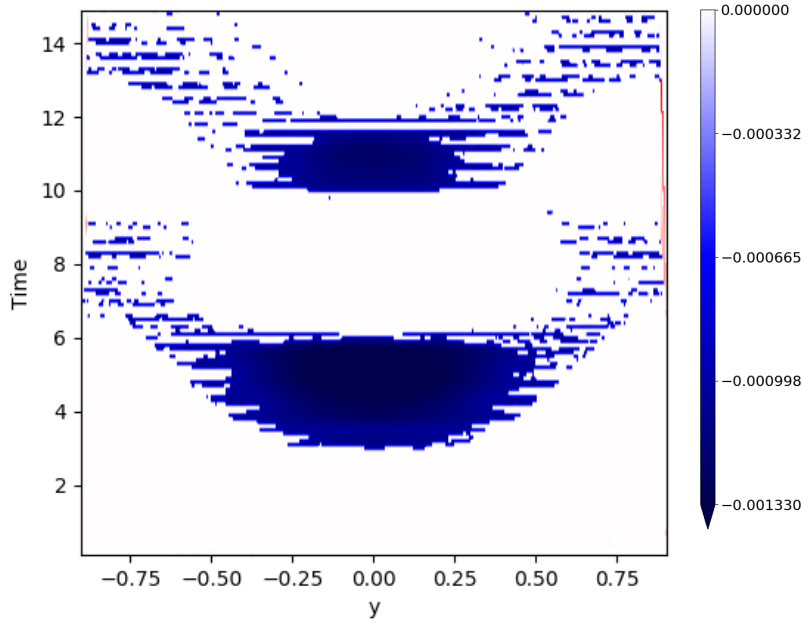


Figure 35: Time evolution of the parallel electric field along the length of the separator (represented by the y -coordinates)

this reconnection is 8 and there are typically between 40 and 90 separators connecting these. After the initial bifurcation at $t = 6.57$, each of the two null points spawns a new pair giving a total of 6, normally connected by around 30 separators. At $t = 6.66$, a second bifurcation occurs at one of the nulls forming an additional pair but this is unstable and disappears before returning again. Figure 36 shows the null positions against time in a rough bifurcation diagram.

There are few examples of topological change during separator reconnection in the literature. In Haynes et al. (2007), there are no separators in the initial condition but as the photospheric sources are moved towards each other, the positive and negative separatrix surfaces reconnect and topological change occurs. The dynamic full MHD experiment consists of six phases, which are identified according to the number of separators connecting the nulls. Initially, the reconnection yields two separators but after successive bifurcations the peak number of connections is five. It is difficult to compare these experiments, since the null points in this chapter maintain their position

to a large extent, except for some slippage during reconnection. On the other hand, the nulls in Haynes et al. (2007) are advected from one side of the domain to the other in order to initiate the reconnection. A more appropriate comparison is with the null point reconnection in Wyper and Pontin (2014a), where a single null point is subjected to boundary driving. As in figure 26a, a pitchfork bifurcation sees the initial null point spawn a new pair of nulls and these in turn undergo further bifurcations.

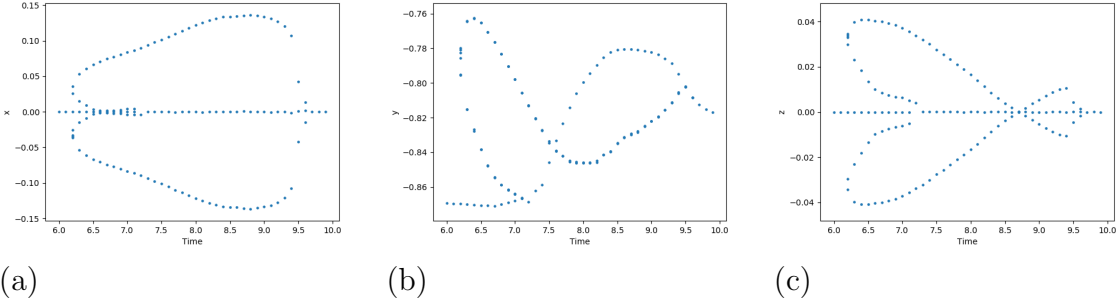


Figure 36: Null positions plotted over time, showing bifurcations during the first reconnection event. The three plots show the x , y and z co-ordinates respectively.

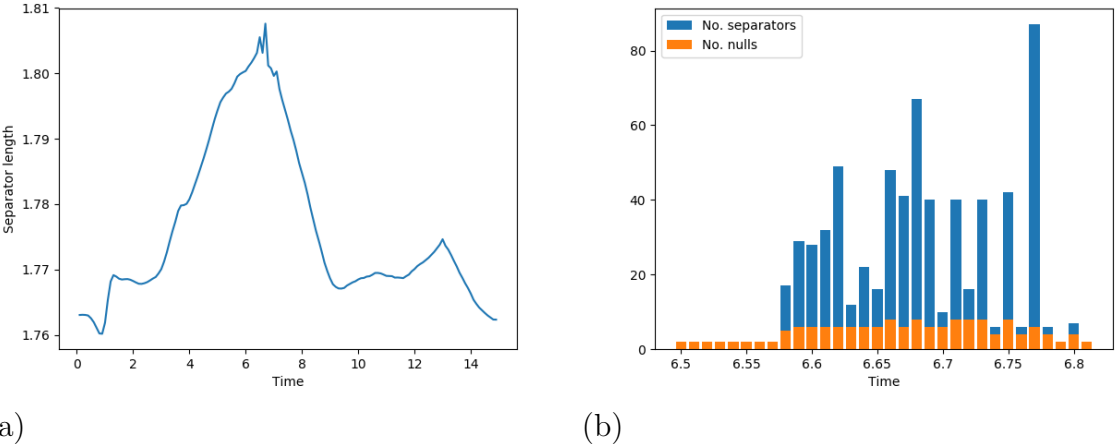


Figure 37: Topological changes during the reconnection experiment: a) time evolution of the length of the main separator; b) total number of nulls/separators in the domain during the first reconnection event, taken at intervals of 0.01.

3.5 Parameter Study

3.5.1 Varying b , c and r

The magnetic field parameters b, c and r were varied collectively to assess the importance of null points in the experiment. The condition for null points is $-cr/b > 1$ so altering any one of these three values would affect the topology but it is preferable to study a grid of experiments to ensure that the effect of changing a particular parameter is not mistaken for the effect of changing the topology. Each of b, c and r was varied from 0.2 to 0.8 (or -0.2 to -0.8 for the parameter c) with an increment of 0.2, meaning there was a grid of 64 experiments in total. These were performed at low resolution (128^3) because of computational limitations but it was first confirmed that the results from the original experiment could be replicated in a qualitative sense, except for yielding fewer topological features in the dynamic phase of the reconnection.

Some of the terms contributing to the energy changes are plotted for the 64 different experiments in figure 38. The initial total force is plotted along the x -axis because this is unique to each of the experiments. Unsurprisingly, each of the three quantities is positively correlated with the total force, although this is not intended to be the focus. The integrated Ohmic and viscous heating are larger in the experiments containing null points. By contrast, the work done by the Lorentz force appears to prefer the experiments that do not contain nulls.

The Ohmic heating plot implies that for two experiments with a given initial total force (and one can assume similar currents), the one containing null points will develop larger currents during the course of its nonlinear evolution. As shown in figure 34, the separatrix surfaces host current layers that are periodically replenished by the plasma flows. The reconnection thus occurs in distinct events, while the global current sheet diffuses continuously. If the topological features are removed, there will be fewer locations in the field where current layers can grow- or the current growth will be less strongly favoured. The existing current sheet will diffuse away as before but there will be no additional reconnection.

If the viscous heating is larger in cases containing nulls, this means that the flows that develop during the course of the experiments are stronger. This agrees with the

statement that the currents must be larger, leading to more reconnection and plasma acceleration. However, the work done by the Lorentz force is usually strongly dependent on the flow speed. In this study, the experiments with no nulls- and consequently weaker flows- do more work via the Lorentz force. This must mean that the $\mathbf{j} \times \mathbf{B}$ force is larger in the non-null cases. In the absence of topological features, the restructuring undergone by the magnetic field will be more limited. It is possible that the periodic transfer of flux towards the separatrix surfaces leads to a more field-aligned current density over time.

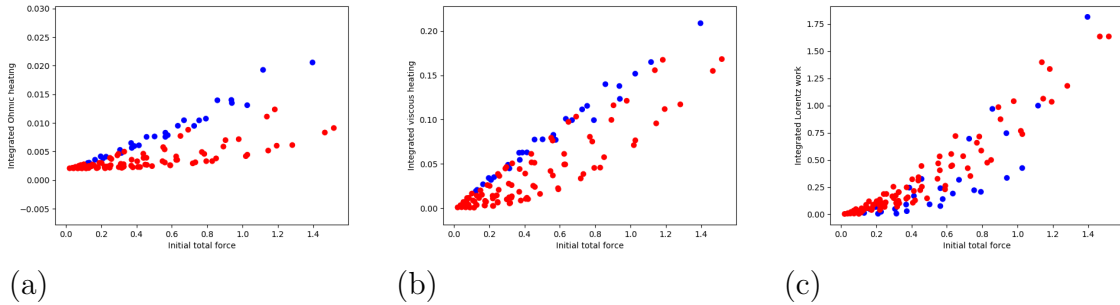


Figure 38: Energy terms plotted against initial total force for the b - c - r parameter study. Each dot represents one of the 64 experiments with a particular combination of the parameters. The blue dots are experiments that have nulls and the red ones do not have nulls. The quantities plotted are (integrated over time and across the volume): a) Ohmic heating; b) viscous heating; c) work done by the Lorentz force.

The results in figure 38 can be better understood by plotting the terms for a subset of the experiments with a shared value of the parameters c and r . The four experiments shown in figure 39 have $c = -0.8$ and $r = 0.6$ and the blue and orange lines show experiments with null points. For larger values of b , it is clear that the initial Ohmic heating rate is smaller and also the secondary heating events are less important. The secondary heating still occurs (at a slower rate) for $b = 0.6$ but the additional peaks are no longer visible in the $b = 0.8$ experiment.

The work done by the Lorentz force has a simple form for the experiments without nulls. This reflects the decaying flow speed, which is more important than the slowly varying Lorentz force. In the cases containing null points, the work done is not only smaller but also has a more complicated time evolution. This is because the current is redistributed along the topological features and the Lorentz force is reduced. Hence the

work done is affected both by the slowing flow speed and the reduction in the Lorentz force.

The time evolution of the viscous heating (including the contribution of the shock viscosity) is shown in figure 39(c) and the background component is plotted separately in (d). The background heating is larger in the experiments containing nulls (and is the quantity plotted in figure 40) but when shock heating is included, the viscous heating is greater in the non-null experiments. This implies that the existence of topological features inhibits the development of shocks in this system.

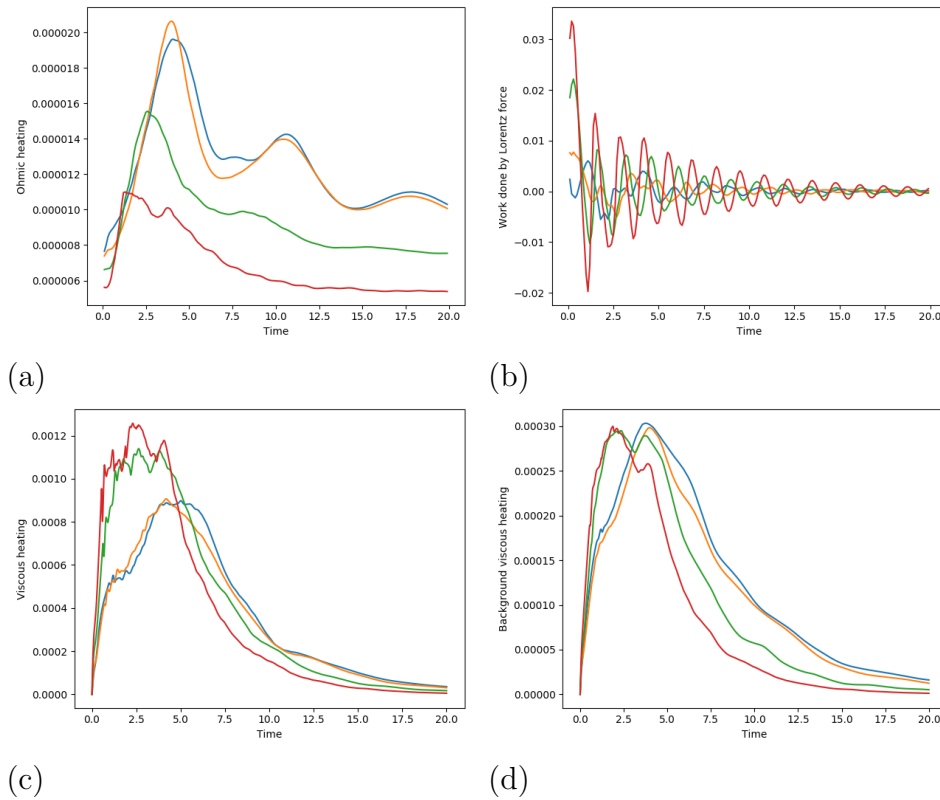


Figure 39: Time evolution of the volume integrated quantities for experiments with different choices for the parameter b (normalised by the initial total energy): a) Ohmic heating; b) work done by the Lorentz force; c) viscous heating; d) background viscous heating. The four experiments have $c = -0.8$, $r = 0.6$ and $b = 0.2$ (blue), $b = 0.4$ (orange), $b = 0.6$ (green), $b = 0.8$ (red).

In figure 40, the integrated Ohmic heating is shown for a number of different values of the parameter b . The key feature of the plot is that after the nulls are removed from

the model at $b = 0.48$, there is a sharp downturn in the Ohmic heating. This decline actually begins at around $b = 0.44$, as the effect of increasing b is to move the nulls closer together. The distance between the nulls tends to zero and they are replaced by a ‘double null’. Hence the length of the separator is small at $0.44 < b < 0.48$ and the area over which current layers can build has been reduced.

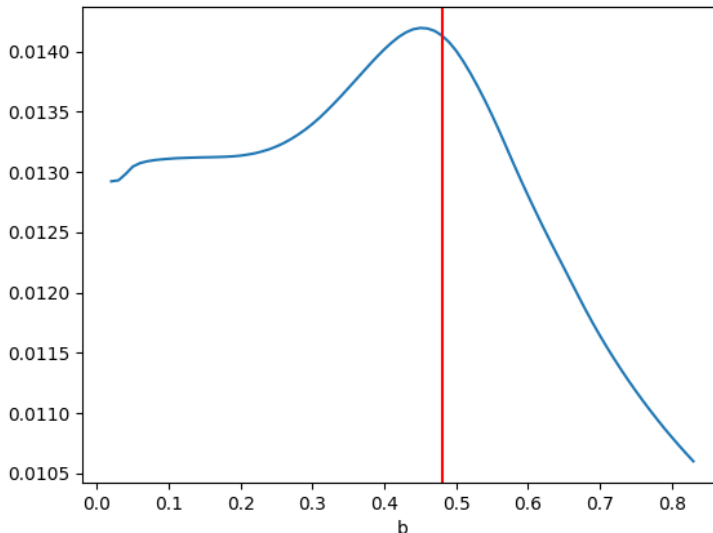


Figure 40: Time and volume integrated Ohmic heating plotted against the parameter b for a range of experiments. The vertical line indicates the value $b = 0.48$ beyond which the model does not have nulls (for the choice of $c = 0.8$ and $r = 0.6$).

3.5.2 Varying d

The parameter d is inversely proportional to the length of the separator. This section will compare the energy changes and reconnection rate for experiments with a factor of $3/2$ difference in the separator length.

First considering the reconnection rate, it is important to remember that figure 41 shows the parallel electric field along the separator alone. In the main experiment, the separator did not experience the strongest reconnection so this is not representative of the entire domain. The integrated positive E_{\parallel} is shown here to emphasise the contrast

between these experiments and the original case (figure 35). Previously, the E_{\parallel} was negative across the length of the separator because the regions of current that were directed opposite to the magnetic field had magnitude less than the critical value. Here, a constant resistivity is used so reconnection occurs over a wider region, introducing areas of positive E_{\parallel} . The reconnection rate is measured as the absolute value of the integrated E_{\parallel} so the negative values make the principal contribution but the pulse-like nature of the positive integral is a better indicator of the distinct reconnection events.

The general trend shown by this figure is for the magnetic fields with shorter separators to experience a higher rate of reconnection. There is little difference between the lines showing the maximum E_{\parallel} , simply because the current is directed opposite to the magnetic field along the majority of fieldlines, meaning the positive E_{\parallel} is weak. Instead concentrating on the minimum reconnection rates, the order of the three lines does not change (until $t = 12$) and the strongest reconnection is found in the fields with longer separators. The difference in the reconnection rates is not proportional to the difference in separator lengths but rather the change in d . This suggests that the length of the separator is not the most important detail of these experiments. The j_x component has a term that is proportional to d^2 so there is significant variation in the magnitude of the current across these experiments.

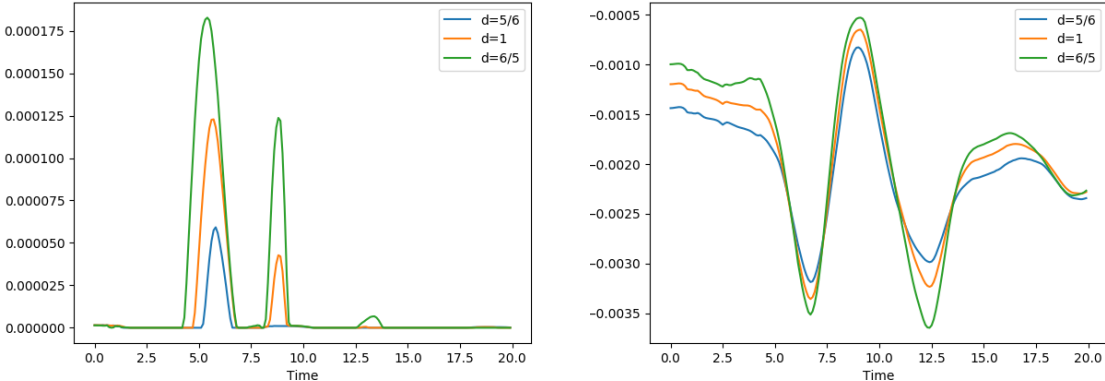


Figure 41: Time evolution of the integrated E_{\parallel} along the separator for three choices of the parameter d . Left: integrated positive E_{\parallel} along the separator; right: integrated negative E_{\parallel} along the separator

As expected, the experiments with the higher reconnection rates convert the largest

amount of magnetic energy. Similarly to the reconnection rates, the two experiments with $d \leq 1$ do not show a large difference in the amount of energy converted, at least in the final frame. In the early part of the experiments where both the magnetic and internal energies drop due to the release of considerable kinetic energy, there is clear separation between the three lines. In all three of the experiments, the viscous heating rate is an order of magnitude higher than the ohmic heating and in spite of the quantitative differences between the experiments, the peaks in these plots occur at approximately the same times. The maximum viscous heating occurs around $t = 7$, roughly coinciding with the first dip in the ohmic heating.

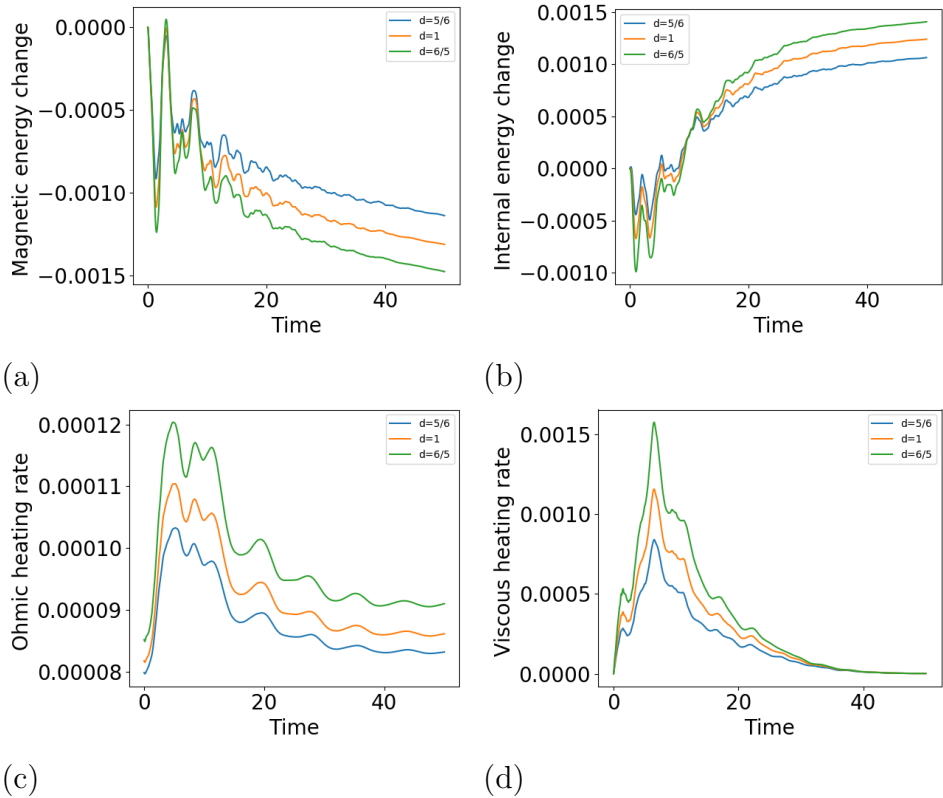


Figure 42: Energy changes for three different choices of the parameter d . Time and volume integrated energy changes normalised by initial total energy: a) magnetic energy; b) internal energy. Volume integrated heating rates: c) Ohmic heating; d) viscous heating.

3.5.3 Varying α

The main experiment uses a fairly extreme choice of the parameter α and this section will offer some justification for this. This parameter dictates how close the 2D Corrugated Sheet Pinch field is to the 1D Harris Sheet. In principle, the value of α should not affect the equilibrium properties of the magnetic field since the 2D field has a balancing pressure that is a function of α . However, the parameter affects the geometry of certain fieldlines in the vicinity of the boundary. If the fieldlines intersect the boundary at an oblique angle, this will encourage the growth of currents due to the line-tied boundary conditions.

The reconnection rate increases with the value of α according to figure 43. The j_y component of the current density contains a term that is proportional to α^2 (similar to the case of the parameter d) and stronger currents translate to higher reconnection rates. The positive and negative values of E_{\parallel} both appear to oscillate more quickly for lower values of α . In the previous parameter study (figure 41), varying the value of d did not affect the location of the peaks in the reconnection rate in spite of their differing magnitudes.

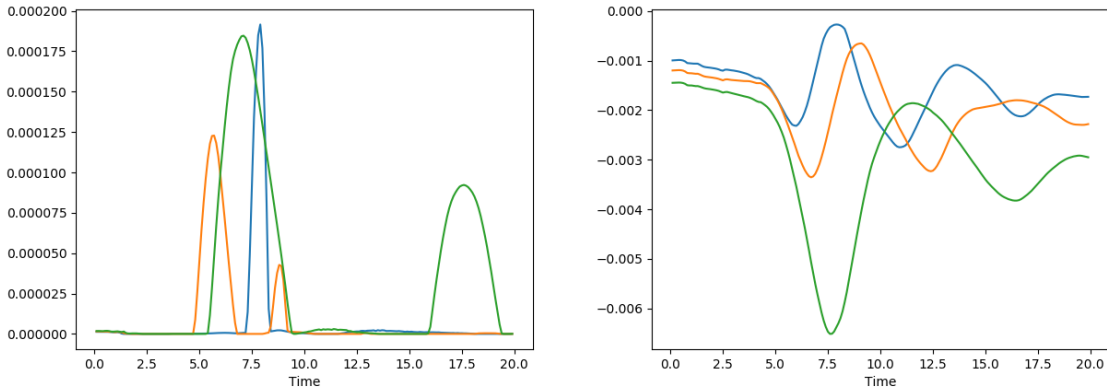


Figure 43: Time evolution of the integrated E_{\parallel} along the separator for three choices of the parameter α . Left: integrated positive E_{\parallel} along the separator; right: integrated negative E_{\parallel} along the separator. Blue: $\alpha = 0.85$, orange: $\alpha = 0.9$, green: $\alpha = 0.95$.

The energy plots reveal issues with energy conservation in the experiments with smaller values of α . For $\alpha = 0.85$, the total energy change is roughly 10% of the amount of

magnetic energy converted, while for $\alpha = 0.95$ it is merely 1%. In spite of this fact, the $\alpha = 0.95$ experiment converts more magnetic energy to internal energy. This is due to additional viscous (shock) heating which occurs in the middle part of the experiment. The viscous heating rate in all experiments is an order of magnitude higher than the Ohmic heating rate. This means that although the distinction between the different experiments is clearer in figure 44e, it is the apparently minor difference in figure 44f that determines the energy changes. The kinetic energy is also marginally greater in the $\alpha = 0.95$ experiment, as its stronger currents result in a larger work done by the Lorentz force.

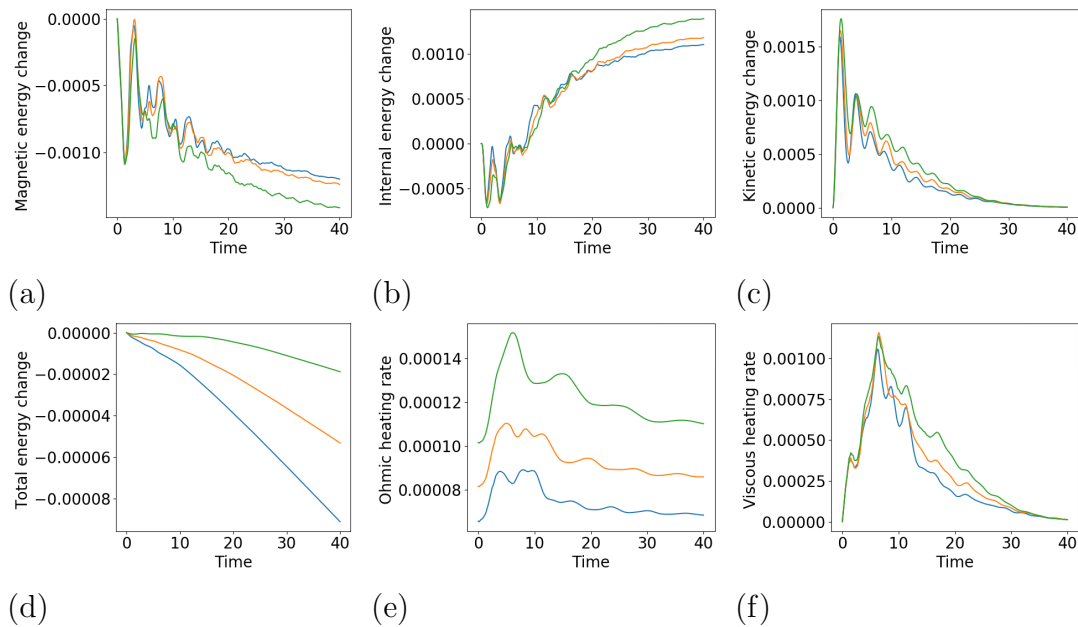


Figure 44: Energy changes for three different choices of the parameter α . Time and volume integrated energy changes normalised by initial total energy: a) magnetic energy; b) internal energy; c) kinetic energy; d) total energy. Volume integrated heating rates: e) Ohmic heating; f) viscous heating. Blue: $\alpha = 0.85$, orange: $\alpha = 0.9$, green: $\alpha = 0.95$.

3.6 Ideal Relaxation

This section will describe an ideal relaxation performed using the magnetic field from the main experiment. The purpose of the ideal experiment is primarily to verify the resistive

results from the previous section. These results offered some evidence of magnetic reconnection, particularly in the topological changes and the parallel electric field along the separator. However, it was clear that the evolution of the system was affected by the initial non-equilibrium, which produced strong flows causing oscillatory behaviour. The ideal results presented in this section should clarify the extent of the involvement of the non-equilibrium flows in the main experiment. Additionally, the final state resulting from the ideal relaxation could be taken as the initial condition for a reconnection experiment following the methodology of Stevenson and Parnell (2015a).

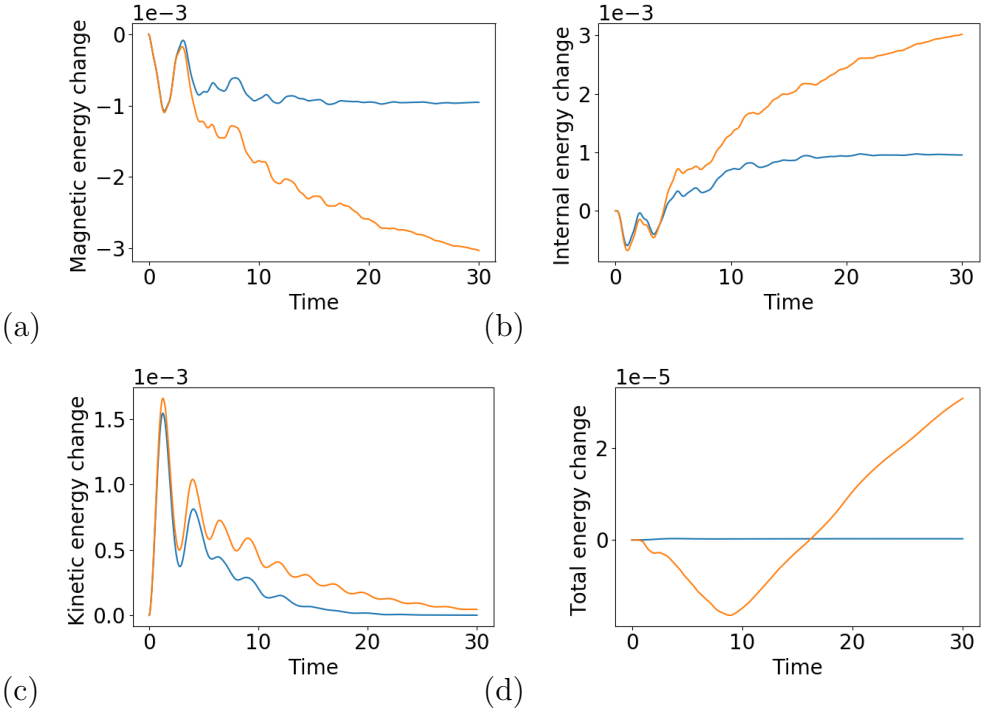


Figure 45: Time and volume integrated energy changes (normalised by the initial total energy): a) magnetic energy; b) internal energy; c) kinetic energy; d) total energy. The blue line shows the ideal experiment and the orange is the original resistive experiment.

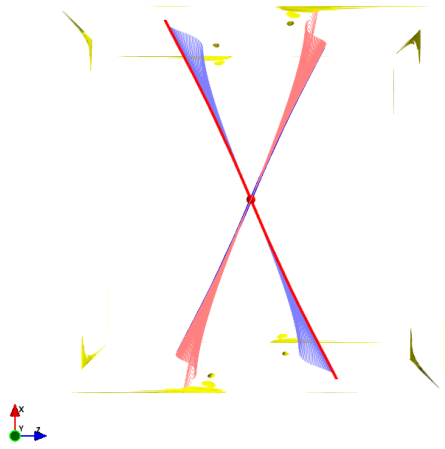
Figure 45 shows the energy changes in the ideal and resistive experiments. In the ideal experiment the integrated magnetic energy loss is around 1×10^{-3} of the initial total energy. The energy is initially converted to kinetic energy but from $t = 5$ onwards, the internal energy grows as the kinetic energy declines.

The ideal and resistive energy changes are in agreement in the early phase because

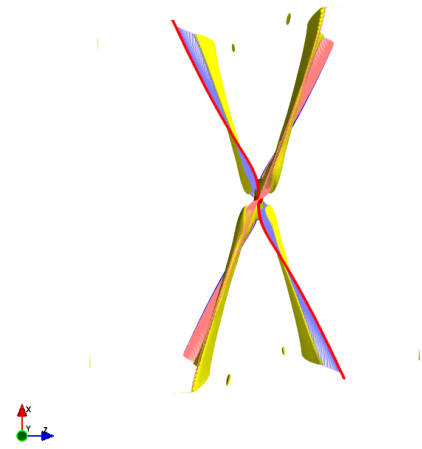
the resistive experiment uses a critical current higher than the initial maximum. The resistivity is only applied where the critical value is exceeded so the system evolves ideally in both experiments until the magnitude of the current exceeds $j_{crit} = 1$. Once the resistivity is activated, the magnetic energy is converted to internal energy at a fairly steady rate, while the ideal energies do not change significantly beyond $t = 10$. The kinetic energy is also higher in the resistive experiment, although its temporal variation is similar to the ideal case.

Figure 46 shows isosurfaces of the current density at the same times previously highlighted in figure 34. It should be noted that the contour used for these plots is $|j| = 1.5$ as opposed to the $|j| = 1$ used before. This is due to the larger current magnitude allowed by the ideal evolution, which peaks at approximately $|j| = 2$ in the final state. As in the resistive experiment, the isosurfaces in the right column show current layers that extend along the separatrix surfaces and pass through the separator. In the left column, the current is confined to the footpoints of the fans at the edge of the box. The key difference between the isosurfaces for the two experiments is the width of the current layer, which is much smaller in the ideal case. It has been seen in the previous chapters that the width of a current layer will reach progressively smaller length scales if the system relaxes ideally. In the resistive case, the strongest current density is dissipated before the small scales can develop. The dissipation also explains the unconsolidated nature of the current layers in figure 34, which are composed of innumerable current fragments unlike the solid layers in figure 46.

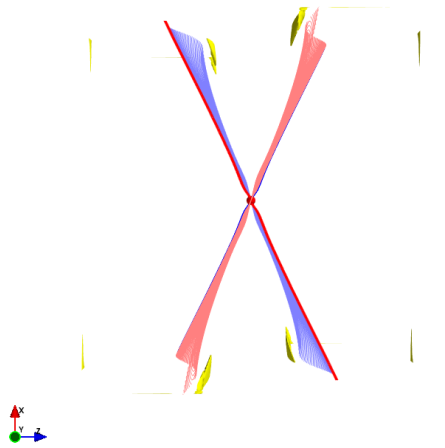
In figure 47, the parallel current is presented as the analogue to the $E_{||}$ plots in figure 35. Since a switch-off resistivity is used in the main experiment, the separator $E_{||}$ is zero at various times but the same periodicity can be observed in both plots. The parallel current along the separator peaks at $t = 5$ and $t = 11$ (agreeing with figure 46) before approaching a state with current distributed along the entire length of the separator. During the initial oscillations, the $j_{||}$ is concentrated in the middle of the separator and the relaxation acts to smooth the gradient between the centre and the nulls. The magnitude of the parallel current along the spine is not sufficient to lead to reconnection in figure 35 and it is also much weaker than the separator $j_{||}$ in figure 47.



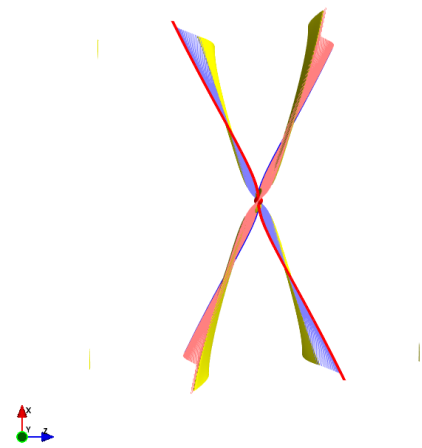
(a) $t = 2$



(b) $t = 5$



(c) $t = 8$



(d) $t = 11$

Figure 46: Current isosurfaces showing $|j| = 1.5$ at different times during the relaxation

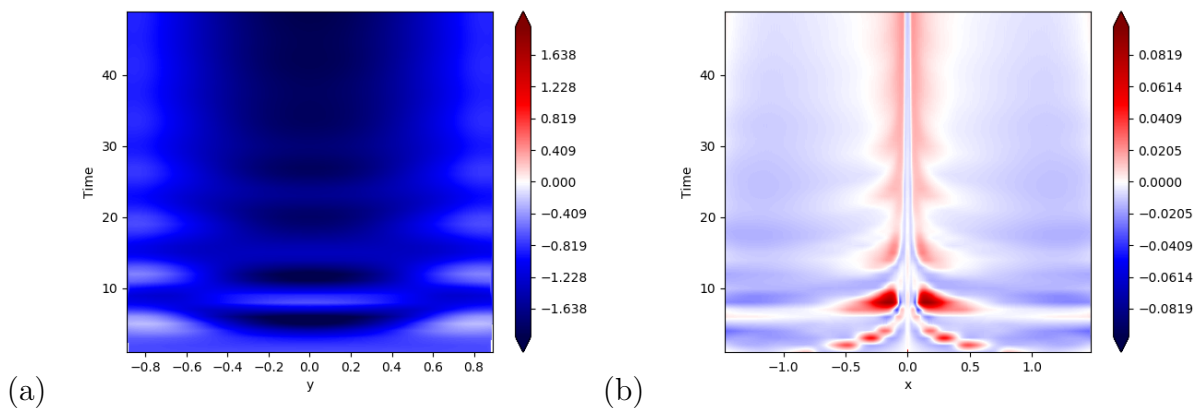


Figure 47: Time-distance plots showing j_{\parallel} along: a) the separator; b) the positive spine

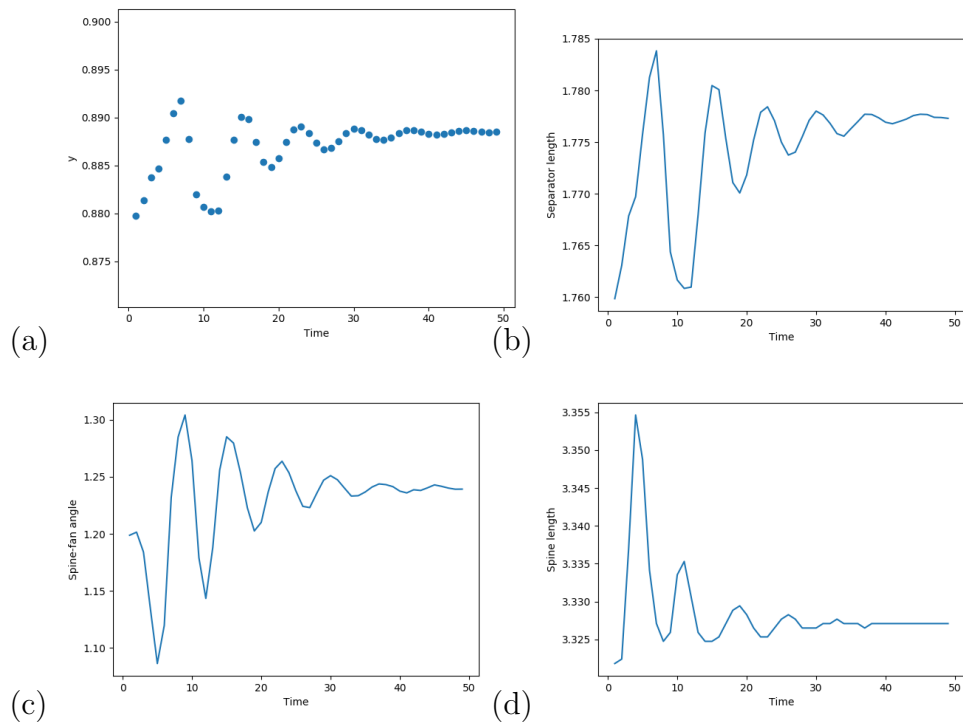


Figure 48: Evolution of the topological features: a) y position of the positive null; b) length of the separator; c) angle between the spine and fan eigenvectors; d) length of the positive spine

3.7 Reconnection from Quasi-equilibrium State

The final state from the ideal experiment can be used as an initial condition for a reconnection experiment in the manner of Stevenson and Parnell (2015a). The reconnection is initiated by the introduction of a nonuniform resistivity which is non-zero above the critical value $j_{crit} = 1.5$. This value was chosen such that there is a localised current layer along the separator. The value of the resistivity inside the diffusion regions is $\eta = 0.001$, while the viscosity has a background value of $\nu = 0.001$ and the coefficients of the shock viscosity (explained in Chapter 1) are $\nu_1 = 0.1$ and $\nu_2 = 0.5$. The boundary conditions remain line-tied, assuming that the reconnection occurs spontaneously due to microinstabilities rather than external driving.

Figure 49 shows the magnitude of the current density in the mid-planes for the initial condition. It is clear that the current has accumulated along the topological features, as the separator current layer can be seen in the $x = 0$ and $z = 0$ planes, while $y = 0$ shows the strong current concentrations at the separatrix surfaces. The remnants of the original large scale current sheet can also be seen in these contours, for instance in the enhancement at $y = 0$ in the $x = 0$ plane, which is more visible in figure 29. In the $z = 0$ plane, the initial current sheets at the x -boundaries are of similar magnitude to the separator current layer. This is the consequence of the line-tied boundary conditions used during the relaxation experiment, which do not allow currents at the boundary to be redistributed.

In figure 50, the magnitude of the total force in the three mid-planes is shown for the initial condition. Across much of the domain, the forces are effectively balanced but this is not the case in the $y = 0$ plane. The force imbalance is strongest along the separatrix surfaces and in the corners of the x - z plane. The former is a characteristic feature of all topological features undergoing relaxation but the latter is linked to the strong current concentrations at the boundary. Even though the pre-relaxation field is closer to a force balance than that in Stevenson and Parnell (2015a), the post-relaxation total force is larger.

The energy changes for the resistive experiment using the relaxed field are shown in figure 51. The amount of magnetic energy transferred to internal energy is three orders of magnitude less than in the main experiment. This is unsurprising, since a large

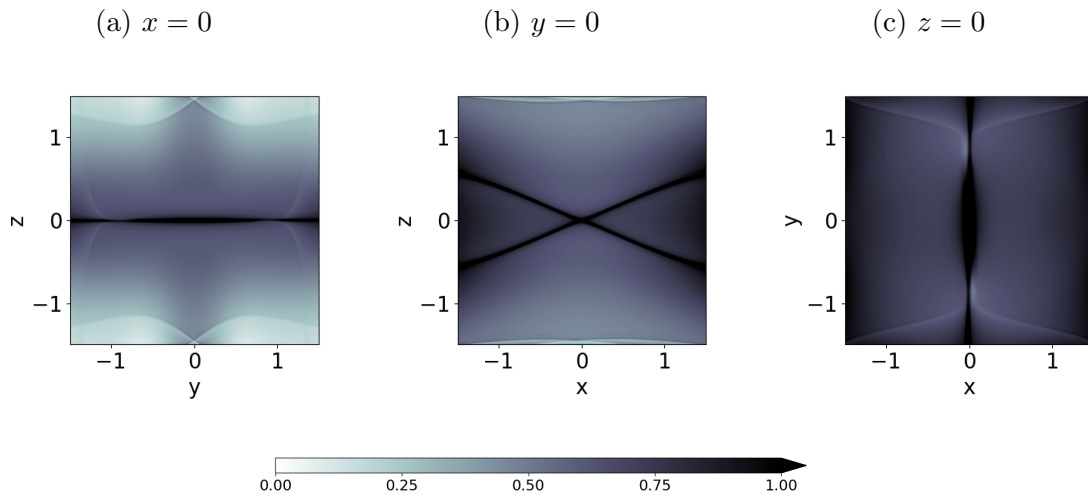


Figure 49: Magnitude of current density

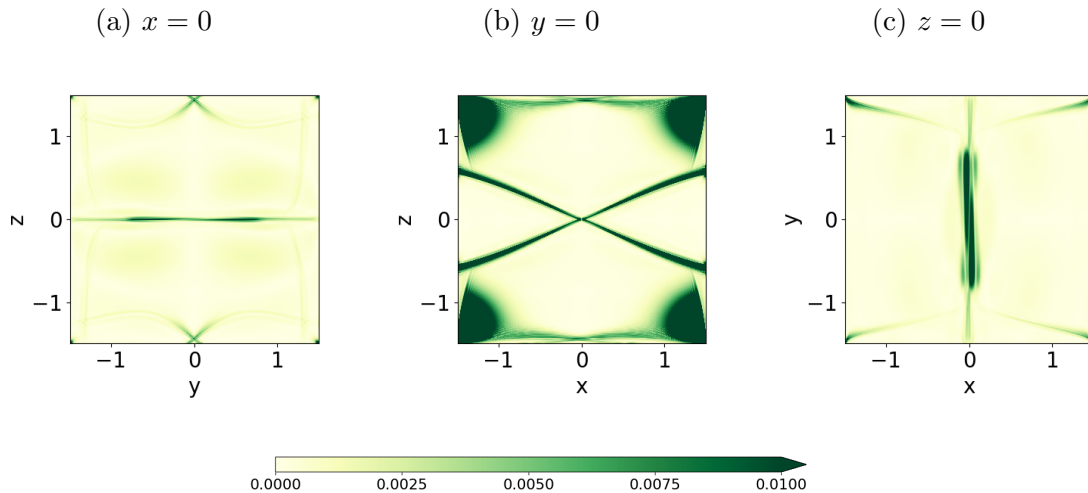


Figure 50: Magnitude of total force

portion of the original energy transport was due to the relaxation process, which has been separated from this experiment. The energies have a similar nonlinear evolution, which is due to the work done by the Lorentz and pressure forces. The Ohmic heating makes a minimal contribution to the internal energy increase, as there is no impulsive reconnection after the diffusion of the current layer at the start of the experiment. The viscous heating occurs at a similar rate, spiking at the onset of the reconnection before settling to a level that does not significantly influence the integrated energy changes. The viscous heating is small because the flow speed has been greatly reduced

by the relaxation. The kinetic energy change is nonetheless negative throughout the experiment, indicating that the initial velocity due to force imbalance is stronger than any reconnection outflows.

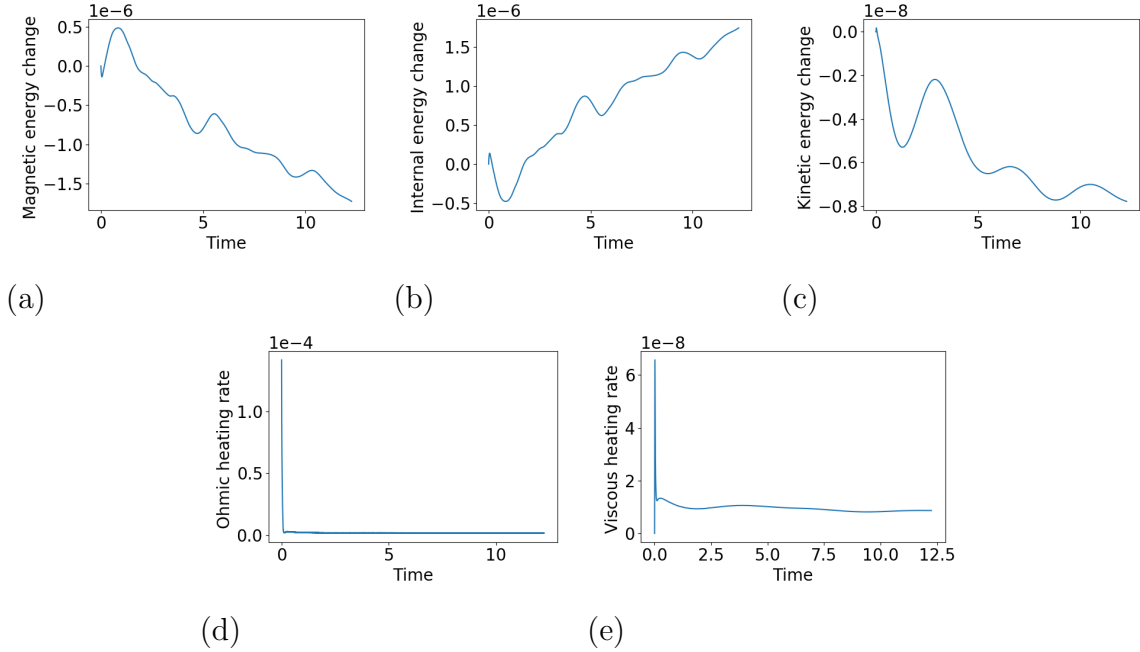


Figure 51: Time and volume integrated energy changes (normalised by the initial total energy): a) magnetic energy; b) internal energy; c) kinetic energy. Heating terms contribution to the energy changes: d) Ohmic heating; e) viscous heating

The parallel electric field was not a good measure of the reconnection rate in the main experiment because of the global scale of the diffusion region and its fragmentary nature. In this case, it should be somewhat more valuable because the reconnection regions are limited to the separatrix surface footpoints and the current layer at the centre of the separator. The separatrix surface reconnection is represented in figure 52, which shows E_{\parallel} along fieldlines passing through $x = 1.4$. The two elongated regions align with the intersections of the fan current layers with the plane, while the smaller regions are the projections of the E_{\parallel} from the opposite x boundary. Each of these four regions contains areas of positive and negative E_{\parallel} , which means that the current is being dissipated on either side of the separatrix surface. Naturally, the parallel electric field is strongest at the start of the experiment, when the current layers contain highly super-critical current. Once the excess current has been dissipated, the E_{\parallel} remains steady at a level

close to that in figure 52(b).

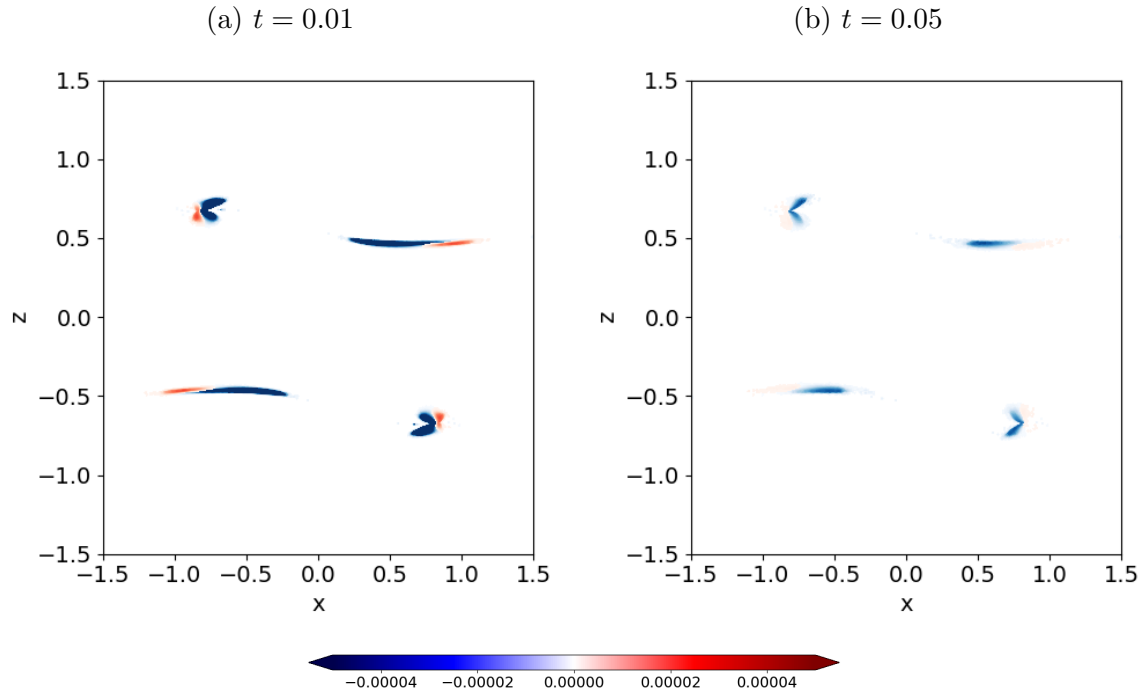


Figure 52: Integral of E_{\parallel} along fieldlines passing through $x = 1.4$

In spite of being theoretically more applicable than in the rest of this chapter, the parallel electric field cannot be measured along the separator or spine. This is simply because the reconnection is too short-lived at the separator, while the spine currents are highly sub-critical. Instead the time evolution of the integrated parallel current is plotted in figure 53. The parallel current along the separator is constant after the initial reconnection event. The magnitude of the current is steady at the critical value and does not exceed the threshold in impulsive bursts. The current along the spine consists of extremely parallel and antiparallel sections which cancel to give the integrated value. This is consistent with the ideal figure from the previous section (figure 47), although it does not exhibit the same time dependence.

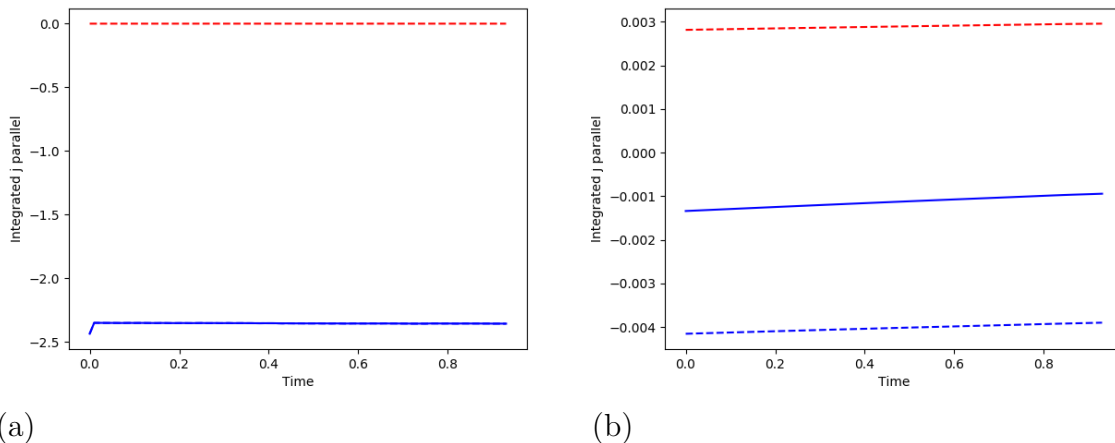


Figure 53: Integral of j_{\parallel} along: a) the separator; b) the positive spine

3.8 Discussion

In this chapter, separator reconnection has been studied numerically using a novel field derived from the Corrugated Sheet Pinch. The fact that the 3D magnetic field is a perturbation to the 2D X-point field immediately presents some limitations, as the individual field components all vanish in particular planes. This would not be the reality in separator topologies occurring in astrophysical magnetic fields but this Chapter emphasises the important of the topology, rather than the geometry of the magnetic field.

The method of studying separator reconnection in this chapter is to perform a numerical experiment using resistive MHD, allowing the initial current sheet to diffuse and drive reconnection along the topological features. The magnetic field parameters that were used were chosen to limit the magnitude of the total forces present in the non-equilibrium initial condition. The effects of this force imbalance are seen initially in the magnetic and internal energy changes but as the Ohmic heating reaches its first peak, the initial plasma motions are no longer important. Subsequently, the energies show a conversion of free magnetic energy into internal energy that occurs in an oscillatory manner as plasma flows reflect off the simulation box to carry magnetic flux into the reconnection region. The initial current sheet is focused at the boundaries away from the separator but as diffusion occurs, the current rebuilds across the entire separatrix

surfaces. However, there is no sign that the separator has a distinguished role in the reconnection. The current density remains strongest closer to the boundaries so the reconnection rate is highest away from the separator. In spite of this fact, the separator reconnection has some interesting properties, as the parallel electric field initially occurs along the central part of the separator, before moving towards the null points.

Aside from the unique initial magnetic field, this chapter also gives the first evidence of topological change in a pre-existing separator configuration. Such dynamic separator reconnection has previously only been seen in the fly-by experiment of Haynes et al. (2007), which has very different initial assumptions. The apparent relationship between reconnection along the separator and subsequent null point reconnection has not been seen in previous work. Stevenson and Parnell (2015a) emphasised the lack of involvement of the nulls in the reconnection, which originally occurred mid-way along the separator as in this experiment. Another interesting result from this chapter is the comparison between the behaviour of the system with and without nulls. The Ohmic heating is clearly higher in the experiments containing nulls because of their multiple reconnection events but this is not manifested in the magnetic energy change due to the larger initial force imbalance in the non-null experiments.

There are some problematic aspects to this work. The principal concern would be the contribution of the initial non-equilibrium to the results. In spite of using the magnetic field parameters that minimised the force imbalance, it could be argued that the dynamic nature of the reconnection is related to the larger flow speeds. The null point reconnection in Chapter 2 showed no signs of topological change, even in the asymmetric cases that had similar oscillations in the reconnection rate. Stevenson and Parnell (2015a) also did not see the creation of additional nulls and separators, since the equilibrium initial condition did not permit the development of significant flows.

4 Multi-separator Reconnection

4.1 Introduction

Oppositely signed pairs of magnetic null points are commonly connected by a single separator. This fieldline marks the intersection of the separatrix surfaces and divides the magnetic field into four flux domains whose fieldlines have different asymptotic behaviour. It is natural to assume that a single pair of nulls can only be connected by a single separator but this is actually not the case. If the separatrix surfaces are warped, they can intersect with each other multiple times and the pair of nulls will be connected by multiple separators. In such a scenario, the magnetic field geometry is more complicated and the number of flux domains is increased. There have been no dedicated studies of reconnection in magnetic fields with multiple separators between a pair of nulls. Previous numerical models have noted the presence of such configurations (e.g. Haynes et al. (2007)) without discussing the details of the reconnection. Hence this chapter will attempt the first systematic study of magnetic reconnection at multiply-connected null points.

Recent observation-based studies have shown that in systems containing null points, it is common for multiple separators to originate from (or terminate at) a single null. Originally, the PFSS extrapolations in Platten et al. (2014) found 40-60 coronal null points connected by 20-40 separators at solar maximum and 80-130 nulls with 40-85 separators at solar minimum. This suggested that each coronal null connects to one other null at a single separator. However, Williams (2018) increased the number of spherical harmonics in the extrapolation from $L = 81$ to $L = 641$ and found a greater number of separators per null. At solar minimum, 4167-4700 nulls were connected by 4140-5261 separators, while at solar maximum there were 3118-3742 nulls and 2660-3790 separators. The majority of these separators form a large network involving around half of the null points but there are also smaller networks, including separator rings similar to that studied in this chapter. There were at most 10 isolated ring structures found in the study, although there is no record of the frequency of multiply-connected nulls. In the observation-based magnetic field models of Close et al. (2004), there were 7.63 separators per null point and an average of 0.99 additional separators for every

connected null-null pair. This suggests that it is normal for two nulls to be connected by two separators, although the method of representing magnetic fragments by point sources is less reliable than some other extrapolation methods.

There is further evidence for multiply-connected null points provided by numerical and analytical models. In Haynes et al. (2007), two null points are driven past each other so that their separatrix surfaces intersect temporarily. Using a potential assumption, the skeleton contains a single separator for the duration of the interaction but the dynamical MHD evolution is more topologically complex. When the separatrices intersect a pair of separators is formed and although one of these is soon destroyed, the maximum number of separators connecting the nulls at a later time is five. Parnell et al. (2010) analysed the topology of a numerical simulation of magnetic flux emergence. During the dynamic phase of the reconnection, a total of 229 separators were found connecting 18 null points. At a later time, the reconnection rate becomes steady and the number of separators declines to 11 (with 10 null points). In Wilmot-Smith and Hornig (2011), the process of separator bifurcation is illustrated by a time-dependent magnetic field. Although this model does not solve the MHD equations and its reconnection is implicit, the work demonstrates how the complex topologies of the numerical experiments can be achieved by successive bifurcations.

When studying reconnection at multiple separators, it is important to keep in mind the previous work focusing on a single separator. Reconnection at a single separator has been studied both analytically and numerically as discussed in the previous chapter. The most relevant study for the work in this chapter is Stevenson and Parnell (2015a), which performed a numerical experiment to study single separator reconnection beginning with an equilibrium current layer. In that study, the current layer is rapidly dissipated in a phase of fast reconnection, which is followed by impulsive reconnection as the separator current layer rebuilds. The reconnection is largely confined to a small radius surrounding the separator and does not extend as far as the nulls. In the previous chapter, an alternative view of separator reconnection was presented. In this case, the reconnection rate oscillates as the flows carry magnetic flux into and away from the topological features. The reconnection is not confined to the separator and is in fact more intense along the separatrix surfaces. In spite of this, there is some evidence of reconnection along the separator which spreads to the null points, resulting

in bifurcations creating extra nulls and separators.

The approach that will be adopted in this chapter has several facets in common with Stevenson and Parnell (2015a). The starting point will be an analytical double separator model that will be used to perform a numerical reconnection experiment in Lare3D. The non-potential initial condition will first undergo ideal relaxation in order to create a quasi-equilibrium containing a separator current layer. Then the reconnection experiment will be undertaken with a nonuniform resistivity, using the equilibrium current layer as the new initial condition. The key differences in the method employed here are analytical, as the numerical procedure is broadly consistent with Stevenson and Parnell (2015a). The analytical field derived in the next section is a potential double separator model instead of a non-potential single separator field. The current will be introduced to the field by the addition of a flux ring, which imparts a localised twist on the magnetic field.

There are a number of questions this work will try to address. The overall goal is to determine whether there are significant qualitative differences between reconnection occurring in a two null system with one or two separators. A related question is whether the two separators in this experiment will interact during reconnection at one or both of the separators. A number of possible separator configurations will also be explored, as will flux rings of varying intensity and dimensions.

4.2 Double Separator Potential Field

4.2.1 Derivation

The starting point for the investigation is a three-dimensional potential field containing two null points. The components of the field are as follows:

$$B_x = \frac{B_0}{L_0} \left(-(a-b)Lx - cLz - (c+d)x^2 + dy^2 + cz^2 - 2exy - (2b+f)xz \right) \quad (71)$$

$$B_y = \frac{B_0}{L_0} \left(aLy - ex^2 + ey^2 + 2dxy + fyz \right) \quad (72)$$

$$B_z = \frac{B_0}{L_0} \left(-cLx - bLz - \frac{1}{2}(2b+f)x^2 + \frac{f}{2}y^2 + bz^2 + 2cxz \right) \quad (73)$$

The two null points were chosen to lie along the z -axis at $z = 0$ and $z = L$. It is necessary to perform a linear analysis of the magnetic field local to the null points (in the manner of Parnell et al. (1996)) to derive valuable constraints on the values of the constants a - f appearing in the magnetic field components. These constraints ensure that the null point at the origin has the following properties:

- It is a positive null
- The spine is located in the x - z plane (with a negative gradient)
- The fan is locally aligned with the y -axis and a line in the x - z plane (with positive gradient)

The null point at $(0, 0, L)$ satisfies the following:

- It is a negative null
- The spine is located in the x - z plane (with a positive gradient)
- The fan is locally aligned with the y -axis and a line in the x - z plane (with negative gradient)

Linearising about the origin, the new variables are $x = X, y = Y, z = Z$, which are assumed to be small perturbations about the null. Products of the new variables can be neglected since they are small, leaving the following linearised magnetic field:

$$B = \frac{B_0}{L_0} \begin{pmatrix} -L(a-b) & 0 & -cL \\ 0 & aL & 0 \\ -cL & 0 & -bL \end{pmatrix} \begin{pmatrix} X \\ Y \\ Z \end{pmatrix} \quad (74)$$

Since the fan plane is aligned with the y -axis, its associated eigenvector is the y unit vector so the first eigenvalue can be read off as $\lambda_1 = a$. The characteristic equation can then be solved for the remaining eigenvalues:

$$\lambda_{2,3} = \frac{-a \pm \sqrt{a^2 - 4(-b^2 - c^2 + ab)}}{2} \quad (75)$$

The spine of a 3D null is always associated with the eigenvalue that has opposite sign to the two others so for a positive null, this is the negative eigenvalue. Consequently, the eigenvalues found from the characteristic equation must have opposite sign, since these both have eigenvectors in the x-z plane and one must represent the spine. This yields the simple result that a must be positive to ensure that there are two positive eigenvalues. A second constraint can be derived by observing that the value under the square root in (75) must be greater than a^2 to ensure that λ_1 and λ_2 have opposite sign.

$$\begin{aligned} a^2 - 4(-b^2 - c^2 + ab) &> a^2 \\ b^2 + c^2 - ab &> 0 \end{aligned} \quad (76)$$

Now turning to the case of the negative null, we linearise the variables by setting $x = X, y = Y, z = L + Z$. Substituting these forms into the magnetic field gives the following (again expressed in matrix form):

$$B = \frac{B_0}{L_0} \begin{pmatrix} -L(a+b+f) & 0 & cL \\ 0 & L(a+f) & 0 \\ cL & 0 & bL \end{pmatrix} \begin{pmatrix} X \\ Y \\ Z \end{pmatrix} \quad (77)$$

Once more, the fact that one of the fan planes is aligned with the y-axis means that its associated eigenvector is the y unit vector and we can see from the matrix that $\lambda_1 = a + f$. The characteristic equation gives the two eigenvalues with eigenvectors in the x-z plane:

$$\lambda_{2,3} = \frac{-(a+f) \pm \sqrt{(a+f)^2 + 4(b^2 + c^2 + ab + bf^2)}}{2} \quad (78)$$

The correct alignment of the spine in the x-z plane is achieved if one of these two eigenvalues is positive, which immediately tells us that the third is negative, $a + f < 0$. For a negative null, we require two negative eigenvalues so the value under the square root must be greater than $(a + f)^2$ to ensure that λ_2 and λ_3 have opposite signs. This

gives the fourth constraint on the values of the field parameters a - f :

$$\begin{aligned} (a + f)^2 + 4(b^2 + c^2 + ab + bf) &> (a + f)^2 \\ b^2 + c^2 + bf + ab &> 0 \end{aligned} \quad (79)$$

Four constraints have been obtained, including (79) and the following:

$$a > 0 \quad (80)$$

$$f < -a \quad (81)$$

$$b^2 + c^2 - ab > 0 \quad (82)$$

These conditions are essential to ensure that the model contains exactly two nulls connected by two separators. There are a number of free parameters (d, e, L) that are unconstrained by (79) and (80). This implies that altering these values affects the geometry of the field but not the magnetic topology. The parameter study in the next section will verify this assumption.

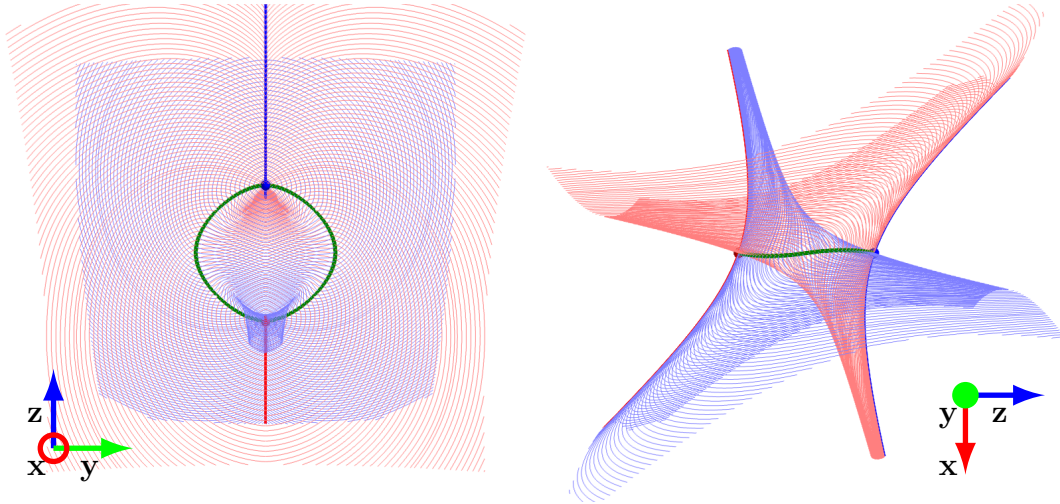


Figure 54: Double separator potential field with $B_0 = L_0 = 1$, $a = 0.5$, $b = -1.0$, $c = 1.0$, $d = 1.0$, $e = 0$, $f = -1.0$, $L = 2$

4.2.2 Parameter Study

Beginning with the potential magnetic field in figure 54, each of the parameters was varied individually. The remaining parameters were kept constant in order to determine the contribution made by each to the null point structure.

According to the constraints laid out in the previous section, the value of the magnetic field parameter a is strictly positive and its magnitude is greater than that of the parameter f . Beginning with the set of parameters defining the magnetic field shown in figure 54 and varying the value of a , one knows that it must lie in the range $0 < a < 1$. Figure 55 shows the effect of changing this value on the shape of the separators. The left figure shows the height of the separators (or the distance between its minimum and maximum x positions), while the right shows the maximum distance between the two separators (the difference between the two y positions with greatest magnitude). The distance between the two separators does not really change according to figure 55 but figures 56 and 57 show that the location of the maximum distance shifts along the z -axis as a is varied. For $a < 0.5$, the separator ring is widest near to the positive null and narrows towards the negative null, while the shape is flipped along the y -axis for $a > 0.5$. One can achieve the same effects by varying f , only a smaller magnitude of f causes the ring to widen at the negative null.

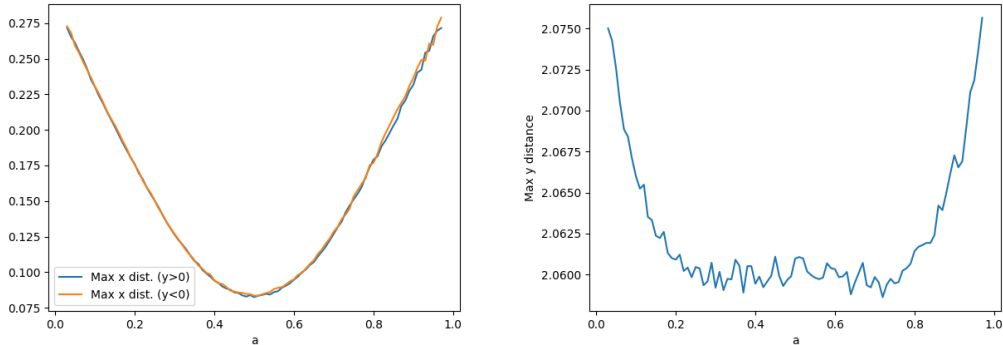


Figure 55: Effects of varying a on the shape of the separators. Left: height of the two separators, given by the difference between their maximum and minimum x -coordinates. Right: width of the separator ring, given by the difference between its maximum and minimum y -coordinates.

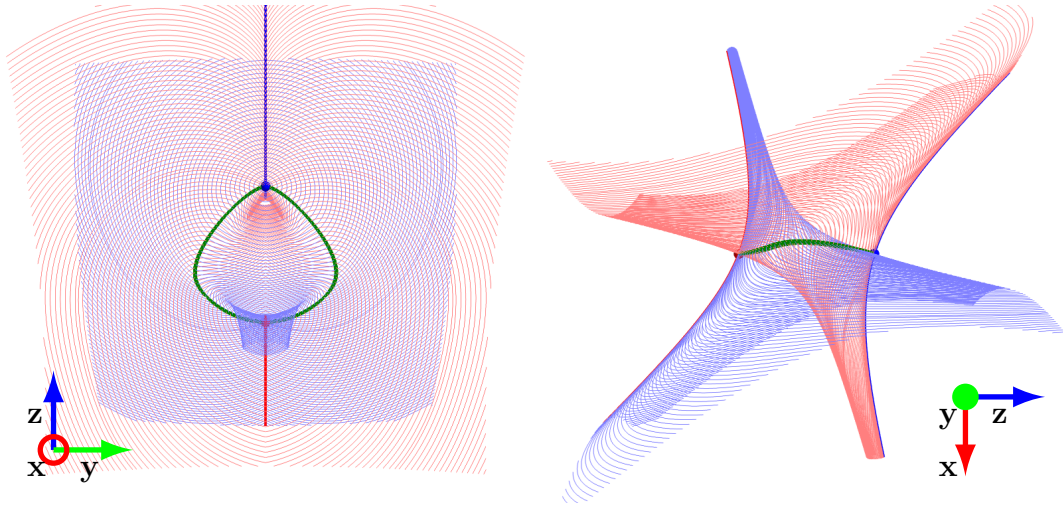


Figure 56: Double separator potential field with $a=0.2$

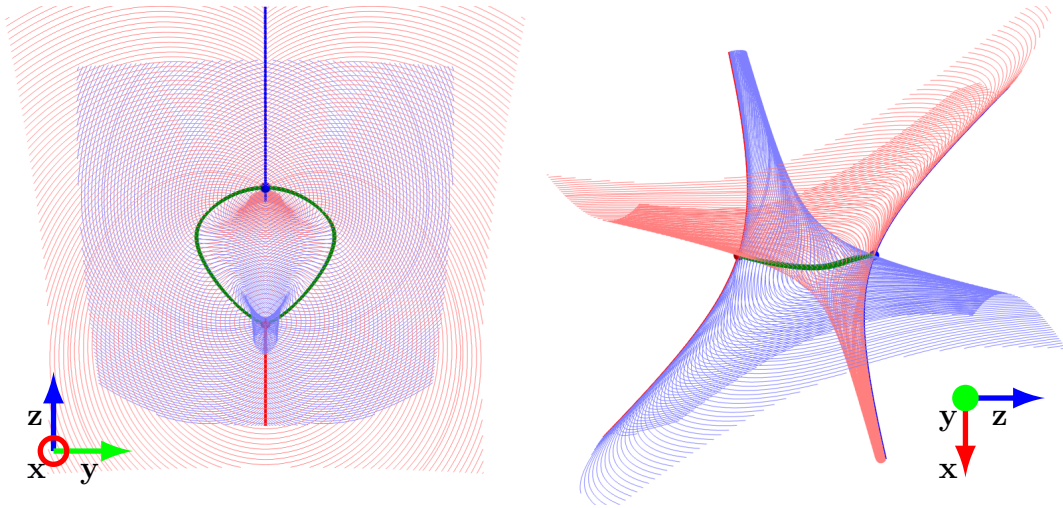


Figure 57: Double separator potential field with $a=0.8$

Although the four constraints in the previous section do not prescribe the sign of b , the parameter study reveals that it must be negative (at least for this choice of the other parameters). For more negative values of b , the separator ring becomes more square, as the fieldlines run along the entire length of the separators instead of diverging at $z = 0$. The distance between the separators is reduced as the fieldlines move less towards the y boundaries but the variation in the x -direction (figure 58) is largely unaffected by b unless it is too close to zero.

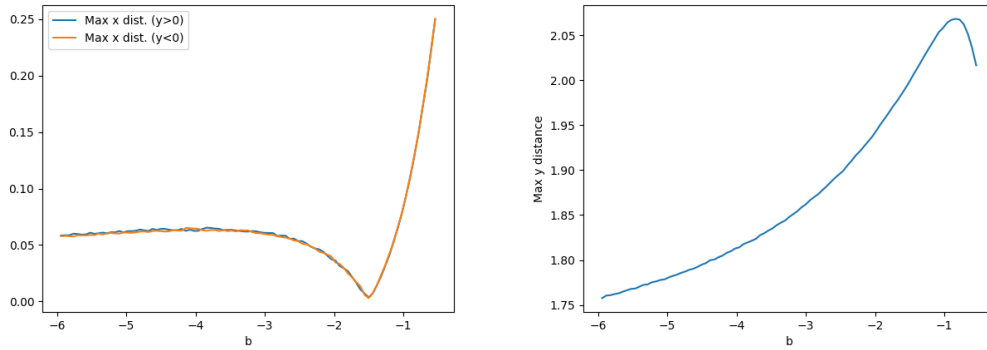


Figure 58: Effects of varying b on the shape of the separators. Left: height of the two separators, given by the difference between their maximum and minimum x -coordinates. Right: width of the separator ring, given by the difference between its maximum and minimum y -coordinates.

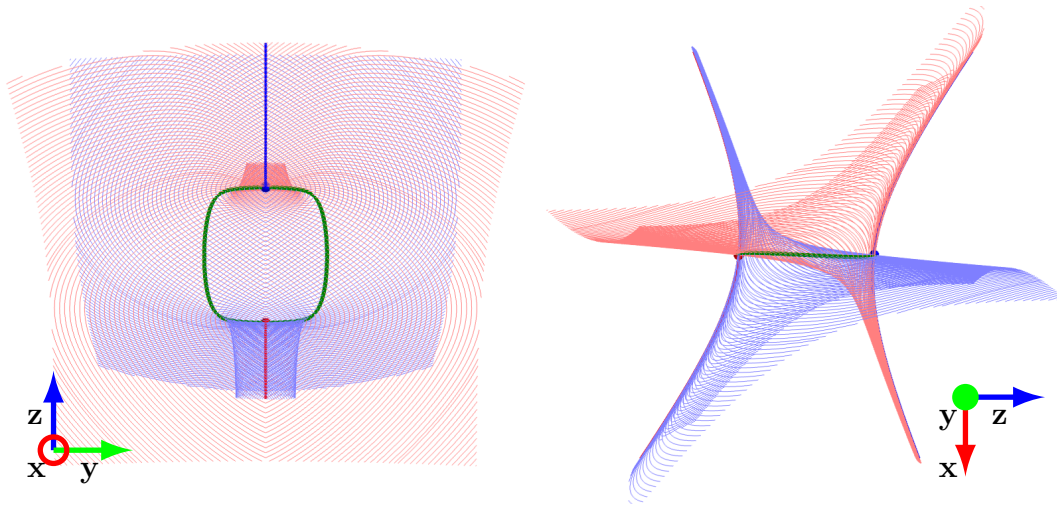


Figure 59: Double separator potential field with $b=-4.0$

By varying the parameter c , one can significantly alter the width of the separator ring as shown in figures 62 and 63. As the value of c approaches zero, the two separators close on the y -axis and their x variation also diminishes. From figure 61, it can be seen that a larger value of c increases the height of the separators, as the fieldlines dip slightly towards the opposing z boundaries close to the nulls. The effects of varying d mirror those shown here, with a larger value of d resulting in a narrower separator configuration and vice versa.

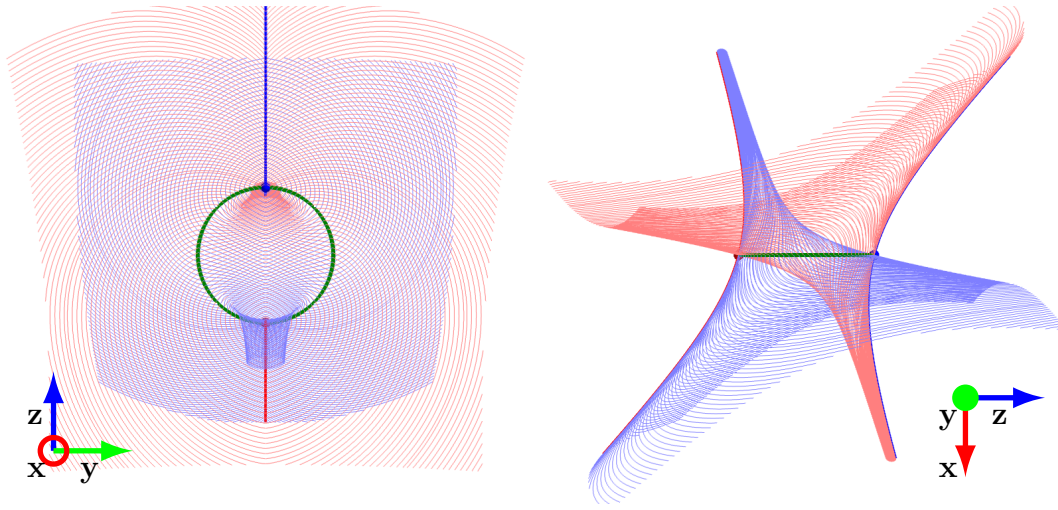


Figure 60: Double separator potential field with $b=-1.5$

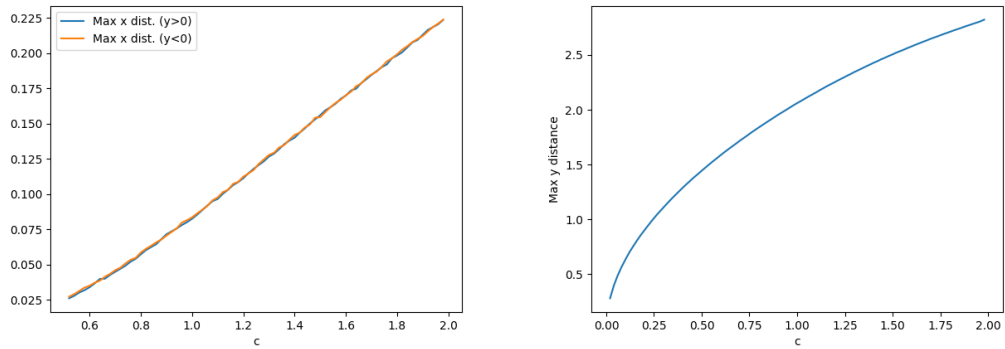


Figure 61: Effects of varying c on the shape of the separators. Left: height of the two separators, given by the difference between their maximum and minimum x -coordinates. Right: width of the separator ring, given by the difference between its maximum and minimum y -coordinates.

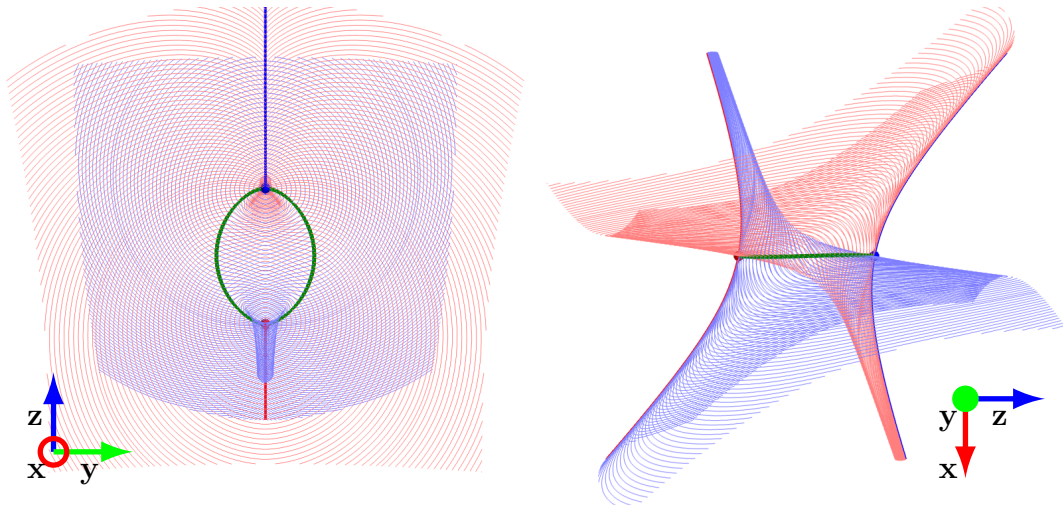


Figure 62: Double separator potential field with $c=0.5$

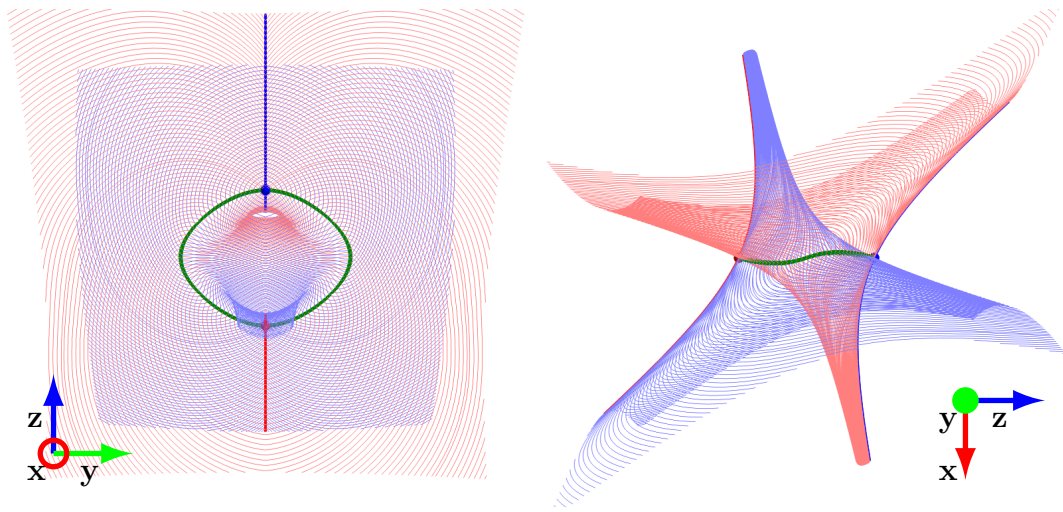


Figure 63: Double separator potential field with $c=1.5$

4.3 Non-potential Component

4.3.1 Introduction

This research introduces a localised current to a double separator potential field in order to study the locally non-ideal processes that take place once a new equilibrium has been reached. This configuration is achieved by adding a component to the magnetic field which corresponds to the field due to a ring of current (or flux ring). Since this local field component is assumed to fall off exponentially, it can be added smoothly to the pre-existing potential field. The resulting non-potential field is continuously differentiable across the domain. This work will attempt to produce a numerical model with similar characteristics to Longcope and Cowley (1996), which proposed adding an infinitesimally thin current ribbon to a potential separator ring such that the plasma motions remain ideal. The idealness of the plasma will be imposed numerically, so that the current should relax towards the infinitesimal layer described in the previous work.

The decision to manipulate the potential field with a flux ring was motivated by a number of considerations. In the first place, it has been shown by a number of authors including Haynes et al. (2007) and Stevenson and Parnell (2015a) that the current in a system containing 3D nulls will collect about the topological features and about the separators in particular. Therefore by aligning a ring of current with the two separators in our system, we are taking an initial condition for the subsequent relaxation that bears a resemblance to the desired equilibrium field. Such an approach does increase the likelihood that the reconnection will be dominated by the separators but this is an allowable initial assumption. The advantage of this method is that it reduces the Lorentz force to theoretically allow for faster relaxation. Since the sole purpose of the relaxation is to create the initial conditions for our reconnection experiment, it is desirable to accelerate the process where possible. A further advantage of such a current distribution over a uniform alternative like that used in Stevenson and Parnell (2015a) is that it keeps the current away from the boundaries of the domain. Since the numerical experiment makes use of line-tied boundary conditions, any initial current in proximity to the boundary is likely to be preserved for the duration of the investigation. One hopes to eliminate such numerical effects when trying to build a realistic model.

A further question which had to be addressed at this stage concerned the direction of the current in our flux ring. On the one hand, the two separator fieldlines are clearly directed from the positive to the negative null, which suggests the current ought to be directed similarly from one null to the other. However, if the current ring lies in the y - z plane, the resulting magnetic field component will be in the x direction so should not cancel with (or enhance) the existing field. The flux rings were instead chosen to be oppositely directed. Although these initially diminish in magnitude towards the nulls, it could allow for a closed current loop to form during the relaxation, which would ensure that the current would stay away from the boundaries of the domain.

4.3.2 Mathematical Form of the Flux Ring

The flux ring approach of Wilmot-Smith and Hornig (2011) was adapted to introduce a localised current in the neighbourhood of the separator. Since the authors were studying reconnection along a single (initially) straight separator, they required a vertical electric field which was assumed to experience a Gaussian fall-off away from the separator. This was achieved by adding terms to the x and y components of the magnetic field whose form was dictated by Maxwell's laws. By expressing the non-potential magnetic field in terms of a vector potential, the solenoidal constraint was automatically satisfied.

$$\mathbf{B}_p = \nabla \times \left(-B_0 \exp \left(-\frac{(x-x_c)^2}{p^2} - \frac{(y-y_c)^2}{q^2} - \frac{(z-z_c)^2}{s^2} \right) \hat{\mathbf{z}} \right) \quad (83)$$

This experiment uses the same form for the perturbation magnetic field as in Wilmot-Smith and Hornig (2011) but the purpose of the flux ring here is quite different. The previous authors did not study the reconnection process itself but rather added the component in (83) to a potential separator field to simulate the effect of reconnection. They observed that the non-zero $\mathbf{E} \cdot \mathbf{B}$ term that is necessary for 3D reconnection is a source term in the equation for helicity density, thereby justifying the introduction of a localised twist to the separator by the addition of the flux ring. In this experiment, the flux ring will merely be used to perturb the potential magnetic field.

The current associated with a magnetic field of the form in (83) (or a potential field

with this added component) has the following form:

$$\begin{aligned}
j_x &= \frac{4B_0(x - x_c)(z_c - z)}{p^2 s^2} e^\Lambda \\
j_y &= \frac{4B_0(y - y_c)(z_c - z)}{q^2 s^2} e^\Lambda \\
j_z &= \frac{2B_0}{p^2 q^2} \left[-p^2 - q^2 + \frac{2q^2(x - x_c)^2}{p^2} + \frac{2p^2(y - y_c)^2}{q^2} \right] e^\Lambda
\end{aligned} \tag{84}$$

Here, $\Lambda = -\frac{(x-x_c)^2}{p^2} - \frac{(y-y_c)^2}{q^2} - \frac{(z-z_c)^2}{s^2}$ is the exponent in the flux ring magnetic field component (83). The presence of this exponential term ensures that the current components all experience a Gaussian fall-off away from the flux ring centre. The x and y components of the current density can be loosely described as the ‘perpendicular current’, since the magnetic field is approximately parallel to the z -axis where the flux ring will be applied. The perpendicular current vanishes at $z = z_c$ and is directed radially away from the flux ring centre for $z < z_c$ and radially towards the centre for $z > z_c$. The magnitude of the perpendicular current vanishes at (x_c, y_c) and in a plane of constant z it covers an annular region (figure 64(a)). The ‘parallel current’ (j_z) consists of a strong positive core and an outer negative shell. The change in sign occurs along an ellipse whose dimensions are dependent upon p and q . The magnitude of the parallel current is greatest at the flux ring centre (where the perpendicular current vanishes), so figure 64(a) and (b) show different z cuts. The setup in the main experiment ensures that the parallel current is the most important component, as it is strongest closer to the separator where the perpendicular components are close to zero.

4.3.3 Flux Ring Parameters

For the main experiment, two oppositely directed flux rings were superposed to the magnetic field. These were centred at the points where the separator is farthest from the y -axis, since this is where the magnetic field would be almost parallel to the z -axis. It is clear from figure 65 that these points lie closer to the negative null, owing to the slight asymmetry of the potential field.

For the parameter choices $p = q = 0.01$, $s = 0.02$, $B_0 = 0.1$, the flux rings are localised

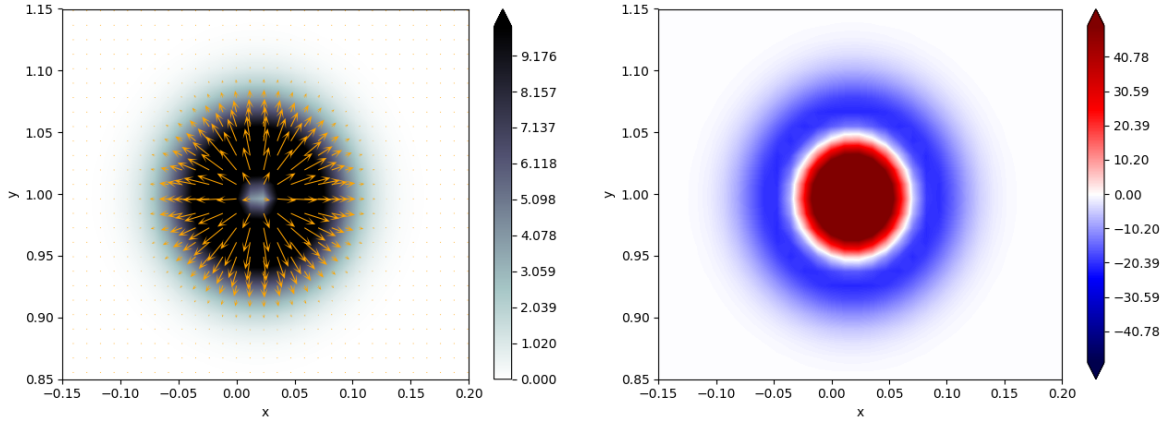


Figure 64: Flux ring current components: (a) perpendicular current at $z = 1.26$; (b) parallel current at $z = 1.18$

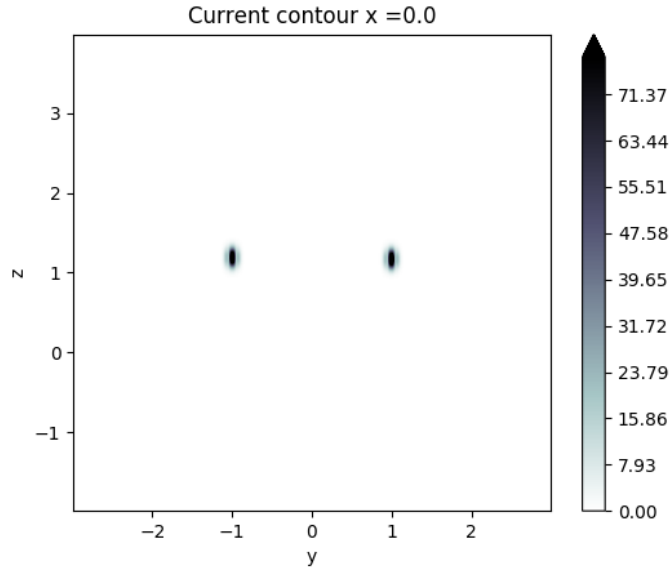


Figure 65: Magnitude of the current density for two flux rings with $p = q = 0.01$, $s = 0.02$ and $B_0 = 0.1$, centred at the widest points of the separator ring. These are the parameters used in the initial condition for the reconnection experiment.

so that their length is much less than the length of the separator and the topology of the magnetic field is unchanged. Looking at equation (84), the Gaussian will decay faster for smaller values of p, q and s . Hence, a slightly larger value of s has been used to extend the flux ring along the length of the separator. The values of p and q are

chosen to be the same since the xy -plane is almost perpendicular to the separator at the flux ring centre, so it can be assumed that the shape of the separator does not influence the current distribution there.

By varying the parameters p (assumed to be equal to q), s and B_0 , it is possible to alter the initial magnetic topology, as shown in figure 66. The greatest number of separators is found in the experiments with a small value of p and large values of s and B_0 . The small value of p (and q) means that the flux ring is confined to a small radius surrounding the separator. The larger s elongates the structure so that it stretches (approximately) along the separator.

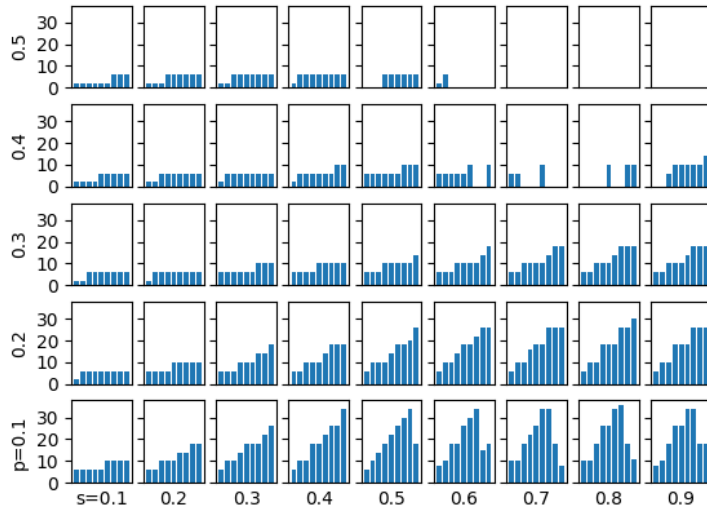


Figure 66: Number of separators for different flux ring parameter combinations. Each bar represents a different value of B_0 , ranging from 0.1 to 0.9.

4.4 MHD Relaxation

The non-potential magnetic field developed in the previous section could be taken as the initial condition for a reconnection experiment. However, the field is first relaxed here to create a quasi-equilibrium state where the current is confined to thin layers surrounding the separators. The motivation for the relaxation is twofold: first, the

magnetic Reynolds number in the corona is sufficiently high to justify the use of the ideal MHD equations, since the magnetic field is frozen-in to the plasma and diffusion effects are globally negligible. Therefore, the system should be allowed to evolve physically until small length scales naturally arise as a result of the magnetic forces in the initial non-potential field. The second explanation for the relaxation phase is the need to clarify the effects of reconnection. The addition of the flux ring to the potential field is an artificial means of introducing electric current to the system and the associated Lorentz force will lead to plasma flows that cannot be explained by any physical process. As the magnetic field reconfigured itself, the picture would begin to resemble the expected reconnection inflows and outflows but earlier results would be uninformative.

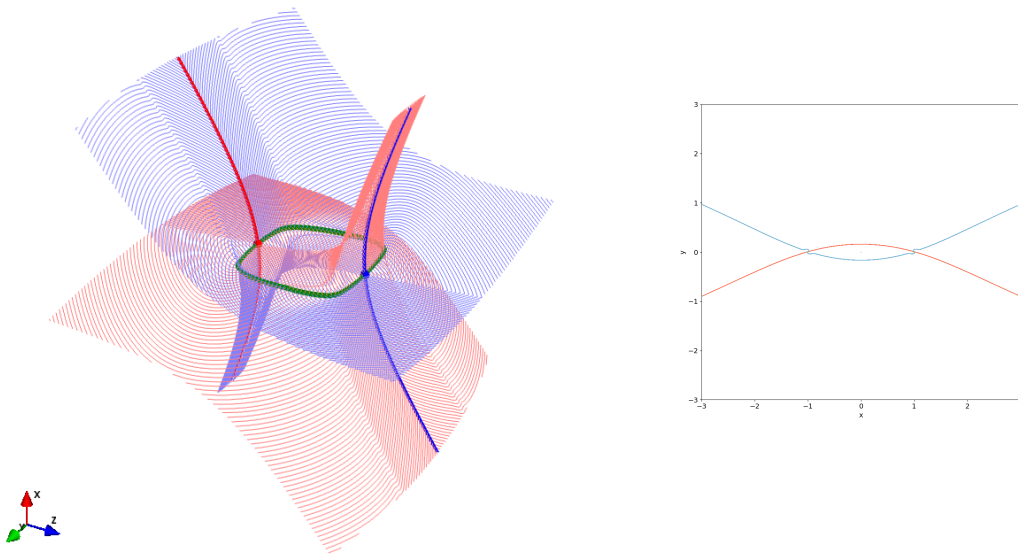


Figure 67: Initial condition for the relaxation. Left: magnetic skeleton of the double separator field with added flux rings. The potential field parameters are $a = 0.5$, $b = -6$, $c = 1$, $d = 1$, $f = -1$ and $L = 0$. Right: cut through the separatrix surfaces at $z = 1$.

4.4.1 Initial Setup

The relaxation was performed using the Lare3D code described in chapter 1. The initial conditions were given by the potential field in equation (71) with the parameters shown in figure 67 plus the flux ring from equation (84) with parameters from figure 65. The simulation box consisted of 512^3 points with $-3.0 < x, y < 3.0$ and $-2.0 < z < 4.0$. At every grid point, the initial velocity was set to zero and the plasma density $\rho = 1.0$ and internal energy $\epsilon = 1.5$ were chosen such that the plasma pressure was initially $p = 1$. The plasma beta was less than one across most of the domain, except for at the null points and neighbouring parts of the separators. At the centre of the separators, the value was $\beta \approx 0.1$, which is an order of magnitude larger than a typical value in the solar corona. Line-tied boundary conditions were used, meaning derivatives of \mathbf{B}, ρ and ϵ were set to zero across the boundaries and all components of the velocity were set to zero. The resistivity was set to zero for the duration of the relaxation, meaning the ideal MHD equations were solved. The flows in the system resulting from the initial non-equilibrium were damped using a high background viscosity, $\nu = 0.01$.

4.4.2 Separatrix Surfaces

Since the relaxation is performed by solving the ideal MHD equations, there cannot be any change in the number of topological features. However, figure 68 shows that the geometry of the separatrix surfaces is changed significantly by the relaxation process. This could be described as a transfer from the self-helicity in the initial negative separatrix surface to the mutual helicity of both surfaces.

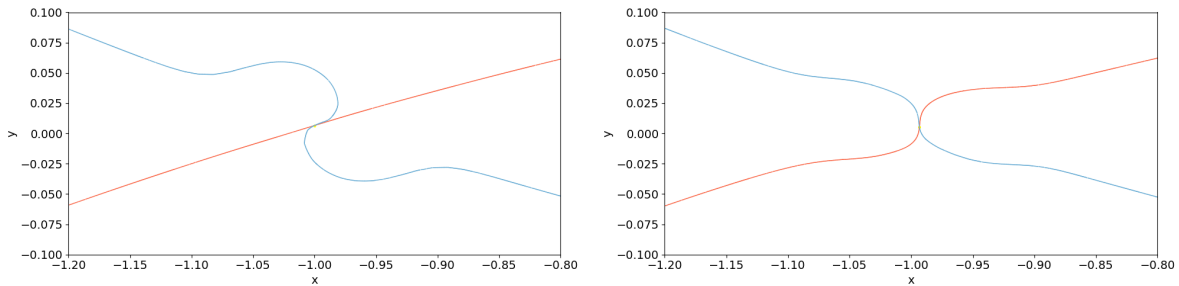


Figure 68: Cuts through the separatrix surfaces, focusing on the separator at $y < 0$. Left: pre-relaxation; right: post-relaxation.

4.4.3 Perpendicular Magnetic Field

It has previously been shown by Parnell et al. (2010) that the perpendicular magnetic field local to a separator can be either X-type or O-type. It is clear from figure 68 that the global magnetic topology is hyperbolic, as the separator divides the surrounding field into four distinct flux domains. However, the hyperbolic topology does not necessarily imply an X-type magnetic field.

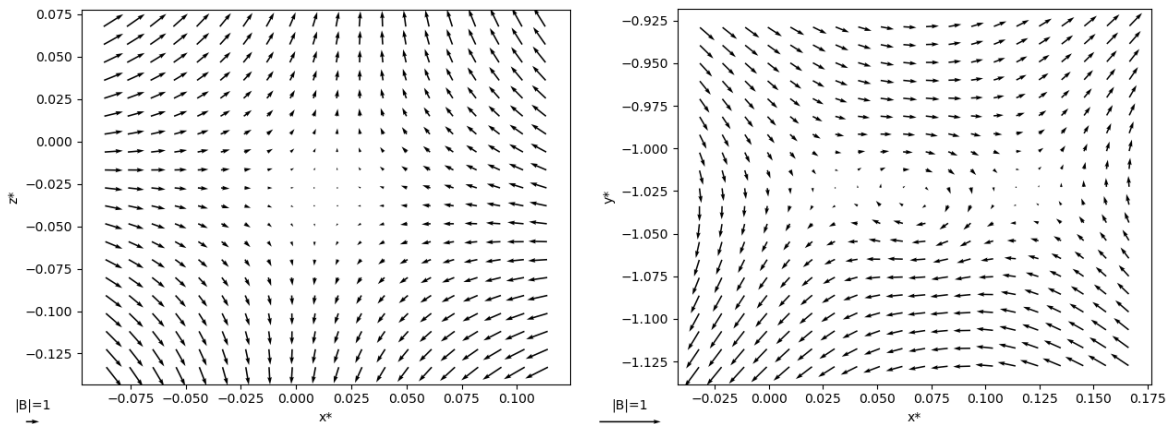
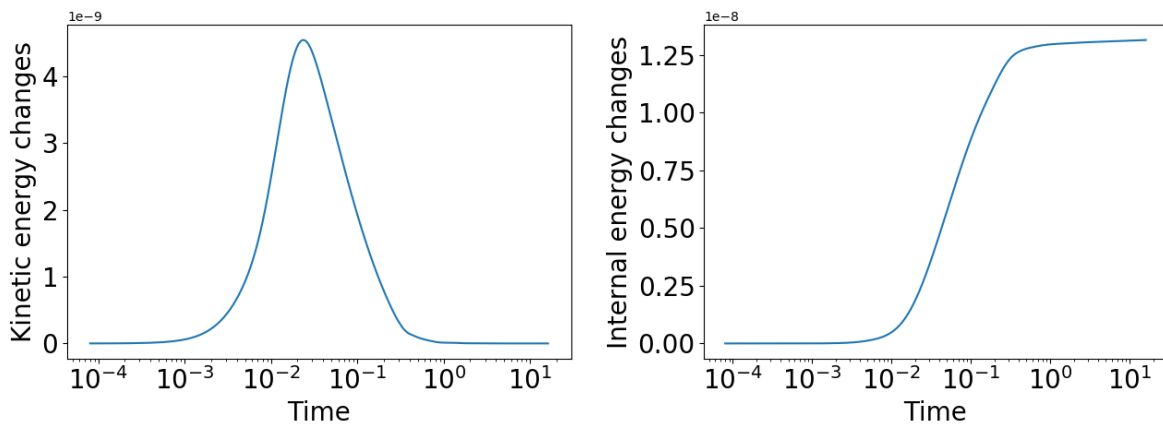


Figure 69: Magnetic field in planes perpendicular to the $y < 0$ separator. Left: $y = -0.5$, right: $z = 1$. The Cartesian coordinates have been rotated so that the basis vectors lie in the plane. x^* , y^* and z^* use the new basis vectors.

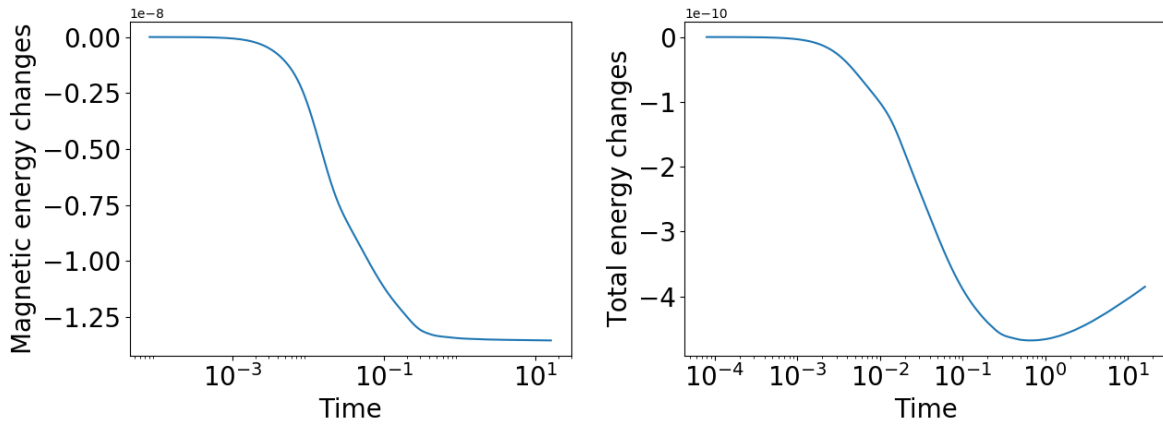
Figure 69 shows that in the vicinity of the null point at $z = 0$, the perpendicular magnetic field is locally X-type in agreement with the global topology. By contrast, at the mid-point of the separator ($z = 1$), the field is locally O-type. This is consistent

with the reconnection experiment of Parnell et al. (2010), where the perpendicular field is typically X-type at the null points (1/5 of the length of the separator) and O-type in the middle 3/5 of the length. In figure 69, there is additional complexity because the O-point centred on the separator has neighbouring X-points at $x^* = 0.03$ and $x^* = 0.11$. This feature is attributable to the flux ring magnetic field that has been superposed to the middle part of the separator.

4.4.4 Energies



(a) Evolution of the integrated kinetic energy (b) Evolution of the integrated internal energy



(c) Evolution of the integrated magnetic energy (d) Evolution of the integrated total energy

Figure 70: Time and volume integrated energy changes for the double separator relaxation, normalised by initial total energy

The relaxation process initially causes the conversion of magnetic energy into kinetic energy when the magnetoacoustic waves are released into the system. After the initial spike in the kinetic energy value, the waves are damped by viscous damping and the internal energy is increased by the resulting heating. The experiment conserves total energy with a relative error of the order 10^{-10} .

4.4.5 Current Density

Figures 71 and 72 show that the high current density is localised about the separators. From figure 71(a), it is clear that the current extends along the part of each separator that is parallel to the z -axis and rapidly decays to zero as the separators bend parallel to the y -axis at $z = 0$ and $z = 2$. There is also a weak current density stretching from the ends of the current layer to the y -boundaries. In the $y = 1$ plane, the separator current layer is again the dominant feature but there is also a significant build-up along the separatrix surfaces. There are also weaker striations (due to numerical effects) that loop from the fan plane intersections towards $x = 0$ and back to the separator. By contrast, at $z = 1$, the current is highly localised about the two points where the separators pierce the plane. Within a small radius of the separator intersections, the current does cover the separatrix surfaces but these do not extend towards the boundaries as in $y = 1$.

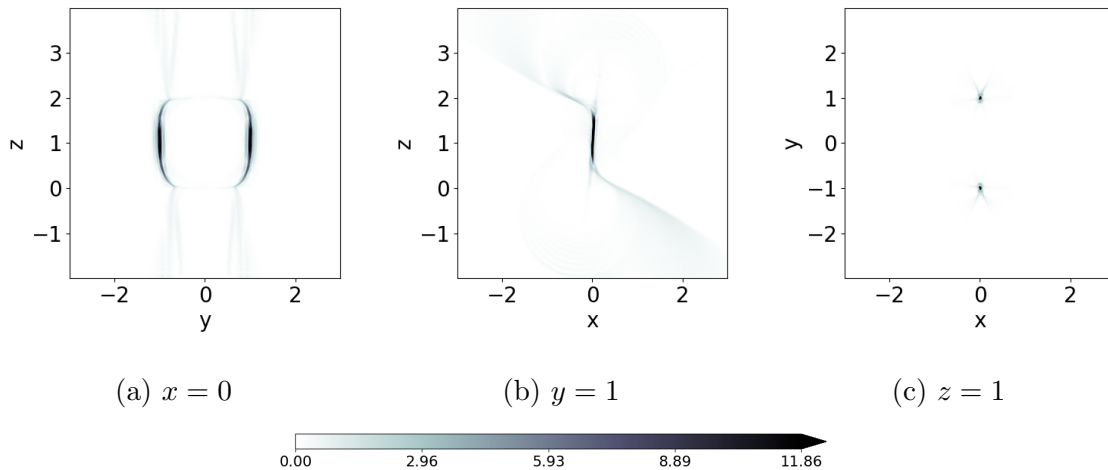


Figure 71: Magnitude of the current density in the quasi-equilibrium state

The separator current layers in this work are defined by the locations where the mag-

nitude of the current density exceeds the critical current $j_{crit} = 5$. This threshold has been chosen because it selects the regions of strong current that are localised about the separators, as shown by figure 72. Moreover, the current layers define two continuous volumes with measurable dimensions.

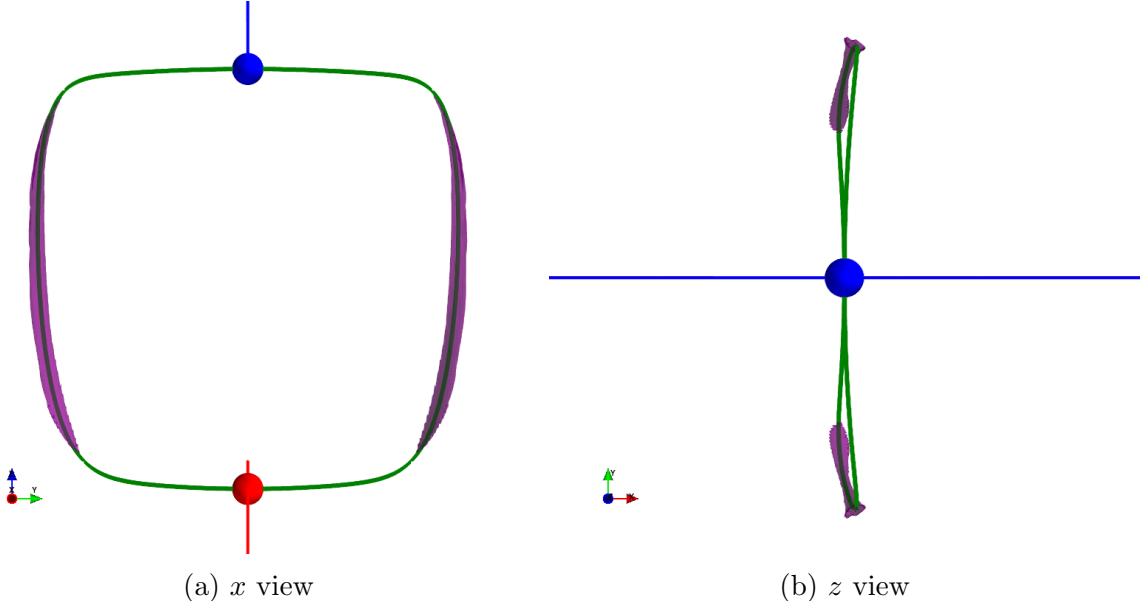


Figure 72: Current isosurface showing $|j| = 5$ for the quasi-equilibrium state

Unlike in chapter 2, the current layer does not appear to relax towards an infinite singularity so the length, width and depth are all considerably larger than the grid scale. Figure 73 shows that after $t = 1$, the current layer dimensions do not experience major changes. The length (in the z direction) gradually increases as the width (in the y direction) decreases, in the manner of a 2D collapse. The depth of the current layer remains constant after $t = 2$, which is surprising as one would expect it to asymptotically approach the grid scale to create a current ribbon resembling that in Longcope and Cowley (1996). The magnitude of the current is still increasing at a significant rate when the relaxation is terminated. This phase of the experiment could not be allowed to proceed further as the numerical boundary currents (visible in figure 71(a)) are beginning to grow beyond acceptable levels.

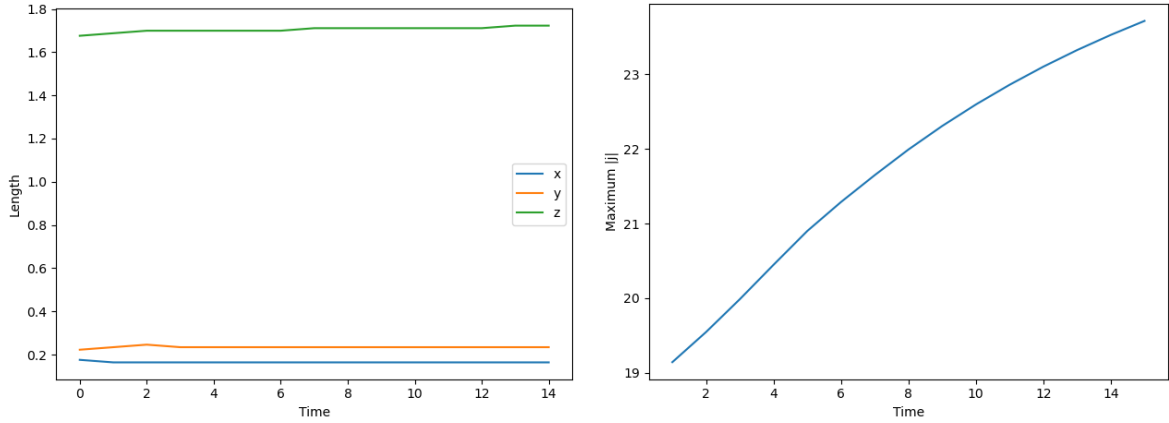


Figure 73: Time evolution of the current layer properties. Left: dimensions of the layer (volume satisfying $j > 5$); right: maximum magnitude of the current density.

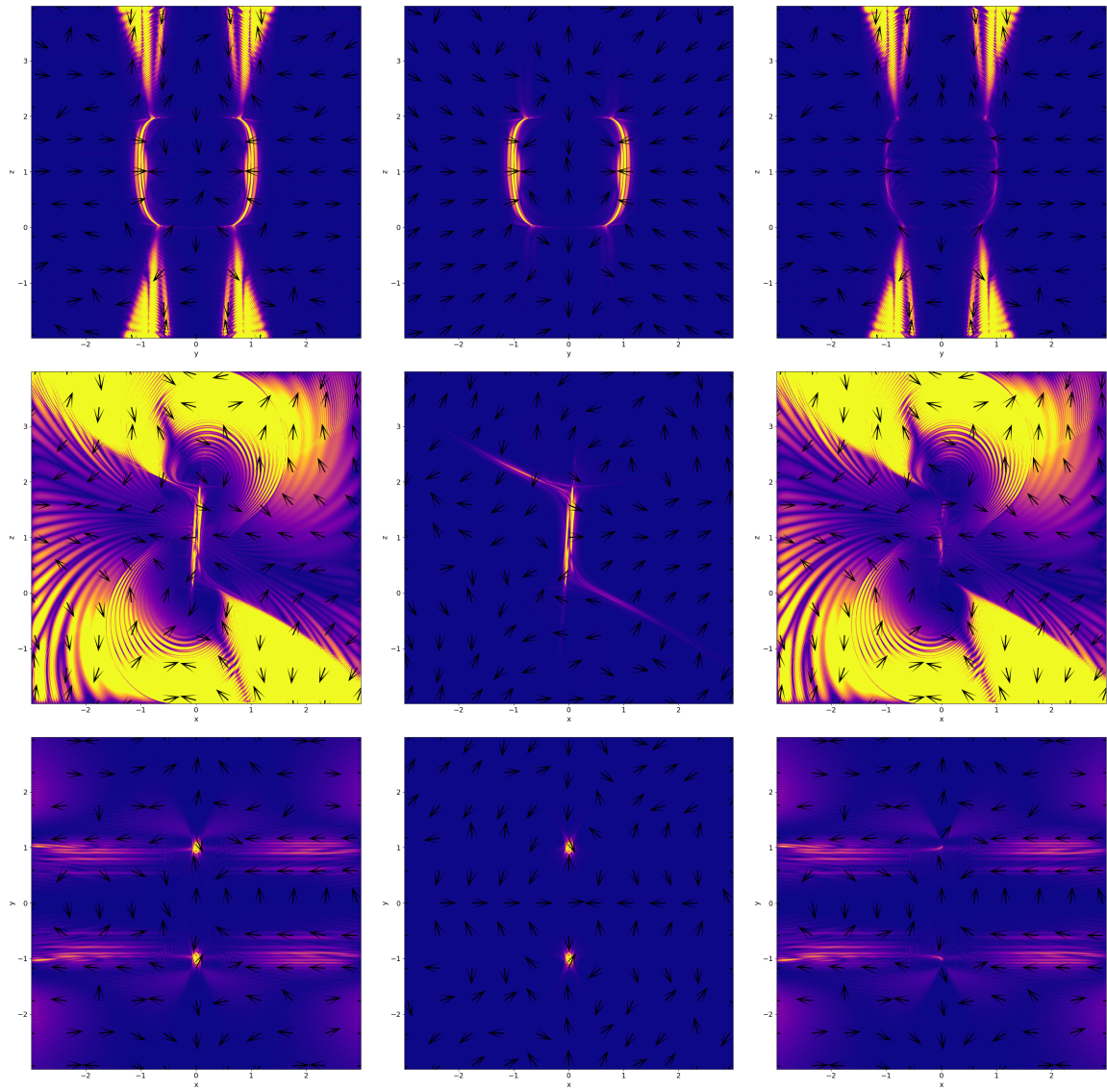
4.4.6 Forces

In order to reach a true equilibrium, we require the forces on the right hand side of the equation of motion to balance each other. Since we neglect gravitational effects in this model, this means that we require:

$$\mathbf{j} \times \mathbf{B} - \nabla p = 0 \quad (85)$$

Figure 74(a) shows the Lorentz force in three different cuts through the domain. These cuts are the same as those used in figure 71 to show the current density and as expected, the high current regions along the separators in $x = 0$ and $z = 1$ match up with a stronger Lorentz force. There are other regions of strong Lorentz force that can be attributed to numerical effects at the boundary, both in $x = 0$ and $y = 1$. The magnitude of these forces can be as much as five times higher than that found near to the separator, in spite of the current being considerably weaker. This is due to the quadratic growth of the magnetic field, which is strongest at the boundaries. These boundary effects do not appear to have a significant effect on the dynamics of the reconnection, as will be seen in the next section.

The pressure force in figure 74(b) is enhanced at the topological features, where it cancels with the Lorentz force. However there is no pressure force to cancel with the



(a) Lorentz force

(b) Pressure force

(c) Total force



Figure 74: Post-relaxation forces. The three rows show the forces in the $x = 0$, $y = 1$ and $z = 1$ planes respectively.

Lorentz force away from the separators so the third column shows force imbalances, particularly at $y = 1$. By consulting the $z = 1$ total force, it can be seen that the stronger forces in planes of constant y are limited to $0.7 < |y| < 1.1$. Away from

these regions the system has relaxed to a quasi-equilibrium. This figure has certain undesirable properties but the force imbalance does not directly affect the region where reconnection will occur. It will be seen in section 4.5 that the flows in the reconnection experiment are to a large extent localised about the topological features, suggesting that the force imbalance does not play an important role. Furthermore, the stopping criterion for the relaxation was that the integrated kinetic energy dropped below 10^{-8} , indicating that any residual forces do not accelerate the plasma to significant speeds. The final kinetic energy in figure 70 is several orders of magnitude lower than the peak value, which implies that the relaxation has been successful in attenuating the net force in the system. The aim of the relaxation was not to achieve a perfect equilibrium but rather to establish an initial condition from which the effects of reconnection can be clearly identified.

4.5 Summary of the Relaxation

This work has so far been aimed at constructing an initial condition for a reconnection experiment involving a system of two doubly connected nulls. It made use of an initial potential field where the two separators were flattened such that there was minimal variation in the x direction and the separator shape in the $y - z$ plane is square. This potential equilibrium was then disturbed by the addition of a flux ring at the widest point of the two separators. These flux rings had magnetic field parallel to the z -axis in agreement with the potential field, which is approximately vertical at these points.

The non-potential field was then relaxed ideally using Lare3D until a quasi-equilibrium state was achieved. The relaxed field contained separator current layers running parallel to the y -axis away from the null points. The shape of the separatrix surfaces has been altered such that the twist originally imparted on the negative surface (by the flux rings) has now been shared with the positive surface. The resulting force balance is far from perfect but the strongest imbalances are located away from the separator current layers and it is hoped these will not significantly impact the reconnection.

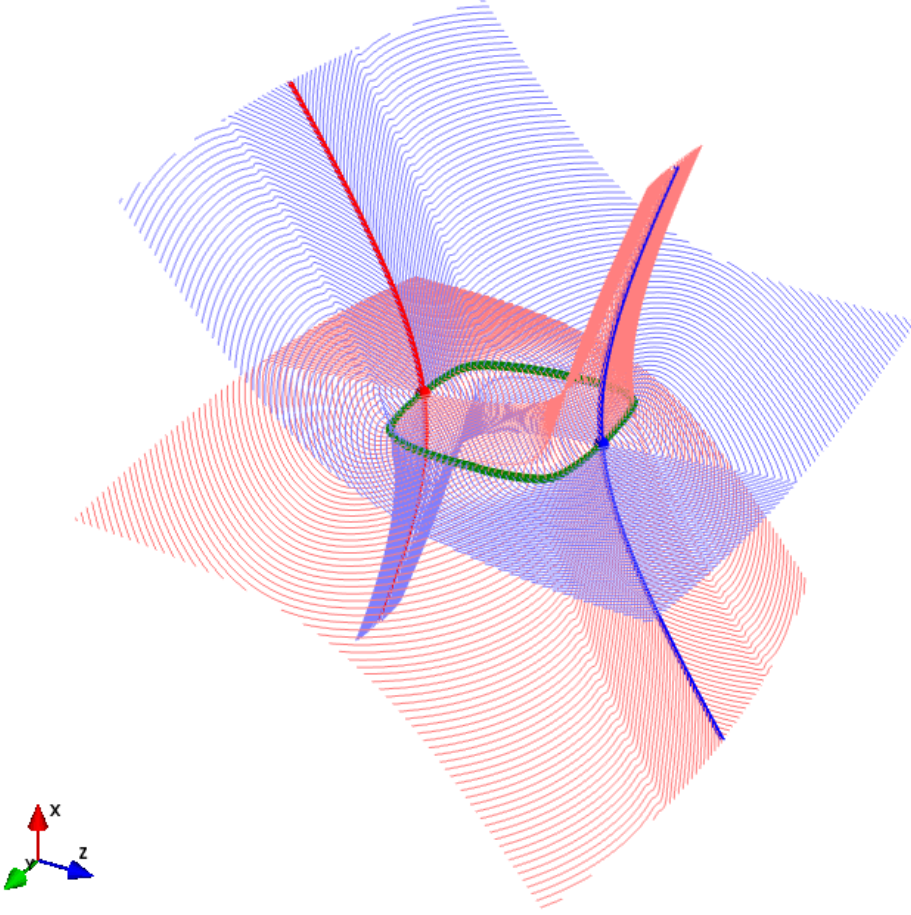


Figure 75: Quasi-equilibrium magnetic skeleton. This relaxed field will be taken as the initial condition for reconnection.

4.6 Reconnection

The reconnection results presented in this section use the original quasi-equilibrium field from the previous section as the initial state (shown in figure 75). The field is evolved by solving the resistive MHD equations using the Lare3D code. The grid size, resolution and boundary conditions all remain as before but the background viscosity

has been reduced by two orders of magnitude to $\nu = 1.0 \times 10^{-4}$. The experiment uses an anomalous resistivity:

$$\eta = \begin{cases} 0.01 & \text{for } j \geq j_{crit} \\ 0 & \text{for } j < j_{crit} \end{cases} \quad (86)$$

Here the threshold $j_{crit} = 5$ has been chosen to localise the current about the separators as seen in the isosurface in figure 72. The value of the resistivity is intended to expedite the initial reconnection at the current layer. It would be possible to perform the experiment with the lower resistivity value used in previous chapters.

4.6.1 Energies

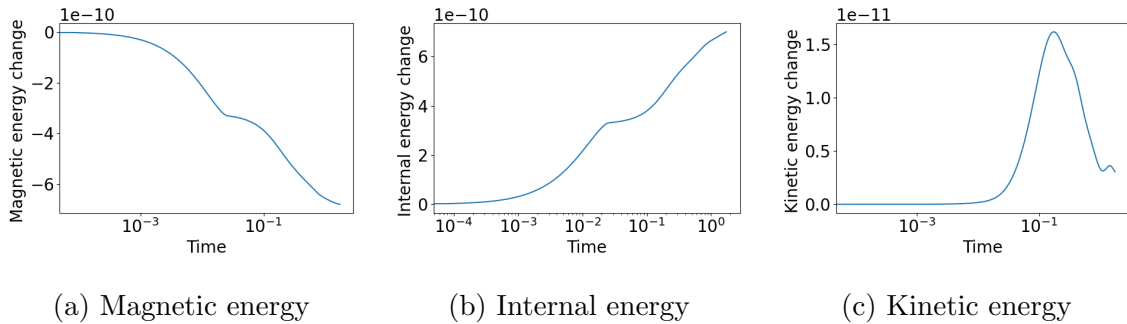


Figure 76: Time and volume integrated energy changes for the double separator reconnection, normalised by initial total energy

The reconnection process has the effect of converting the free magnetic energy in the system to internal energy and kinetic energy. It is clear that there are two stages in this energy conversion, the first of which lasts from the beginning of the experiment until just after $t = 0.02$. During this phase, the magnetic energy is transformed directly to internal energy and the kinetic energy in the system remains negligible. In the second phase, there is an increase in the kinetic energy (although the amplitude is still quite small) and the magnetic and internal energies are changing at a slower rate.

These energy changes are consistent with those seen in Stevenson and Parnell (2015a), although a quantitative comparison is not possible due to differences in the setup. The defining feature is the two distinct phases, which were also found by Fuentes-Fernández et al. (2012a) and Fuentes-Fernández et al. (2012b) in a 2D null point reconnection

experiment. It would appear that the fast reconnection followed by impulsive reconnection is a consequence of the combination of an equilibrium initial condition and nonuniform resistivity.

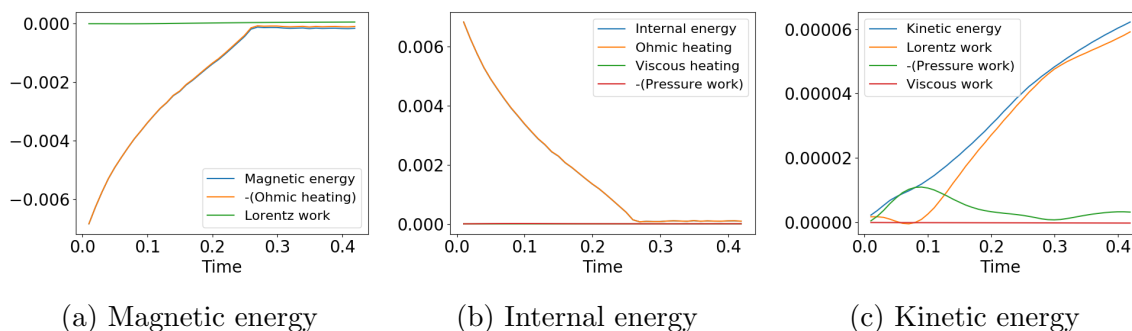


Figure 77: Terms contributing to the rates of energy change during the double separator reconnection, integrated across the volume.

Figure 77 shows the different terms that contribute to the rate of change of internal, magnetic and kinetic energies. It is clear that the first phase of the experiment is dominated by Ohmic dissipation, as the orange lines showing Ohmic heating agree well with the blue showing the overall rates of change. The strong Ohmic heating is caused by the high current regions surrounding the two separators and once this current has been dissipated, both the Ohmic heating and magnetic/internal energy rates of change drop to virtually zero.

After $t = 0.1$, the work done by the Lorentz force becomes more important and it is apparent in figure 77(a) that the magnetic energy loss is slightly greater than the value accounted for by Ohmic heating. The effect of this work done by the Lorentz force is felt most keenly by the kinetic energy, as figure 77(c) shows the magnitude of the rate of kinetic energy change is the same as this work done after $t = 0.1$ and the sum of the work done by the Lorentz and pressure forces gives the kinetic energy curve. The work done by the pressure force peaks in the first part of the experiment around $t = 0.1$, at which time the Lorentz force is unimportant. The pressure force subsequently diminishes as the Lorentz force increases so that around $t = 0.3$ the kinetic energy change is almost entirely caused by the Lorentz force.

4.6.2 Parallel Electric Field

In this section, reconnection sites will be identified using the definition from Hesse and Schindler (1988). This work associates 3D reconnection with a non-zero component of the electric field acting parallel to the magnetic field:

$$\int \mathbf{E} \cdot \mathbf{B} dl \neq 0 \quad (87)$$

This condition must be satisfied across a finite region; it is not sufficient to have a non-zero E_{\parallel} along an isolated fieldline. The reconnection rate is then given by the maximum value of the integral of E_{\parallel} in the region.

Since the current layers have formed around the two separators in this experiment, one would expect the reconnection rate to agree with the value of E_{\parallel} integrated along the separators. Figure 78 shows that this is indeed the case. There is initially fast reconnection, as the current that has been stored in the layers surrounding the separators is rapidly dissipated after the resistivity is activated. The diffusion region remains intact until $t = 0.026$, after which time the majority of the current layer has magnitude less than j_{crit} and the reconnection becomes impulsive. The reconnection rate during this second phase is low but the energy changes taking place at this time are significant, as seen in figure 76. The separator E_{\parallel} drops to zero at the start of the impulsive phase and does not deviate significantly from this mark, whereas the E_{\parallel} across the whole domain is of the order 10^{-3} . Clearly, this implies that the impulsive reconnection is not localised about the separator, unlike the preceding fast reconnection.

As with the energy changes, the reconnection rates corroborate those seen in Stevenson and Parnell (2015a). The period of fast reconnection expires sooner here, due to the higher value of resistivity. The dark lines in figure 78 indicate that the reconnection occurs continuously even during the transition from fast to impulsive behaviour. However, Stevenson and Parnell (2015a) plot the reconnection rate along the separator so the light coloured lines should be used in a comparison, which do show a brief delay before the commencement of the impulsive reconnection. The other major difference is of course the presence of both positive and negative E_{\parallel} in this experiment. This is caused by the oppositely directed initial flux rings rather than the reconnection dynamics.

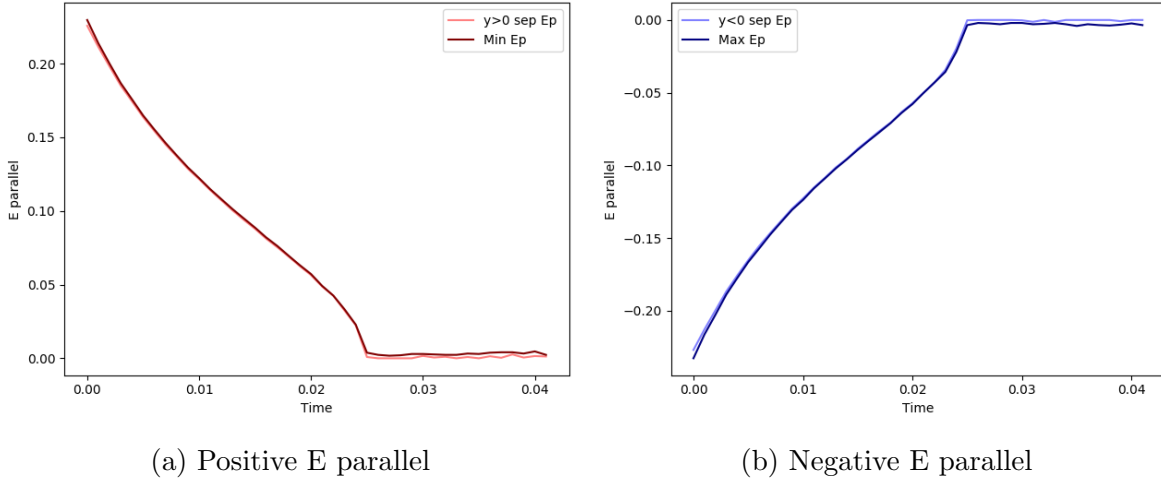


Figure 78: Reconnection rates for the double separator reconnection. Left: time evolution of the maximum integrated E_{\parallel} along fieldlines passing through $z = 1$, compared with the integrated E_{\parallel} along the $y > 0$ separator. Right: time evolution of the minimum integrated E_{\parallel} along fieldlines passing through $z = 1$, compared with the integrated E_{\parallel} along the $y < 0$ separator.

Figure 79 gives an indication of where the reconnection takes place in the domain at $t = 0.001$. The E_{\parallel} contours shown are given by integrating along the fieldlines which pass through a grid of start points in the plane $z = 0.5$. The grey line is a projection of the shape of the two separators when viewed from a plane of constant z . Clearly the patches of non-zero E_{\parallel} are close to the widest parts of the separator ring where $y = \pm 1$. This figure shows that the fast reconnection in this experiment is localised about the separators. Although figure 79 only represents the reconnection at a single instant during the simulation, the frames in figure 80 confirm that the E_{\parallel} does not occupy a larger volume at later times.

Figure 80 focuses on the positive and negative regions separately, providing 2D projections of the volumes within which the parallel electric field is non-zero. On either side of the y -axis, it is the negative separatrix surface that has been twisted chiefly, so that the width of the reconnection region corresponds to the initial perpendicular displacement of the negative fan plane. The strongest E_{\parallel} is located at the centre of these regions where the separator intersects the z -cut but as time progresses the areas with the strongest E_{\parallel} decay the quickest, meaning the gradients in the non-zero region

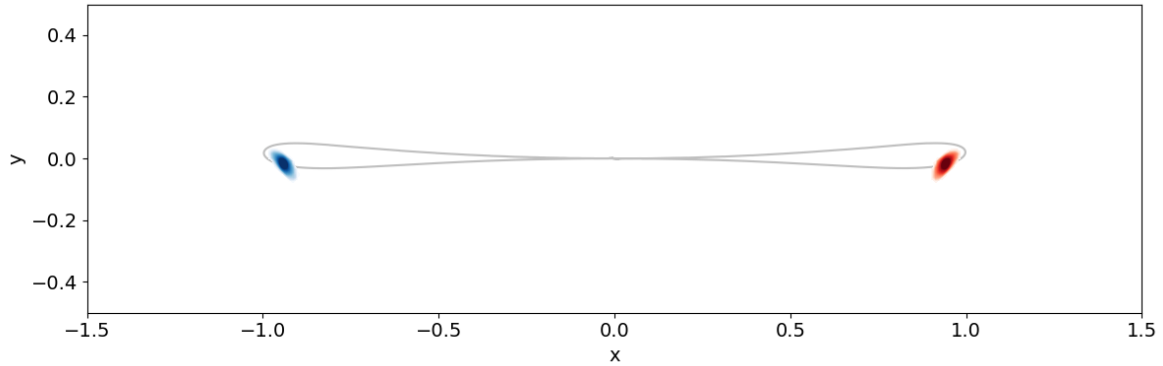


Figure 79: Integral of E_{\parallel} at $t = 0.001$ with projected view of the separators

become weaker, as the outer parts continue to reconnect at a slow rate. The middle panel $t = 0.015$ also shows some expansion at the fringes of the non-zero regions, indicating that magnetic flux is being transported into the region as the resistive experiment progresses, so that sections of current that were initially below the critical current have now exceeded this threshold. As the reconnection progresses, the twist in the negative separatrix surface diminishes and the angle between the fan planes approaches 90 degrees. By $t = 0.026$, the excess current has been completely dissipated and the parallel electric field now is only found in small patches that match the location of the original layer to a large extent but are much smaller in amplitude.

The spatial variation in E_{\parallel} seen here is rather different from that in Stevenson and Parnell (2015a). The E_{\parallel} in this experiment is localised about the separator but constitutes a simple region that is not misshapen due to the separatrix surfaces. The previous work had a strong core of E_{\parallel} focused on the separator but also thin arms of weaker E_{\parallel} extending along the separatrix surfaces. This could be attributed to the fact that the current layer arises due to localised twist and not the more large scale narrowing of the cusp regions seen in Stevenson and Parnell (2015a). Here the reconnection acts to relieve the build-up of magnetic tension whereas the other experiment reduces magnetic pressure in the cusp regions.

Finally, the parallel electric field along the separators has been plotted through time for both separators. It can be seen that the reconnection on either side of the y -axis shows good symmetry. The strongest E_{\parallel} occurs close to the midpoint of the two separators

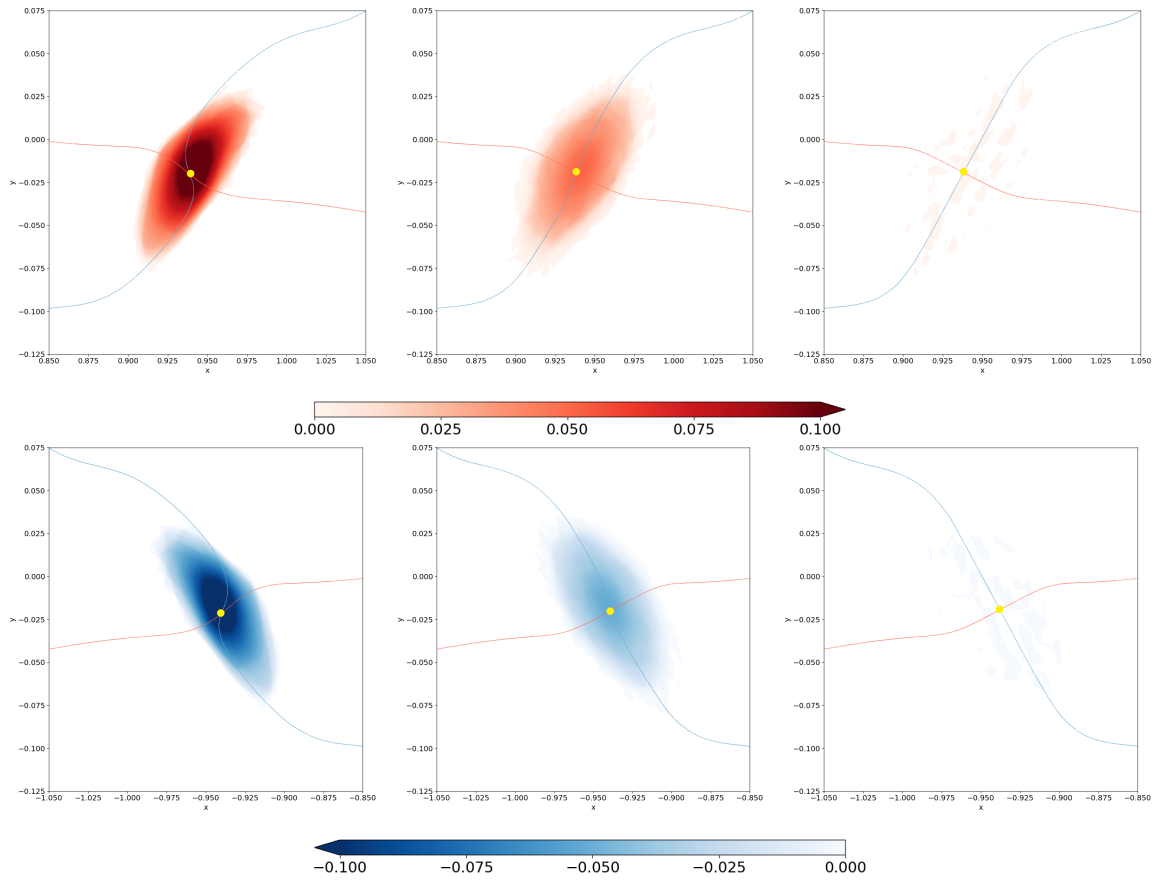


Figure 80: Parallel electric field integrated along fieldlines passing through $z = 1$ at: (a) $t = 0.001$, (b) $t = 0.015$, (c) $t = 0.026$. Top row: $y > 0$ separator; bottom row: $y < 0$ separator

and the reconnection site does not extend as far as the nulls. After the fast reconnection expires at $t = 0.025$, there is no longer a continuous region of non-zero E_{\parallel} and we instead see scattered bursts of reconnection. The impulsive phase seems to be somewhat more significant for the $y < 0$ separator.

The separator E_{\parallel} is much more localised about the midpoint than in Stevenson and Parnell (2015a). There are a few possible reasons for this. The simplest explanation is that the critical current used in this experiment was chosen to localise the current layers along the parts of the separator that are approximately parallel to the y -axis. A lower value for the critical current would allow for reconnection closer to the nulls, although the previous work did not use an especially small j_{crit} . Another reason for

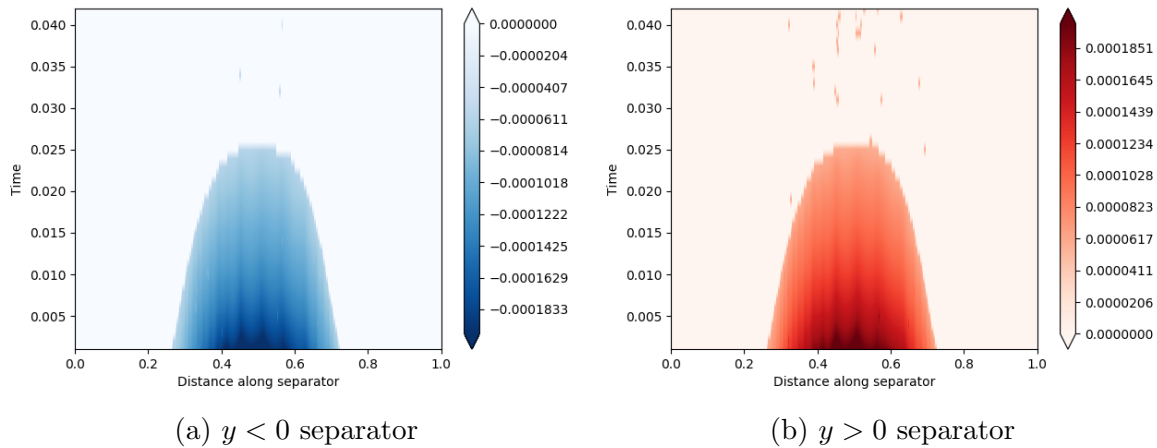


Figure 81: Distance-time plot showing the evolution of E_{\parallel} along the separators

the distribution of E_{\parallel} is the shape of the separators, which appears to discourage the growth of current close to the nulls. The flux ring current was mostly directed parallel to the separators at $y = \pm 1$ and consequently the current layer did not extend to the sections parallel to the z -axis. Additionally, the flux rings applied a more localised disturbance as discussed previously. In the single separator work, the angle between the separatrix surfaces along the length of the separator is much more consistent.

4.6.3 Connectivity Changes

Although the parallel electric field is a useful measure of the reconnection rate, it should be paired with fieldline plots to gain a clearer understanding of the dynamics of the experiment. Figure 82 shows the evolution of two flux tubes that initially coincide with the current layers along the two separators. The initial flux tubes are blue and the fieldlines remain this colour until they reconnect. Fieldlines are retraced from both of their initial footpoints and if this results in two separate fieldlines, these are coloured green (traced from the negative x footpoint) and orange (traced from positive x).

It appears that the majority of the reconnection occurs before $t = 0.02$ in keeping with the reconnection rate in figure 78. The last remaining blue fieldlines are reconnected between $t = 0.01$ and $t = 0.02$ but it is important to remember that this does not mean

the reconnection ceases. A well-known property of 3D reconnection is that fieldlines threading the diffusion region will reconnect continuously, so it is possible to identify differences in individual fieldlines between $t = 0.03$ and $t = 0.04$, although the overall appearance of the flux tubes is similar.

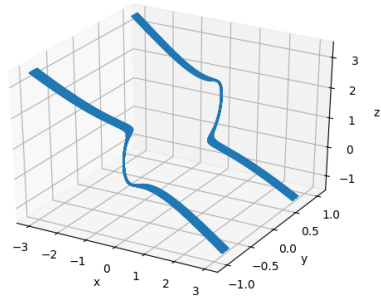
4.6.4 Flows

One can visualise the reconnection outflows by following perturbations in the plasma pressure in figure 83. The wave clearly propagates in all directions, although the shape is more elongated when the length of the current layer is visible. At the start of the experiment, a pressure deficit marks the regions where current is dissipated as the plasma motions relieve the pressure build-up around the original current layer. Of course, these flows transport the plasma to other parts of the domain so we observe the pressure decrease moving away from the separator. The wave consists of a plasma deficit and two weaker enhancements- one leading and one trailing. These are due to the local loss of equilibrium caused by the progress of the wave through the domain.

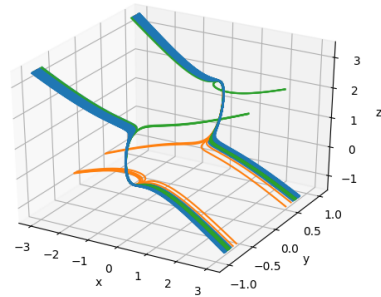
The $x = 0$ cut offers a view of the full length of the waves due to both separators, which emanate from the parts that are parallel to the z -axis. The strongest pressure perturbations are visible in this plane (of the three locations shown in figure 83). In spite of their relative strength, the waves pass through each other without reflection and do not appear to interact with the opposing reconnection site at later times. The purple bands in the space vacated by the wave are evidence of plasma inflows, which act to restore the equilibrium in the vicinity of the separator.

At $y = 1$, the length of the wave released by one of the separators can be seen. The separatrix surfaces are also outlined faintly by a pressure enhancement, which has a steady intensity. The amplitude of the wave seen at $t = 0.015$ is lower than that seen for $x = 0$ and it has been almost completely damped by $t = 0.026$. Away from the wave, the pressure builds up at the centre of the separator but decreases closer to the nulls.

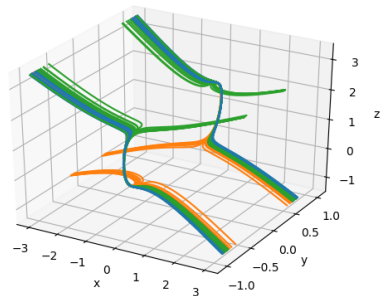
In the $z = 1$ plane, a cut through the centre of the length of the waves is seen. The variation in the magnitude of the disturbance is visible, as the parts of the wave prop-



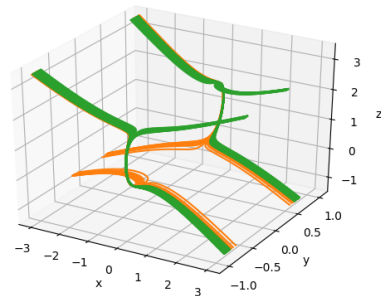
(a) $t = 0.0$



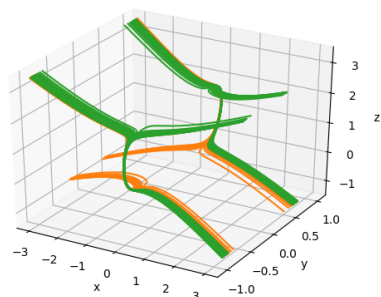
(b) $t = 0.005$



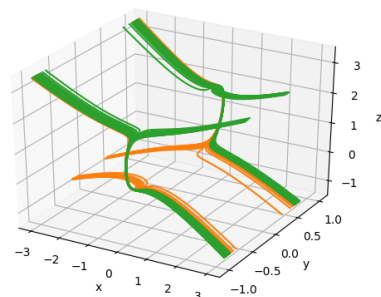
(c) $t = 0.01$



(d) $t = 0.02$



(e) $t = 0.03$



(f) $t = 0.04$

Figure 82: Connectivity changes for two initial flux tubes (blue). Fieldlines traced from $x = -3$ are shown in green and those from $x = 3$ are orange.

agating towards the x -boundaries have a greater amplitude than those moving towards the y -boundaries. The wavefront experiences a transition between $t = 0.016$, where it is concave, and $t = 0.026$ where it is convex. This is presumably caused by the waves colliding with the x -boundary and splitting into two parts, which move away from each other.

The pressure perturbations in Stevenson and Parnell (2015a) are visualised by a static difference $p - p_0$ rather than a running difference. As a result, the regions of enhanced and reduced pressure are much larger than in figure 83. One interesting difference is that the nature of the pressure perturbation for the static difference was dependent on the direction of the flow. Hence an enhancement in the pressure occurred in the cusp regions while a deficit was seen in the non-cusp regions. In this experiment, it seems that the nature of the perturbation (but not the magnitude) is independent of the flow direction, since a pattern of enhancement-deficit-enhancement is clearly seen in each cut at $t = 0.015$. There is evidence of asymmetry in the $y = 1$ plane at $t = 0.026$ but this is not connected to the propagating wave.

Now looking at the flows parallel to the separator, there is a clear change in sign about the midpoint of the two separators. This point coincides with the maximum $|E_{\parallel}|$ as the flows are moving away from this point as the reconnection proceeds. The v_{\parallel} is spatially localised along the parts of the separator parallel to the z -axis, which suggests that it is strongly related to the initial current distribution. The flows moving towards the null at $z = 2$ are in the direction of the magnetic field while those moving towards $z = 0$ move against the field. Although these divergent flows can be linked to reconnection, their magnitude is weakest during the fast reconnection. Figure 76 shows that the volume integrated kinetic energy peaks around $t = 0.2$, so the behaviour along the separator reflects the global development. The maximum speed of the parallel flows is 0.1% of the Alfvén speed, which is 100 times smaller than the maximum speeds achieved by the plasma during the experiment.

After the wave leaves the reconnection site, the flow pattern in the midplane half-way along each separator is a quadrupolar vortex. The flow is split into four quadrants which rotate in the opposite sense to their neighbours. Figure 85 shows the flows in this plane at $t = 0.06$, shortly after the wave is released and later at $t = 0.2$. The

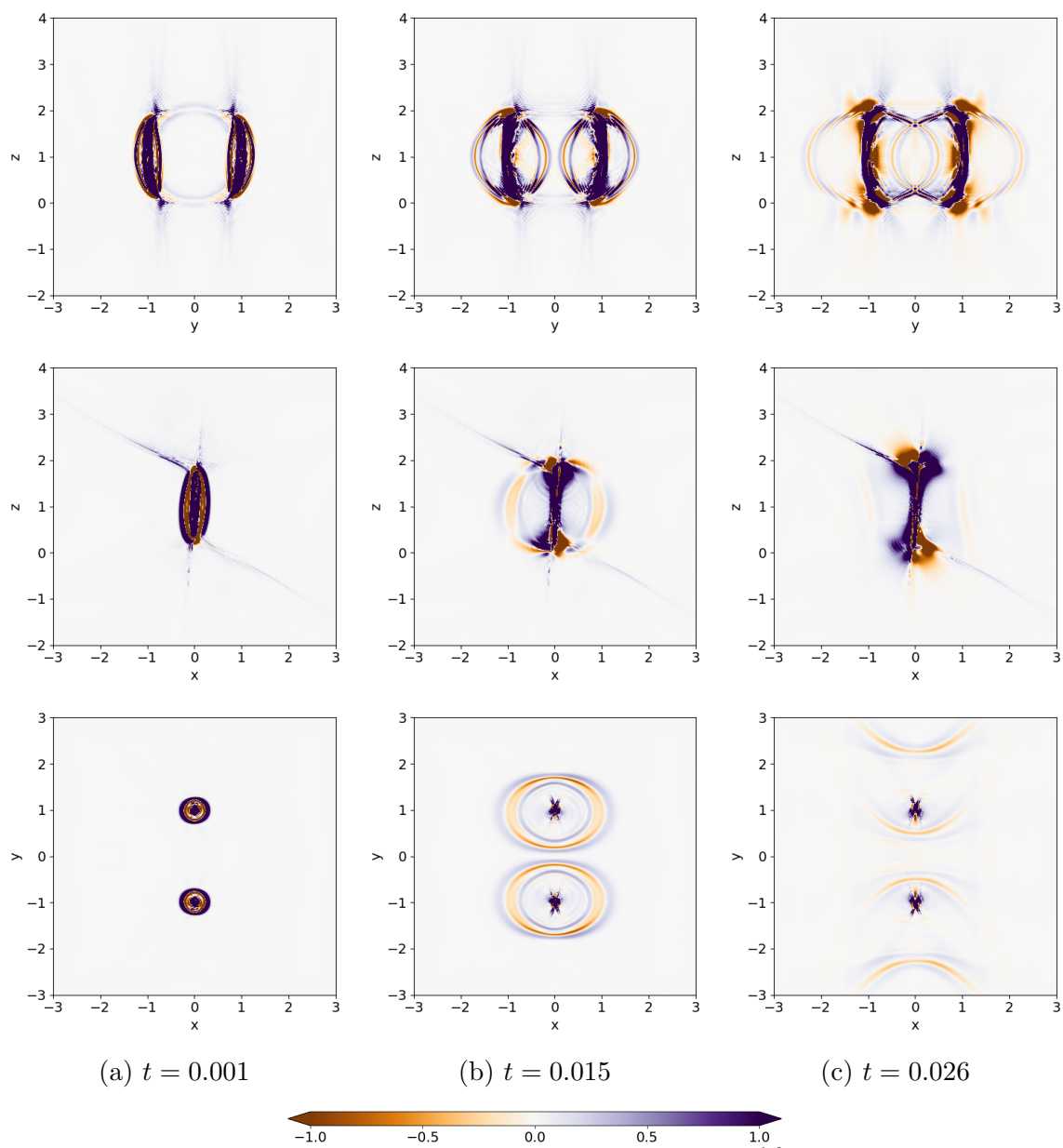


Figure 83: Running difference contours showing pressure perturbations ($\times 10^{-5}$) at three instants in time. The three rows show cuts through the $x = 0$, $y = 1$ and $z = 1$ planes respectively. The time interval between frames is 0.001.

two frames both show a stagnation point flow centred upon the separator, with plasma being swept towards the separator along the y -axis and then moving away from the separator parallel to the x -axis. The inflows in the cusp regions carry magnetic flux to

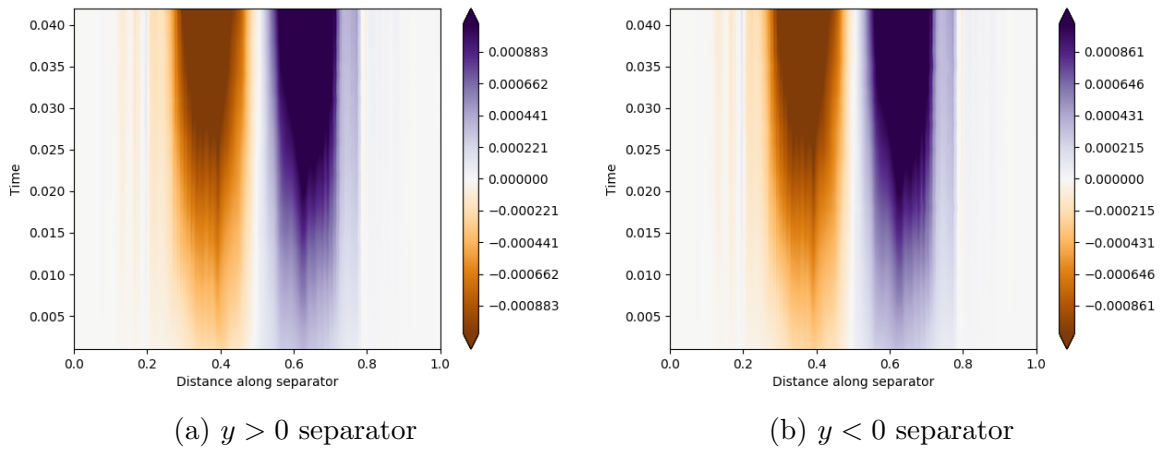


Figure 84: v_{\parallel} along the separators

rebuild the current layer along the separator but the outflows are not necessarily caused by reconnection, as they remain steady once the reconnection pauses at $t = 0.26$.

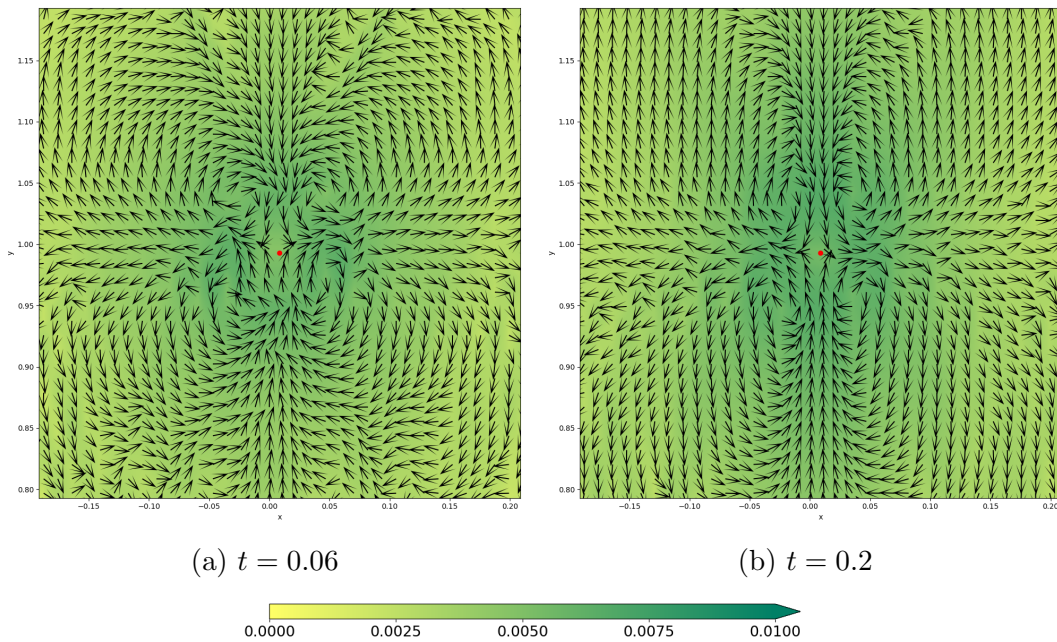


Figure 85: Plasma velocity in the $z = 1$ plane

There are two types of flow in the domain, namely the weak global flow caused by the passage of the wave through the domain and the stronger local flows associated with the

separator relaxation and reconnection processes. As the wave moves radially away from the separators, the space it vacates is occupied by a plasma backflow which interacts with the flows local to either separator. At $t = 0.06$, the wave has just left the separator so the backflow due to the wave diverts the separator outflows seen in figure 85(a). The plasma flows into the cusp regions where it becomes part of the separator inflow once more. This flow pattern is sustained at later times, except that the influence of the backflows due to the wave is diminished. In figure 85(b) one can see that the outflow again feeds in to the cusp regions but the plasma is not being diverted to the extent that it was before, as the streamlines for $|x| > 0.1$ are almost radial where the flow was previously azimuthal.

4.7 Six Separator Case

It was shown in section 4.3 that by varying the parameters of the flux ring added to the potential field, it is possible to alter the topology of the initial magnetic field. This section will investigate the dynamics of a reconnection experiment involving six separators. To be more precise, there are two clusters of three separators, so it will be interesting to observe whether the evolution recognises the six distinct separators. It should be possible to judge whether the number of separators is significant in determining the reconnection rate. The additional separators are the result of increasing the disturbance to the potential field so it will be necessary to weigh the importance of the larger perturbation and the greater number of separators.

Here, the factor B_0 determining the magnitude of the added field has been increased by a factor of two. The effect of this is to introduce more twist to the separatrix surfaces such that on either side of the y -axis, there are three separators initially. As in the double separator experiment, a current layer is developed through ideal relaxation. A quasi-equilibrium is achieved once the internal and magnetic energies are constant and the magnitude of the kinetic energy is of the order 10^{-9} . The setup for the reconnection experiment is no different to the previous section, although the critical current has been doubled to $j_{crit} = 10$ to account for the stronger currents caused by the choice of B_0 .

4.7.1 Energies

The energy changes for the reconnection experiment with six separators are shown in figure 86. Clearly the same process is at work as in the two separator experiment, as the magnetic and internal energy changes again occur in two phases, with the second beginning around $t = 0.02$. The kinetic energy spikes after the initial phase of the reconnection but the magnitude of the change is only of the order 10^{-11} relative to the initial total.

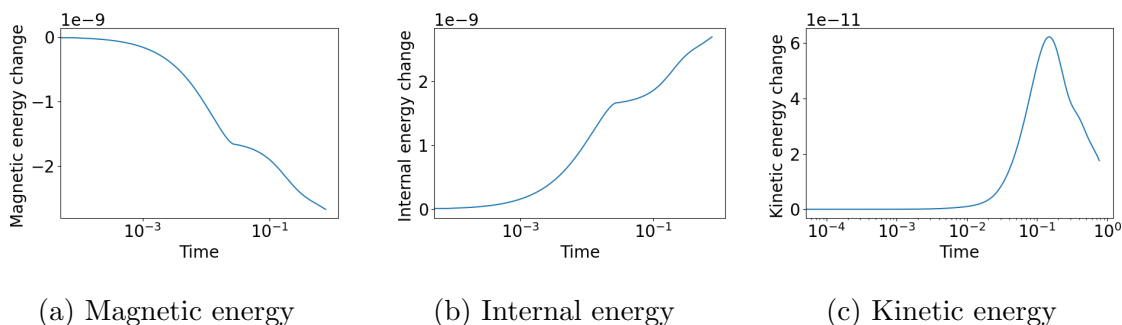


Figure 86: Time and volume integrated energy changes for the six separator reconnection, normalised by initial total energy

Ohmic heating is the main factor affecting the energy changes during the first phase of the experiment. The viscous heating steadily increases with the magnitude of the flows in the system but the rate of viscous heating is still an order of magnitude less than the ohmic heating rate during the second phase, when the diffusion region is no longer intact.

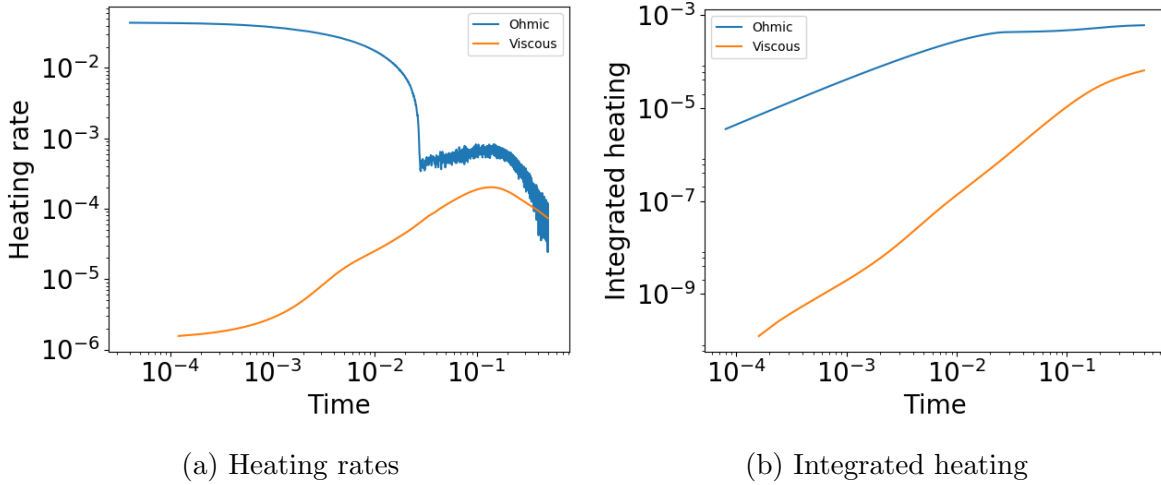


Figure 87: Time evolution of the ohmic and viscous heating for the six separator reconnection

4.7.2 Parallel Electric Field

The reconnection rate was calculated in the same manner as during the first experiment, integrating the parallel electric field along fieldlines passing through $z = 1$. The magnitude of the current in this experiment is twice that in the two separator case, due to the intensification of the flux rings. Consequently the magnitude of the integrated E_{\parallel} is also two times larger in this experiment but the qualitative behaviour is the same. Figure 89 shows that the reconnection is locally different around the new separators, since the parallel electric field is oppositely directed. However the reconnection along the central separator dwarfs the two new separators on either side of the y -axis so when considering the maximum value in the volume as in figure 88, these differences are lost. The parallel electric field is strongest at the start of the experiment and declines almost linearly until around $t = 0.025$, when it almost reaches zero. After this point the reconnection proceeds in a bursty fashion with the parallel electric field showing small ripples as the current exceeds the threshold in patches and is dissipated.

Figure 89 shows contours of the integrated parallel electric field in the plane $z = 1$ at three different times. In the first two frames, there are three separators passing through the plane, which are marked by yellow circles. The lines where the separatrix surfaces intersect with the plane are also shown and the separators are of course located

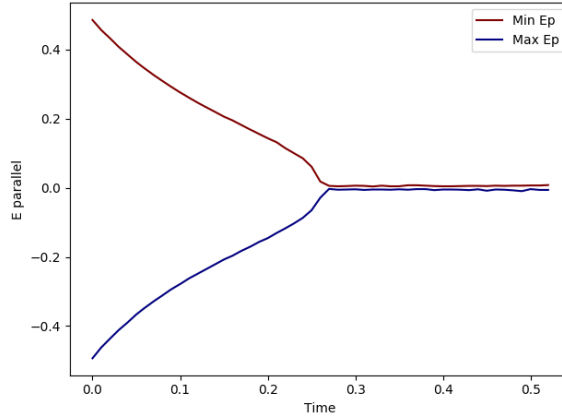


Figure 88: Time evolution of the maximum and minimum integrated E_{\parallel} along fieldlines passing through $z = 1$.

where these lines meet. At the beginning of the experiment, there is a region of strong positive E_{\parallel} coinciding with the central separator and there are weak patches of negative E_{\parallel} close to the other separators. The negative E_{\parallel} quickly vanishes before $t = 0.003$ as the separatrix surfaces untwist themselves and the two new separators move inwards towards the central separator. At the start of the experiment, the positive fan is only slightly twisted but the negative fan is sigmoidal in this plane and the new flux domains are formed from the protrusions in the negative fan. As time progresses, these central flux domains are drained as the flux is transferred into neighbouring regions and the protrusions diminish while the separators migrate inwards. Shortly before $t = 0.016$, two of the separators annihilate, leaving only the left separator, which continues to move towards the centre of the high current region.

The picture is similar for the three separators on the positive side of the y -axis (the second row in figure 89). In this case the strong central E_{\parallel} is negative and the fringes are positive but it is still the negative fan plane that is highly twisted and must unravel to cause the separator bifurcation. Here, the oppositely signed E_{\parallel} again disappears before $t = 0.003$ and the middle and right separators annihilate before $t = 0.015$. It is interesting that the more distant pair of separators annihilate unlike for $y < 0$. This is related to the amount of flux contained within the central flux domains and also the local reconnection rates, which in turn are determined by the strength of the currents.

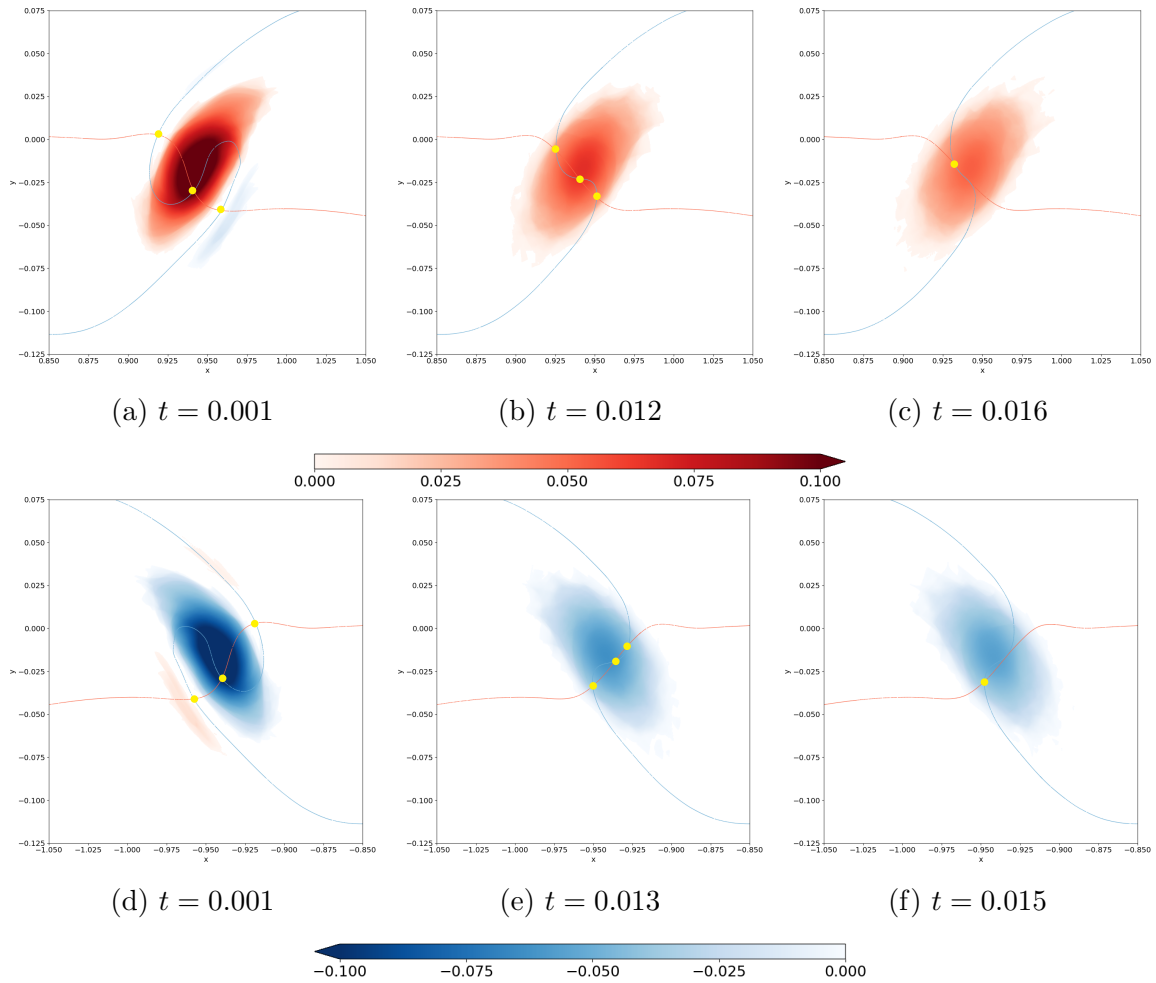


Figure 89: Parallel electric field integrated along fieldlines passing through $z = 1$. Top row: $y > 0$ separators; bottom row: $y < 0$ separators.

Figure 90 shows how the parallel electric field along the length of each of the six separators progresses over time. As shown in figure 89, only the left separator remains at the end of the experiment and the horizontal dashed indicates the instant in time where the separator bifurcation occurs. The parallel electric field is non-zero along the middle third of each separator and it is clear that the null points (located at 0 and 1 on the normalised scale) do not contribute directly to the reconnection. The major point of inconsistency between these plots and figure 89 is that the sign of the E_{\parallel} along the left separators does not change during the experiment. In figure 89 we saw that the left separator was initially associated with the oppositely signed E_{\parallel} before the separator

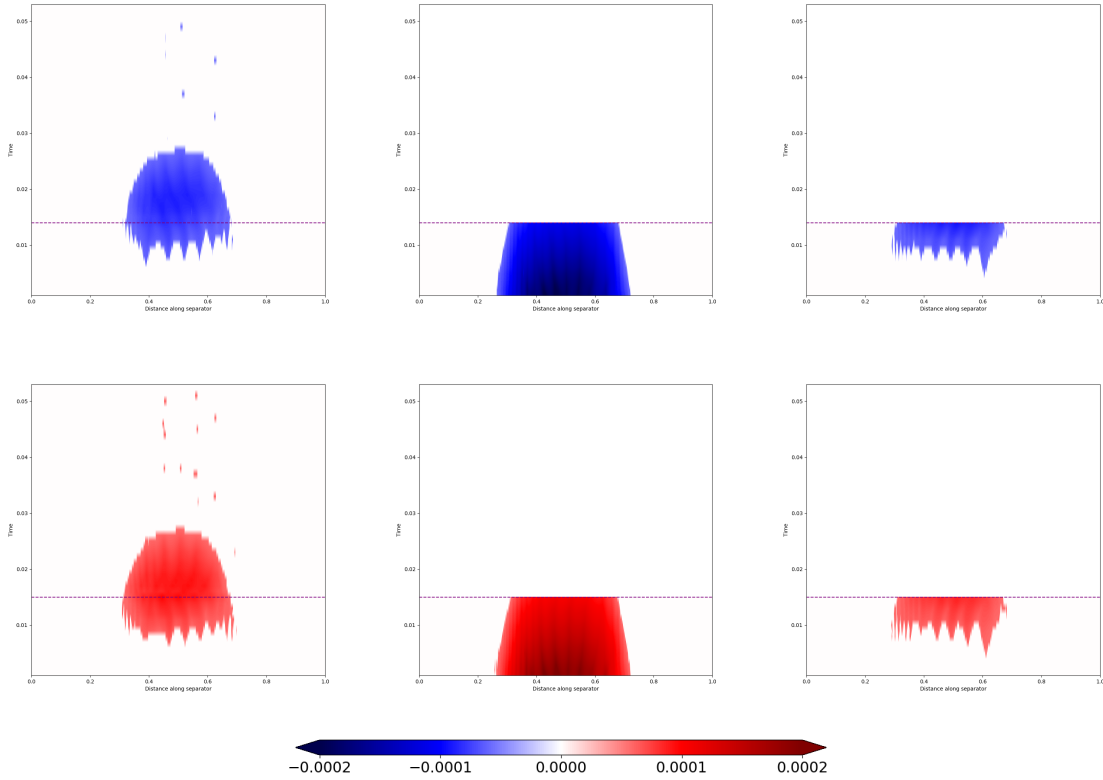


Figure 90: Distance-time plot showing the time evolution of E_{\parallel} along each of the six separators. Top row: $y < 0$; bottom row: $y > 0$

drifted into the main region, settling at the centre of the high current region after the bifurcation eliminated its neighbours. However, a closer inspection reveals that these parasitic regions of E_{\parallel} lie on the outside of the negative fan plane and do not coincide with the separator.

4.7.3 Flows

Figure 91 shows the time evolution of the parallel velocity along each of the three separators with $y > 0$. As in figure 90 a horizontal line highlights the moment when the right separator annihilates with the central separator. Prior to this time, the parallel velocity is strongest along the central separator and has the same divergent nature as the flows seen in the double separator experiment (figure 84). Along the other two

separators, the flow is more homogeneous until shortly before the bifurcation when they enter the diffusion region. Once the annihilation has occurred and the left separator takes its place at the centre of the diffusion region, it develops the strong divergent parallel velocity seen in figure 84. The flow appears to stretch farther along the length of the separator than in the double separator experiment and there appears to be a slight asymmetry in favour of the positive velocity towards the negative null.

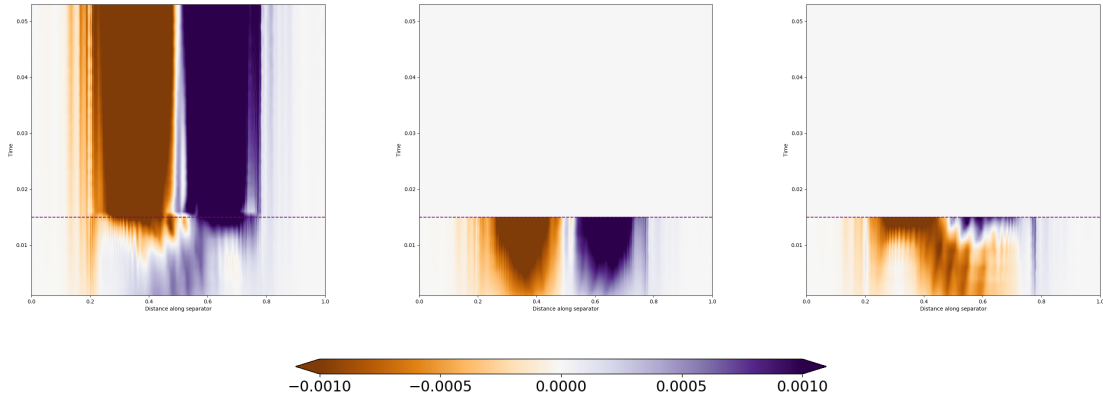


Figure 91: Parallel velocity along the separators ($y > 0$)

4.8 Asymmetric Cases

The two experiments previously discussed in this chapter both assume that there are current layers along both of the original separators. It is natural to begin by studying a symmetric system but it could be argued that given the typical length scales of separators connecting nulls in the solar atmosphere, the current layers could not arise simultaneously. Hence this section will consider the asymmetric case where a current layer initially exists along one of the two separators. Once more the energy changes and reconnection rate will be studied, with the primary aim of identifying any differences with the symmetric case. It will also be interesting to observe whether the reconnection at the initial current layer causes any reconnection or current build-up at the second separator.

Three different asymmetric experiments will be considered here. The first case is the

same as the original double separator experiment, except that the flux ring at the $y > 0$ separator has been removed. In each of the three experiments, there is initially a single flux ring centred on the separator at $y = -1$ and the magnetic field is relaxed until the kinetic energy drops below 10^{-8} (relative to the initial total energy). In the second experiment, the initial plasma density is reduced from $\rho = 1$ to $\rho = 0.1$. The third case uses a larger flux ring with parameter values $p = q = 0.4$, $s = 0.5$ and $B_0 = 0.1$. As before, the reconnection process is triggered by introducing a non-uniform resistivity, $\eta = 0.01$, where the current exceeded the critical value. For these experiments, the critical value is taken to be one fifth of the maximum magnitude of the current density. The viscosity is reduced from the value used during the relaxation (by two orders of magnitude) to $\nu = 0.0001$.

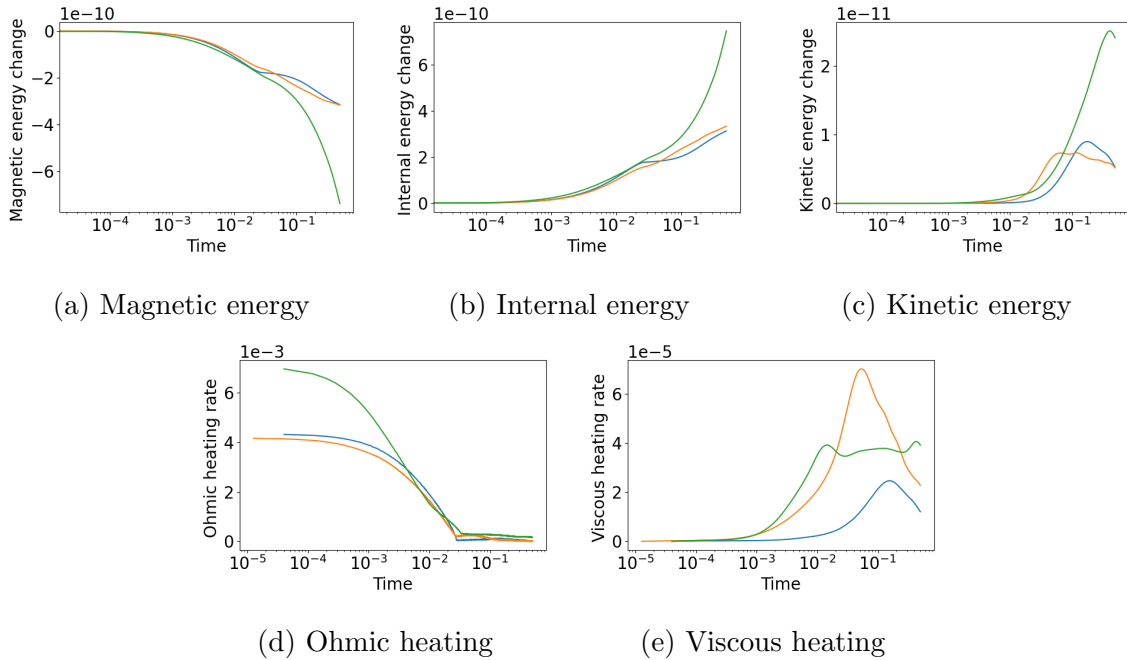


Figure 92: (a)-(c) Time and volume integrated energy changes for the asymmetric double separator reconnection, normalised by initial total energy. (d)-(e) Rates of heating. Blue: Original asymmetric experiment; yellow: low beta; green: large flux ring.

As in the symmetric case, there are two phases to the energy conversion. Before $t = 0.02$, the Ohmic heating is important in all three experiments but after this time, its magnitude is similar to the viscous heating. The viscous heating is greatest in the case

with the low plasma beta due to the higher flow speeds but this does not translate into a large energy change. Figure 92 shows that the experiment with the large flux ring converts the most magnetic energy. The significant energy conversion occurring beyond $t = 0.1$ is due to adiabatic effects, as there is a more widespread pressure gradient owing to the larger initial perturbation.

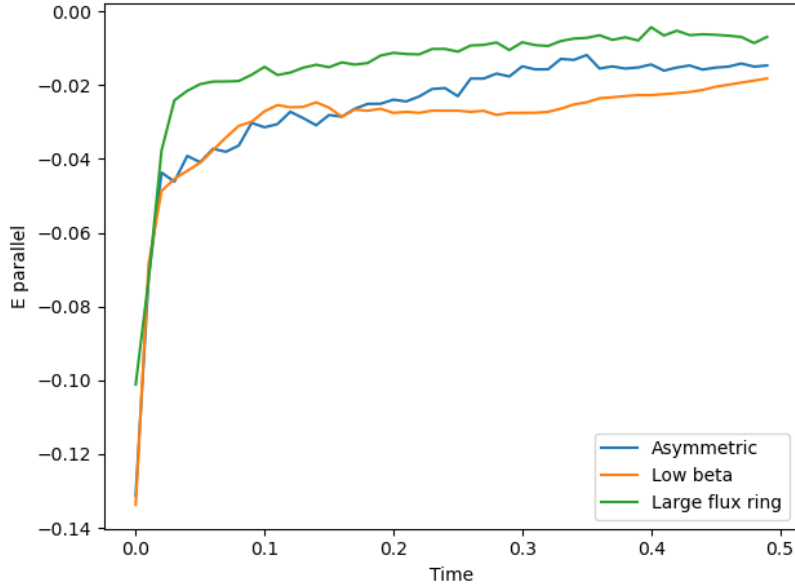


Figure 93: Time evolution of the minimum integrated E_{\parallel} along fieldlines passing through $z = 1$.

The time evolution of E_{\parallel} is similar for each of the three asymmetric experiments, as shown in figure 93. The super-critical current is rapidly dissipated at the start of the experiment and at later times the reconnection rate is almost steady. There is no impulsive behaviour because the choice of critical current is so low that the resistivity is unable to dissipate all of the super-critical current before the current layer rebuilds. The experiment with the large flux ring has a maximum current magnitude that is almost a factor of two less than the other experiments but the current layer spreads along a larger portion of the separator, meaning that the integrated E_{\parallel} is not always proportionally small. The low beta case has the strongest reconnection rate, since the lower plasma density allows for stronger flows, which replenish the current layers faster. Figure 93 does not show the spatial extent of the E_{\parallel} but it has been confirmed that this is mostly consistent with the original experiment. Of course, the double flux ring

case also had a patch of positive E_{\parallel} that is not matched here due to the lack of current surrounding the $y > 0$ separator.

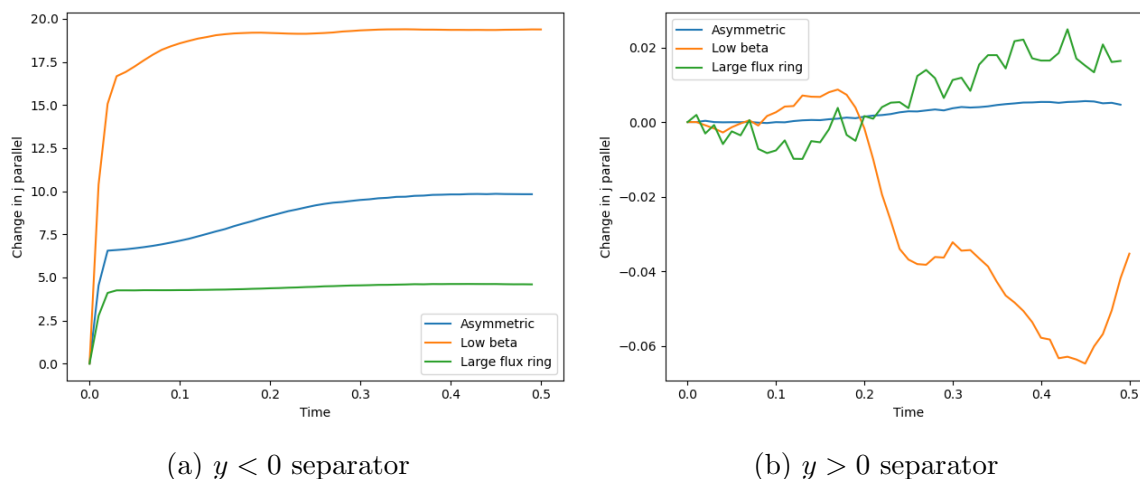


Figure 94: Time evolution of the integral of j_{\parallel} along the separators

Figure 94 shows the change in the integral of the parallel current density along both of the separators. The asymmetry between the two separators is very clear, as the change differs by three orders of magnitude in the original case. The parallel current increases significantly at the $y < 0$ separator because the direction of the current density is opposite to the magnetic field, so as its magnitude decreases, there is a positive change in the j_{\parallel} . The parallel current becomes steady in both cases beyond $t = 0.3$, indicating that the majority of the super-critical current in the separator current layer has been dissipated. There is no reconnection at the $y > 0$ separator because the current layer is mostly confined to $y < 0$. There is also little evidence of reconnection at $y < 0$ causing current build-up along the opposing separator.

4.9 Discussion

This chapter has studied the reconnection occurring in magnetic fields where a single pair of nulls is connected by more than one separator. A current density is introduced to the analytical magnetic field before the system is relaxed ideally to create separator current layers. The quasi-equilibrium field is then used in a reconnection experiment which makes use of a nonuniform resistivity that is non-zero where the current exceeds

a critical value. The main experiment uses a double separator configuration and flux rings are added to both separators with oppositely directed current.

The reconnection experiment has a number of similarities with that seen in Stevenson and Parnell (2015a). This is particularly true of the integrated quantities, namely the energy changes and the reconnection rate. The reconnection rate (and energy conversion) is highest at the start of the experiment. This period of fast reconnection expires quickly and is followed by impulsive behaviour, as the reconnection along the separator occurs in frequent bursts. During the fast reconnection, the free magnetic energy is converted directly to internal energy via Ohmic heating but the kinetic energy becomes more significant in the impulsive phase.

One must look closely at the parallel electric field to identify the differences with Stevenson and Parnell (2015a). In both experiments, the reconnection is localised about the separator in a current layer. However, the original experiment used a non-potential magnetic field with constant current, compared with a flux ring added smoothly to a potential field. Consequently, the current layer here is due to localised twist, rather than a large scale merging of the separatrix surfaces. This translates to a parallel electric field that does not extend along the separatrix surfaces and is localised around the centre of the separator. The differences between the experiments appear to be attributable to distinct approaches to the initial current density, rather than differing reconnection mechanics.

A second reconnection experiment was performed using a quasi-equilibrium field containing six separators. This initial condition was created by adding a flux ring to both the separators in the potential field as before, only using a stronger perturbation magnetic field. Although the presence of multiple separators in the main experiment did not appear to significantly alter the dynamics of the reconnection, the three separators on either side of the y -axis in this case were much closer together. This increased the likelihood of interaction between reconnecting separators.

The six separator experiment mirrored the double separator case in its energy conversion and reconnection rate. The energy changes differed by a factor of two because of the higher current but experienced a transition from fast to impulsive reconnection at a similar time. The parallel electric field showed interesting behaviour, as the central

separators on either side of the y -axis have a strong E_{\parallel} initially, while the other separators do not experience reconnection. As the experiment progresses, the magnetic field untwists and the outer separators move into the regions of E_{\parallel} before one of them annihilates with the central separator. The reconnection after the annihilation follows the double separator case, with the fast reconnection dissipating the excess current before the onset of impulsive reconnection.

A third reconnection experiment was completed, in which a flux ring was only added to one of the potential separators. The aim of this experiment was to investigate the effect of this asymmetry in the current distribution on the separator reconnection. The differences were not pronounced, as the energies once more showed similar qualitative behaviour to the original case, while the reconnection rate was almost indistinguishable except for minor differences in the impulsive phase. By plotting the magnitude of the current along both separators against time, it was clearly demonstrated that the reconnection at $y < 0$ did not have a noticeable effect on the separator at $y > 0$.

This work is the first attempt to study separator reconnection in a system containing multiply-connected null points. It has highlighted some interesting properties of the reconnection process, in particular the bifurcation of the six separator case and the movement of the separators into the high current regions. This conflicted with the expectations because the separators were assumed to have their own identity associated with a particular polarity of E_{\parallel} , while bifurcations are traditionally seen as violent events occurring over shorter time scales. One aspect of all these experiments which differs from previous work is the initially twisted separator configuration, which means that the reconnection acts to reduce the magnetic tension force. It is debatable whether this twisted configuration could be seen in nature as it would require localised vortical flows. However, in spite of the fundamentally different types of current layer, this work still bears strong similarities to Stevenson and Parnell (2015a). The appendix of this thesis will investigate whether radically different behaviour can be achieved by applying a boundary driver to the potential double separator field.

5 Conclusions

This thesis aimed to build on our understanding of magnetic reconnection at topological features of the magnetic field. It intended to study the reconnection process in detail and isolate its features, meaning it was necessary to use somewhat artificial models. The second chapter is a numerical study of 3D null point reconnection, which is a very active area of research, particularly in the solar flare community. The challenge they face is to determine whether topological features are significant in flaring activity, and if so to understand their exact role in the process. There are still fundamental questions regarding null point reconnection that need to be discussed, such as how it can occur in an undriven system, or at a null with a generic current distribution and what is the exact energy partition? Chapter 2 is concerned with the latter class of abstract questions, although it is hoped they could be applied to specific solar phenomena in the future. Chapters 3 and 4 deal with separator reconnection, which is relatively unexplored in the literature. In contrast to the null point reconnection studies, there are no driven numerical experiments beginning with a separator configuration. Again, there are not currently any examples of separator reconnection using a generic initial current. There is a fundamental question about how this type of reconnection relates to null point reconnection and whether they can occur in tandem. It is also not known whether reconnection in systems containing multiple nulls and separators is the sum of its parts or there are coupled events that trigger each other.

In chapter 2, reconnection for a specific class of null points has been studied, using the classification of linear nulls in Parnell et al. (1996). There were six experiments in all, three of which were spiral nulls and two were improper nulls (with one non-generic case). These experiments were grouped according to the value of the parameter b , since this had previously been shown to have a bearing on the nature of the reconnection. The method used in this chapter was to perform ideal relaxation of the initial field to achieve a quasi-equilibrium containing current layers, before proceeding with the reconnection experiment. The reconnection is commenced by specifying a critical current above which a constant resistivity is applied. The experiment is run for approximately two Alfvén wave crossing times, since every crossing introduces boundary effects to the reconnection. As previously mentioned, there has been little attention paid to undriven

reconnection and the idea of using a quasi-equilibrium initial condition has only previously been realised in Williams (2018). There are also few studies that attempt to differentiate between reconnection at spiral and improper nulls. The different types of null point were found to have a very similar resistive evolution both in a qualitative and quantitative sense. The reconnection rate at the improper nulls was slightly higher but owing to its impulsive nature there were instances where the spiral reconnection was stronger. In all cases, the reconnection was split into three phases, with the fast initial reconnection and the impulsive phase being separated by a brief pause. The free magnetic energy is converted mostly to internal energy with only 1% going to kinetic energy. This change is effected in part by Ohmic heating but also by adiabatic effects, with the dominant mechanism depending on the stage of the reconnection. In spite of the different methodology, the work supports the conclusion of Al-Hachami and Pontin (2010) regarding the parameter b , as the fieldlines in the $b = 2/3$ experiment have a larger integrated E_{\parallel} compared with $b = 1$ due to the larger current layer. However, there is little difference between the $b = 1$ and $b = 3/2$ cases, indicating that the dimensions of the current layer are the critical factor and not the parameter b .

There are several possible improvements to the null point reconnection model that could be considered. In the first place, although the current distribution is more generic than those previously seen in the literature, the initial current is still not completely generic. A realistic model would have to find a way to introduce a fully 3D current. The quasi-equilibrium initial condition for the reconnection is limited by the MHD code used during the relaxation. If the initial condition were closer to an equilibrium, it would be clear that any flows were generated by the reconnection. The relaxation uses viscous damping to reduce the plasma velocity but a more convincing numerical equilibrium could be accessed by a purely Lagrangian code. The small amount of kinetic energy achieved during the reconnection is not consistent with previous work, which generally states that the Ohmic heating is less important than the acceleration of the plasma. It would appear that this inconsistency is caused by the quasi-equilibrium initial condition. Having a quiescent initial state in a simulation of an explosive process implies that there is an instability that occurs at some stage during the relaxation of the field. This instability does not occur during the experiment but is rather assumed to have occurred in between the relaxation and reconnection experiments. An approach

that incorporated the instability in a self-consistent way would be more likely to exhibit explosive properties such as the acceleration of the plasma. Finally, it could be argued that finite difference methods are not well-suited to such a problem, where the key feature is the interface at the separatrix surface, which splits the domain in half. A numerical method that explicitly acknowledges these barriers would at least allow for calculations of the flux transfer between flux domains and the plasma flows across the fan. A stretched grid with a greater density of cells around the fan would be the simplest way to improve the numerical setup but it also might be possible to explore finite element or spectral methods.

Chapter 3 investigates separator reconnection using a magnetic field that is adapted from a 2D equilibrium. The 3D field is regarded as a perturbation to the Corrugated Sheet Pinch and is thus sufficiently ‘close’ to an equilibrium to be taken as the initial condition for reconnection. The reconnection is again initiated using a non-uniform resistivity, whose critical current is slightly larger than the initial maximum. This allows the current to redistribute itself prior to reconnection, as the separator is embedded in a global current sheet that initially lacks small scale structure. The resistive experiment was terminated once the energy changes showed the system was relaxing towards an equilibrium. This main experiment was then contrasted with an ideal relaxation, to determine the relative importance of the initial force imbalance and the current dissipation to the overall dynamics. There are very few analytical separator models but this case is unique in that the magnetic field components are finite. In addition, the fact that there is a global current sheet means that the separator is less isolated than other models, being part of a more global field. The idea of treating the separator field as a perturbation to a 2D equilibrium is also new and it facilitates a reconnection study that is not directly driven but also does not start with an equilibrium. A consequence of this approach is that the reconnection is somewhat difficult to distinguish from the relaxation which occurs in the ideal study. In both experiments, the plasma flows transport current from the boundaries to the topological features in a periodic manner. The current accumulates across the entire separatrix surfaces and the separator does not play a special role in the reconnection. However, the null points undergo bifurcation during the peak reconnection, creating great topological complexity for a short period of time. This is one of the first examples of topological change at a pre-existing separator

configuration during a reconnection experiment.

An exemplary separator reconnection experiment would use an unstable equilibrium field as its initial condition. Such a field is inaccessible by analytical methods and current layers obtained by relaxation appear to be quite stable in that they favour a more diffusive type of reconnection. This experiment did produce more dynamic reconnection but at the expense of the initial equilibrium, which is desirable in a controlled experiment. The flows that carry magnetic flux towards the topological features are not realistic since they result from the force imbalance introduced when extending the field to three dimensions. A more realistic scenario could be achieved by driving a potential separator field, although provisional studies suggest that it is difficult for the current to penetrate the central flux domain when the boundary is disturbed. Another issue with the results presented in chapter 3 is that the global current sheet does not diffuse quickly and strongly affects the integrated quantities throughout the experiment. An obvious way to overcome this problem would be to use a different magnetic field where the initial current is not strong at the boundaries. The boundary currents are especially problematic in section 3.7, where the system has relaxed to a separator current layer whose magnitude is less than the boundary accumulations. When the resistivity is switched on, the separator current instantly dissipates and the subsequent energy changes are due to steady Ohmic heating from the boundary. The line-tied boundary conditions are largely responsible for the boundary currents. However, there are no clear alternatives because of the need to preserve the magnetic skeleton. It might be possible to cut out the central portion of the box containing the current layer and complete the resistive experiment over a smaller grid, although this is not supported by Lare3d.

Chapter 4 presents a model for separator reconnection occurring at multiply-connected null points. The analytical potential separator field is derived using an expansion method similar to that of Stevenson et al. (2015), with the orientation of the two null points being fixed so that their separatrix surfaces intersect along two separators to form a ring. This magnetic field is then perturbed by the addition of localised flux rings located at the mid-points of the separators. Ideal relaxation is performed so that the current concentrations associated with the flux rings can spread along the separators, while the field approaches a quasi-equilibrium. The resulting field is taken

as the initial condition for the reconnection experiment, using a non-uniform resistivity so that the diffusion regions are confined to the central part of the separators. The novel aspects of this experiment are the complicated initial topology and the use of flux rings to perturb the potential field. The experiment converts magnetic energy through a combination of Ohmic and adiabatic heating. The maximum kinetic energy is only 1% of the net energy transfer and the flows remain mostly localised, except for the low amplitude wave passing through the surrounding plasma. The reconnection rate consists of distinct phases as in chapter 2, which suggests that this time evolution is linked to the quasi-equilibrium starting point. In the case with six separators, the reconnection acts to untwist the separatrix surfaces, causing a pair of separators to annihilate on either side of the y -axis. The asymmetric experiment reveals the lack of interaction between neighbouring separators, as reconnection at one current layer does not lead to significant current build-up elsewhere.

The differences between this multiple separator experiment and Stevenson and Parnell (2015a) are surprisingly subtle. It generally seems that the reconnection in this experiment is more localised than before because of the fact that each flux ring only perturbs a small volume. Increasing the length of the flux ring might increase the similarity between the experiments but the reconnection resulting from quasi-equilibria is still characteristically diffusive. The fact that the effects of this reconnection are not widespread precludes any sympathetic behaviour between the separators. One possible way to change this is to attempt a low beta experiment. This can be challenging in a magnetic field containing null points because numerical reconnection can lead to topological change in a supposedly ideal plasma. It might be possible to use a non-uniform density that is highest at the nulls to attempt to control the rate of numerical diffusion. It is possible that increasing the grid resolution local to the separator would lead to more dynamic reconnection if there would be more small scale structure in the current layer. However, the layer does not appear to relax towards a singularity, maintaining a finite radius around the separator. Because it does not have the same extreme aspect ratio seen in the current layers in null point reconnection, one would not expect it to be susceptible to the tearing instability. If there is no instability, this raises questions about whether spontaneous reconnection can occur in the manner suggested by this experiment. For this reason, the possibility of driven separator reconnection should

again be considered.

6 Appendix

This section will study driven reconnection at the double separator field described in Chapter 4. It is necessary to study the MHD evolution with more than one numerical approach in order to distinguish the properties of the reconnection that are intrinsic to the magnetic field. Boundary driving is the most common method of studying 3D null point reconnection (as practised by for example, Pontin et al. (2007), Galsgaard and Pontin (2011b), Wyper and Pontin (2014b)). However, there are few separator reconnection studies employing a driver (Galsgaard et al. (2000b) and Haynes et al. (2007)). The presence of multiple nulls in the simulation box presents additional complications to a driven numerical study, as it is not obvious where the driving should be applied.

In null point reconnection studies, current is introduced to a potential field by advecting the spine footpoints in opposite directions. The driving initiates the collapse of the null point in the direction of the eigenvector associated with the larger eigenvalue. Galsgaard and Pontin (2011a) showed that this will happen for a range of different driving directions, except in the case where the driving is perpendicular to the eigenvector. A current layer typically forms along the fan plane at the location of the null point.

There is no separator connecting the two null points initially in Haynes et al. (2007). Since the nulls are located at the boundaries, the driver causes them to move across the length of the box. As they are driven past each other, the separatrix surfaces intersect and bifurcations occur, leading to a maximum of five separators connecting the nulls. Galsgaard et al. (2000b) use a constant- α force-free field with eight null points connected by separators. The driving is imposed at a single boundary and introduces a shear flow to the separatrix surfaces of both null points. Focusing on one of the null-null pairs, a current layer is formed along the separator with an orientation of ± 45 degrees relative to the spine. The previous separator reconnection works did not apply driving to a potential field and also did not explore driving at the spine footpoints. These are the defining characteristics of the driven separator reconnection experiment discussed in this section.

The numerical experiment was carried out using Lare3D as in the previous chapters of this thesis. The initial magnetic field is the potential field from Chapter 4 equation

(71), which contains two null points located at $(0, 0, 0)$ and $(0, 0, L)$ connected by two separators. Unless otherwise stated, the magnetic field parameters used in this chapter are $L = 2$, $a = 1$, $b = -1$, $c = 0.5$, $d = 1$, $e = 0$ and $f = -1$. The numerical domain covers $-3 < x, y < 3$ and $-2 < z < 4$. The plasma density is initially uniform ($\rho = 1$) and the internal energy ($\epsilon = 1.5$) is chosen so that the plasma pressure is $p = 1$. The plasma velocity is initially zero everywhere except at the driven boundaries. For the main experiment, the resistivity has a value of $\eta = 0.001$ and the background viscosity is $\nu = 0.001$.

The boundary conditions are line-tied with the driving velocity having the same form as that used in Galsgaard and Pontin (2011b):

$$v_z = v_f (\tanh((y_d - y_0)/y_h) - \tanh((y_d + y_0)/y_h)) (\tanh((z_d - z_0)/z_h) - \tanh((z_d + z_0)/z_h)) \quad (88)$$

$v_f = v_d \tanh(t/t_d)$ is a function specifying the time dependence of the driving velocity, which has a peak value of v_d . The form of the driver in (88) assumes that the driving is applied at the x -boundaries. In this case, $y_d = y - y_c$ and $z_d = z - z_c$ are the coordinates relative to the centre of the driving patch (y_c, z_c) . y_0 and z_0 are the lengths separating the peak velocity from the point with half its magnitude and y_h and z_h are the half-widths of the hyperbolic tangent functions.

A logical starting point is to apply the driver to the spine footpoints in the tradition of the null point reconnection studies previously mentioned. The velocity is only applied to one of the footpoints at either boundary in order to limit the mass drainage occurring due to the compressible flows.

The magnitude of the current density is highest at the null points, as shown by figure 95(a). This is not surprising, as it is consistent with the null point reconnection results employing similar driving profiles. However, this figure is not in agreement with the work in chapter 4 (figure 71), which suggested that the current would accumulate away from the nulls in the double separator system. Clearly it has spread across the entire separator ring, although the magnitude at the widest part ($y = \pm 0.73$) is weaker than at both the nulls and the neighbouring separatrix surface. The asymmetry in the current distribution along the separatrix surfaces in figure 95(b) is related to the fact that only one of the spines is driven at either boundary, although this is not evident in planes of

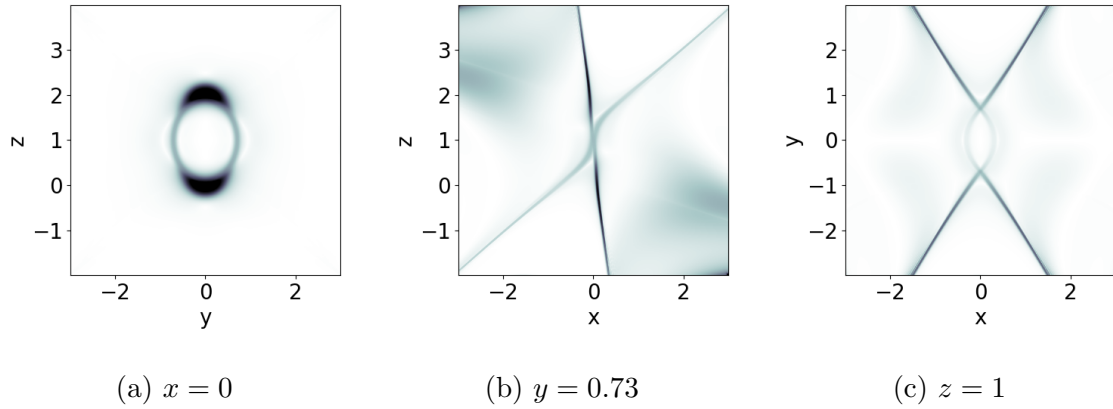


Figure 95: Magnitude of the current density

constant z .

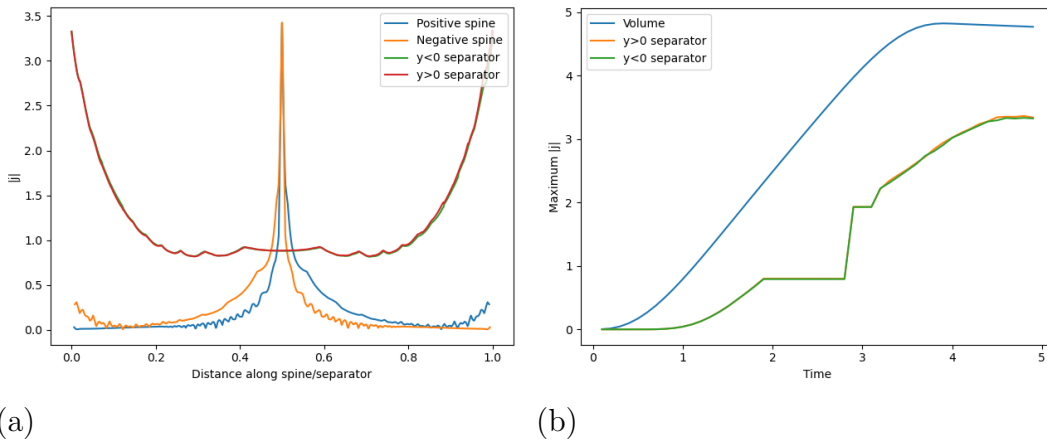


Figure 96: Spatial and temporal variation of the maximum current. Left: Magnitude of j along the spines and separators. The lengths of these fieldlines have been normalised to one. Right: Time evolution of the maximum $|j|$ in the domain and along the separators.

Figure 96(a) shows the magnitude of the current density along the topological features of the field. The strongest current is found at the two null points, which are at the ends of the two separators and the centres of the spines. The weakest current at the separator is still stronger than at 95% of the spine lines. This means that the spine is not a preferred location for current accumulation, as it was already shown in figure 95 that the weaker separator currents are small compared with those at the separatrix surfaces (away from the spines). This is somewhat unexpected, since the driving is

focused on the spine footpoints and should lead to their deformation. The asymmetry in the current along the two spines is accounted for by the fact that they are driven from opposite ends.

The time evolution of the maximum current (figure 96(b)) follows that of the driving velocity, growing almost linearly until the driving is switched off at $t = 4$. After this time, the system slowly relaxes and the current is redistributed across the domain, leading to a slight reduction in the maximum. The peak current is in fact located at the boundaries but this numerical error can be improved by varying the driver parameters. The magnitude of the current density at the nulls is at least 60% of the numerical maximum and the difference between these values could be reduced if the system is allowed to relax further. Another issue that should be noted is that the null detection fails at $2 < t < 3$. The MSAT software assumes that the magnetic field is trilinear in the vicinity of the nulls, which is unlikely to be valid when the nulls are embedded in current layers.

The potential field parameters were varied in order to determine whether the geometry of the magnetic field is important to the reconnection. Figure 97 shows that regardless of the choice of parameters, the current will accumulate at the null points. However the extent of the current along the separators seems to vary with the field geometry. For instance, the field with $c = 1.5$ has two long current layers that cover more than half of the length of the separators. By contrast for $c = 0.5$ (figure 95), the narrow separator ring has a more localised current distribution. In the $b = -3$ case, the strongest current is again localised at the nulls but there is weaker current extending to the z -boundaries. Of the seven experiments, this example most resembles the magnetic field from chapter 4, where the B_z component is generally dominant. Although the driving is not effective for this case, the addition of a flux ring directed parallel to the z -axis results in an equilibrium current layer. The remaining experiments develop current layers when subjected to driving but cannot relax to an equilibrium when the flux rings are applied.

The maximum current density (figure 98) in the different potential field cases is very similar, with the exception of $b = -3$. As before, the impulsive driving is evident in the time variation of the current, which becomes almost steady after $t = 4$. The

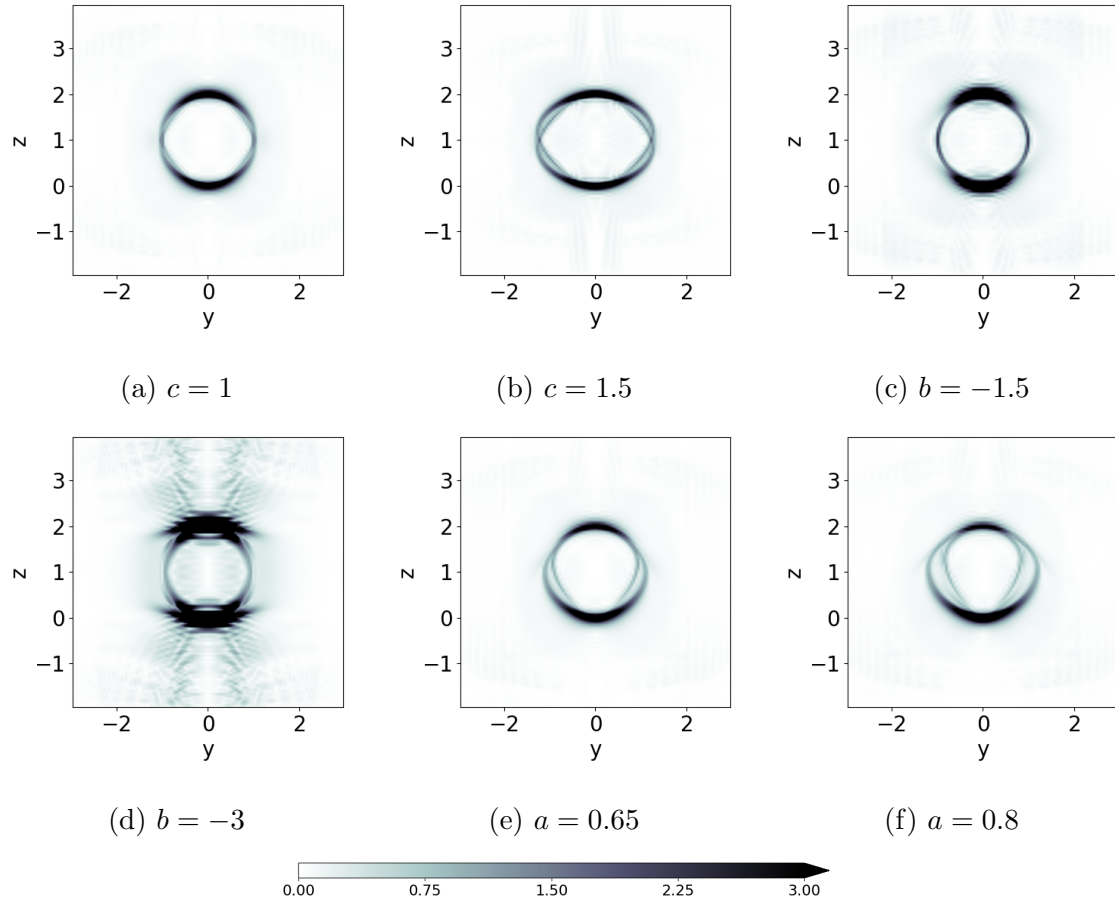


Figure 97: Magnitude of the current density at $t = 8$ in the $x = 0$ plane for different potential field parameters. The parameters are chosen to be $a = 0.5$, $b = -1$, $c = 1$, $d = 1$, $f = -1$ and $L = 2$ (with the exception of the parameter specified under each cut).

minor differences in the magnitude of the current are probably related to the strength of the magnetic field. The parallel electric field along the separator is greater in the $c = 1.5$ experiment than for $a = 0.8$, in spite of the latter having a larger maximum current. Of course, the fact that the E_{\parallel} is integrated along the separator means that it will not necessarily agree with the maximum current values. However it is clear that these experiments are similar in a quantitative sense, as well as having similar current distributions according to figure 97.

Figure 99 shows how the magnitude of the current density and the parallel electric

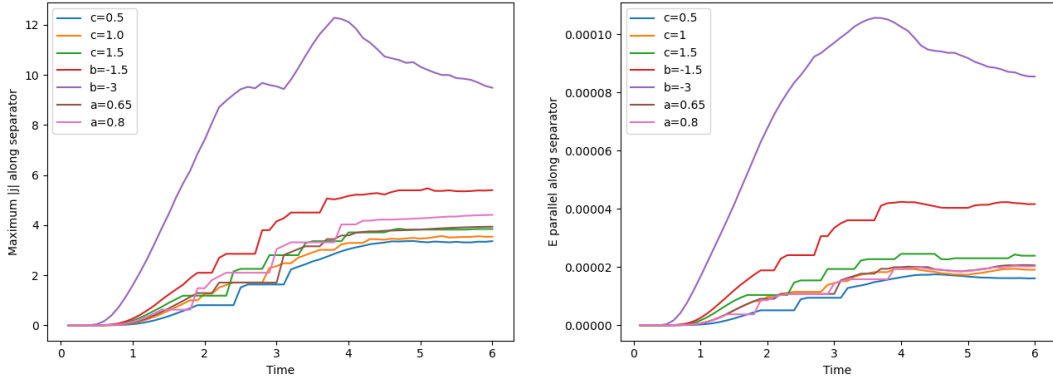


Figure 98: Time variation of the current density (left) and parallel electric field (right). The current density is the maximum value along the $y > 0$ separator and the E_{\parallel} is integrated along the $y > 0$ separator.

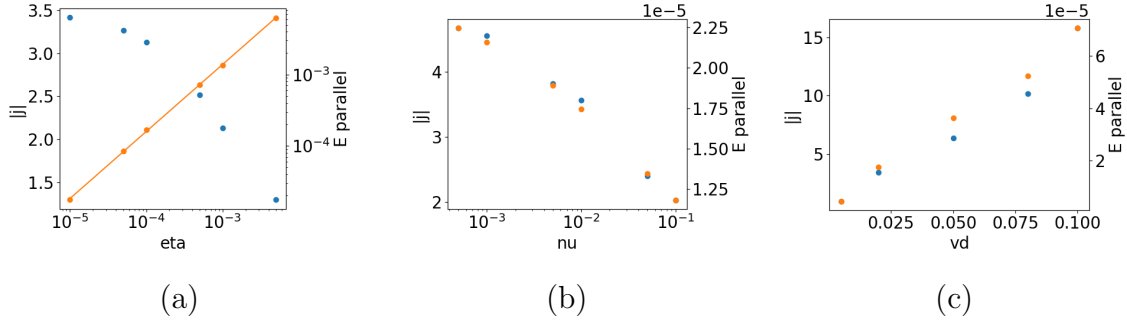


Figure 99: Variation of peak $|j|$ (blue) and separator E_{\parallel} (orange) with: a) resistivity, b) viscosity, c) driving velocity

field vary with certain parameters. The peak current does not vary significantly as the resistivity and viscosity are changed by three orders of magnitude. As a result, the E_{\parallel} (calculated as the resistivity multiplied by the integral of j_{\parallel} along the separator) is directly proportional to the resistivity. This does not agree with the scaling law $E_{\parallel} \sim \eta^{0.65}$ found in the null point reconnection study of Galsgaard and Pontin (2011b). In figure 99 (b) and (c), the parallel electric field is proportional to the current as the resistivity is held constant. By increasing the magnitude of the driving velocity, one can achieve a significant increase in the magnitude of the current density. However, there are numerical disadvantages to a larger driving velocity, as the current accumulations at the boundary become more prevalent.

These preliminary results show that it is possible for the null points to play a role in reconnection at a separator configuration. Chapter 4 indicated that the nulls do not play a role in separator reconnection, which could be attributed to the location of the flux rings. The null points are not merely involved in the reconnection process in this section but rather are the locations where the current is strongest. This is consistent with null point reconnection studies, which use a similar type of driving. It could be suggested that this experiment is an example of null point reconnection in a separator configuration but other types of driving should be explored before making a statement of that kind.

References

- Al-Hachami, A. K. and Pontin, D. I. (2010). Magnetic reconnection at 3D null points: effect of magnetic field asymmetry. *Astronomy and Astrophysics*, 512:A84.
- Antiochos, S. K., DeVore, C. R., and Klimchuk, J. A. (1999). A Model for Solar Coronal Mass Ejections. *Astrophysical Journal*, 510(1):485–493.
- Antiochos, S. K., Mikić, Z., Titov, V. S., Lionello, R., and Linker, J. A. (2011). A Model for the Sources of the Slow Solar Wind. *Astrophysical Journal*, 731(2):112.
- Arber, T. D., Longbottom, A. W., Gerrard, C. L., and Milne, A. M. (2001). A Staggered Grid, Lagrangian-Eulerian Remap Code for 3-D MHD Simulations. *Journal of Computational Physics*, 171(1):151–181.
- Axford, W. I. (1984). Magnetic field reconnection. *Washington DC American Geophysical Union Geophysical Monograph Series*, 30:1–8.
- Baumann, G., Galsgaard, K., and Nordlund, Å. (2013). 3D Solar Null Point Reconnection MHD Simulations. *Solar Physics*, 284(2):467–487.
- Benz, A. O. (2017). Flare Observations. *Living Reviews in Solar Physics*, 14(1):2.
- Biskamp, D. (1986). Magnetic reconnection via current sheets. *Physics of Fluids*, 29(5):1520–1531.
- Biskamp, D. (2000). *Magnetic Reconnection in Plasmas*, volume 3. Cambridge University Press.
- Burch, J. L., Moore, T. E., Torbert, R. B., and Giles, B. L. (2016). Magnetospheric Multiscale Overview and Science Objectives. *Space Science Reviews*, 199(1-4):5–21.
- Buzulukova, N., Dorelli, J., and Glocer, A. (2017). Separator Reconnection at Earth’s Dayside Magnetopause: MMS Observations Compared to Global Simulations. *arXiv e-prints*, page arXiv:1708.01320.
- Caramana, E. J., Shashkov, M. J., and Whalen, P. P. (1998). Formulations of Artificial Viscosity for Multi-dimensional Shock Wave Computations. *Journal of Computational Physics*, 144(1):70–97.

- Carmichael, H. (1964). *A Process for Flares*, volume 50, page 451. NASA Special Publication.
- Chandra, R., Schmieder, B., Mandrini, C. H., Démoulin, P., Parlat, E., Török, T., and Uddin, W. (2011). Homologous Flares and Magnetic Field Topology in Active Region NOAA 10501 on 20 November 2003. *Solar Physics*, 269(1):83–104.
- Charbonneau, P. (2020). Dynamo models of the solar cycle. *Living Reviews in Solar Physics*, 17(1):4.
- Close, R. M., Parnell, C. E., Longcope, D. W., and Priest, E. R. (2004). Recycling of the Solar Corona’s Magnetic Field. *Astrophysical Journal, Letters*, 612(1):L81–L84.
- Cohen, R. S., Spitzer, L., and Routly, P. M. (1950). The Electrical Conductivity of an Ionized Gas. *Physical Review*, 80(2):230–238.
- Cook, G. R., Mackay, D. H., and Nandy, D. (2009). Solar Cycle Variations of Coronal Null Points: Implications for the Magnetic Breakout Model of Coronal Mass Ejections. *Astrophysical Journal*, 704(2):1021–1035.
- Cowley, S. W. H. (1973). A qualitative study of the reconnection between the Earth’s magnetic field and an interplanetary field of arbitrary orientation. *Radio Science*, 8(11):903–913.
- Dorelli, J. C., Bhattacharjee, A., and Raeder, J. (2007). Separator reconnection at Earth’s dayside magnetopause under generic northward interplanetary magnetic field conditions. *Journal of Geophysical Research (Space Physics)*, 112(A2):A02202.
- Edwards, S. J. and Parnell, C. E. (2015). Null Point Distribution in Global Coronal Potential Field Extrapolations. *Solar Physics*, 290(7):2055–2076.
- Escoubet, C. P., Fehringer, M., and Goldstein, M. (2001). Introduction The Cluster mission. *Annales Geophysicae*, 19:1197–1200.
- Evans, C. R. and Hawley, J. F. (1988). Simulation of Magnetohydrodynamic Flows: A Constrained Transport Model. *Astrophysical Journal*, 332:659.
- Filippov, B. (1999). Observation of a 3d Magnetic Null Point in the Solar Corona. *Solar Physics*, 185(2):297–309.

- Fletcher, L., Dennis, B. R., Hudson, H. S., Krucker, S., Phillips, K., Veronig, A., Battaglia, M., Bone, L., Caspi, A., Chen, Q., Gallagher, P., Grigis, P. T., Ji, H., Liu, W., Milligan, R. O., and Temmer, M. (2011). An Observational Overview of Solar Flares. *Space Science Reviews*, 159(1-4):19–106.
- Freed, M. S., Longcope, D. W., and McKenzie, D. E. (2015). Three-Year Global Survey of Coronal Null Points from Potential-Field-Source-Surface (PFSS) Modeling and Solar Dynamics Observatory (SDO) Observations. *Solar Physics*, 290(2):467–490.
- Fuentes-Fernández, J. and Parnell, C. E. (2013). Magnetohydrodynamics dynamical relaxation of coronal magnetic fields. IV. 3D tilted nulls. *Astronomy and Astrophysics*, 554:A145.
- Fuentes-Fernández, J., Parnell, C. E., Hood, A. W., Priest, E. R., and Longcope, D. W. (2012a). Consequences of spontaneous reconnection at a two-dimensional non-force-free current layer. *Physics of Plasmas*, 19(2):022901–022901.
- Fuentes-Fernández, J., Parnell, C. E., and Priest, E. R. (2012b). The onset of impulsive bursty reconnection at a two-dimensional current layer. *Physics of Plasmas*, 19(7):072901.
- Fukao, S., Ugai, M., and Tsuda, T. (1975). Topological study of magnetic field near a neutral point. *Report of Ionosphere and Space Research in Japan*, 29(3):133–139.
- Galsgaard, K. and Nordlund, Å. (1997). Heating and activity of the solar corona. 3. Dynamics of a low beta plasma with three-dimensional null points. *Journal of Geophysics Research*, 102(A1):231–248.
- Galsgaard, K., Parnell, C. E., and Blaizot, J. (2000a). Elementary heating events - Magnetic interactions between two flux sources. *Astronomy and Astrophysics*, 362:395–405.
- Galsgaard, K. and Pontin, D. I. (2011a). Current accumulation at an asymmetric 3D null point caused by generic shearing motions. *Astronomy and Astrophysics*, 534:A2.
- Galsgaard, K. and Pontin, D. I. (2011b). Steady state reconnection at a single 3D magnetic null point. *Astronomy and Astrophysics*, 529:A20.

- Galsgaard, K., Priest, E. R., and Nordlund, Å. (2000b). Three-dimensional Separator Reconnection - How Does It Occur? *Solar Physics*, 193:1–16.
- Glocer, A., Dorelli, J., Toth, G., Komar, C. M., and Cassak, P. A. (2016). Separator reconnection at the magnetopause for predominantly northward and southward IMF: Techniques and results. *Journal of Geophysical Research (Space Physics)*, 121(1):140–156.
- Gopalswamy, N., Shimojo, M., Lu, W., Yashiro, S., Shibasaki, K., and Howard, R. A. (2003). Prominence Eruptions and Coronal Mass Ejection: A Statistical Study Using Microwave Observations. *Astrophysical Journal*, 586(1):562–578.
- Guo, R., Pu, Z., Xiao, C., Wang, X., Fu, S., Xie, L., Zong, Q., He, J., Yao, Z., Zhong, J., and Li, J. (2013). Separator reconnection with antiparallel/component features observed in magnetotail plasmas. *Journal of Geophysical Research (Space Physics)*, 118(10):6116–6126.
- Haynes, A. L. and Parnell, C. E. (2007). A trilinear method for finding null points in a three-dimensional vector space. *Physics of Plasmas*, 14(8):082107–082107.
- Haynes, A. L., Parnell, C. E., Galsgaard, K., and Priest, E. R. (2007). Magnetohydrodynamic evolution of magnetic skeletons. *Proceedings of the Royal Society of London Series A*, 463.
- Hesse, M. and Birn, J. (1993). Parallel electric fields as acceleration mechanisms in three-dimensional magnetic reconnection. *Advances in Space Research*, 13(4):249–252.
- Hesse, M. and Schindler, K. (1988). A theoretical foundation of general magnetic reconnection. *Journal of Geophysical Research*, 93(A6):5559–5567.
- Hirayama, T. (1974). Theoretical Model of Flares and Prominences. I: Evaporating Flare Model. *Solar Physics*, 34(2):323–338.
- Janvier, M. (2017). Three-dimensional magnetic reconnection and its application to solar flares. *Journal of Plasma Physics*, 83(1):535830101.

- Klimchuk, J. A. (2006). On Solving the Coronal Heating Problem. *Solar Physics*, 234(1):41–77.
- Kopp, R. A. and Pneuman, G. W. (1976). Magnetic reconnection in the corona and the loop prominence phenomenon. *Solar Physics*, 50(1):85–98.
- Lang, K. R. (2006). *Sun, Earth and Sky*. Springer, New York.
- Lau, Y.-T. and Finn, J. M. (1990). Three-dimensional Kinematic Reconnection in the Presence of Field Nulls and Closed Field Lines. *Astrophysical Journal*, 350:672.
- Longcope, D. W. (2001). Separator current sheets: Generic features in minimum-energy magnetic fields subject to flux constraints. *Physics of Plasmas*, 8(12):5277–5290.
- Longcope, D. W. and Cowley, S. C. (1996). Current sheet formation along three-dimensional magnetic separators. *Physics of Plasmas*, 3(8):2885–2897.
- Longcope, D. W. and Priest, E. R. (2007). Fast magnetosonic waves launched by transient, current sheet reconnection. *Physics of Plasmas*, 14(12):122905.
- Masson, S., Pariat, E., Aulanier, G., and Schrijver, C. J. (2009). The Nature of Flare Ribbons in Coronal Null-Point Topology. *Astrophysical Journal*, 700(1):559–578.
- Masuda, S., Kosugi, T., Hara, H., Tsuneta, S., and Ogawara, Y. (1994). A loop-top hard X-ray source in a compact solar flare as evidence for magnetic reconnection. *Nature*, 371(6497):495–497.
- Murphy, N. A., Parnell, C. E., and Haynes, A. L. (2015). The appearance, motion, and disappearance of three-dimensional magnetic null points. *Physics of Plasmas*, 22(10):102117.
- Pariat, E., Antiochos, S. K., and DeVore, C. R. (2009). A Model for Solar Polar Jets. *Astrophysical Journal*, 691(1):61–74.
- Parker, E. N. (1957). Sweet’s Mechanism for Merging Magnetic Fields in Conducting Fluids. *Journal of Geophysical Research*, 62(4):509–520.

- Parnell, C. E., Haynes, A. L., and Galsgaard, K. (2010). Structure of magnetic separators and separator reconnection. *Journal of Geophysical Research (Space Physics)*, 115(A2):A02102.
- Parnell, C. E., Smith, J. M., Neukirch, T., and Priest, E. R. (1996). The structure of three-dimensional magnetic neutral points. *Physics of Plasmas*, 3(3):759–770.
- Petrie, G. J. D. (2015). Solar Magnetism in the Polar Regions. *Living Reviews in Solar Physics*, 12(1):5.
- Petschek, H. E. (1964). Magnetic Field Annihilation. In *The Physics of Solar Flares, Proceedings of the AAS-NASA Symposium held 28-30 October, 1963 at the Goddard Space Flight Center, Greenbelt, MD. Edited by Wilmot N. Hess. Washington, DC: National Aeronautics and Space Administration, Science and Technical Information Division, 1964., p.425*, volume 50, page 425.
- Platten, S. J., Parnell, C. E., Haynes, A. L., Priest, E. R., and Mackay, D. H. (2014). The solar cycle variation of topological structures in the global solar corona. *Astronomy and Astrophysics*, 565:A44.
- Pontin, D. I., Bhattacharjee, A., and Galsgaard, K. (2007). Current sheet formation and nonideal behavior at three-dimensional magnetic null points. *Physics of Plasmas*, 14(5):052106–052106.
- Pontin, D. I. and Craig, I. J. D. (2006). Dynamic Three-dimensional Reconnection in a Separator Geometry with Two Null Points. *Astrophysical Journal*, 642(1):568–578.
- Pontin, D. I. and Galsgaard, K. (2007). Current amplification and magnetic reconnection at a three-dimensional null point: Physical characteristics. *Journal of Geophysical Research (Space Physics)*, 112:A03103.
- Pontin, D. I., Hornig, G., and Priest, E. R. (2004). Kinematic reconnection at a magnetic null point: spine-aligned current. *Geophysical and Astrophysical Fluid Dynamics*, 98(5):407–428.
- Pontin, D. I., Hornig, G., and Priest, E. R. (2005). Kinematic reconnection at a magnetic null point: fan-aligned current. *Geophysical and Astrophysical Fluid Dynamics*, 99:77–93.

- Priest, E. (2014). *Magnetohydrodynamics of the Sun*. Cambridge University Press.
- Priest, E. and Forbes, T. (2000). *Magnetic Reconnection*. Cambridge University Press.
- Priest, E. R. and Démoulin, P. (1995). Three-dimensional magnetic reconnection without null points. 1. Basic theory of magnetic flipping. *Journal of Geophysics Research*, 100(A12):23443–23464.
- Priest, E. R. and Forbes, T. G. (2002). The magnetic nature of solar flares. *Astronomy and Astrophysics Reviews*, 10(4):313–377.
- Priest, E. R. and Pontin, D. I. (2009). Three-dimensional null point reconnection regimes. *Physics of Plasmas*, 16(12):122101–122101.
- Raouafi, N. E., Patsourakos, S., Parlat, E., Young, P. R., Sterling, A. C., Savcheva, A., Shimojo, M., Moreno-Insertis, F., DeVore, C. R., Archontis, V., Török, T., Mason, H., Curdt, W., Meyer, K., Dalmasse, K., and Matsui, Y. (2016). Solar Coronal Jets: Observations, Theory, and Modeling. *Space Science Reviews*, 201(1-4):1–53.
- Reale, F. (2014). Coronal Loops: Observations and Modeling of Confined Plasma. *Living Reviews in Solar Physics*, 11(1):4.
- Régnier, S., Parnell, C. E., and Haynes, A. L. (2008). A new view of quiet-Sun topology from Hinode/SOT. *Astronomy and Astrophysics*, 484(3):L47–L50.
- Reid, H. A. S., Vilmer, N., Aulanier, G., and Parlat, E. (2012). X-ray and ultraviolet investigation into the magnetic connectivity of a solar flare. *Astronomy and Astrophysics*, 547:A52.
- Rincon, F. and Rieutord, M. (2018). The Sun’s supergranulation. *Living Reviews in Solar Physics*, 15(1):6.
- Robbrecht, E., Patsourakos, S., and Vourlidas, A. (2009). No Trace Left Behind: STEREO Observation of a Coronal Mass Ejection Without Low Coronal Signatures. *Astrophysical Journal*, 701(1):283–291.
- Schindler, K. (2006). *Physics of Space Plasma Activity*. Cambridge University Press.

- Schindler, K., Hesse, M., and Birn, J. (1988). General magnetic reconnection, parallel electric fields, and helicity. *Journal of Geophysics Research*, 93(A6):5547–5557.
- Shibata, K. and Magara, T. (2011). Solar Flares: Magnetohydrodynamic Processes. *Living Reviews in Solar Physics*, 8(1):6.
- Shibata, K., Masuda, S., Shimojo, M., Hara, H., Yokoyama, T., Tsuneta, S., Kosugi, T., and Ogawara, Y. (1995). Hot-Plasma Ejections Associated with Compact-Loop Solar Flares. *Astrophysical Journal, Letters*, 451:L83.
- Stevenson, J. E. H. and Parnell, C. E. (2015a). Spontaneous reconnection at a separator current layer: 1. Nature of the reconnection. *Journal of Geophysical Research (Space Physics)*, 120(A9):10.
- Stevenson, J. E. H. and Parnell, C. E. (2015b). Spontaneous reconnection at a separator current layer: 2. Nature of the waves and flows. *Journal of Geophysical Research (Space Physics)*, 120(12):10,353–10,369.
- Stevenson, J. E. H., Parnell, C. E., Priest, E. R., and Haynes, A. L. (2015). The nature of separator current layers in MHS equilibria. I. Current parallel to the separator. *Astronomy and Astrophysics*, 573:A44.
- Stix, M. (2004). *The sun : an introduction*. Springer, Berlin.
- Sturrock, P. A. (1966). Model of the High-Energy Phase of Solar Flares. *Nature*, 211(5050):695–697.
- Sun, J. Q., Cheng, X., Guo, Y., Ding, M. D., and Li, Y. (2014). Dynamic Evolution of an X-shaped Structure above a Trans-equatorial Quadrupole Solar Active Region Group. *Astrophysical Journal, Letters*, 787(2):L27.
- Sweet, P. A. (1958). The Neutral Point Theory of Solar Flares. In Lehnert, B., editor, *Electromagnetic Phenomena in Cosmical Physics*, volume 6, page 123.
- Thurgood, J. O., Pontin, D. I., and McLaughlin, J. A. (2018). Implosive Collapse about Magnetic Null Points: A Quantitative Comparison between 2D and 3D Nulls. *Astrophysical Journal*, 855(1):50.

- Tsuneta, S. (1996). Structure and Dynamics of Magnetic Reconnection in a Solar Flare. *Astrophysical Journal*, 456:840.
- Uzdensky, D. A. and Kulsrud, R. M. (2000). Two-dimensional numerical simulation of the resistive reconnection layer. *Physics of Plasmas*, 7(10):4018–4030.
- Vasyliunas, V. M. (1975). Theoretical models of magnetic field line merging, 1. *Reviews of Geophysics and Space Physics*, 13:303–336.
- Williams, B. M. (2018). *The Dynamic Topology of the Solar Corona: Mapping the Sun’s Three Dimensional Magnetic Skeleton*. PhD thesis, University of St. Andrews.
- Wilmot-Smith, A. L. and Hornig, G. (2011). A Time-dependent Model for Magnetic Reconnection in the Presence of a Separator. *Astrophys. J.*, 740:89.
- Wyper, P. F. and Pontin, D. I. (2014a). Dynamic topology and flux rope evolution during non-linear tearing of 3D null point current sheets. *Physics of Plasmas*, 21(10):102102.
- Wyper, P. F. and Pontin, D. I. (2014b). Non-linear tearing of 3D null point current sheets. *Physics of Plasmas*, 21(8):082114.
- Xiao, C. J., Wang, X. G., Pu, Z. Y., Zhao, H., Wang, J. X., Ma, Z. W., Fu, S. Y., Kivelson, M. G., Liu, Z. X., Zong, Q. G., Glassmeier, K. H., Balogh, A., Korth, A., Reme, H., and Escoubet, C. P. (2006). In situ evidence for the structure of the magnetic null in a 3D reconnection event in the Earth’s magnetotail. *Nature Physics*, 2(7):478–483.
- Yamada, M., Kulsrud, R., and Ji, H. (2010). Magnetic reconnection. *Reviews of Modern Physics*, 82(1):603–664.
- Yang, K., Guo, Y., and Ding, M. D. (2015). On the 2012 October 23 Circular Ribbon Flare: Emission Features and Magnetic Topology. *Astrophysical Journal*, 806(2):171.
- Yashiro, S., Akiyama, S., Gopalswamy, N., and Howard, R. A. (2006). Different Power-Law Indices in the Frequency Distributions of Flares with and without Coronal Mass Ejections. *Astrophysical Journal, Letters*, 650(2):L143–L146.

Yokoyama, T., Akita, K., Morimoto, T., Inoue, K., and Newmark, J. (2001). Clear Evidence of Reconnection Inflow of a Solar Flare. *Astrophysical Journal, Letters*, 546(1):L69–L72.

Zweibel, E. G. and Yamada, M. (2009). Magnetic Reconnection in Astrophysical and Laboratory Plasmas. *Annual Review of Astron and Astrophys*, 47(1):291–332.